A FLAG-BASED ALGORITHM FOR EXPLOSIVES DETECTION IN SEA-LAND CARGO CONTAINERS USING ACTIVE NEUTRON INTERROGATION

by

Adrienne Lynn Lehnert

A dissertation submitted in partial fulfillment
of the requirements for the degree of
Doctor of Philosophy
(Nuclear Engineering and Radiological Sciences)
in The University of Michigan
2012

Doctoral Committee:

Professor Kimberlee J. Kearfott, Chair
Professor Edward D. Rothman
Associate Professor Sara A. Pozzi
Assistant Professor Michael R. Hartman

Acknowledgements

This work would not have been possible without the input and advice of my advisor Professor Kimberlee Kearfott. Valuable input was also provided by Professor Ronald Fleming, Professor Edward Rothman, Assistant Professor Michael Hartman, Associate Professor Sara Pozzi and Dr. Marek Flaska. In particular, Dr. Hartman's help with the neutron generator, Dr. Pozzi's generosity with neutron detectors, melamine, and the use of post-processing software, and Dr. Flaska's expertise with PoliMi, Matlab, and neutron detectors were essential. Eric Miller and Jennifer Dolan helped with the post-processing software. Further assistance with data analysis was provided by Zachary Whetstone.

I would like to thank my family for their love and support, especially my husband Matthew for putting up with all the ups and downs of a dissertation and my mother, Dr. Stella Hansen for showing it could be done. I also would not have finished if not for the support, sanity, and occasional spare bed from John Harvey, Nick Touran, Candi and Paul Vollweiler, Sonal and Willy Kaye, and Jason and Hiroko Stolaruk.

This research was performed under appointment to the Department of Homeland Security (DHS) Scholarship and Fellowship Program, administered by the Oak Ridge Institute for Science and Education (ORISE) through an interagency agreement between the U.S. Department of Energy (DOE) and DHS. ORISE is managed by Oak Ridge Associated Universities (ORAU) under DOE contract number DE-AC05-06OR23100. All opinions expressed in this paper are the authors' and do not necessarily reflect the policies and views of DHS, DOE, or ORAU/ORISE.

Table of Contents

List of Figures

List of Tables

List of Appendices

Abstract

The high volume and minimal screening of sea-land cargo containers presents a vulnerability in which explosive devices may be smuggled across national borders. Fast neutrons are a strong candidate for use in container screening due to their high target penetration and ability to discriminate between materials of low atomic mass, such as explosives and non-metallic container contents. An algorithm has been developed that uses flags, calculated from specific measurements of the reflected neutrons and photons produced during active neutron interrogation, to discern explosives hidden in cargo containers. Steps in algorithm development included Monte Carlo simulations for scatter characterization, identification of flags in idealized scenarios, refinement of flags in realistic scenarios, combining the flags into a detection algorithm, and evaluation of the algorithm and associated detection system. Simulations compared favorably with small-scale neutron scatter measurements using the explosives-surrogate, melamine. The detection algorithm included corrections for different types of cargo contents and cargo inhomogeneity, surrounding environment, and realistic neutron sources and radiation detectors. The proposed algorithm has two variations, one of which can be easily implemented with today's technology. The proposed scanning system utilizes a shielded 14.1 MeV neutron generator, eleven large liquid scintillators neutron detectors, and several inorganic scintillators for photon spectroscopy. This system should cost less than $1M to install and dose estimates fall well within acceptable levels for both operators and smuggled persons. Algorithm performance has been quantified with various explosive sizes and positions, as well as heterogeneous cargo configurations, with typical minimum detectable amounts not exceeding 200 kg.

Chapter 1: Introduction

The detection of hidden explosives has been an area of intense study for several decades. A solution has become more urgent with the increase of terrorism and other violence perpetrated independent of any national government. One particular vulnerability is the enormous volume of sealed shipping container traffic entering the country at busy seaports. The vast majority of these containers pass by unsearched, providing an easy route for the passage of conventional explosives. Most of the current methods of contraband scanning depend on X-ray images of cargo and the use of explosive-sniffing dogs. However, dogs have several crucial limitations and X-ray scanning is unable to clearly distinguish the presence of most explosive materials due to their lack of high atomic massed components. Furthermore, the large size of cargo containers makes X-ray scanning very difficult. One solution to this problem is to use fast neutron interrogation, as the neutrons react strongly with low-Z elements and are highly penetrating, especially of metallic objects. Possible strategies in fast neutron interrogation include thermal neutron activation (TNA) measurements, detection of the photons produced in neutron inelastic scatter, and measurements of the scattered neutrons.

The method proposed here is unique in that it combines the information provided by both the scattered neutrons and scatter-produced characteristic photons at all scatter angles through specific calculations that provide a yes/no decision point about the presence of explosives. These specific calculations, or flags, are formed from features such as the ratios of photon peaks, ratios of elastic or inelastic neutron scatter peaks at specific scatter angles, or the total number of neutrons that undergo backscatter when interrogating an unknown target. Other flags are calculated from more general measurements, such as the ratio of neutron counts at two angles, the number of certain characteristic photons normalized by neutron count ratios, or the number of high- or low-energy neutrons measured at specific angles. Still other flags are formed directly from the neutron detector pulse height distributions. These flags have then been combined to take into account the type of cargo, different explosive materials, and correcting for inhomogeneities in the cargo container.

Throughout this document the flags are described using the terms “flag strength” and “flag value". As mentioned above, a flag is a specific calculation made from the neutron or photon tallies in a given simulation. Flag value (*f*) refers to the actual numerical value of the flag under these particular conditions. The mathematical definition of flag value will change according to the particular flag, but the general form is:

$$f = \frac{n(E_1, A_1)}{n(E_2, A_2)} \quad \text{or} \quad f = \frac{p(E_1)}{p(E_2)}, \tag{1.1}$$

in which $n(E,A)$ is the neutron tally at a particular energy or energy range and angle and $p(E)$ is the photon tally at a particular energy or energy range. Some neutron-based flags may use the same energy for E_1 and E_2. Flag strength (S) is a quantity that was used when determining which flags should be used to find explosives. This quantity is defined as:

$$S = \left| \frac{f_e - f_i}{f_i} \right|, \tag{1.2}$$

in which the flag strength (S) is a function of the flag value with only inert cargo, (f_i) and the flag value with an explosive present (f_e). The flag strength may be thought of as the absolute value of the percent difference between cases with and without explosive. Flags with the greatest flag strength are the most sensitive to the presence of explosive and are potentially the best flags to use in a detection algorithm. Uncertainties in flag value and flag strength are determined by propagating the statistical error provided in the simulation output through the flag value and flag strength calculations.

This dissertation describes the process of algorithm development and how it fits into the wider scheme of explosives detection, including a review of current detection technologies. Early chapters involve the characterization of fast neutron scatter in single-element targets as well as compounds such as the explosive RDX ($C_3H_6N_6O_6$), air, water, vegetable oil, and steel. Laboratory measurements using a D-D neutron generator and small scatter targets in a small-scale screening scenario confirmed the results of simulations. Later simulations combined explosive and inert cargo in idealized conditions to find the best places in the neutron and photon spectra to find potential flags. These flags were then tested under more realistic conditions, including a shielded neutron generator, surrounding environment, different types of cargo, and a realistic distribution of cargo within a container.

Finally, the flags were combined into a detection algorithm that took into account several variables in typical screening scenarios, such as cargo type and cargo inhomogeneities. This detection algorithm has been integrated into a preliminary screening system design containing a shielded D-T neutron generator, seven liquid scintillation neutron detectors, and at least one scintillator-based detector for photons. This system would measure the neutrons and photons produced at during neutron interrogation at several points along the length of the container, calculate flag values at each of these points, and use the flag-based algorithm to determine if explosives are present.

Chapter 2: The Detection of Explosive Materials: Review of Considerations and Methods

Abstract

With increasing terrorist threats of different types, explosives detection for various types and forms of explosives is of growing interest. This paper reviews the broad array of possible methods of explosives detection, both using nuclear and non-nuclear based instruments, with their advantages and disadvantages for different scenarios. An explanation of the fundamental physics for each approach is accompanied by its general applicability and citations to the relevant scientific literature.

Introduction

The issue of explosives detection, although hardly new, has become increasingly pertinent with the rise in successful terrorist attacks in recent years and subsequent tightening of security. The problem is complicated by the fact that hidden explosives may come in many chemical forms and configurations and threaten security under vastly differing circumstances. Detection scenarios may range from buried landmines and improvised explosive devices (IEDs) concealed along roadways to small bombs hidden in the mail or under clothing to large vehicle-mounted devices capable of destroying large structures. Especially sensitive is the security needed at airports due to the vulnerabilities of in-air aircraft to explosive damage and terrorism. Also of concern are explosives smuggled across national borders in sea-land shipping containers. All of these scenarios differ considerably in the potential size of the explosive device, but all require screening methods of high specificity, with a negligible number of missed positives and a low false positive rate. Also necessary in the vast majority of screening scenarios are short examination times, as these scenarios require large throughputs. Many different strategies of explosives detection have been studied, with varying results. These methods exploit several different characteristics of explosive materials, including geometry, auxiliary components, smell, density, and chemical composition.

This review paper outlines some of the characteristics of explosives that either facilitate or detract from their detection and summarizes most of the vast array of detection methodologies in use today. These methodologies may be based on the trace detection of small amounts of explosive material, or the detection of larger amounts of bulk explosives. Included are methodologies ranging from chemical trace technologies, biological systems, and interrogation by both ionizing and non-ionizing radiation. Advantages and disadvantages of all included methods are discussed.

Characteristics of Common Explosive Materials and Devices

One of the traditional methods of explosive weapons detection relies on the presence of metallic components such as casings or detonator components. Trained operators can use metal detectors or traditional X-ray machines to scan for suspicious material. However, many explosive devices contain little or no metal and are therefore difficult to discern from surrounding material in that fashion. In such cases it is necessary to detect the explosives material itself.

Many explosive materials have a density between that of most innocuous material and metallic objects. This means that explosive devices would be discernable on a typical X-ray, if the shape of the explosive material was such as to arouse suspicion. However, there is no typical shape for explosive devices, as evidenced by recent attempts to smuggle explosives in shoes or under clothing, and without a priori knowledge it would be very difficult to distinguish most explosive materials using only the density knowledge provided by a traditional X-ray machine. Another characteristic of most explosive materials is that these compounds tend to be quite “sticky,” in that residue tends to cling to hands, clothing, and other surfaces that come in contact with the explosive [1]. Several explosives-detection techniques exploit this fact through the use chemical trace analysis of air sampling or physical swabbing of potential carriers of explosives residue.

The most successful explosives detection methods all rely on the chemical composition of the energetic materials themselves. This may include the response in the olfactory organs of canines or rats, the ion mobility present in explosive vapors, or the characteristic ratios of the elements hydrogen, carbon, oxygen, and nitrogen. These ratios have proven especially useful, as most explosive materials have relatively high nitrogen and oxygen densities as well as correspondingly low amounts of carbon or hydrogen [1,2]. It is this high concentration of nitrogen that has pushed the development of several methods enlisting nuclear science.

Other explosive materials, such as gasoline, black powder, or peroxide-based liquid explosives, do not contain any nitrogen, and will therefore slip past a vast majority of the nuclear-based detection methods. It is therefore often necessary to use several complementary methods in many security-screening scenarios. These methods can be divided into those that detect trace amounts of explosive residue and those that detect the entire explosive device, known as a bulk explosive detection method.

Overview of Non-Nuclear Explosives Detection Methods

Chemical trace-based explosives detection methods

Ion mobility spectrometry

Many of the explosives-detection techniques rely on the detection of trace amounts of nitro-organic explosive materials that cling to surfaces such as clothing, skin, or luggage. One of the most common applications of this principle is found in ion mobility spectrometry (IMS). The ions needed for IMS may be collected through both physical swiping of the sample or through the use of air “puffers” and vacuum collection that gather trace residue from the clothing and skin of people passing through a checkpoint. The IMS method exploits the proclivity of explosive materials to form stable, negative ions at atmospheric pressure. These ion are passed through a weak magnetic field and are then characterized by their movement in the field, which will depend on the ions molecular mass as well as the magnitude of the negative charge.[3]

Gas chromatography

One way to improve the efficiency of many trace detection techniques is to maximize the number of negative ions, generally nitro (NO_2) or nitrate (NO_3) groups, collected from the explosives residue. One way of accomplishing this is through gas chromatography (GC), a process that separates a mixture of different substances by type. In GC, a vapor sample is passed through a chromatographic column, a hollow tube packed with beads covered by a substance that reacts at a different rate with different substances, causing the different molecules to exit at different times. This process isolates the negative ions present in explosive residue, which may then be detected using methods such as electron capture, mass spectroscopy, flame ionization, chemiluminescence, or surface acoustic wave methods [1,3].

Electron capture detection

In electron capture, a method usually applied to detection of explosives in soil, an electron capture detector (ECD) uses a beta source, usually ^{63}Ni, whose particles collide with detector gas to produce a reference current at the detector anode [4]. This steady stream of low-energy electrons provides a reference current. When negative ions from the GC, such as those produced by explosives, reach the detector active volume they are swept out in a voltage pulse, which maintains a constant current. The frequency of these pulses is proportional to the concentration of negative ions [4].

Mass spectroscopy

In mass spectroscopy (MS), the relative amounts of a sample's component elements are determined by passing ions through a magnetic field and measuring atomic mass by the amount of displacement. MS is highly specific and shows promise in trace explosives detection, though is rarely used due to high cost, complexity and the necessity of maintaining a high vacuum. Furthermore, detection limits are highly dependent on the chemical structure of the explosive [1,5]. Recent advancements in faster gas chromatography and lower detection limits of mass spectroscopy have improved measurement times and reduced the need for pre-concentration [6].

Flame ionization

A flame ionization detector uses a hydrogen-air flame that ionized carbon in the sample, which is then detected through current induced in the nearby collector place [7]. This method is not widely used in explosives detection, as it is sensitive to carbon, but not nitrogen.

Chemiluminescence

Chemiluminescence is based on the characteristic emission of radiation, by a substance when in an excited electronic state, as triggered by an exothermic chemical reaction [1,8]. This principle has been applied to explosives detection by creating nitric oxide (NO) from the explosive molecules, which then react with ozone (O_3) in the detector to form excited nitrogen dioxide (NO_2^*) molecules. The excited NO_2^* molecules then fall back to ground state, releasing infrared radiation with a frequency between 0.6-2.8 μm [1].

Surface acoustic wave

Surface acoustic wave (SAW) detectors are based on the principle that when materials of different masses condense on the surface of a piezoelectric crystal, the resonant frequency with respect to acoustic waves of the crystal will change [1]. For explosives detection, the several piezoelectric crystals are coated with film that preferentially absorbs molecules from different types of explosive compounds. When an explosive is present the increased condensation will change the resonant frequency of at least one of the crystals, creating a response pattern that is easily recognizable. Many SAW systems rely on equipment that pre-concentrates the explosive material, such as a GC system, though it is not always required [1,9].

Antibody

Another vapor-detection technique is based on the use of highly specific antibodies. This system works by coupling the antibodies to a fluorescent-labeled explosive analog. When an explosives molecule is present in the sample airstream, it will displace the labeled analog, which is easily detectable downstream [10]. This method is fairly inexpensive and fast, as well as easily automated, but antibodies for every possible explosive material compound variant are needed.

Human and biological-based methods

Animal

Trained dogs with experienced handlers are commonly used for explosives detection. Advantages of canine screening include reliable and efficient operation in a wide range of situations, including airports and border crossings [11]. Disadvantages include the extensive training and “calibration” time, as well as the limitations associated with use of animals, such as rest, feeding, and medical care. More recently, researchers have explored the use of other animals, such as trained rats [12] or conditioned honeybees [13].

Manual inspection

In scenarios for which canine screening is impractical, or in order to confirm a positive identification, a trained professional often performs a manual inspection of the possible explosive. One example of this is the established method of humanitarian landmines using a combination of metal detectors and probing rods in the hands of experienced personnel [14,15]. Although well established, such methods are time consuming and pose a considerable risk to personnel.

Non-ionizing radiation based methods

Electromagnetic Induction

Many explosives-detection techniques are based on electromagnetic induction metal detection [10]. Metal detectors based on electromagnetic induction function through use of a pulsing electromagnetic field that stimulates creation of an electromagnetic field in any nearby conducting objects. This induced magnetic field may then be detected either in the transmitter coil, or in a separate receiver coil, where the changing magnetic field induces a measurable current in the receiver. The obvious disadvantage to using metal detectors is that the lack of significantly large metal components in many explosive devices makes them difficult to discern using only electromagnetic induction techniques. However, they may be used in conjunction with a bulk detection method, increasing the detection efficiency of the bulk detection method [16].

Radar interrogation

Radar interrogation is useful in determining the presence, proximity, and size of objects within interrogation range through the reflection of radio waves off solid objects. When the high-energy radio waves are focused under the ground, and reflection from the surface filtered out, the presence of underground objects may be discerned by examination of the reflected radio waves due to the different material densities and changing interaction with radar waves at the object boundary. This forms the basis for one of the most promising methods for detecting buried explosives, ground-penetrating radar, when used with complementary technology, such as neutron backscatter or other bulk detection method [17,18].

Nuclear magnetic resonance

Nuclear magnetic resonance analysis techniques are based on the principle that the nuclei of isotopes containing an odd number of nucleons have a half-integer total spin, and will therefore align themselves along the magnetic field lines when subjected to an external magnetic field. Magnetic resonance is determined by perturbation of the aligned nuclei by a specific radiofrequency pulse, related to the difference between ground and excited state, and measuring the rate of return to alignment. The resonance frequency of this magnetic moment depends on the strength of the external magnetic field and the hydrogen content of the substances involved. Nuclear magnetic resonance (NMR) techniques, especially those that concentrate on hydrogen content have been investigated for explosives detection [19]. However, as samples must pass through the powerful magnetic coils of the aligning magnetic field and any metallic shielding completely obscures the target, commercial application of this technology has proven difficult [1].

Nuclear quadrupole resonance

Like NMR, nuclear quadrupole resonance (NQR) is another technique that relies on the resonance of target nuclei alignment with incident radiofrequency radiation. However, unlike NMR, NQR does not require a strong external magnetic field to measure nuclei with spin ≥1, such as ^{14}N, ^{35}Cl, or ^{63}Cu. These nuclei have a distinct quadrupole moment and show a distinct precession in the internal electric field of crystalline solids containing the elements. The rate of precession depends on the type of material. NQR interrogation equipment contains a radiofrequency (RF) power source, a coil to produce the excitation RF pulse and a receiver coil, along with other support components. When a radiofrequency pulse of the same frequency as characteristic precession interrogates a target material, the changing angle of the nuclei will induce an electric potential in the receiver coil. As this method is very specific, prior knowledge of the type of explosive, as may be the case in landmine detection, is helpful [20]. NQR has the advantage of being specifically sensitive to the material of choice, but is unable to sense liquid explosives and can easily be completely obscured by metallic shielding. Furthermore, NQR is sensitive to RF interference, especially when scanning for the common explosive TNT, as the resonant frequency of TNT falls within the amplitude modulated (AM) radio frequencies [20].

Terahertz imaging and spectroscopy

Terahertz (THz) radiation, also known as sub-millimeter radiation or T-rays, refers to the range of the electromagnetic spectrum between high-energy microwaves and the far infra-red wavelengths. As such, they easily penetrate materials such as clothing and paper, while are absorbed by metal, water, and other dense media. The THz radiation used in explosives-screening scenarios is generally produced by illuminating a voltage-biased ultrafast semiconductor, such as GaAs, with an ultrashort pulsed near-infrared laser, such as titanium-sapphire (Ti:Al_2O_3). The movement of the charge carriers in the semiconductor produces THz radiation, which is then emitted from an integrated antenna. THz radiation is detected using a similar semiconductor-laser combination, as the THz radiation will induce a measurable current in the unbiased semiconductor with amplitude proportional to THz energy [21].

Advantages of using terahertz interrogation include a higher penetrability than other non-ionizing radiation, the unique spectral response of certain materials to electromagnetic waves in the THz range, and the fact that, as it is non-ionizing, will not provide a radiation dose [21,22]. Furthermore, THz radiation may be used to both image target structure and provide spectral fingerprints unique to the material of interest. The unique spectral fingerprints come from the resonant absorption of THz radiation when the energy of the incoming radiation matched that of the rotational motions of dipoles in the material or the vibrations of atoms within the molecular lattice. However, metallic objects are opaque to terahertz radiation, and therefore metallic shielding may prevent a thorough investigation. Additionally, although crystalline high explosives have characteristic signatures, homemade or improvised devices do not. THz imaging and spectroscopy is also limited by current technology related to stand-off distance [21].

Millimeter wave interrogation

Recent deployment of full-body scanners based on millimeter wave technology at several airports has brought this technology into intense public scrutiny. Millimeter waves, which lie right below terahertz radiation and in the upper frequencies of the microwave range in the 30-300 GHz range of the electromagnetic spectrum, are able to penetrate through most clothing, but will reflect off tissue or concealed objects to produce images with resolutions of 1-10 mm [23]. Like other microwave devices, millimeter waves may be produced through use of vacuum tube devices, such as magnetrons, or solid-state devices, and are then directed and focused with an antenna. In the systems currently deployed in several airports, the millimeter waves are transmitted over a person's body by two rapidly rotating antennas [24,25]. The reflected millimeter waves are detected in much the same was as other microwaves, with broadband detectors and antenna-coupled bolometers.

Recent applications seek to create three-dimensional holographic images through use of two simultaneously-emitting transmitting antennas as they circle the target body. Advantages of this method include excellent spatial resolution and the lack of radiation dose due to the use of non-ionizing radiation. Currently, the most prominent deterrence to widespread deployment of millimeter wave imaging technology are the privacy concerns associated with human scanning [24]. The controversy associated with privacy concerns stems from the high-resolution holographic images formed by the distinct reflection of millimeter waves reflecting off tissue. Millimeter wave holography produces recognizable images of individuals and therefore presents significant privacy concerns, especially in the imaging of minors. Current protocols in airports call for the blurring of facial features and anonymity of image screening by personnel. Other safeguards include the fact that the images, seen on a monitor in another room, are never stored, transmitted, or printed and are deleted immediately after viewing [25].

Nuclear-Based Methods for Explosives Detection

Ionizing photon interrogation

Photon transmission

X-ray transmission imaging has been in use for many years at screening checkpoints, but is mainly concerned with finding the metallic objects associated with explosive device and not the explosive material itself, as the relatively low-Z components of explosives show very low contrast on transmission X-ray images [1]. Photon transmission techniques are limited to the scanning of luggage and other inanimate cargo due to the potentially high radiation doses. Isolation of the signals of low-Z materials, such as explosives, is improved with the use of two different energies of X-rays. By contrasting the X-ray attenuation at two specific different energies it is possible to isolate materials with a certain equivalent Z as explosives [2]. The most sophisticated method relying solely on transmitted X-rays is computed tomography (CT) [26]. CT, which is widely used in the medical fields and could prove useful in explosives detection, would still only provide information on localized electron density and may therefore alarm with inert materials of a similar electron density to that of explosives, such as many plastics [2]. It has been shown that dual energy CT is better able to discern explosives than single energy CT, though difficulties still remain [27]. Similarly, gamma-rays may be used to create transmission images, though these techniques have the same problems telling the difference between low-Z materials [1].

Photon scattering

Backscatter X-ray techniques are generally better at discerning low-Z materials than transmission X-ray methods are, as the larger relatively higher Compton scatter component of photon interactions in low-Z materials means that more photons are scattered than transmitted [1,28]. Direct backscatter imaging, while very simple to implement using an X-ray source and imaging plate, also suffers from difficulty in differentiating between explosives and other low-Z materials due to their very similar electron density. Several other X-ray scatter techniques have been studied including X-ray diffraction, which provides information on target crystalline structure [29], and coded aperture methods, especially useful in landmine detection [30].

One way of improving photon scatter methods is to employ the use of coded aperture masks when creating an image of the target using scattered photons. The masks, containing a known configuration of transparent and opaque pixels, can focus incoming photons in much the same way as a pinhole camera. The large number of transparent pixels works to drastically increase the number of photons collected, but create a pattern of overlapping images that must be deconstructed using computer algorithms. This is an effective way of improving backscatter photon images [31,32]. Another way to improve backscatter photon images is through use of a Compton camera, which uses a combination of photon scatter in one detector plane and absorption in another detector plane to localize the scatter event in the target [27,30]. Several systems have been deployed in airports that are used to screen passengers through the use of backscatter X-ray imaging. As in the case of millimeter wave imaging, several privacy issues have been raised [25].

Gamma-ray resonant absorption

The photon-based techniques discussed thus far have depended on changes in target electron density, and therefore atomic number, in finding hidden explosives. Another way of finding explosives is to exploit particular nuclear reactions unique to nitrogen instead of relying solely on relative electron density. As these methods do not have as good an imaging capability as some of the techniques discussed above, the two methods are often combined.

One such method used the highly probable, 2 b cross section, nuclear resonance absorption of ^{14}N of 9.17 MeV gamma rays [33,34]. In this technique, monoenergetic gamma rays are transmitted through the target and a high level of attenuation indicates the presence of large amounts of nitrogen. Although this method is well understood theoretically, difficulties arise in the production of monoenergetic 9.17 MeV gamma rays [28]. Another possible reaction of choice is the positron emission of ^{13}N via the $^{14}N(\gamma,n)^{13}N$ reaction that occurs with a when a gamma ray of energy at least 10.6 MeV is used to interrogate the target and the resulting coincident 511 keV photons are detected [35]. The main disadvantage of this method is the low interaction probability, 1 mb, of the $^{14}N(\gamma,n)^{13}N$ reaction, which is more than twenty times smaller than the analogous reaction in copper, a common component in electronics, and therefore easily interferes with explosives detection [28].

Nuclear resonance fluorescence

The method of nuclear resonance fluorescence (NRF), in which an incident gamma ray excites target nuclei to an energetic state, from which they emit characteristic gamma rays as they fall back to ground state. Strengths of NRF include its ability to quantify the presence of carbon, nitrogen, and oxygen, and will not activate cargo, though it is blind to hydrogen concentration. Other difficulties include the production of high-energy monoenergetic gamma rays of the specific energies needed [28].

Neutron interrogation methods

Due to their highly penetrating nature, and the fact that they interact directly with target nuclei, active neutron interrogation has been widely studied as an explosives detection technique. Various strategies have employed either fast [36] or thermal neutrons [28,37]. The interrogating neutrons may be monoenergetic or widely varying in energy. Fast neutron interrogation may be based on one of three different neutron interactions with target materials: fast neutron absorption, neutron inelastic scatter (NIS), and neutron elastic scatter (NES). Other technologies, such as associated particle imaging (API) and fast-pulsed neutron generators discussed below have become increasingly relevant as the technology associated with neutron generators and the detection of the associated particles as improved in the past few years.

Thermal neutron activation

Some of the best and longest-studied explosives detection strategies are based on thermal neutron activation (TNA) [37]. Most of these techniques involve incident fast neutrons that thermalize inside the target, are absorbed through (n,γ) reactions, and emit characteristic gamma rays, as the use of incident fast neutrons improves target penetration in larger targets. In some cases, the use of additional moderating material increases the production of these characteristic gamma rays, while decreasing personnel dose [38]. The most important capture gamma for explosives detection is the 10.8 MeV photon from the activation of ^{14}N [36,38,39]. The high-energy photons produced via TNA are easily detectable, as there is little neutron background in the 10 MeV range. However, reaction cross sections for neutron activation reactions are relatively low and the method leaves target materials mildly radioactive [40,41].

Neutron backscatter

Thermal neutrons have also been used in backscatter measurements that screen for buried explosives [16,42,43,44]. In this backscatter technique, fast neutrons, usually from an isotopic source, are directed towards the ground and the thermal neutron flux emanating from the surface is measured. This method relies on the principle that hydrogen is more efficient at moderating fast neutrons to thermal energies than heavier elements, such that changes in the amount of reflected thermal neutrons is indicative of target hydrogen content.

Thermal neutron imaging

Transmission imaging using thermal neutrons is a well-established technology that is often used to image hydrogenous matter inside metallic or other high-Z materials. In traditional neutron radiography, spatial maps of neutron attenuation factors are created by passing monochromatic thermal neutron beams through the target. Recent advances, such as the use of polarized neutron beams and Bragg-edge radiography have improved spatial resolution and allowed exploration of target interior magnetic fields [45]. Thermal neutron transmission imaging may be used to image small objects for the presence of hydrogenous or other highly neutron-absorbing materials such as boron or cadmium [28]. However, thermal neutrons are only able to penetrate a few centimeters into most target materials, so incident fast neutrons are more useful to scan large objects.

Fast neutron absorption

In fast neutron absorption, as in thermal neutron absorption, the incident neutron is absorbed into a target nucleus, which then decays, emitting a characteristic photon. Although this photon is generally high-energy and therefore easily detectable, neutron absorption is highly unlikely at fast incident neutron energies, so one must either wait for the neutrons to thermalize in the target or use a large incident flux. This creates problems in personnel dose, large amounts of shielding, and induced target radioactivity [2].

Neutron inelastic scatter

Probably the most common application of fast neutron interrogation depends on the detection photons produced in inelastic neutron scatter [36,46,47]. In this interaction, fast neutrons collide with target nuclei and excite them to a higher energy state. When the target nuclei decay back to their ground state, characteristic photons are emitted. Many of the most relevant photons in neutron inelastic scatter may be seen in Table 2.1. Advantages of this method include a higher interaction probability, and therefore lower personnel dose, as compared with neutron absorption and the distinct photons produced during nuclei de-excitation.

Neutron elastic scatter

The final way in which fast neutrons interact with target nuclei is through fast neutron scatter. In this reaction, by far the most common at fast neutron energies, no photon is produced as the neutron scatters off the target, conserving kinetic energy and momentum. Use of neutron elastic scatter depends on the collection of pulse height distributions of scattered neutrons with sufficient energy resolution to distinguish between the scattered neutrons from carbon, nitrogen, and oxygen collisions. The advantage of this method is that an accurate measurement of a singly-scattered neutron’s energy and scatter angle provides clear knowledge of the target’s atomic mass [46,48,49]. In this way a clear picture of a target’s relative amounts of carbon, nitrogen, and oxygen, which is characteristic of the material, may be determined.

Advancements in neutron interrogation: pulsed neutron sources

In recent years several innovations have increased the feasibility of widespread application of neutron-based explosives detection techniques. Several of the discussed methods have the potential to improve greatly if time-of-flight calculations are used to minimize signal noise due to multiple scatters, localize the relevant neutron scatter reactions in the target, as well as provide more accurate information on neutron energy. New advances in sub-nanosecond timing of the pulsed neutron generator have made this possible [50,51]. This information on collision location allows for an elimination of much of the neutron background scatter and vastly improved imaging capabilities [36,52].

Tagged neutrons and associated particle imaging

One of the problems associated with time-of-flight, and therefore neutron energy, calculations is the expense of reaching sub-nanosecond pulses from neutron generators as well as the difficulty in collimating neutrons [36]. Another innovation driving the use of neutron interrogation in explosives detection is the development and optimization of API technology. API techniques are based on measurement of the associated ^{3}He or ^{4}He nuclei produced in the D(D, n)^{3}He or D(T, n)^{4}He reactions in D-D or D-T neutron generators. API technology allows time-of-flight neutron calculations by “tagging” the neutron as it is produced by measuring the angle and exact timing of the coincident alpha particle emitted in the opposite direction from the neutron [53,54]. APIs are generally used in conjunction with neutron inelastic scatter techniques [55], though have also been applied the TNA and neutron radiography techniques [56], or in conjunction with other screening technology [57,58]. Applications range from baggage screening

[59], automotive screening [60], cargo containers [61,62], to even underwater applications [63].

Conclusions

As has been shown, there is enormous variety in the different technologies used to find hidden explosives, ranging from trained animals, chemical trace analysis, to interrogation with ionizing radiation. A summary and comparison of these methods may be found in Table 2.2. The enormous range of target environments, from buried landmines, air and mail cargo, to human screening means that no one method is superior to others in all situations. The constraints of fast measurement times, negligible false negatives, minimal false-positives and expensive equipment combine to define a very difficult problem that will remain an issue for some time to come. Perhaps the best solution would come in the form of hybrid methodologies that make use of as much information possible and tailored to the screening scenario.

Tables

Table 2-1. Relevant photons in neutron inelastic scatter.

Isotope	De-excitation photon (MeV)
^{1}H	none
^{12}C	4.43
^{14}N	1.64, 2.31, 5.11
^{16}O	6.13

Table 2-2. Summary of explosives detection methods.

	Applications	Detection mechanism	Major advantages and disadvantages
Ion Mobility	luggage, mail	Concentration of NO_2^- and NO_3^- ions	Specific, difficulties in collection of sufficient ions
Gas chromatography	luggage, mail	Concentration of NO_2^- and NO_3^- ions	Better ion collection, slower analysis
Electron capture	luggage, mail	Concentration of NO_2^- and NO_3^- ions	High sensitivity, cannot tell exact type of explosives
Mass spectroscopy	luggage, mail	Relative concentrations of C, N, O as signatures	Highly specific, complex and expensive equipment
Flame ionization	luggage, mail	Concentration of carbon	Fast, limited sensitivity to nitrogen content
Chemiluminescence	luggage, mail	Concentration of nitrogenous compounds	High sensitivity, cannot tell exact type of explosives
Surface acoustic waves	luggage, mail	Presence of specific explosive compound	Specific to particular explosive compounds
Antibody	luggage, mail	Presence of specific explosive compound	Specific to particular explosive compounds
Animal	almost all	Olfactory signal of explosive compound	Fast and inexpensive, time-intensive training needed
Manual inspection	almost all	Recognition by trained personnel	Inexpensive, slow, dangerous to operators
	Non-ionizing radiation interrogation		
Electromagnetic induction	luggage, buried, human	Presence of metal components	Fast, inexpensive, limited to metallic objects
Radar interrogation	buried	Suspicious outline in radar image	Mainly confirmatory for metal detector
Nuclear magnetic resonance	luggage, mail	Suspicious outline in hydrogen concentration image	Expensive, requires strong magnetic field
Nuclear quadrupole resonance	buried, luggage, mail	Resonance signal of nitrogen in specific explosive compounds	N sensitive, no external magnetic field, highly specific, RF interference
Terahertz	human	Suspicious outline in image formed by THz image	Good spatial resolution, non-ionizing, privacy concerns
Millimeter wave	human	Suspicious outline in millimeter wave image	Good spatial resolution, non-ionizing, privacy concerns

Table 2-2. Summary of explosives detection methods (continued).

	Applications	Detection mechanism	Major advantages and disadvantages
Ionizing radiation (nuclear) interrogation			
Photon transmission	almost all except buried and human	Suspicious outline in electron-density image	Well established, difficulty in discerning low-Z materials
Photon scattering	almost all except human	Suspicious outline in electron-density image	Difficulty in discerning low-Z materials, though better than photon transmission
Gamma-ray resonant absorption	almost all except human	Concentration of ^{14}N in target	Good ^{14}N detection, difficult to produce incident photons
Nuclear resonance fluorescence	almost all except human	Relative concentrations of C, N, and O	Good ^{14}N detection, difficult to produce incident photons, competing reactions
Thermal neutron activation	luggage, mail, other small cargo	Concentration of ^{14}N in target	Easily detectable signal, high flux and latent target radioactivity
Neutron backscatter	buried	Changing flux of reflected neutrons due to presence of H	Inexpensive source and detector, signal not very specific
Thermal neutron imaging	luggage, mail, other small cargo	Suspicious outline in thermal neutron attenuation image	Low target penetrability
Fast neutron absorption	luggage, mail, other cargo	Concentration of ^{14}N in target	Easily detectable signal, high flux and latent target radioactivity
Neutron inelastic scatter	luggage, mail, other cargo	Relative concentrations of C, N, and O	Clear signal, difficulty in localization of interactions
Neutron elastic scatter	luggage, mail, other cargo	Relative concentrations of C, N, and O	Highly probably reactions, good neutron spectroscopy needed

References

1. C. Bruschini, Commercial systems for the direct detection of explosives (for explosive ordnance disposal tasks), École Polytechnique Fédérale de Lausanne (EPFL), 2001.
2. E. Hussein, “Detection of explosive materials using nuclear radiation: a critical review”, P. SPIE 1736 (1992) 130-137.
3. J. Yinon, S. Zitrin, “Modern methods and applications in analysis of explosives”, John Wiley and Sons Ltd., West Sussex, England, 1993, 42-66.
4. M.E. Walsh, “Determination of nitroaromatic, nitramine, and nitrate ester explosives in soil by gas chromatography and an electron capture detector”, Talanta 54 (2001) 427-438.
5. M.E. Sigman, C.-Y. Ma, “Detection Limits for GC/MS Analysis of Organic Explosives”, J. Forensic Sci. 46 (2001) 6-11.
6. O. Collin, C.M. Zimmermann, G.P. Jackson, “Fast gas chromatography negative chemical ionization tandem mass spectrometry of explosive compounds using dynamic collision-induced dissociation”, Int. J. Mass Spectrom. 279 (2009) 93-99.
7. J.T. Scanlon, D.E. Willis, “Calculation of flame ionization detector relative response factors using the effective carbon number concept“, J. Chromatogr. Sci. 23 (1985) 333-340.
8. A.M. Jimenez, M.J. Navas, “Chemiluminescence detection systems for the analysis of explosives”, J. Hazard. Mater. 106A (2004) 1-8.
9. G.K. Kannan, A.T. Nimal, U. Mittal, R.D.S. Yadava, J.C. Kapoor, “Adsorption studies of carbowax coated surface acoustic wave (SAW) sensor for 2,4-dinitro toluene (DNT) vapour detection“, Sensor. Actuator. B-Chem. 101 (2004) 328-334.
10. S. Singh, M. Singh, “Explosives detection systems (EDS) for aviation security (review)”, Signal Process. 83 (2003) 31-55.
11. K. Furton, L. Myers, “The scientific foundation and efficacy of the use of canines as chemical detectors for explosives”, Talanta 54 (2001) 487-500.
12. R. Verhagen, C. Cox, M. Mauchangu, B. Weetjens, M. Billet, Preliminary results on the use of Cricetomys rats as indicators of buried explosives in field conditions., in: GICHD (Ed.) Mine detection dogs: training, operations and odour detection, Geneva, Switzerland, 2003, pp. 175-193.
13. J.A. Shaw, N.L. Seldonridge, D.L. Dunkle, P.W. Nugen, L.H. Spangler, “Polarization lidar measurements of honeybees in flight for locating landmines”, Opt. Express 13 (2005) 5853.
14. M.K. Habib, “Mine clearance techniques and technologies for effective humanitarian demining”, J. Mine Action, 6 1 (2002).
15. F.D. Brooks, A. Buffler, M.S. Allie, “Detection of anti-personnel landmines using neutrons and gamma-rays“, Radiat. Phys. Chem. 71 (2004) 749-757.

16. C.P. Datema, V.R. Bom, C. vanEijk, “Monte Carlo simulations of landmine detection using neutron backscattering imaging”, Nucl. Instrum. Methods Phys. Res. A 513 (2003) 398-402.
17. M. Cinsauser, M. Lunardon, G. Nebbia, S. Pesente, G. Viesti, V. Filippini, “Development of a thermal neutron sensor for humanitarian demining“, Appl. Radiat. Isot. 61 (2004) 59-66.
18. C. Bruschini, B. Gros, F. Guerne, P.-Y. Pièce, O. Carmona, “Ground penetrating radar and imaging metal detector for antipersonnel mine detection”, J. Appl. Geophysics 40 (1998) 59-71.
19. E. Gudmundson, A. Jakobsson, I.J.F. Poplett, J.A.S. Smith, Detection and classification of liquid explosives using NMR, in: 2009 IEEE International Conference on Acoustics, Speech and Signal Processing, Taipei, Taiwan, 2009, pp. 3053-3056.
20. R. Deas, I. Burch, D. Port, "The detection of RDX and TNT mine like targets by nuclear quadrupole resonance", P. SPIE 4742 (2002) 482-489.
21. J.F. Federici, B. Schulkin, F. Huang, D. Gary, R. Barat, F. Oliveira, D. Zimdars, “THz imaging and sensing for security applications-explosives, weapons and drugs”, Semicond. Sci. Tech. 20 (2005) S266-S280.
22. Y.C. Shen, T. Lo, P.F. Taday, B.E. Cole, W.R. Tribe, M.C. Kemp, “Detection and identification of explosives using terahertz pulsed spectroscopic imaging”, Appl. Phys. Lett. 86 (2005) 241116.
23. D.M. Sheen, D.L. McMakin, H.D. Collins, T.E. Hall, R.H. Severtsen, “Concealed explosive detection on personnel using a wideband holographic millimeter-wave imaging system”, P. SPIE 2755 (1996) 503-513.
24. D.M. Sheen, D.L. McMakin, T.E. Hall, “Three-dimensional millimeter-wave imaging for concealed weapon detection”, IEEE T. Microw. Theory 49 (2001) 1581-1592.
25. J. Solomon, “Does the TSA have stage fright? Then why are they picturing you naked?”, J. Air Law Commer. 73 (2008) 643-671.
26. K.W. Dolan, R.W. Ryon, D.J. Schneberk, H.E. Martz, R.D. Rikard, “Explosives detection limitations using dual-energy radiography and computed tomography”, Proceedings of the First International Symposium on Explosive Detection Technology (1992) 252-260.
27. G. Harding, “X-ray scatter tomography for explosives detection”, Radiat. Phys. Chem. 71 (2004) 869-881.
28. R.C. Runkle, T.A. White, E.A. Miller, J.A. Caggiano, B.A. Collins, “Photon and neutron interrogation techniques for chemical explosives detection in air cargo: A critical review”, Nucl. Instrum. Methods Phys. Res. A 603 (2009) 510-528.
29. M. Green, L. Partain, “High throughput baggage scanning employing x-ray diffraction for accurate explosives detection”, P. SPIE 5048 (2003) 63-72.
30. S.-S. Tang, E. Hussein, “Use of isotopic gamma sources for identifying anti-personnel landmines”, Appl. Radiat. Isot. 61 (2004) 3-10.

31. A.A. Faust, R.E. Rothschild, W.A. Heindl, “Development of a coded aperture backscatter imager using the UC San Diego HEXIS detector”, P. SPIE 5089 (2003) 95-106.
32. A. Faust, “Detection of explosive devices using x-ray backscatter radiation”, P. SPIE 4785 (2002) 17-28.
33. T.J.T. Kwan, R.E. Morgado, Tai-Sen F. Wang, B. Vodolaga, V. Terekhin, L.M. Onischenko, S.B. Vorozhtsov, E.V. Samsonov, A.S. Vorozhtsov, Y.G. Alenitsky, E.E. Perpelkin, A.A. Glazov, D.L. Novikov, V. Parkhomchuk, V. Reva, V. Vostrikov, V.A. Mashinin, S.N. Fedotov, S.A. Minayev, Detection of Explosives Using Nuclear Resonance Absorption of Gamma Rays in Nitrogen: A Russian/US Collaboration in: Detection of liquid explosives and flammable agents in connection with terrorism, Springer Netherlands, 2008, pp. 97-116.
34. D. Vartsky, G. Engler, M.B. Goldberg, “A method for detection of explosives based on nuclear resonance absorption of gamma rays in N-14”, Nucl. Instrum. Methods Phys. Res. A 348 (1994) 688-691.
35. K.W. Habiger, J.R. Clifford, R.B. Miller, W.F. McCullough, “Explosives detection with energetic photons”, Nucl. Instrum. Methods Phys. Res. B 56 (1991) 834-838.
36. A. Buffler, Radiat. “Contraband detection with fast neutrons”, Phys. Chem. 71 (2004) 853-861.
37. T. Gozani, “A review of neutron based non-intrusive inspection technologies”, in: Conference on Technology for Preventing Terrorism, Ancore Corporation Sanford University, Stanford, California, 2002.
38. H.-H. Hsu, K.J. Kearfott, “Effects of neutron source selection on land-mine detection efficiency”, Nucl. Instrum. Methods Phys. Res. A, 422 (1999) 914-917.
39. D. Brown, T. Gozani, “Thermal neutron analysis technology”, P. SPIE 2936 (1997) 85-94.
40. P. Shea, T. Gozani, H. Bozorgmanesh, “A TNA explosives-detection system in airline baggage”, Nucl. Instrum. Methods Phys. Res. A, 299 (1990) 444-448.
41. D. Slaughter, M. Accatino, A. Bernstein, J. Candy, A. Dougan, J. Hall, A. Loshak, d. Manatt, A. Meyer, B. Pohl, S. Prussin, R. Walling, D. Weirup, “Detection of special nuclear material in cargo containers using neutron interrogation”, UCRL-ID-155315, Lawrence Livermore National Laboratory, Livermore, California, 2003.
42. E. Hussein, M. Desrosiers, E. Waller, "On the use of radiation scattering for the detection of landmines”, Radiat. Phys. Chem. 73 (2005) 7-19.
43. C. Datema, L. van der Schoor, V. Bom, C. van Eijk, "Landmine detection with the neutron backscattering method", Nuclear Science Symposium Conference Record, 2001 IEEE 1 (2001) 406-409.
44. B. Kiraly, L. Olah, J. Csikai, "Neutron-based techniques for detection of explosives and drugs", Radiat. Phys. Chem. 61 (2001) 781-784.

45. N. Kardjilov, A. Hilger, I. Manke, M. Strobl, M. Dawson, J. Banhart, "New trends in neutron imaging", Nucl. Instrum. Methods Phys. Res. A 605 (2009) 13-15.
46. A. Buffler, K. Bharuth-Ram, F.D. Brooks, M.S. Allie, M. Herbert, M.R. Nchodu, B.R. Simpson, "Element analysis by fast neutron scattering" P. SPIE 2867 (1997) 192-197.
47. T. Gozani, Nucl. Instrum. "Novel applications of fast neutron interrogation methods", Nucl. Instrum. Methods Phys. Res. A 353 (1994) 635-640.
48. A. Buffler, F. Brooks, M. Allie, K. Bharuth-Ram, M. Nchodu, "Material classification by fast neutron scattering", Nucl. Instrum. Methods Phys. Res. B 173 (2001) 483-502.
49. F.D. Brooks, A. Buffler, M.S. Allie, K. Bharuth-Ram, M.R. Nchodu, B.R.S. Simpson, "Determination of HCNO concentrations by fast neutron scattering analysis", Nucl. Instrum. Methods Phys. Res. A 410 (1998) 319-328.
50. D.R. Brown, T. Gozani, R. Loveman, J. Bendahan, P. Ryge, J. Stevenson, F. Liu, M. Sivakumar, "Application of pulsed fast neutrons analysis to cargo inspection", Nucl. Instrum. Methods Phys. Res. A 353 (1994) 684-688.
51. G. Vourvopoulos, P.C. Womble, "Pulsed fast thermal neutron analysis: a technique for explosives detection", Talanta 54 (2001) 459-468.
52. J.C. Overley, M.S. Chmelik, R.J. Rasmussen, R.M.S. Schofield, H.E. Lefevre, "Explosives detection through fast-neutron time-of-flight attenuation measurements", Nucl. Instrum. Methods Phys. Res. B 99 (1995) 728-732.
53. K.P. Hong, C.M. Sim, V. Em, S.W. Lee, Y.J. Kim, S.Y. Park, J. Park, H.J. Kim, “Fast neutron interrogation systems for detection of hazardous materials”, in: International Symposium on Research Reactor and Neutron Science, Daejeon, Korea, 2005, pp. 457-459.
54. S. Pesente, G. Nebbia, M. Lunardon, G. Viesti, D. Sudac, K. Nad, S. Blagus, V. Valkovic, "Detection of hidden explosives by using tagged neutron beams with sub-nanosecond time resolution", Nucl. Instrum. Methods Phys. Res. B 531 (2004) 657-667.
55. G. Headley, A. Beyerle, R. Durkee, P. Hurley, L. Tunnell, “Four-dimensional image display for associated particle imaging", Nucl. Instrum. Methods Phys. Res. A 353 (1994) 344-346.
56. M. Lunardon, G. Nebbia, S. Pesente, G. Viesti, M. Barbui, M. Cinausero, G. D'Erasmo, M. Palomba, A. Pantaleo, V. Filippini, "Detection of landmines by using 14 MeV neutron tagged beams", Appl. Radiat. Isot. 61 (2004) 43-49.
57. G. Viesti, S. Pesente, G. Nebbia, M. Lunardon, D. Sudac, K. Nad, S. Blagus, V. Valkovic, "Detection of hidden explosives by using tagged neutron beams: Status and perspectives", Nucl. Instrum. Methods Phys. Res. B 241 (2005) 748-752.
58. C. Carasco, B. Perot, J.-L. Ma, A. Mariani, A.-C. Raoux, P. Pras, E. Cusset, R. Vogler, M. Gmar, G. Sannie, S. Normand, “Detection of chemical agents with a portable neutron inspection system”, in: Nuclear Science Symposium, IEEE, Dresden, Germany, 2008, pp. 660-666.

59. E. Hussein, E. Waller, "Review of one-side approaches to radiographic imaging for detection of explosives and narcotics", Radiat. Meas. 29 (1998) 581-591.
60. G. Viesti, A. Donzella, G. Bonomi, C. Botosso, D. Fabris, M. Lunardon, S. Moretto, G. Nebbia, S. Pesente, F. Pino, L. Sajo-Bohus, A. Zenoni, “Search of explosives in vehicles by using tagged neutrons”, in: Detection of liquid explosives and flammable agents in connection with terrorism, Springer Netherlands, 2008, pp. 39-46.
61. S. Pesente, G. Nebbia, G. Viesti, F. Daniele, D. Fabris, M. Lunardon, S. Moretto, K. Nad, D. Sudac, V. Valkovic, "Monte Carlo analysis of tagged neutron beams for cargo container inspection", Nucl. Instrum. Methods Phys. Res. B 261 (2007) 268-271.
62. G. Vourvopoulos, "Accelerator based techniques for contraband detection", Nucl. Instrum. Methods Phys. Res. B 89 (1994) 388-393.
63. V. Valkovic, D. Sudac, D. Matika, "Fast neutron sensor for detection of explosives and chemical warfare agents", Appl. Radiat. Isot. 68 (2009) 888-892.

Chapter 3: Simplified Simulation of Fast Neutron Scattering for an Explosives Detection Application

Abstract

In developing applications for fast neutron scattering in explosives detection, Monte Carlo simulations were completed that characterized the scattering behavior of fast neutrons in a simplified geometry. Targets included C, N, O, and Fe, as well as air, water, oil and the explosive RDX ($C_3H_6N_6O_6$). Work included a study of energy binning, particle histories, and statistical uncertainty. Results of the simulations closely matched expected scatter behavior. Energy bins of 0.2 MeV and 1×10^8 particle histories provided ample statistical certainty.

Introduction

Neutrons in explosives detection scenarios

There are several reasons why active neutron, as opposed to photon, interrogation techniques have been pursued in explosives detection [1-5]. This is mainly because neutron interrogation is much better at separating the signals from low atomic weight materials, such as explosives and many common inert cargos [6]. Furthermore, fast neutrons are highly penetrating and can easily pass though metallic shielding. Some difficulties encountered in neutron-based interrogation methods include the challenges inherent in performing neutron spectroscopy with a reasonable detection efficiency and energy resolution, production of a well-defined monoenergetic neutron beam, and personnel shielding [2,7].

Several different neutron interrogation strategies have been pursued in contraband detection. Thermal neutron activation analysis formed the basis of many material composition analysis techniques, as the characteristic gamma rays provide a clear indicator of target identity [8-11]. Incident fast neutrons that then thermalize are often used in this method, as thermal neutron beams are quickly attenuated. Further issues involve excessive measurement times due to the low interaction probability and decreased detection efficiency of high energy gamma-rays [1].

Inelastic neutron scatter has been thoroughly studied, as the characteristic de-excitation photons provide a measurement of the relative atomic abundances in an unknown target [12-14]. Much of the recent work has centered around combining de-excitation gamma-rays with neutrons that have been “tagged” using associated particle technology [15,16]. Unfortunately, it relatively low interaction probability requires higher neutron fluxes in order to achieve adequate detection sensitivity [17]. Other methods include neutron radiography, backscatter and attenuation methods, in which changes in the strength of the neutron beam provide information on target elemental composition [18,19].

Neutron interactions

There are three basic types of neutron interactions that are utilized in explosives-detection scenarios. These include neutron absorption (n, γ), neutron inelastic scatter, (n, n’), and neutron elastic scatter (n, n). Other neutron interactions, such as proton- and alpha-producing charged particle reactions, multiple neutron-producing reactions, and fission, were not studied here. This is because these reactions do not occur in the low atomic number target materials, have quickly-absorbed products, or require very high-energy incident neutrons.

In neutron absorption, with a very low cross section outside the thermal neutron energy range, the incident neutron is absorbed into the target nucleus, increasing its atomic mass by one. If radioactive, the activated product will undergo beta decay and may release one or more characteristic gamma-rays.

Fast neutrons, defined as those with more than 100 keV of kinetic energy, have interactions that are dominated by neutron scattering [20]. In neutron inelastic scattering the incident neutron scatters off the target nucleus and leaves it at an excited state. This nuclei will then fall back to ground state, emitting a characteristic gamma-ray equal in energy to the difference between the two energy levels [21]. In neutron elastic scatter, the most probable interaction for fast neutrons, the incident neutron imparts kinetic energy to the target nucleus and continues traveling in a different direction with a lower energy. Because of conservation of kinetic energy, it is possible to determine target atomic mass by measuring recoil neutron energy and angle. This may be expressed in the laboratory frame of reference as:

$$E' = E_0\left[1 - \frac{2A(1-\cos\theta)}{(1+A)^2}\right], \tag{3.1}$$

where E' is the scattered neutron's energy, E_o the incident neutron's energy, A represents the mass number of the target nucleus, and θ is the scatter angle of the neutron [21].

Monte Carlo techniques

There are several advantages inherent to using computer simulations at this very preliminary stage. These include a high level of control of variables in the screening scenario, ease and minimal expense of optimization and exploring different variables, and the ability to isolate the results of the neutron interactions without the influence of detector response or surrounding materials. Of course, the results achieved via simulations are not necessarily an accurate portrayal of physical scenarios and should therefore be benchmarked against actual measurements once the detection system has been developed.

An explosives-detection technique based on neutron scatter

The method now being developed will combine both the neutron and photon information produced by simulated neutron interactions. Strategic data points will comprise decision-point flags as part of an explosives-detection algorithm. Use of the information produced by both inelastic and elastic neutron scatter will decrease the number of interrogating neutrons, and therefore the measurement time and dose to personnel. Although the data presented here shows the results from both D-D and D-T incident neutrons, it is highly probably that the final system will only use D-T neutrons. However, even these neutrons would undergo significant attenuation, with only 1 in 10^6 passing through 2 m of cargo unaffected, with most of the remaining neutrons still present at lower energies. Because the discussed method depends on the results of specific data points produced with interrogation by a commercially-available neutron generator, the need for expensive imaging equipment is minimized.

The information presented here on the scattering behavior of fast neutrons in a variety of materials provides the raw data needed in order to develop and optimize an explosives-detection algorithm. The final algorithm may include the aforementioned flags as well as neutron absorption photons or neutron transmission information.

Materials and Methods

Monte Carlo simulation

The efforts described in this paper were devoted to characterizing the behavior of incident fast neutrons on a variety of targets relevant to explosives screening scenarios. This work mainly consisted of MCNP5 [22] radiation transport simulations. In some cases MCNP5-PoliMi [23] was used to simulate a realistic ^{252}Cf source.

Simulation geometry, materials and sources

The basic geometry used in all simulations is shown in Fig. 3-1, and consisted of a standard air-filled steel cargo container. This container had dimensions 2.4 m x 6.2 m x 2.6 m, with 0.317 cm thick walls, and was centered on very large 93 cm radius target sphere. This large sphere was later replaced by a more realistic sphere of radius 18.72 cm to allow full target penetration by 14.1 MeV neutrons. A conical approximation of an isotropic neutron source was located 3.04 m from the target center and was biased towards the detector to save computational resources. Sources simulated included D-T (14.1 MeV) neutrons, D-D (2.4 MeV) neutrons, and the built-in ^{252}Cf source found in MCNP-PoliMi, which included both a fission neutron spectrum and the relevant source gamma rays. Seven hemispherical surfaces of 0.78 m radius surrounded the container 3.04 m from target center. These tally surfaces covered 180° range of azimuthal scatter. The large hemispherical surfaces were used in order to improve counting statistics as well as blur the angular resolution of the scattered neutrons.

The simulated cargo container was composed of steel, density 7.87 g cm^{-3}, which was also used in characterization simulations as a target sphere. The first set of simulations used target spheres of natural isotopic mixtures of the elements carbon, nitrogen, and oxygen. Other simulations used vegetable oil ($C_{55}H_{103}O_6$), density 0.918 g cm^{-3}, water at unit density, and the explosive RDX ($C_3H_6N_6O_6$), density 1.82 g cm^{-3}. Dry air, density 0.0012 g cm^{-3} and containing 78.4% N_2, 21.1% O_2, 0.46% Ar, and 0.02% CO_2 [24], was included in all simulations, both inside and outside the cargo container. An example of MCNP input for a RDX target may be found in Appendix A.

Simulation detector and energy tallies

While eventual implementation will depend on detector capabilities, at this preliminary stage it was considered more important to get an accurate representation of the neutron scattering behavior than to simulate the actual detector response. Therefore, neutron and gamma current (MCNP F1) tallies were calculated on the inside surface of the seven hemispheres described above. Separate tallies for photons and neutrons used 0.2 MeV energy bins from 0 to 15 MeV, with one additional bin for any 15-20 MeV neutrons. This uniform bin distribution is finer than a typical neutron detector energy resolution and will later be multiplied by an appropriate detector response function.

Particle histories, variance reduction, and counting statistics

In order to find an appropriate balance between computational time, energy bin width, and statistical certainty a series of simulations was completed using the 14.1 MeV neutron source on a sphere of RDX inside the cargo container. The number of particle histories varied from 1×10^6 to 8×10^8 with energy bins widths of 0.05, 0.1, 0.2, or 0.4 MeV. The results were compared with special attention given to the statistical uncertainty of bins corresponding to peaks in the neutron spectrum as well as to the separation between the peaks. Acceptable levels of uncertainty were chosen to be less than 5% for physically possible scattered neutrons and less than 1% for bins corresponding neutron or photon peaks.

To further decrease computational time neutrons were discounted after their energies fell below 0.05 MeV. While significantly decreasing computational time, this energy cut-off eliminated all thermal neutron interactions, including neutron absorption. However, this was not an issue, as the purpose of this paper focuses on single neutron scatters. MCNP5 provides for many other variance-reduction strategies, such as particle splitting, which were not utilized at this time.

Results and Discussion

Elemental target simulations

The neutron tallies from the simulations of C, N, O, and Fe targets for ^{252}Cf, D-D, and D-T sources showed both the expected elastic scatter peaks and several inelastic scatter peaks. The energy of each of these peaks changed as a function of neutron scatter angle, as shown in Fig. 3-2. Scatter peaks were most prevalent in the 165° to 180° scattered neutrons, with peak magnitude decreasing with decreasing scatter angle with the exception of low-angle elastic scatter, which increased in magnitude as more uncollided or weakly collided neutrons penetrate the large target. The values of the peaks for backscattered (180°) neutrons for D-D and D-T sources are shown in Table 3-2 for the cases of MCNP tally and calculated using eqn (3.1). Neutron energy distributions for the D-T neutron source is shown in parts a of Figs. 3-3 through 3-6, with the relevant neutron scatter peaks labeled.

Due to the low average energy and continuum nature of the ^{252}Cf neutron spectrum, it was impossible to discern the elastic scatter peaks for any of the nuclides of interest. Furthermore, only a few ^{252}Cf neutrons are energetic enough to produce inelastic photons. This source, used alone, would thus not be a viable choice for the proposed new method.

As expected, the energy of the peaks produced from the photon current tallies did not depend on the source-target-detector angle, consistent with the physics of inelastic neutron scatter. Photon emission was mildly anisotropic, with the tally surfaces corresponding to the highest incident particle scatter showing the highest photon peak magnitudes. These photon peaks are listed in Table 3-3, with energy distributions from the backscatter tally surface shown in part b of Figs. 3-3 through 3-6. Only one energy level in ^{14}N is low enough to be excited by 2.4 MeV incident neutrons, so only the 14.1 MeV source produced significant inelastic scatter photon peaks. Especially prominent among these were the 6.4 MeV and 5.8 MeV peaks in the ^{12}C and ^{16}O tallies, respectively. These correspond to energy levels at 4.44 and 6.05 MeV, which are found in the 4.5 MeV and 6.1 MeV energy bins. Other neutron peaks were also discernable, though they were not as prominent, but may still be used in future detection algorithms.

Compound target simulations

As expected, the results from simulations containing the compounds water, oil, air, or RDX resembled a superposition of the results from the component elements with the relative peak magnitudes corresponding to the atom percents and interaction cross sections of the constituents. Neutron and photon energy distributions from the tallies for a D-T source and water, oil, or RDX targets may be seen in Figs. 3-7 through 3-9. Especially interesting, and of importance to the energy bin width investigation, was the separation of the C, N, and O neutron elastic scatter peaks. Due to the physics of elastic scatter, this separation was greater with higher energy source particles and increased angle of scatter. In the case of a D-T neutron source, a 0.2 MeV energy bin width was sufficient to distinguish between the neutron elastic scatter peaks of C, N, and O.

Particle histories, energy bin width and statistical uncertainty

The median uncertainties for nonzero backscattered neutron energy bins as a function of energy bin width and number of particle histories are compared in Fig. 3-10a . Due to the simplicity of the variance reduction strategies employed, the median uncertainty drops as one over the square root of the number of histories. Similarly, the decrease in uncertainty drops with the same relationship in increasing energy bin size, as shown in Fig. 3-10b. Using the 0.2 MeV energy bin and 1 x 10^8 particles, the median nonzero uncertainty was found to be 3.9%, with a less than 1% uncertainty for the energy bins corresponding to the neutron scatter peaks. Median uncertainty levels for physically achievable energy bins falls from 6.4% with 0.05 MeV energy levels to 2.4% with 0.4 MeV energy bins. This decrease by a factor of 2.7 is close to the factor of 2.8 decrease that would be expected for an eight-fold increase in particle histories that would be found if the energy distribution was uniform. Future simulations containing realistic detector response will use the information provided here to determine the appropriate number of particle histories and if additional variance reduction efforts are needed.

Application to explosives detection

There are several factors that must be considered when applying the results found here to an actual explosives-detection system. First of all, the high degree of neutron scatter in the cargo container contents and surrounding environment will obscure the signal produced by single neutron scatters off the explosives. Furthermore, many of the neutrons that actually do interact with explosives may undergo additional scatter before reaching the detector and the original information will be lost in this multiple scatter. The explosive device would be hidden inside an unknown benign cargo at an unknown location and amount. Another issue stems from the difficulty in performing neutron spectroscopy with good energy resolution and efficiency. Introduction of shielding around the neutron source will also degrade the monoenergetic nature of the generator-produced neutrons and further obscure the desired signal. Also, the scan must take place quickly and with high accuracy, as throughput is very high and the consequences of a false negative very serious. Other concerns associated with nuclear techniques include shielding and personnel dose concerns, high equipment costs, and the difficulty in penetrating large targets such as cargo containers. The proposed method, for which the results presented here plays a crucial role, will use information based on both the neutrons and photons produced during fast neutron interrogation in combinations that best compensate for changing screening scenarios.

Conclusions and Future Work

Simulations have been completed that thoroughly model the neutron scattering behavior off C, N, O, Fe, air, the explosive material RDX, water, and oil inside a standard cargo container. These highly simplified simulations demonstrated that it is possible to discern neutron scatter peaks as well as the photons produced through neutron inelastic scatter. In particular, neutron elastic scatter peaks were clearly defined in the neutron tally produced using a simulated D-T neutron generator. Other neutron peaks were visible in this tally, including inelastic scatter peaks, which corresponded to characteristic photons in the photon tally.

Considerable efforts were spent analyzing the statistical uncertainties of the neutron tallies. It was found that 1×10^8 particle histories were sufficient to bring the median uncertainty for physically achievable neutron tally bins to 3.2% with energy bins of 0.2 MeV. These efforts found that the expected relationship between number of particle histories, energy bin width, and statistical uncertainty holds true and provided guidance on the number of histories needed for future simulations.

The proposed method of using the elastically scattered neutrons as the basis for explosives detection merits further studies. Future simulations should include more various sizes, types, and locations of explosives, a variety of cargo container contents and surrounding environments, and more realistic detector responses. These will allow a clearer definition and optimization of the specific detection algorithm that takes advantage of all the scattered neutron and de-excitation photon information produced in fast neutron interrogation.

Figures

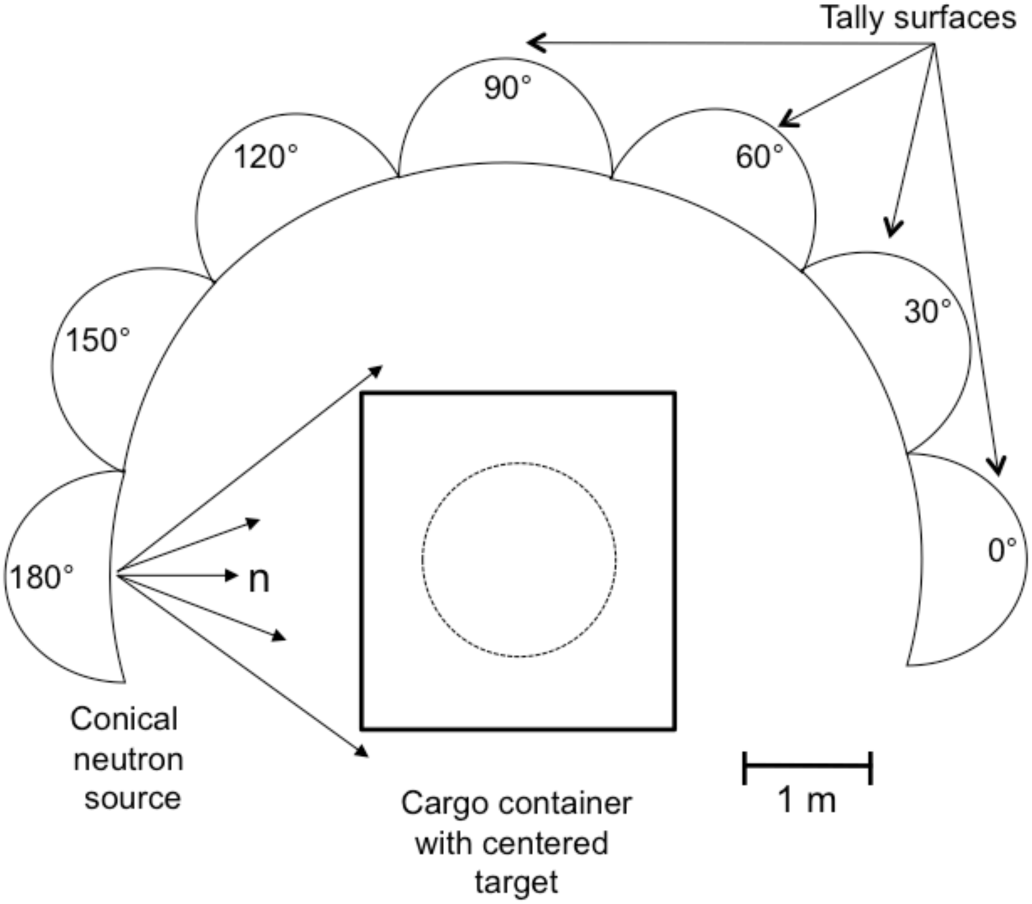

Figure 3-1. Cross-sectional view for the MCNP5 simulation, showing the steel cargo container, target sphere, neutron source and detector tally surfaces.

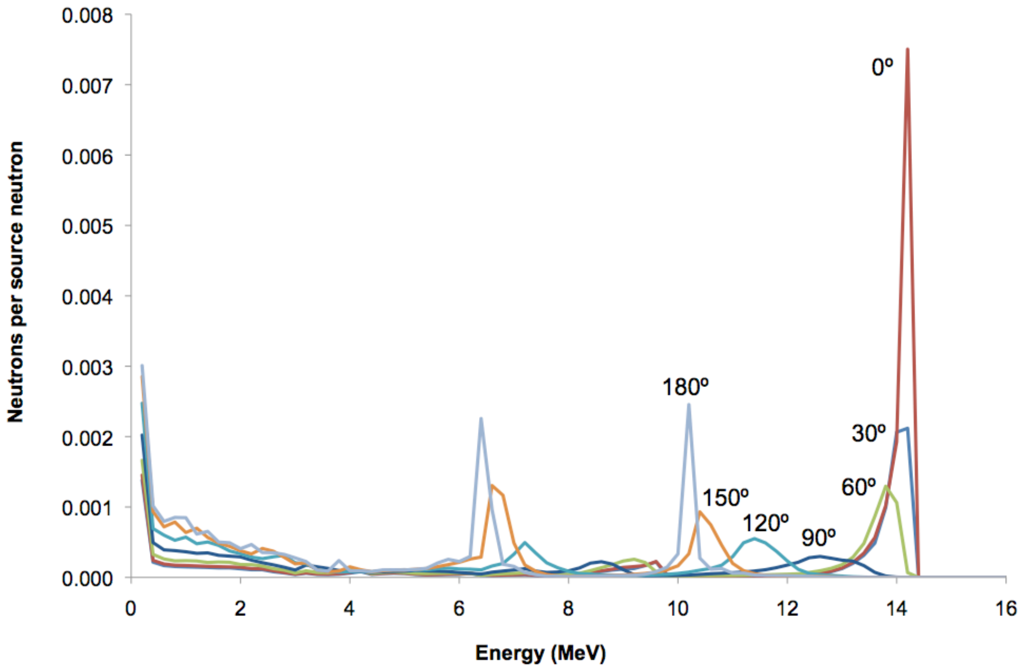

Figure 3-2. Illustration of downward shifting of neutron scatter peaks with increasing scatter angle. Small peak magnitude of lower scatter peaks due to attenuation in target.

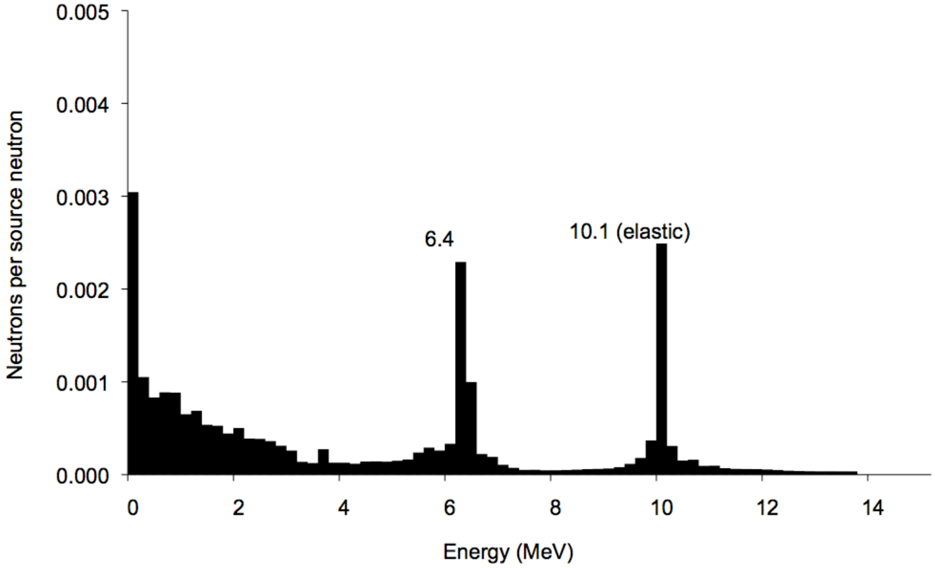

a.

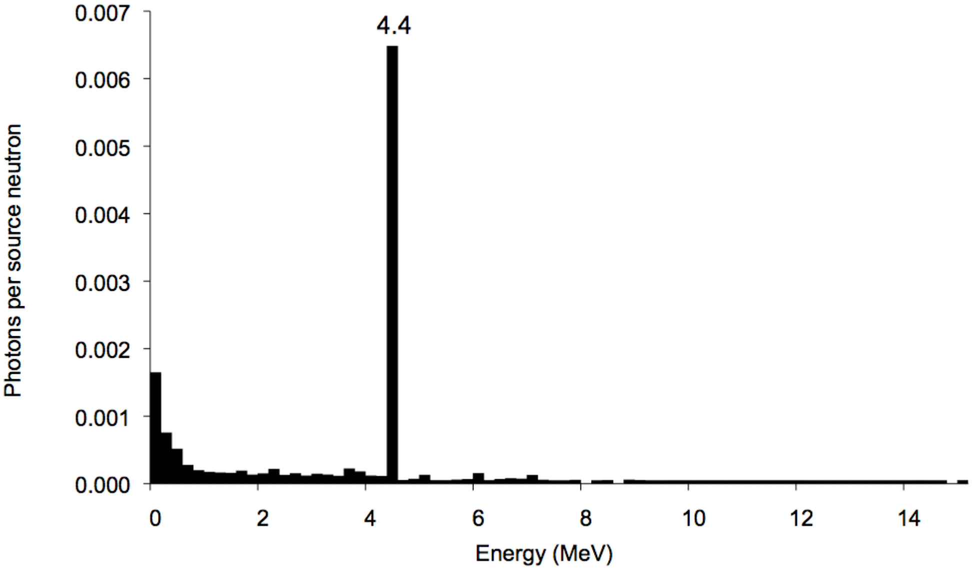

b.

Figure 3-3. Energy distribution for simulated ^{12}C target and 14.1 MeV monoenergetic neutron source for a) backscattered neutrons with elastic and inelastic scatter peaks and b) photons, with 4.4 MeV de-excitation peak.

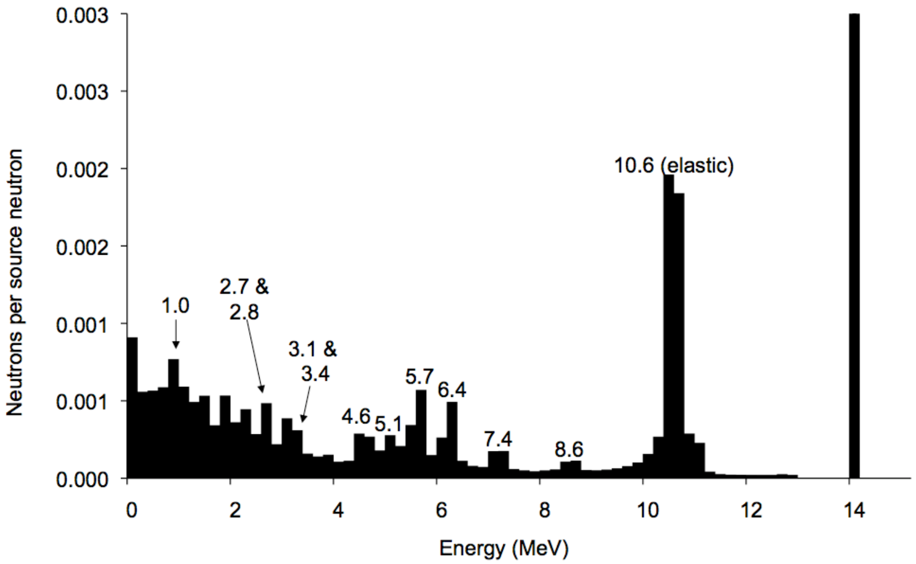

a.

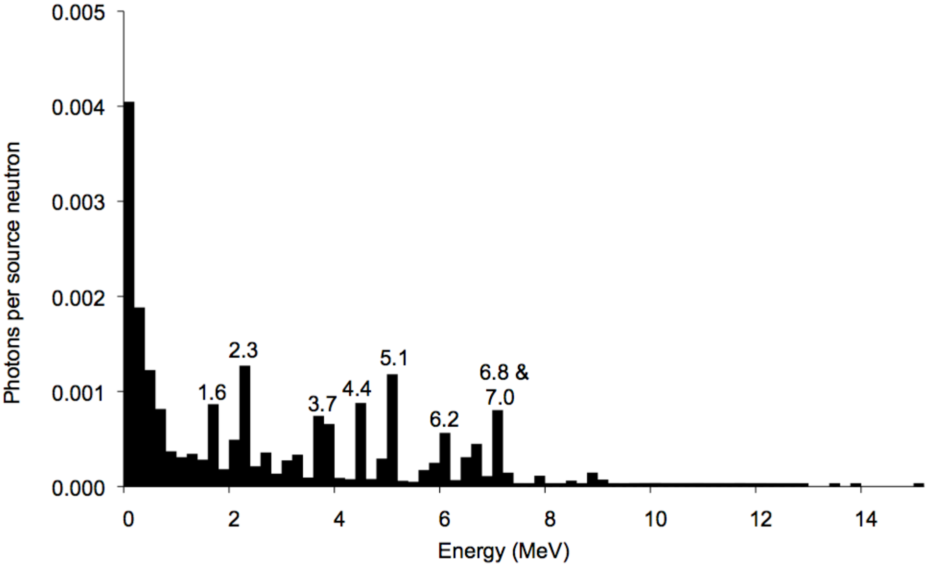

b.

Figure 3-4. Energy distribution for simulated ^{14}N target and 14.1 MeV monoenergetic neutron source for a) backscattered neutrons with 10.6 MeV elastic and several inelastic scatter peaks and b) photons, with several de-excitation peaks.

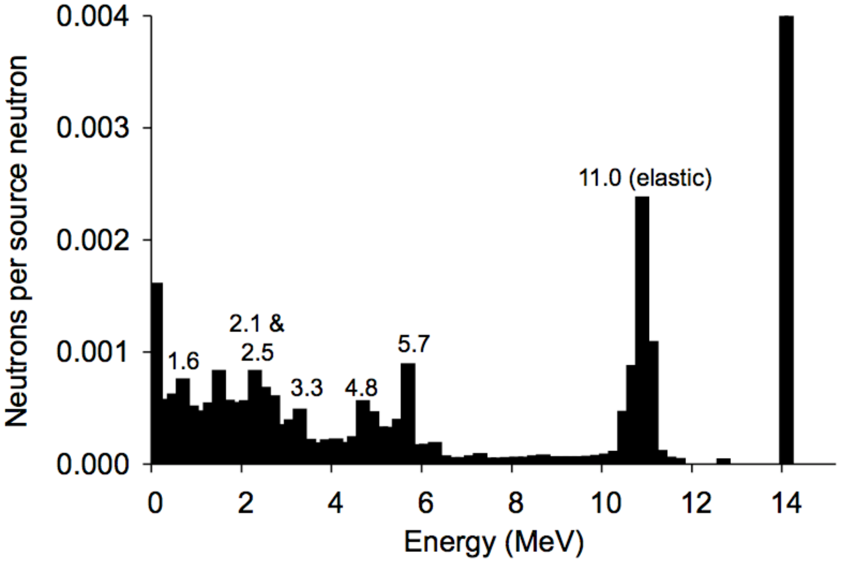

a.

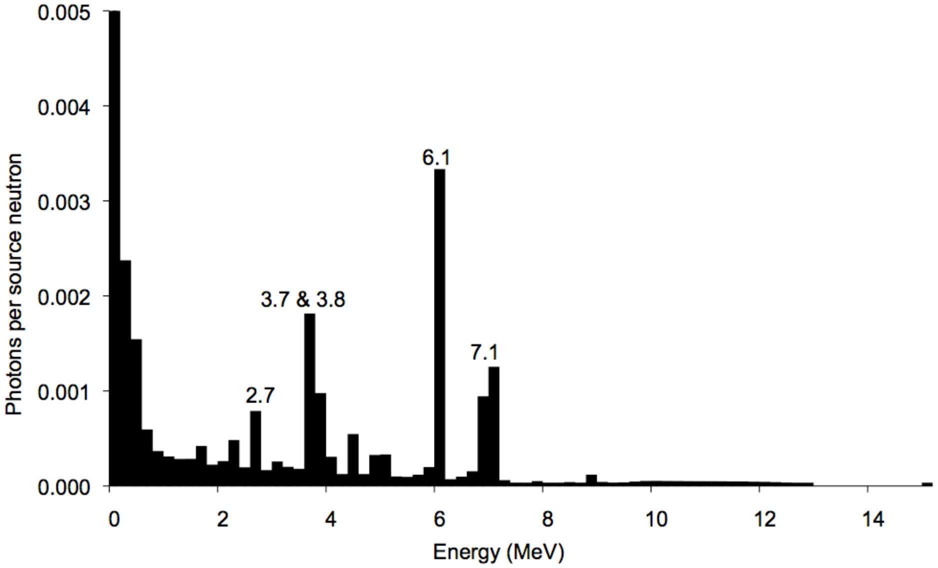

b.

Figure 3-5. Energy distribution for simulated ^{16}O target and 14.1 MeV monoenergetic neutron source for a) backscattered neutrons with 11.0 MeV elastic and several inelastic scatter peaks and b) photons, with several de-excitation peaks, including prominent 6.1 MeV peak.

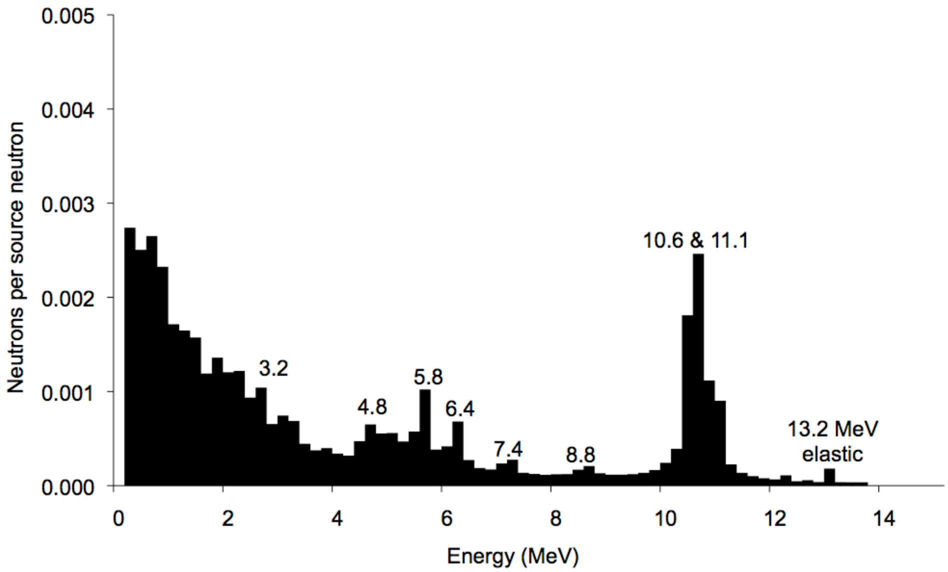

a.

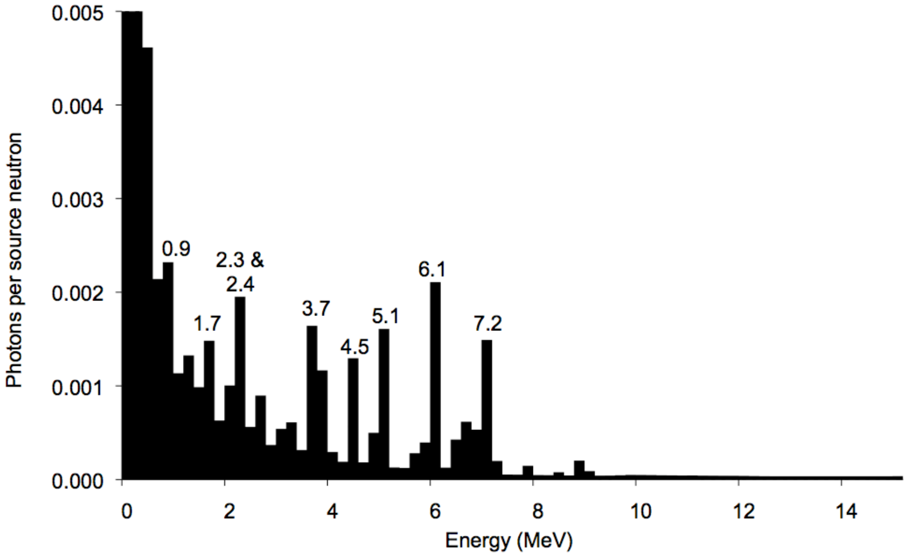

b.

Figure 3-6. Energy distribution for simulated ^{56}Fe target and 14.1 MeV monoenergetic neutron source for a) backscattered neutrons with 13.2 MeV elastic and several inelastic scatter peaks and b) photons, with several de-excitation peaks.

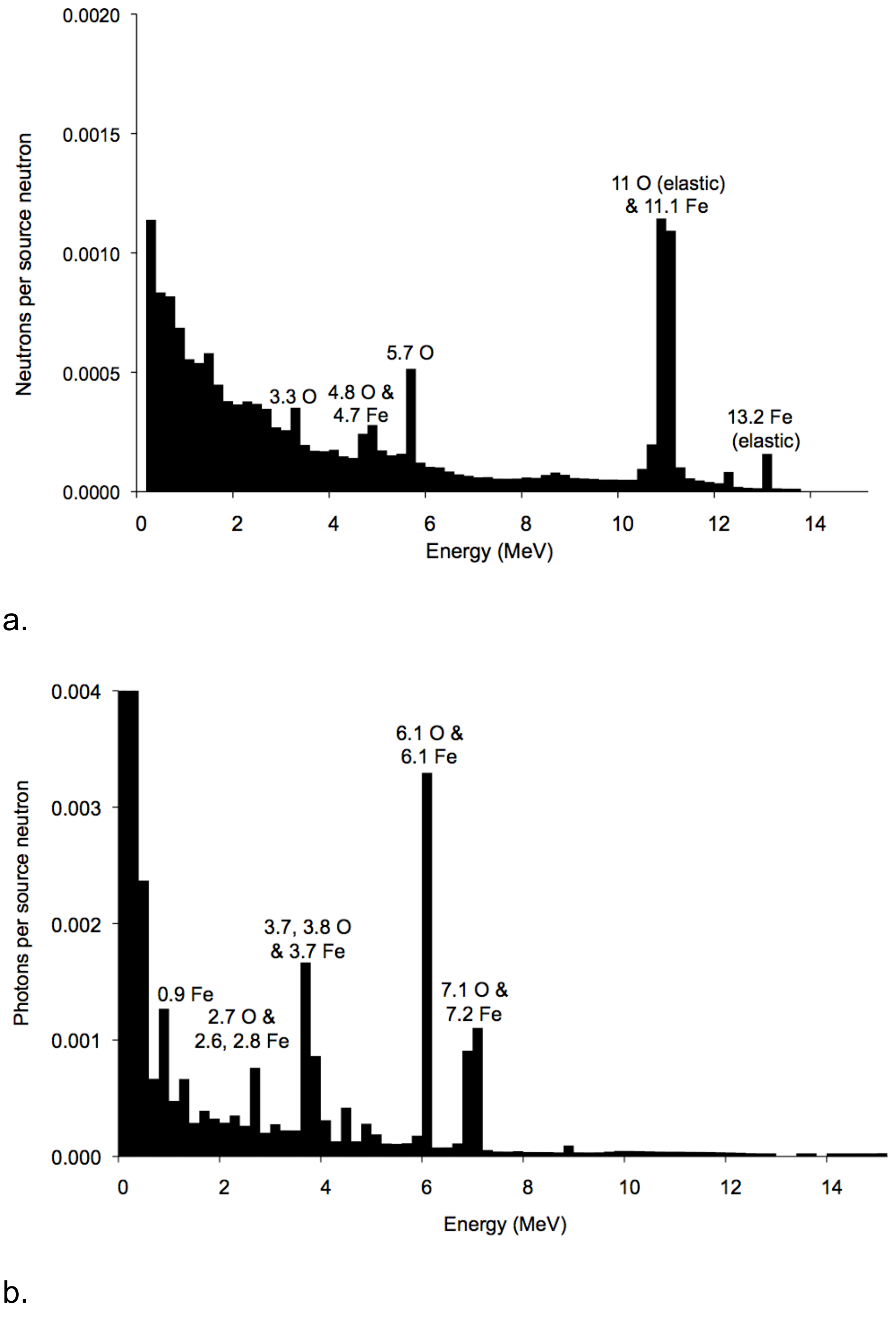

Figure 3-7. Energy distribution for simulated water target and 14.1 MeV monoenergetic neutron source for a) neutrons with prominent 11 MeV oxygen elastic scatter peak and several inelastic scatter peaks and b) photons, with several de-excitation peaks for both oxygen and iron.

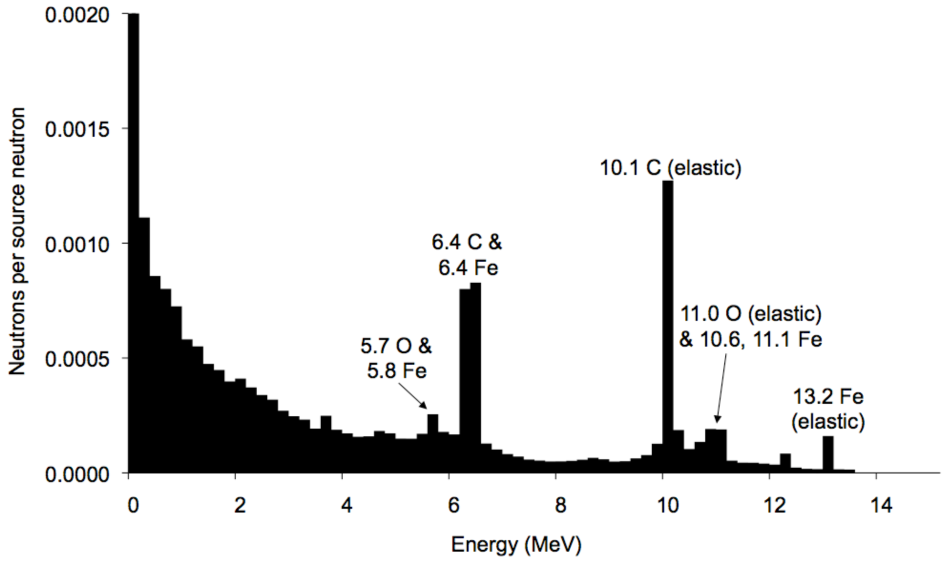

a.

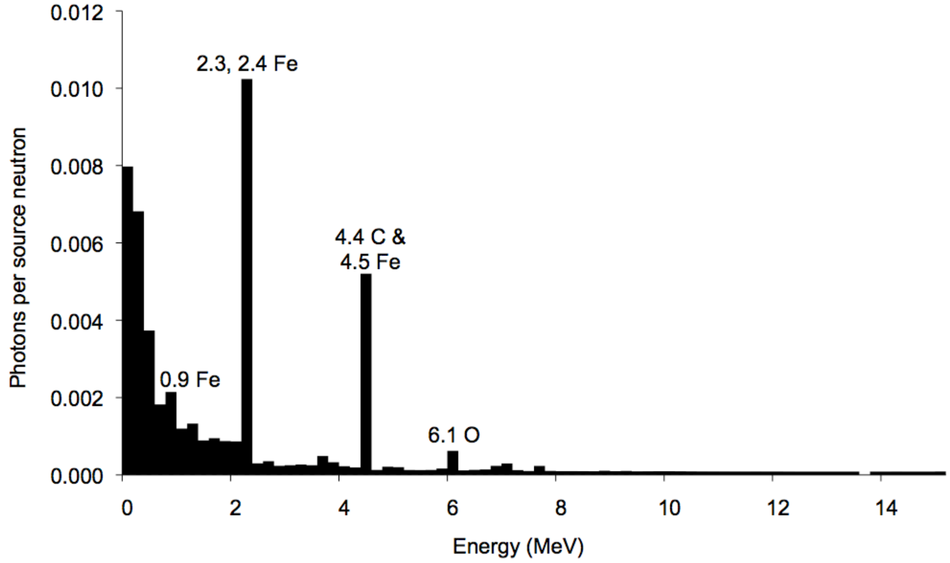

b.

Figure 3-8. Energy distribution for simulated oil target and 14.1 MeV monoenergetic neutron source for a) neutrons with prominent 10.1 MeV carbon elastic scatter peak and several inelastic scatter and b) photons, with several de-excitation peaks for both carbon, oxygen and iron.

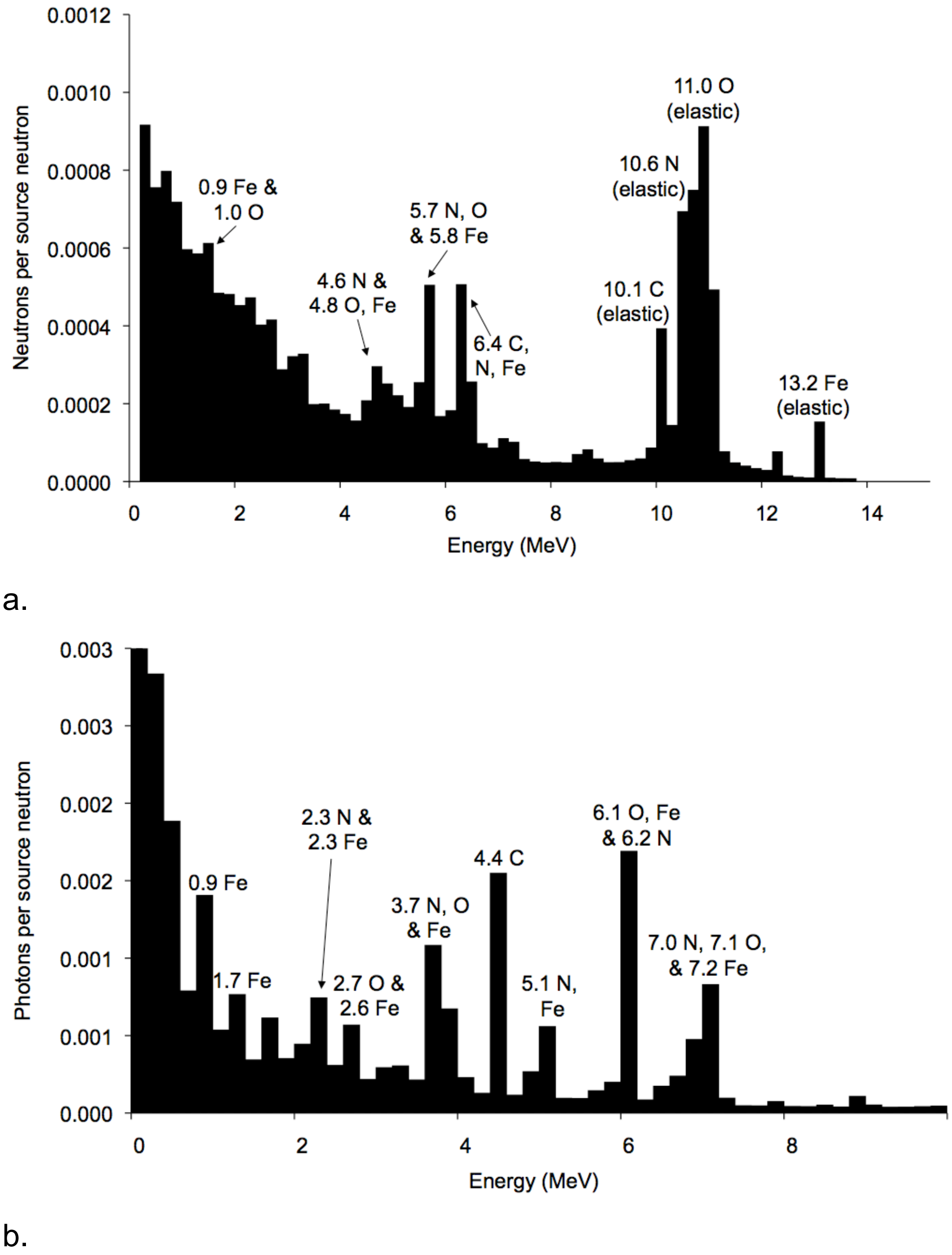

Figure 3-9. Energy distribution for simulated RDX target and 14.1 MeV monoenergetic neutron source for a) neutrons with carbon, nitrogen, and oxygen elastic scatter peaks and several inelastic scatter peaks for carbon, nitrogen, oxygen and the iron container and b) photons, with several de-excitation peaks for both carbon, nitrogen, oxygen and iron.

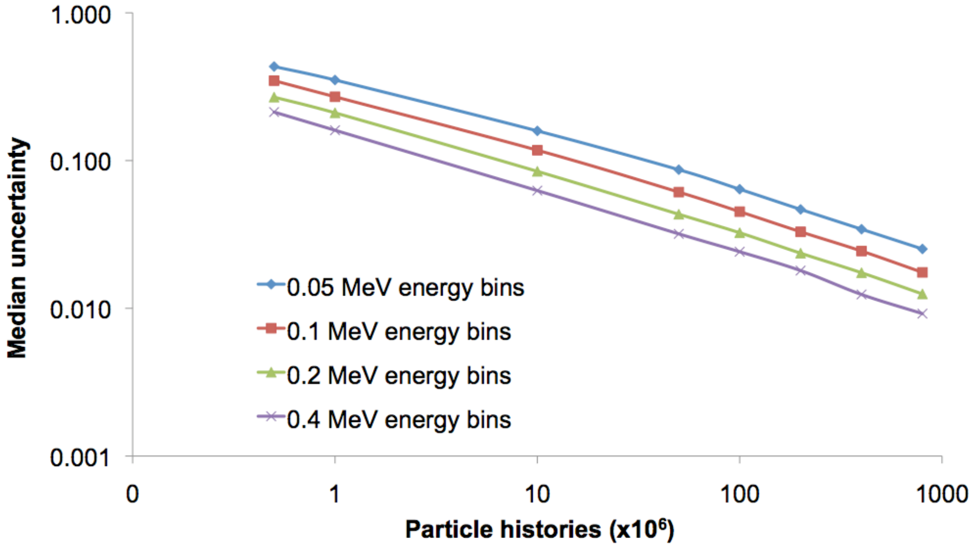

a.

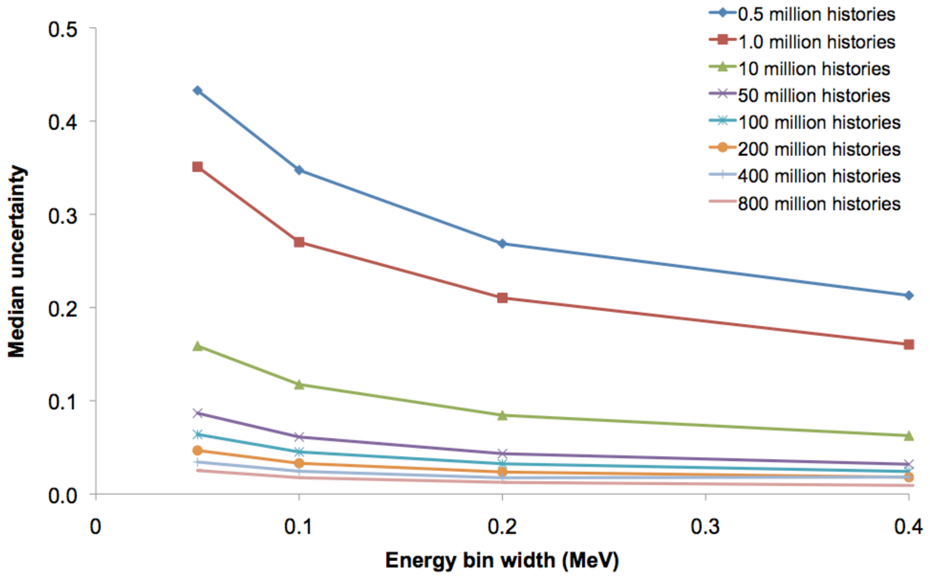

b.

Figure 3-10. Backscattered neutron tally statistical uncertainty as a function of a) number of particle histories and b) energy bin width.

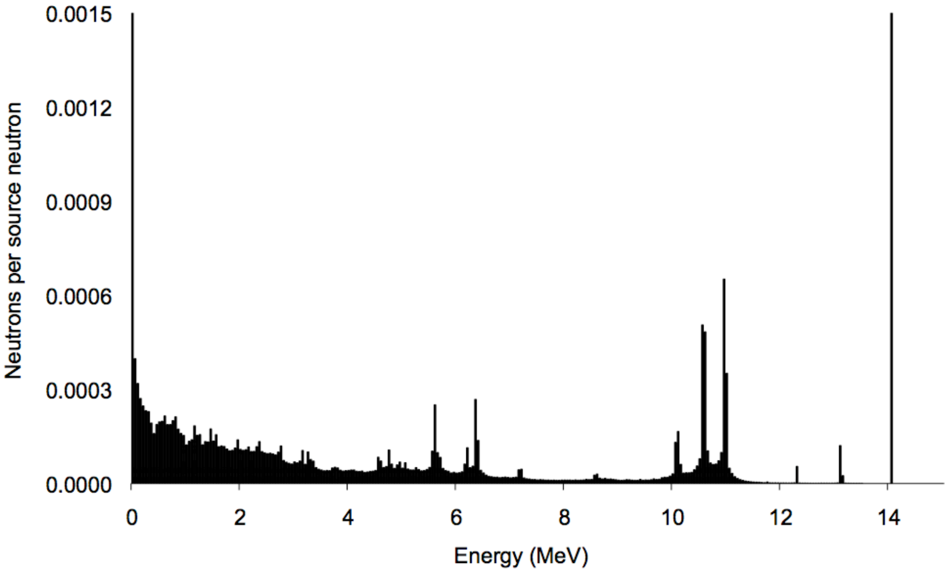

a.

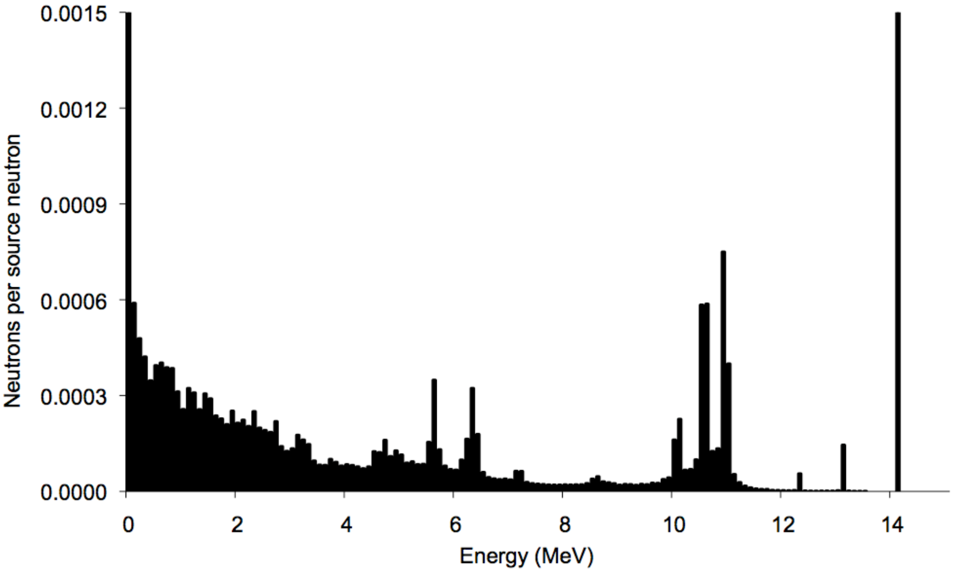

b.

Figure 3-11. Backscattered neutron spectra for 10^8 particle histories, with energy bin widths equal to a) 0.05 MeV, b) 0.1 MeV, c) 0.2 MeV, and d) 0.4 MeV.

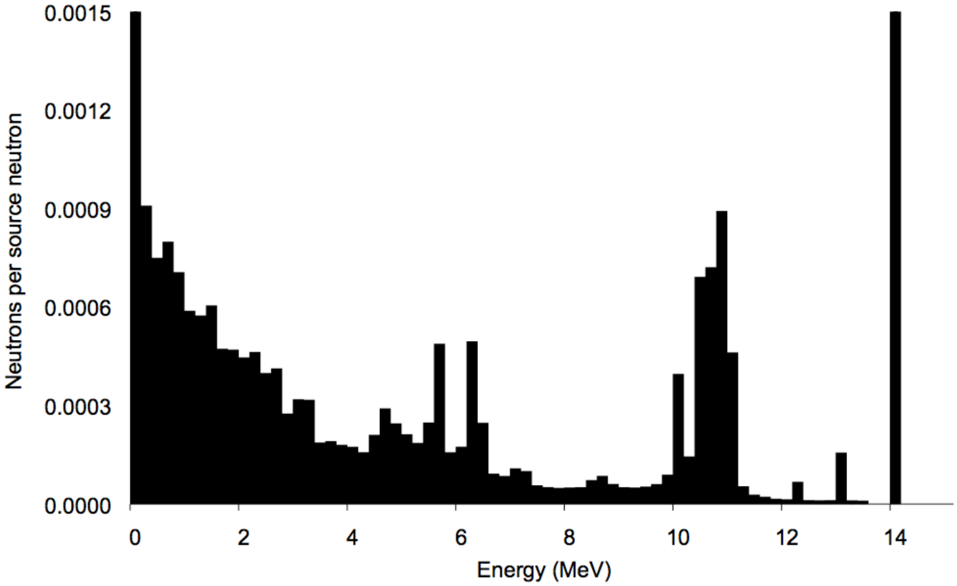

c.

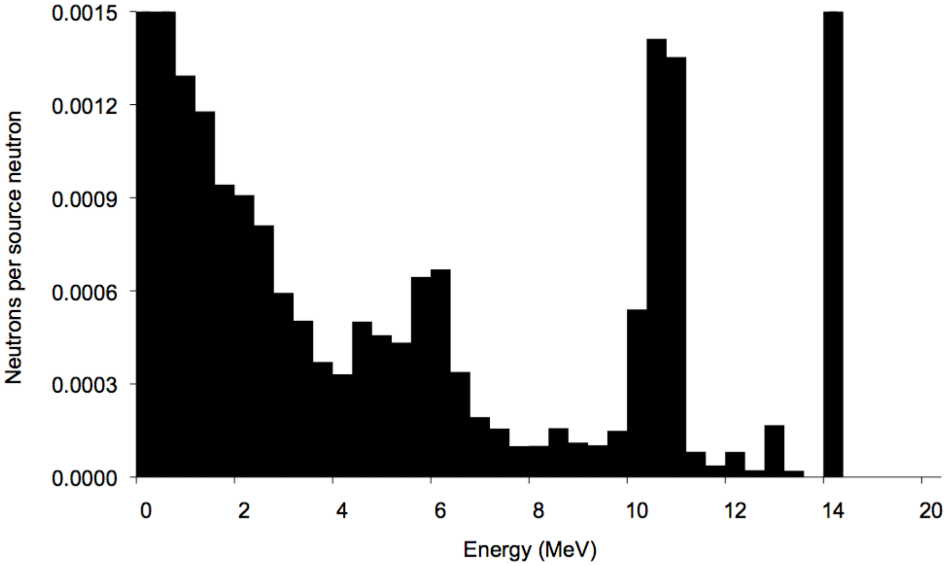

d.

Figure 3-11 (continued). Backscattered neutron spectra for 10^8 particle histories, with energy bin widths equal to a) 0.05 MeV, b) 0.1 MeV, c) 0.2 MeV, and d) 0.4 MeV.

Tables

Table 3-1. A comparison of the median nonzero statistical uncertainties for neutron current tallies corresponding to neutron scatters as a function of energy bin width and number of particle histories.

Particle histories (millions)	0.5	1	10	50	100	200	400	800
0.05 MeV energy bins	0.433	0.351	0.159	0.087	0.064	0.047	0.034	0.025
0.1 MeV energy bins	0.347	0.270	0.118	0.061	0.045	0.033	0.024	0.018
0.2 MeV energy bins	0.269	0.210	0.085	0.043	0.032	0.024	0.017	0.013
0.4 MeV energy bins	0.213	0.160	0.063	0.032	0.024	0.018	0.012	0.009

Table 3-2. Expected and tallied neutron backscatter peaks for carbon, nitrogen, oxygen, and iron with the most prominent peaks shown in bold. Neutron peak energies specified by median of 0.2 MeV energy bin.

Target	Expected (D-T source)	Tallied (D-T source)	Expected (D-D source)	Tallied (D-D source)
^{12}C, elastic	10.1	10.1	1.72	1.7
^{12}C, inelastic	3.75, **6.37**	3.7, **6.3**	none	none
^{14}N, elastic	10.59	10.5	1.80	1.7
^{14}N, inelastic	0.99, 1.81, 1.97, 2.82, 3.03, 3.13, 5.07, **5.71**, 6.2, **6.37**	0.9, 1.9, 2.9, 3.1, 5.1, **5.7**, **6.3**	none	none
O, elastic	11.0	10.9	1.87	1.9
^{16}O, inelastic	0.72, 1.46, 1.48, 1.57, 3.29, **5.69**	0.7, 1.5, 3.3, **5.7**	none	none
^{56}Fe, elastic	13.1	13.1	2.23	2.3

Table 3-3. Expected and observed photon peaks for carbon, nitrogen, and oxygen with the most prominent peaks shown in bold. Neutron peak energies specified by median of 0.2 MeV energy bin.

Target	Expected (D-T source)	Tallied (D-T source)	Expected (D-D source)	Tallied (D-D source)
^{12}C	4.44	4.5	none	1.7
^{14}N	**1.64**, **2.31**, 3.68, 4.40, **5.11**, 6.2, 7.03	**1.7, 2.3**, 3.7, 4.5, **5.1**, 6.1, 6.7, 7.1	none	1.9
^{16}O	2.74, 3.66, 3.80, **6.13**, 7.12	2.7, 3.7, **6.1**, 7.1,	none	1.9, 0.7

References

1. R.C. Runkle, T.A. White, E.A. Miller, J.A. Caggiano, B.A. Collins, “Photon and neutron interrogation techniques for chemical explosives detection in air cargo: A critical review”, Nucl. Instrum. Methods Phys. Res. A 603 (2009) 510-528.
2. E. Hussein, “Detection of explosive materials using nuclear radiation: a critical review”, P. SPIE 1736 (1993) 130-137.
3. F.D. Brooks, A. Buffler, M.S. Allie, “Detection of anti-personnel landmines using neutrons and gamma-rays”, Radiat. Phys. Chem. 71 (2004) 749-757.
4. T. Gozani, D. Strellis, “Principles and applications of neutron-based inspection techniques “, Nucl. Instrum. Methods Phys. Res. B 261 (2007) 311-315.
5. C. Fink, B. Micklich, T. Yule, P. Humm, L. Sagalovsky, M. Martin, “”Evaluation of neutron techniques for illicit substance detection”, Nucl. Instrum. Methods Phys. Res. B 99 (1995) 748 752.
6. A. Buffler, F. Brooks, M. Allie, K. Bharuth-Ram, M. Nchodu, “Contraband detection by fast neutron scattering”, Nucl. Instrum. Methods Phys. Res. B 173 (2001) 483-502.
7. A. Buffler, “Contraband detection with fast neutrons”, Radiat. Phys. Chem. 71 (2004) 853-861.
8. E. Hussein, M. Desrosiers, E. Waller, “On the use of radiation scattering for the detection of landmines”, Radiat. Phys. Chem. 73 (2005) 7-19.
9. G. Nebbia, S. Pesente, M. Lunardon, S. Moretto, G. Viesti, M. Cinausero, M. Barbui, E. Fioretto, V. Filippini, D. Sudac, K. Nad, S. Blagus, V. Valkovic, “Detection of buried landmines and hidden explosives using neutron, x-ray and gamma-ray probes”, Nucl. Instrum. Methods Phys. Res. A 752 (2005) 649c-658.
10. P. Shea, T. Gozani, H. Bozorgmanesh, “A TNA explosives-detection system in airline baggage”, Nucl. Instrum. Methods Phys. Res. A 299 (1990) 444-448.
11. T. Gozani, P. Ryge, P. Shea, “Explosive detection system based on thermal neutron activation”, in: IEEE Aerospace and Electronic Systems, 1989, pp. 17-20.
12. D.R. Brown, T. Gozani, “Cargo inspection system based on pulsed fast neutron analysis”, Nucl. Instrum. Methods Phys. Res. B 99 (1995) 753-756.
13. D.R. Brown, T. Gozani, R. Loveman, J. Bendahan, P. Ryge, J. Stevenson, F. Liu, M. Sivakumar, “Application of pulsed fast neutrons analysis to cargo inspection”, Nucl. Instrum. Methods Phys. Res. A 353 (1994) 684-688.
14. S. Khan, “Comparison of neutron based technologies for the detection of contraband”, P. SPIE 2092 (1993) 548-556.
15. C. Carasco, B. Perot, S. Bernard, A. Mariani, J.-L. Szabo, G. Sannie, T. Roll, V. Valkovic, D. Sudac, G. Viesti, M. Lunardon, C. Bottosso, D. Fabris, G. Nebbia, S. Pesente, S. Moretto, A. Zenoni, A. Donzella, M. Moszynski, M. Gierlik, T. Batsch, D. Wolski, W. Klamra, P.L. Tourneur, M. Lhuissier, A.

Colonna, C. Tintori, P. Peerani, V. Sequeira, M. Salvato, “In-field tests of the EURITRACK tagged neutron inspection system”, Nucl. Instrum. Methods Phys. Res. A 588 (2008) 397-405.

16. B. Perot, C. Carasco, S. Bernard, A. Mariani, J.-L. Szabo, G. Sannie, V. Valkovic, D. Sudac, G. Viesti, M. Lunardon, C. Botosso, G. Nebbia, S. Pesente, S. Moretto, A. Zenoni, A. Donzella, M. Moszynski, M. Gierlik, W. Klamra, P.L. Tourneur, M. Lhuissier, A. Colonna, C. Tintori, P. Peerani, V. Sequeira, M. Salvato, “Measurement of 14 MeV neutron-induced prompt gamma-ray spectra from 15 elements found in cargo containers “, Appl. Radiat. Isot. 66 (2008) 421-434.
17. F.D. Brooks, A. Buffler, M.S. Allie, K. Bharuth-Ram, M.R. Nchodu, B.R.S. Simpson, “Determination of HCNO concentrations by fast neutron scattering analysis”, Nucl. Instrum. Methods Phys. Res. A 410 (1998) 319-328.
18. J.C. Overley, “Determination of H, C, N, O content of bulk materials from neutron-attenuation measurements”, Int. J. Appl. Radiat. Isot. 36 (1985) 185-191.
19. J.C. Overley, M.S. Chmelik, R.J. Rasmussen, R.M.S. Schofield, H.E. Lefevre, ”Explosives detection through fast-neutron time-of-flight attenuation measurements”, Nucl. Instrum. Methods Phys. Res. B 99 (1995) 728-732.
20. G.F. Knoll, Radiation detection and measurements, Third ed., John Wiley and Sons, Inc., Ann Arbor, Michigan, 2000.
21. K. Krane, Introductory Nuclear Physics, 2 ed., John Wiley & Sons, Inc., 1988.
22. R.A. Forster, L.J. Cox, R.F. Barrett, T.E. Booth, J.F. Briesmeister, F.B. Brown, J.S. Bull, G.C. Geisler, J.T. Goorley, R.D. Mosteller, S.E. Post, R.E. Prael, E.C. Selcow, A. Sood, “MCNP Version 5”, Nucl. Instrum. Methods Phys. Res. B 213 (2004) 82-86.
23. S. Pozzi, E. Padovani, M. Marseguerra, “MCNP-PoliMi: a Monte-Carlo code for correlation measurements”, Nucl. Instrum. Methods Phys. Res. A 513 (2003) 550-558.
24. R.G. Williams III, C.J. Gesh, R.T. Pagh, “Compendium of material composition data for radiation transport modeling”, Report PNNL-15870, Pacific Northwest National Laboratory, Richland, Washington, 2006.

Chapter 4: D-D Neutron-Scatter Measurements for a Novel Explosives-Detection Technique

Abstract

A series of measurements has been completed that provides a benchmark for Monte Carlo simulations related to an algorithm for explosives detection using active neutron interrogation. The original simulations used in algorithm development, based on sea-land cargo container screening, have been adapted to model active neutron interrogation of smaller targets. These smaller-scale measurements are easily accomplished in a laboratory environment. Benchmarking measurements were completed using a D-D neutron generator, two neutron detectors, as well as a variety of scatter media including the explosives surrogate melamine ($C_3H_6N_6$). Measurements included 90°, 120°, or 150° neutron scatter geometries and variations in source-detector shielding, target presence, and target identity. Comparisons of measured and simulated neutron fluxes were similar, with correlation coefficients greater than 0.7. The simulated detector responses also matched very closely with the measured photon and neutron pulse height distributions, with correlation coefficients exceeding 0.9. The experiments and simulations also provided insight into potential application of the new method to the problem of explosives detection in small objects such as luggage and small packages.

Introduction

Explosives detection with active neutron interrogation

Thermal neutron activation (TNA)-based explosives detection relies upon the detection of characteristic photons produced when target nuclei absorb incident neutrons. Another strategy relies on the characteristic de-excitation photons emitted when incident neutrons undergo inelastic scatter. A third strategy strategy uses measurements of the interacted neutron beam, such as in transmission imaging, neutron flux measurements, or neutron spectroscopy. Each strategy has its own advantages and disadvantages, including interaction probability, optimal target size, and ease of signal discrimination [1-3].

Neutron scatter measurements for the detection algorithm

The explosives-detection technique explored for this work represents a unique combination of the prior approaches. It uses the neutron and photon information produced during fast-neutron interrogation to calculate specific flags that are part of an explosives-detection algorithm. These flags are generally in the form of ratios of specific neutron or photon measurements at two different scatter angles. Earlier work was devoted to characterizing the neutron scatter in large targets [4] and identifying flags in simplified [5] and semi-realistic [6] screening scenarios of sea-land cargo containers. Some flags are used to determine the type of cargo, which determines which other flags are best suited for detecting explosives in that particular cargo. Specific changes in these explosives-sensitive flags then used to “trigger” in the presence of a possible explosive.

This paper presents various benchmarking measurements for the generalized type of neutron-scatter characterization simulations essential to the development of the method. Although on a considerably smaller scale than the original simulations, these measurements provide justification for the simulated detector responses, demonstrate the close relationship between measurements and simulations, and provide insight into future efforts concerning smaller targets, such as luggage screening. Measurements included targets of the explosives-surrogate melamine, vegetable oil, water, and paper. Three different scatter angle geometries were considered, as the cargo screening system will utilize photon and neutron measurements at several different angles. Due to equipment constraints, only a D-D generator, with its 2.45-MeV neutrons, was available to perform the measurements.

The available detectors provided two avenues of comparison with Monte Carlo simulations. The first involved the change in total neutron flux at the detector due to shielding between it and the source, as well as presence of scattering media in the target location. Furthermore, limited neutron spectroscopic capabilities in one of the detectors allowed similar comparisons for the higher energy unscattered- or slightly-scattered neutrons reaching the detector. Similar results for the experiments and simulation would demonstrate that the approximations made in the simulation geometry are appropriate to neutron scatter measurement scenarios. The second point of comparison with simulations was the accurate calculation of the liquid scintillation detector response to scattered neutrons and associated photons. Simulations that showed similar pulse height distributions (PHDs) to those actually produced by the neutron detector would provide an important benchmark as to the reliability of the simulations.

Neutron-Interrogation Methods

Materials for neutron-scatter measurements

Facility and infrastructure

Irradiations were conducted behind cinderblock shielding on adjoining wooden tables that held the neutron source, target material, neutron detectors, and in some cases source-detector shielding. The first table was 0.60 m wide × 1.8 m long × 0.05 m thick wooden tabletop with 0.9 m tall metal legs, while the other was 0.91 m wide × 0.76 m long × 0.05 m thick. Both tabletops were approximately 1 m above a concrete floor.

Neutron source

A D-D neutron generator (MP320, Thermo Fisher Scientific Inc. 5074 List Drive, Colorado Springs, CO 80919) provided fast neutrons. It produced monoenergetic 2.45-MeV neutrons at a rate of 2×10^6 n s^{-1} and was operated at a 100% duty cycle for all measurements.

Neutron detectors

One neutron detector used in the scatter measurements, hereafter referred to as detector A, was a customized neutron spectroscopy and dosimetry system (Microspec-2, Bubble Technology Industries Inc., 31278 Hwy 17, Chalk River, Ontario, Canada K0J1J0) with the addition of a neutron probe module [7]. This system contained a 5-cm diameter, 5-cm long NE-213 liquid scintillator for fast neutrons and a ^{3}He counter for energy ranges from thermal to 1.5 MeV. A pulse shape discrimination (PSD) algorithm (FERDOR) incorporated into the computer software was used to reject photons at a ratio of approximately 1000:1 [8], enabling both dosimetric measurements and neutron spectroscopy [9]. The unfolding algorithm sorted neutrons into 0.5-MeV energy bins for energies < 2.0 MeV, 1-MeV bins for 2.0-10 MeV neutrons, and 2-MeV intervals for 12-18 MeV neutrons. One experimental complication was that the short physical connection between the detection system control box and detector prohibited remote activation after the neutron beam was established. Therefore, the counting period commenced prior to beam ramp-up, which produced some inconsistencies in calculated count rates due to variations in generator ramp-up and shut-down between measurements.

Another type of detector, hereafter referred to as detector B, used in scatter measurements used a 12-cm diameter, 13-cm long, 0.5-cm thick, aluminum-walled cylinder filled with EJ-309 liquid scintillator fluid (Eljen Technology, 2010 E. Broadway, Sweetwater, TX 79556, USA), with an attached photomultiplier tube (XP4512B, Photonics, Berkshire Common PO Box 4949, Pittsfield MA 01202, USA) and 12-bit, 250-MHz waveform digitizer (V1720, CAEN Technologies, Inc., 1140 Bay Street, Suite 2C, Staten Island, NY 10305). Commercially available mathematics software package (MATLAB, 3 Apple Hill Drive, Matick, MA 01760, USA) was employed to implement an optimized PSD method. This method was based on tail-to-total integrals of the waveforms for separating photon- and neutron-produced pulses [10,11], with a minimum threshold set to 80 keVee. The Compton edge in the PHD for a ^{137}Cs check source, at 447 keV, was used to determine the detector light-output-to-energy conversion factor.

Scattering media

Several different types of scatter media were used. Melamine ($C_3H_6N_6$) has a relatively high nitrogen content and is a common substitute for explosives [12,13]. Either one or two 2.5-kg containers (11.4 cm × 11.4 cm × 20.3 cm) of melamine (Acros Organics, Janssen-Pharmaceuticalaan 3a, Geel, 2440, Belgium) were used as scatter targets. Other targets included 2.3-L (10.2 cm × 14.2 cm × 22.9 cm) containers of tap water, 3.8-L (12.7 cm × 14.0 cm × 25.4 cm) containers of vegetable oil, and a 2.25-kg (15 cm × 15 cm × 16 cm) ream of office paper. Either the above containers of water or larger 12-L (19 cm × 29 cm × 23.5 cm) containers of tap water were used in some measurements as shielding between the source and detector.

Neutron-Interrogation Measurements

Detector A with 90°, 120° and 150° neutron scatter

For the first set of neutron scatter measurements, scatter media was placed 1.2 m from the source and 0.53 m from detector A such that a 90° scatter angle was present between the source, target, and detector. Each of these twelve measurements lasted 7 min. The six target configurations included no target, two containers of melamine, oil, or water, as well as two measurements in which two containers of melamine were concealed by the two containers of either water or oil. Six measurements were made with no source-detector shielding and the other six contained two of the smaller water containers placed between the source and detector A. A photograph of the melamine target with source-detector shielding is shown in Fig. 4-1a, with the corresponding simulation geometry in Fig. 4-1b.

These six target geometries were again used in six 7-min measurements, and corresponding simulations, in which the targets were placed 91 cm from the source and 58 cm from the detector for a 120° neutron scatter. A further six 7-min measurements were taken using a 150° neutron scatter geometry, in which source-target and target-detector distances were 81 cm and 91 cm, respectively.

The change in the number of total and singly-scattered neutrons with and without source-detector shielding was calculated for the 90° scatter measurements and simulations. Further calculations involved the change in the number of total and singly-scattered neutrons due to the presence of scatter media in the target location in all scatter geometries for both measurements and simulations. The results for the simulations and measurements were then compared.

Detectors A and B with 90° neutron scatter

Further measurements were made using a 90° neutron scatter geometry and both detector A and detector B. Three 6-min measurements were made with a source-target location of 41.9 cm and 30.5 cm between the target and both detector A and detector B, as illustrated in the photograph shown in Fig. 4-2a, with the corresponding simulation input geometry shown in Fig. 4-2b. One 6-min count was made with no target and no source-detector shielding to compare the relative efficiencies of the two systems. The other two 6-min measurements in this geometry had the larger blocks of water placed between the source and both detectors A and B to shield them from unscattered neutrons. The target was either absent or one container of melamine.

In a final set of five 5-min measurements the same 90° scatter geometry was used, though a redistribution of laboratory equipment during the intervening time period required the change of a wooden lab bench and wooden stool in the place of the two wooden tables used in all other measurements. This necessitated a decrease in the source-target and target-detector distances, which should magnify the effect of target media presence. All five measurements utilized the larger containers of water as source-detector shielding. Target materials included one container of melamine, water, oil, or a ream of paper as defined above, or no target. In addition, two 30-min measurements were made, one with no target and one with a single container of melamine.

Computational Methods

Monte Carlo Simulations

All Monte Carlo simulations were completed using Monte Carlo N-Particle 5 (MCNP5) [14] or the related software MCNP-PoliMi, which is better able to simulate time-analysis quantities [15]. Simulated material compositions, drawn from the literature as appropriate [16,17], appear in Table 4-1. Although efforts were made to model the measurements as faithfully as possible, simplifications were present in the geometries of the surrounding environment, neutron generator, and neutron detectors.

The simulations used a simplified surrounding environment in which two wooden tables, or a table and chair, were centered in an air-filled 6 m × 7 m × 3 m room with 1-m thick concrete walls and floor, and none of the piping or other surrounding features. The D-D neutron generator was approximated by a 55.8 cm long, 0.5 cm thick, 10.2 cm exterior diameter aluminum tube. The tube interior was filled with 1.2×10^{-5} g cm^{-3} air and contained a 2.45-MeV isotropic neutron point source 14 cm from one end. On top of the cylinder was a 20.3 cm × 53.3 cm × 20.3 cm box containing a homogenous approximation of typical electronics.

Three different MCNP5 F1 tallies were calculated at the front surface of the active volume of the simulated detector A. These included neutron and photon tallies with 0.2-MeV energy bins and a neutron tally utilizing the same energy bins as detector A, as described above. Two F1 tallies with 0.2-MeV energy bins for photons and neutrons were similarly calculated on the front surface of the simulated detector B.

The same geometries, source, and tallies described above were used in the MCNP-PoliMi simulations that also calculated realistic detector responses. Options in the MCNP-PoliMi input files were set to force analog Monte Carlo processes instead of statistics-based approximations, specify the detector active volume for data collection, format for data output, and a neutron and photon cutoff of 0.1 MeV. Sample MCNP input files for 90° scatter geometry with one or two detectors and a 120° scatter geometry may be found in Appendix A.

Pulse height distributions

Calculation of the simulated PHDs required both MCNP-PoliMi as well as a custom Fortran-based post-processor [11] that calculated detector response, compiling the interaction data into pulse height and time-of-flight distributions. To accomplish this, the post-processor calculated light output (MeVee) in the detector such that the light produced by photon interactions was equal to the energy deposition (MeV). The relationship between neutron energy deposition and light production was more complicated, such that:

$$L = 0.03495E^2 + 0.1424E - 0.036, \qquad (4.1)$$

in which light output in detector *B*, *L* (MeVee) was a quadratic function of neutron energy deposition, *E* (MeV) [11]. The resulting calculated neutron PHDs were compared with the measured neutron PHD that was isolated using aforementioned PSD techniques.

Data analysis

Once the percent change in both total and singly-scattered neutron flux was calculated for the detector A measurements and Monte Carlo simulations a statistics package (SPSS v19, IBM Corporation, 1 New Orchard Rd, Armonk, NY 10504, USA) was used to run two-tailed, paired t-test and bivariate correlations on the data. Similarly, the statistics package was used to calculate the Pearson correlation coefficients between the measured and simulated photon and neutron PHDs. The later necessitated resampling the simulated PHDs so that the same number of data points was used for the simulations and measurements. The paired t-test calculated p-values, which demonstrated statistically significant differences if they were below 0.05, while the correlation coefficients represented a close match if they were close to 1.0.

Results and Discussion

Detector A in a 90°, 120°, and 150° neutron scatter geometries

For the measurements using only detector A in a 90° scatter geometry, the six geometries showed an 83% ± 2.2% decrease in the total count rate when the water shielding blocks were present. Similarly, the total number of measured 2.0-3.0 MeV, unscattered or slightly scattered, neutrons decreased by 80% ± 5.1% when the shielding was in place. This, along with the corresponding results of the MCNP5 simulations, is shown in Table 4-2. The results of the simulations agreed with the measurements, falling within 10% for the change in total neutron count and ~5% for the change in 2.0-3.0 MeV neutrons. This dramatic decrease is expected, as the mean free path of a 2.45 MeV neutron is only a couple of centimeters in water.

Because of this low neutron penetration of the source-detector shield, the vast majority of the neutrons reaching the detector when the shield is in place are those that scatter off surrounding material such as the table or target media. Therefore, the presence of target media is expected to increase both the total number of neutrons and singly-scattered neutrons reaching the detectors, with the amount of change more due to the amount than type of scatter material. As seen in Table 4-3, a 3-6% increase in the total number of neutrons was measured without the source-detector shield, and this change increased to 7-13% when the shielding was present. The number of 2-3 MeV neutrons increased by 3-4% when scatter media was present in the unshielded cases, but varied between 5% and 16% for the shielded scenarios. However, this variation was within the expected 5% from the mean due to propagation of the uncertainty associated with counting statistics. As expected, there was a larger, by a factor of ~2, change in neutron flux when the shield was present. For most cases there was reasonably good agreement between the measured and simulated results in that the measured and simulated changes in neutron flux were within one standard deviation of each other.

The changes due to presence of different scatter targets in the 120° and 150° neutron scatter geometries are summarized in Table 4-3. For the 120° scatter geometry, the presence of scatter media increased the total number of neutrons by 8-18%. D-D Neutrons undergoing a single 120° elastic scatter off carbon, nitrogen, or oxygen decrease in energy to 1.9-2.0 MeV. The bin containing these neutrons, 1.5-2.0 MeV, increased by 7-8% for oil-containing targets, but changed by less than 1% for the other targets. The simulations of the 120° scatter geometry showed similar results. In these simulations the total number of neutrons increased by 4-10%. The number of singly-scattered neutrons increased by 7-12% for most cases, but by less than 3% for melamine and water targets.

Table 4-3 also shows the changes in total and singly-scattered neutron flux for the 150° neutron scatter scenarios. The measured total neutron flux changed by less than 2% for all cases. The change in singly-scattered neutron flux was also relatively small, less than 4% for all cases except for a 7.9% change with the melamine and oil combined target. The results of the 150° simulations all showed increases of less than 2.5% for both the total and singly-scattered neutron tallies. Although all simulations showed the expected increase in neutron tallies, the differences are too small to draw any clear conclusions.

A paired t-test of the data shown in Table 4-3 found p-values of 0.076 and 0.309 for the total and singly-scattered neutron flux, respectively. As both p-values are above 0.05, there is no statistically significant difference between the simulated and measured neutron fluxes. A bivariate correlation calculation found relatively high Pearson correlation coefficients of 0.919 for the change in total neutron flux and 0.757 for the change in singly-scattered neutron flux. The weaker correlation in the singly-scattered neutron flux is probably due to errors introduced in the unfolding of the measured neutron pulse height distribution.

Furthermore, other errors in the measured neutron flux are due to the fact that many of the singly-scattered neutrons do not deposit their full energy in the detector's active volume.

Though there was significant variation in the neutron flux change for different targets in the 120° and 150° scatter scenarios, most of the simulated and measured results were within the margin of error of each other. Exceptions were present in the case of melamine and melamine with oil at 120° scatter and melamine with oil at 150° scatter. Several of the cases showed no significant change in the number of measured singly-scattered neutrons. This is partially because the longer distances between source-target-detector as compared to the source-detector distance for these two scatter geometries. Therefore, very few of the singly-scattered neutrons actually interacted in the target media when compared to the large number scattered in the environment near the source and detector. This leads to both small changes in neutron flux measurements, as well as relatively large errors.

Measurements using two neutron detectors at 90° neutron scatter

For the final set of measurements both detectors were used to measure neutrons in a 90° scatter geometry. Furthermore, the decreased source-target and target-detector distances magnified the effect of target media presence. The results of the simulations and detector A results are shown at the bottom of Table 4-3. These results were more dramatic than previously measured, with increases of between 11-30%, with counting errors in the range of 1% for total neutrons. The change in singly-scattered neutrons was a smaller 3-8% ± 1%. The results of the 30-min measurement showed a similar 18% increase in the total number of neutrons and a 12% increase in 3-4 MeV neutrons when melamine was present. The simulated detector A tallied similar increases in the total number of neutrons: 10% for melamine, 25% for oil and water, and 19% for paper. The change in singly-scattered neutrons ranged from 2-10%, with statistical uncertainties around 3%. Of all the scatter geometries, the ones with dual neutron detectors showed the closest agreement between measurement and simulation. Except for the case of total neutrons and paper target, all neutron flux simulations, for both detectors, were within the margin of error of the measurements.

Measurements using detector B found an increase in neutron count rate for every case that contained additional scatter media. A comparison of the change in total and neutron count rates for measurement, MCNP5, and MCNP-PoliMi due to the presence of scatter media are shown in Table 4-4. For almost all cases, both the MCNP5 and MCNP-PoliMi simulations were within 25% of the measured change in count rates. Furthermore, changes in the total neutron flux were very similar for measurements using detector A and detector B when oil and paper targets were used, and within 15% for melamine and water targets. As expected, there was very close agreement between the MCNP5 and MCNP-PoliMi neutron counts. There was about 3% difference between the MCNP5 and MCNP-PoliMi total counts, probably due to the differences in photon production between the two methods.

Pulse height distributions

The tallied neutron and photon energy distributions at the surface of detector B, an example of which is shown in Fig. 4-3a, are reflected in the calculated photon and neutron PHDs, which are shown in Fig. 4-3b for a melamine target. The corresponding measured PHDs are shown in Fig. 4-3c. In both cases, the Compton edge for 2.2 MeV photons occurs around the expected 1.9 MeVee, though this is more blurred in the measured PHDs. The maximum value of the neutron PHD at ~0.5 MeVee is very close to the expected value of 0.51 MeVee caused by 2.45 MeV neutron scatter in the liquid scintillator. Furthermore, the neutron PHDs of the five different targets were very similar, as is illustrated in Figs. 4-4a and 4-4b. It should be noted that data points are spaced every 0.01 MeVee in the simulated data, but 0.04 MeVee in the measured data.

A comparison of the measured and MCNP-PoliMi simulated photon PHDs may be seen in Fig. 4-5a, with the neutron PHDs shown in Fig. 4-5b. In both figures the number of counts has been normalized to the maximum value to more accurately compare the curve shapes. The shapes of the PHDs are very similar, with most of the variation found in the photon PHD at the highest energies, where the majority of the signal is due to interactions of photons in the liquid scintillator. Another major difference in the photon PHDs is the increased width of the measured PHD as compared to the simulation results. The measured PHD has a more gradual increase and decrease when compared to the idealized case of the simulation. This is mainly due to factors such as the idealistic light collection and timing resolution of the simulation. Statistical analysis of the measured and simulated PHDs led to very high Pearson correlation coefficients of 0.98 for the photon PHDs and 0.97 for the neutron PHDs.

Neutron scatter as part of an explosives-detection algorithm

As mentioned earlier, limitations in the available equipment required that the experiments be confined to the 2.45 MeV neutrons in a scenario closer to luggage-screening than cargo containers. Use of 2.45 MeV neutrons also limited the study of photons produced during inelastic scatter interactions, as the vast majority of de-excitation reaction in hydrogen, carbon, nitrogen, and oxygen require neutron energies of more than 2.45 MeV. However, it has been shown that the neutron scatter behavior of D-D neutrons may be closely approximated using Monte Carlo modeling and that a realistic detector response can be accurately modeled.

These measurements also showed that the simulated changes in neutron flux in detector A varied from the measured fluxes by about 25% for the total neutron flux, and by about 32% for the singly-scattered neutron flux when cases of more than 100% variation were ignored. This is partially explained by the large variations in measured flux rates within a single scatter geometry and with similar targets. This signifies that much of the disagreement is due to errors in measurement with detector A. However, detector B showed a much closer agreement with the simulations, averaging about 11% difference with MCNP5 and 8% difference with MCNP-PoliMi. This signifies that an error margin of about

10% from MCNP-PoliMi simulations would be expected in future measurements using this detector.

This close agreement between simulation and detector B response presents the very real possibility that the explosives-detection flags found using simulated 14.1 MeV neutrons in a cargo-screening scenario would work in actual screening measurements [15,5,6]. The computer simulations, with their inherent precision and customization potential may then be used to determine where to look for the flags that best signal the presence of explosive. Furthermore, these measurements could easily be used to justify future simulations dealing with other explosives-detection scenarios, such as luggage screening.

Conclusions

A series of measurements has been completed to investigate the scattering behavior of monoenergetic 2.45 MeV neutrons at several angles and a variety of target materials, including the explosives surrogate, melamine. The scenarios have also been also been modeled using the Monte Carlo software MCNP5 and MCNP-PoliMi. Favorable comparisons of the simulated and measured neutron flux in a variety of scatter scenarios demonstrated that the level of detail in the simulations was adequate to accurately model the scatter scenarios. Further comparisons were made between calculated and measured detector response to the neutron flux demonstrated that it was possible to accurately model detector response in a mixed radiation field scenario.

Comparisons of the simulated and measured neutron flux showed close agreements, with correlation coefficients of 0.92 and 0.76 for the total and singly-scattered neutrons, respectively. A paired t-test showed no statistically significant difference between measurement and simulation. Furthermore, almost all of the neutron flux calculations for simulations and measurements agreed within the margin of statistical error. Exceptions were present, especially in the 120° and 150° neutron scatter scenarios, in which most of the singly-scattered neutrons were scatters from the environment due to the relatively large source-target-detector distance. Favorable comparisons of the measured and simulated pulse height distributions (PHDs) were also found, although the simulated PHDs were considerably narrower and, as expected, showed greater detail than the measured PHDs. Correlation coefficients matching simulation and measurement were very high, 0.98 and 0.97 for the photon and neutron PHDs, respectively.

The results of this study showed that basic approximations in the simulation geometry, such as simplifications in the surrounding environment, allow an accurate portrayal of neutron scatter in a screening scenario, especially when smaller source-target-detector distances are considered, such as in luggage-screening scenarios. Furthermore, this study has shown that it is possible to accurately model the response of the neutron detectors used in the neutron scatter measurements.

Figures

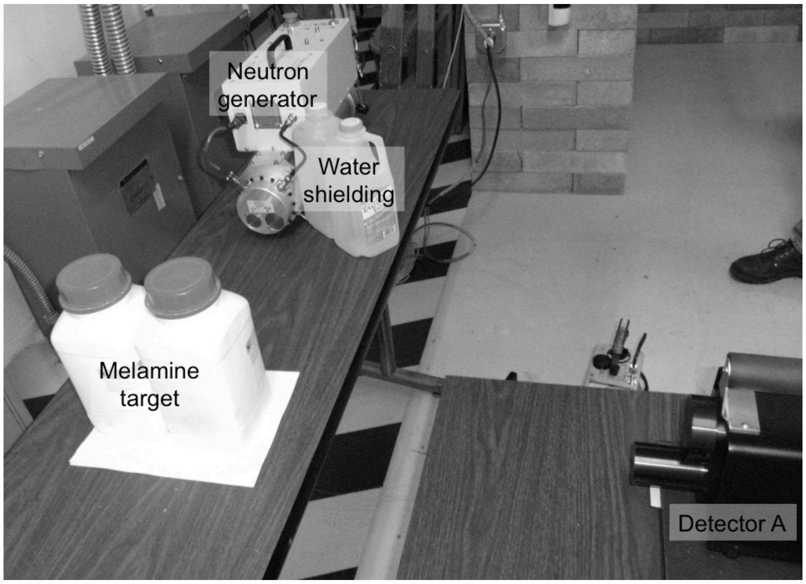

a.

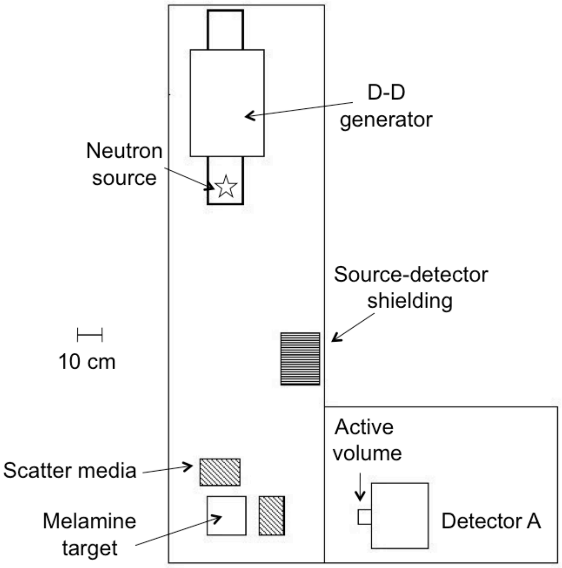

b.

Figure 4-1. D-D neutron generator and detector A in a) measurement and b) simulation with melamine target shielded by scatter media of water or oil, and water shielding block between source and detector active volume. Other cases eliminated the source-detector shielding or scatter media, or used other target materials.

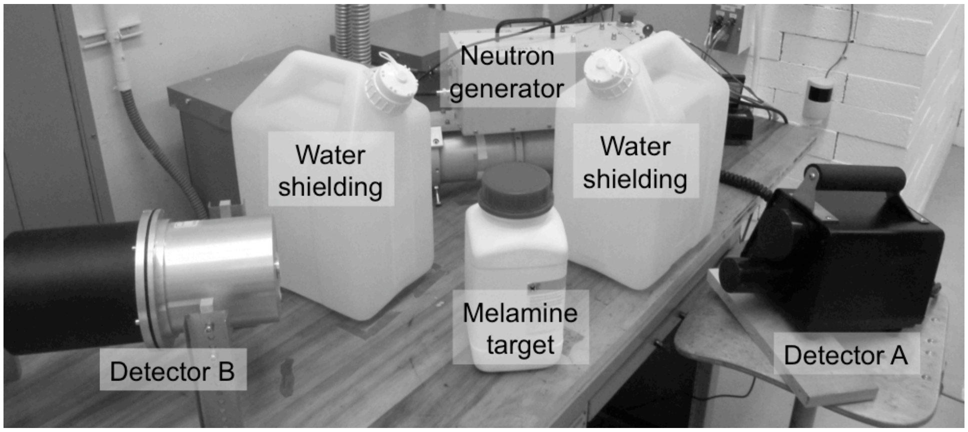

a.

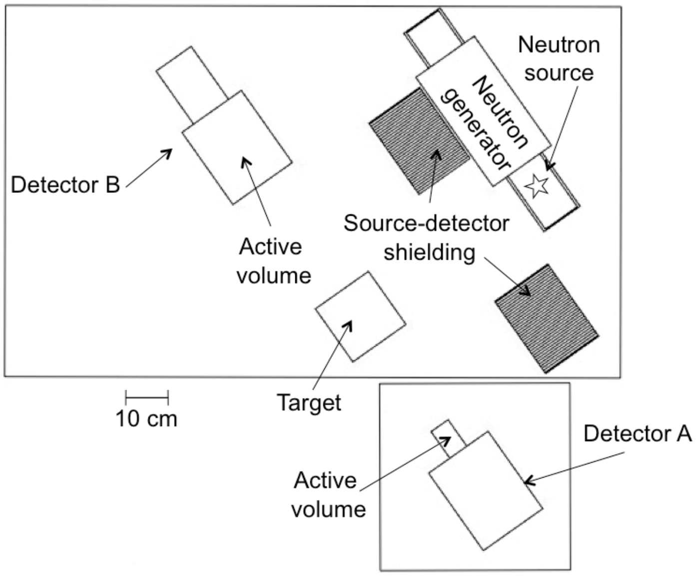

b.

Figure 4-2. D-D neutron generator, source-detector shielding and dual detectors in a 90° scatter geometry for a) measurement with melamine target and b) simulation. Possible target materials in both simulations and measurements included melamine, water, oil, or paper.

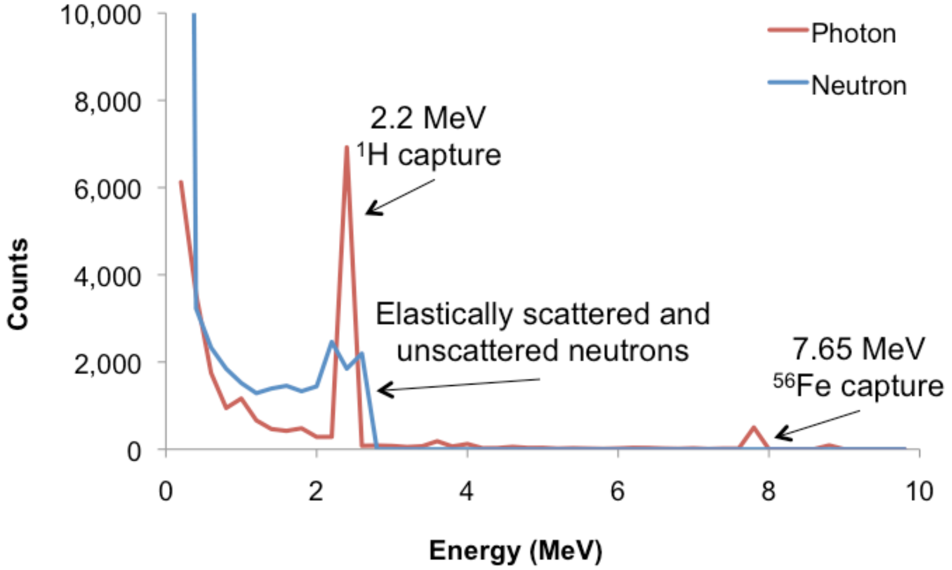

a.

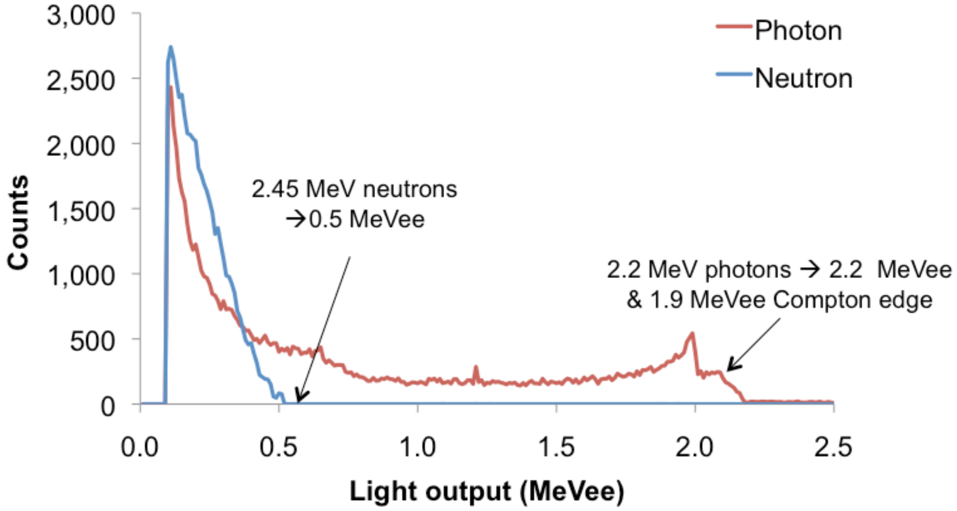

b.

Figure 4-3. Example detector B output for a 90° neutron scatter and melamine target scenario with a) the simulated neutron and photon MCNP5 F1 tallies on the detector face, b) the simulated detector response, and c) the measurement detector response. The ^{56}Fe photons are due to interactions in the table legs.

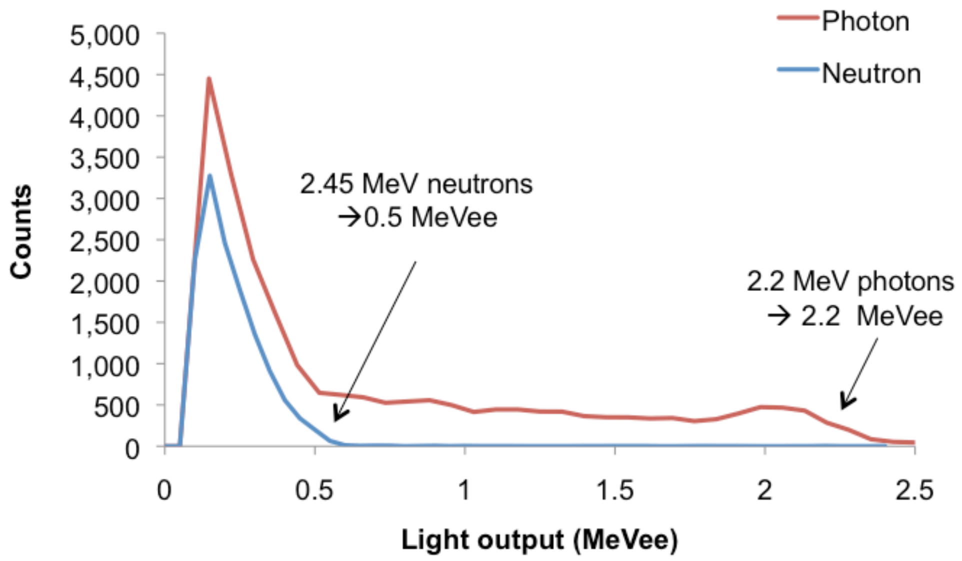

c.

Figure 4-3 (continued). Example detector B output for a 90° neutron scatter and melamine target scenario with a) the simulated neutron and photon MCNP5 F1 tallies on the detector face, b) the simulated detector response, and c) the measurement detector response. The ^{56}Fe photons are due to interactions in the table legs.

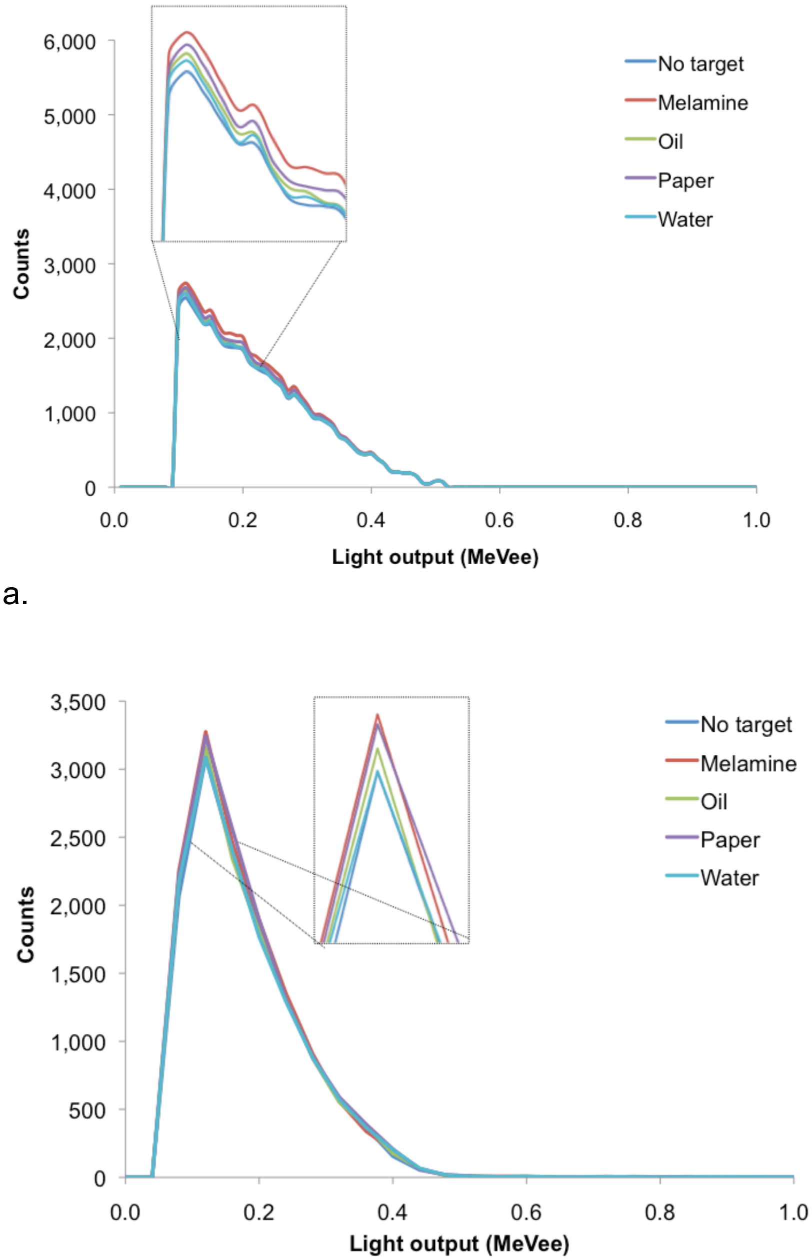

a.

b.

Figure 4-4. a) Simulated and b) measured neutron pulse height distributions for no target and various target materials. Differences between the cases are shown in the detail boxes.

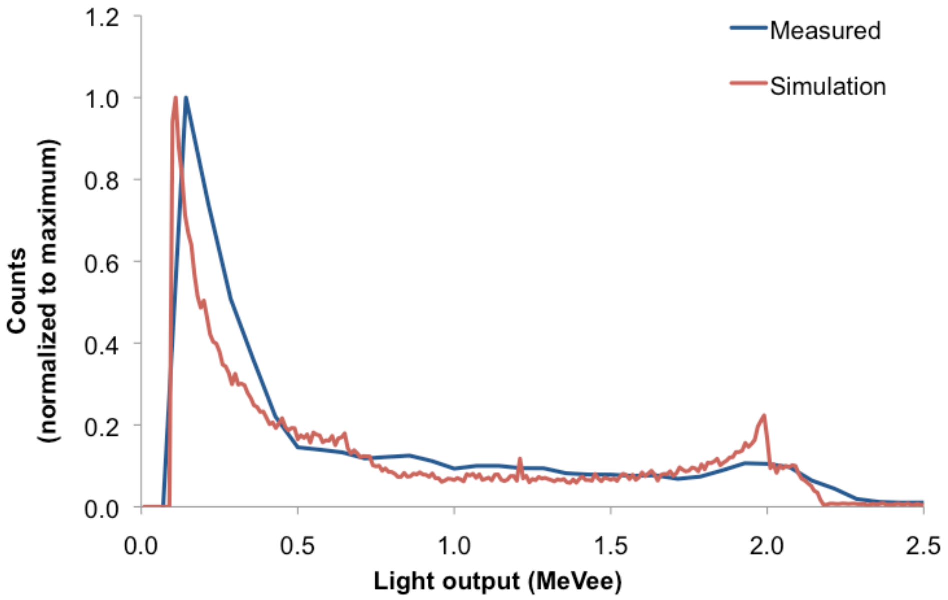

a.

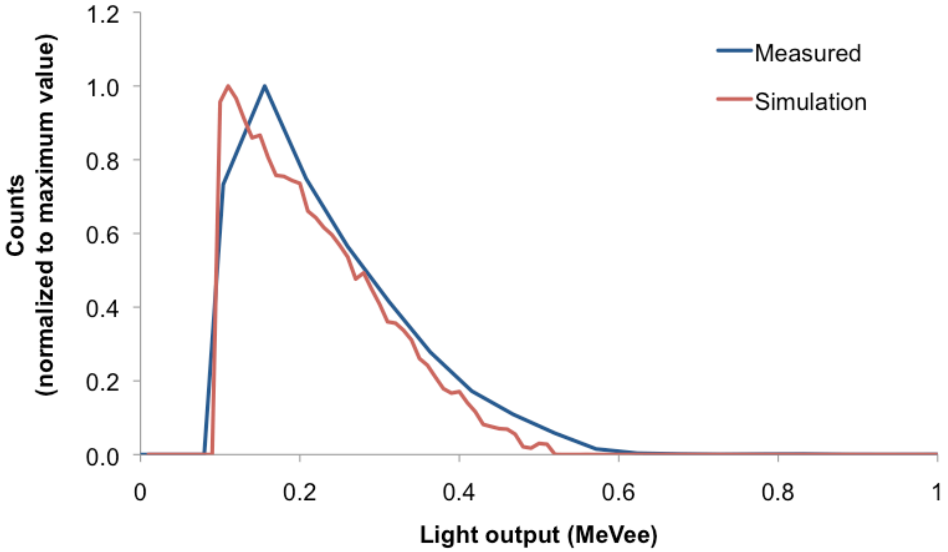

b.

Figure 4-5. Comparison of the measured and simulated a) total and b) neutron pulse height distributions.

Tables

Table 4-1. Atom percent compositions of all materials used in simulations.

Material	Density (g cm^{-3})	H	C	N	O	Other
Air	0.0012		0.01%	75.5%	23.2%	1.30% Ar
Steel	7.87		0.32%			99.6% Fe, 0.050% S, 0.04% P
Wood[11]	0.65	47.6%	28.6%	23.8%		
Water	1.0	66.7%			33.3%	
Melamine	1.57	40.0%	20.0%	40.0%		
Oil	0.92	62.8%	33.5%		3.7%	
Paper[11]	0.60	47.6%	28.6%	23.8%		
NE213	0.87	54.8%	45.2%			
Electronics	0.33	25.7%	1.87%		46.8%	2.59% Al, 12.3% Si, 10.4% Ni, 0.27% Fe
Concrete[11]	2.3	30.4%	0.29%		49.9%	0.92% Na, 1.03% Al, 15.1% Si, 0.71% K, 1.49% Ca, 0.16% Fe
Soil[11]	1.75	29.4%	1.87%		50.5%	2.59% Al, 13.5% Si, 1.43% K, 0.27% Fe

Table 4-2. Percent decrease in the number of neutrons due to the presence of water shielding block between detector A and source for a 90° scatter geometry. Error estimation reflects the uncertainty introduced by counting statistics.

Scatter target	Measurement: total n	Simulation: total n	Measurement: 2.0-3.0 MeV n	Simulation: 2.0-3.0 MeV n
No target	-84 ± 1%	-94 ± 1%	-79 ± 2%	-84 ± 2%
Melamine	-84 ± 1%	-94 ± 2%	-80 ± 2%	-84 ± 3%
Oil	-81 ± 1%	-94 ± 1%	-79 ± 2%	-84 ± 2%
Water	-80 ± 1%	-94 ± 2%	-79 ± 2%	-84 ± 3%
Melamine + oil	-86 ± 1%	-93 ± 2%	-80 ± 2%	-84 ± 3%
Melamine + water	-83 ± 1%	-94 ± 2%	-82 ± 2%	-84 ± 3%

Table 4-3. The percent increase in the number of neutrons at detector A when scatter targets are present. Elevated changes in multiple detector data are due to decreased target-detector distance. Single-scatter neutrons represent the 1.5-2.0 MeV neutron energy bin in the 120° and 150° scatter scenarios and 2.0-3.0 MeV for the 90° cases. Error estimation reflects the uncertainty introduced by counting statistics.

Scatter angle	Scatter target	Total neutrons		Single-scatter neutrons	
		Measurement	Simulation	Measurement	Simulation
No source-detector shield					
90°	Melamine	3.2 ± 0.8	3.4 ± 1.1	3.8 ± 1.1	3.4 ± 3.6
90°	Oil	4.4 ± 0.8	3.4 ± 1.1	3.4 ± 1	3.5 ± 3.6
90°	Water	6.1 ± 0.7	3.3 ± 1.1	3.3 ± 1.1	4.6 ± 3.6
90°	Melamine + oil	4.7 ± 0.7	3.9 ± 1.1	3.4 ± 1.1	3.7 ± 3.6
90°	Melamine + water	4.5 ± 0.7	3.7 ± 1.1	3.6 ± 1	4.0 ± 3.6
Source-detector shield present					
90°	Melamine	9.1 ± 1.9	8.3 ± 2.2	4.9 ± 5.1	7.4 ± 5.4
90°	Oil	9.8 ± 1.8	9.1 ± 2.2	5.3 ± 5.3	4.8 ± 5.4
90°	Water	12 ± 1.8	6.4 ± 2.2	9.4 ± 5.4	4.3 ± 5.4
90°	Melamine + oil	7.4 ± 1.9	9.1 ± 2.9	13 ± 5.0	19 ± 6.7
90°	Melamine + water	13 ± 1.8	14 ± 2.9	16 ± 5.4	14 ± 6.7
120°	Melamine	9.3 ± 1.3	4.1 ± 1.5	-0.36 ± 3.8	1.3 ± 8.2
120°	Oil	10 ± 1.3	8.0 ± 1.5	8.1 ± 3.8	9.5 ± 8.4
120°	Water	8.4 ± 1.3	5.8 ± 1.5	-0.18 ± 3.7	2.9 ± 8.4
120°	Melamine + oil	18 ± 1.3	10 ± 1.5	7.1 ± 3.6	12 ± 8.4
120°	Melamine + water	8.4 ± 1.3	8.5 ± 1.5	-0.73 ± 3.9	6.7 ± 8.4
150°	Melamine	0.4 ± 0.7	0.87 ± 0.9	0.42 ± 1.08	0.68 ± 4.45
150°	Oil	0.2 ± 0.7	1.5 ± 0.89	0.63 ± 1.12	1.9 ± 4.46
150°	Water	1.5 ± 0.7	1.1 ± 0.89	3.1 ± 1.11	1.8 ± 4.46
150°	Melamine + oil	0.1 ± 0.7	2.3 ± 0.89	7.9 ± 1.1	2.2 ± 4.46
150°	Melamine + water	1.0 ± 0.7	1.8 ± 0.89	2.1 ± 1.1	1.6 ± 4.46
Source-detector shield, multiple detectors present					
90°	Melamine	11 ± 0.96	10 ± 0.67	3.8 ± 1.1	2.2 ± 2.7
90°	Oil	20 ± 0.94	25 ± 0.66	7.1 ± 1.1	5.1 ± 2.8
90°	Paper	20 ± 0.94	19 ± 0.67	5.1 ± 1.1	6.1 ± 2.7
90°	Water	31 ± 0.93	24 ± 0.66	7.1 ± 1.1	10 ± 2.8

Table 4-4. Comparison of the change in the total and neutron count rates due to the presence of scatter media for simulation and measurement results in detector B. Error estimation reflects the uncertainty introduced by counting statistics.

Scatter target	Measurement: total	MCNP5: total	PoliMi: total
Melamine	21 ± 1%	14 ± 0.5%	17 ± 0.5%
Oil	22 ± 1%	21 ± 0.5%	24 ± 0.5%
Paper	20 ± 1%	15 ± 0.5%	17 ± 0.5%
Water	23 ± 1%	21 ± 0.5%	23 ± 0.5%
	Measurement: neutrons	MCNP5: neutrons	PoliMi: neutrons
Melamine	23 ± 2%	24 ± 0.3%	24 ± 0.3%
Oil	19 ± 2%	18 ± 0.3%	18 ± 0.3%
Paper	24 ± 2%	24 ± 0.3%	24 ± 0.3%
Water	20 ± 2%	18 ± 0.3%	18 ± 0.3%

References

1. A. Buffler, J.R. Tickner, “Detecting contraband using neutrons: challenges and future directions”, Radiat. Meas. 45 (2010) 1186.
2. T. Gozani, “Principles and applications of neutron-based inspection techniques”, Nucl. Instrum. Methods Phys. Res. B 261 (2007) 344.
3. A.L. Lehnert, K.J. Kearfott, “The detection of explosive materials: review of considerations and methods”, Nucl. Technol. 172 (2010) 325.
4. A.L. Lehnert, K.J. Kearfott, “Simplified simulation of fast neutron scattering for an explosives detection application”, Nucl. Sci. Eng. 168 (2011) 278.
5. A.L. Lehnert, K.J. Kearfott, “Preliminary identification of flags for a novel algorithm-based approach for explosives detection using neutron interrogation for a simulated idealized cargo container scenario”, Nucl. Instrum. Methods Phys. Res. A 638 (2011) 201.
6. A.L. Lehnert, K.J. Kearfott, “Simulations for developing a flag-based active neutron interrogation method for explosives detection in sea-land cargo containers”, Nucl. Technol. (submitted for publication)
7. H. Ing, S. Djeffal, T. Clifford, R. Machrafi, R. Noulty, “Portable spectroscopic neutron probe”, Radiat. Prot. Dosim. 126 (2007) 238.
8. Microspec-2 User’s Manual, version 17, Bubble Technology Industries. Inc., 2002.
9. W.G. Cross, H. Ing, Neutron spectrosopy, in: The dosimetry of ionizing radiation”, Academic Press, New York, 1987.
10. M. Flaska, S. Pozzi, “Identification of shielded neutron sources with the liquid scintillator BC-501A using a digital pulse shape discrimination method”, Nucl. Instrum. Methods Phys. Res. A 577 (2007) 654.
11. E.C. Miller, S.D. Clarke, M. Flaska, S. Pozzi, E. Padovani, “MCNPX-PoliMi Post-Processing Algorithm for Detector Response Simulations”, J. Nucl. Mater. Manag. (in press) (2011).
12. B. Kiraly, L. Olah, J. Csikai, “Neutron-based techniques for detection of explosives and drugs”, Radiat. Phys. Chem. 61 (2001) 781.
13. S. Pesente, M. Cinausero, D. Fabris, E. Fioretto, M. Lunardon, G. Nebbia, G. Prete, G. Viesti, “Effects of soil moisture on the detection of buried explosives by radiative neutron capture”, Nucl. Instrum. Methods Phys. Res. A 459 (2001) 577.
14. R.A. Forster, L.J. Cox, R.F. Barrett, T.E. Booth, J.F. Briesmeister, F.B. Brown, J.S. Bull, G.C. Geisler, J.T. Goorley, R.D. Mosteller, S.E. Post, R.E. Prael, E.C. Selcow, A. Sood, “MCNP Version 5”, Nucl. Instrum. Methods Phys. Res. B 213 (2004) 82.
15. S. Pozzi, E. Padovani, M. Marseguerra, “MCNP-PoliMi: a Monte-Carlo code for correlation measurements”, Nucl. Instrum. Methods Phys. Res. A 513 (2003) 550.
16. R.G. Williams III, C.J. Gesh, R.T. Pagh, “Compendium of material composition data for radiation transport modeling”, Report PNNL-15870, Pacific Northwest National Laboratory, Richland, Washington, 2006.

17. K.F. Eckerman, J.C. Ryman, “External exposure to radionuclides in air, water, and soil”, Federal guidance report 12, US Environmental Protection Agency, Oak Ridge National Laboratory, 1993.

Chapter 5: Development of an Algorithm-Based Model for the Detection of Explosives Using Neutron Scattering Methods in Simulated Idealized Conditions

Abstract

Fast neutron interrogation has potential as a powerful tool in explosives detection, and combining all the information provided by induced photons and scattered neutrons into flags has the potential to minimize the necessary incident neutrons, and therefore the measurement time and personnel dose. This study involves an evaluation of Monte Carlo simulations of an idealized cargo container explosives detection scenario. Several strategies were used to determine possible flags for the explosive RDX ($C_2H_6N_6O_6$). These included changes in backscattered neutron spectra and neutron flux at specific energies as a function of scatter angle. Other flags compared neutron elastic scatter peaks, and photons from neutron inelastic scatter off light elements. An analysis of the effect of changing hidden explosive mass and position on the detectability of the explosive was completed. Preliminary analysis revealed several promising algorithmic flags.

Introduction

Nuclear-based explosives detection methods

Contraband explosives detection has been widely studied, with strategies ranging from trained animals and chemical analysis to nuclear analysis techniques [1-3]. Traditional nuclear-based contraband detection technologies are often based on X-ray interrogation, which are limited by the similar electron density of explosives and inert material [4,5]. In addition, because neutrons are highly penetrating and react strongly with low Z targets, active neutron interrogation has been widely considered a promising alternative [1,5]. One widely studied strategy uses thermal neutron activation (TNA), in which neutrons are absorbed by target nuclei, which then emit characteristic high-energy photons [1,6,7]. Inelastic neutron scattering methods rely upon the detection of the secondary photons, which have a high probability of emission at high incident neutron energies [1,8,9]. A different strategy involves the backscattered neutrons themselves, namely measuring the number of reflected neutrons, neutron energy spectroscopy, or neutron transmission imaging [8,10-12]. One advantage of these approaches is the greater number of signal carriers. However, neutrons are more difficult to detect and energy spectroscopy is challenging due to the high amount of scatter.

Proposed detection method

The method studied here combines the information from the backscattered neutrons, inelastic photons, and neutrons scattered at different angles. This increases the relative number of signal carriers used in the detection process per incident neutron, and thus potentially minimizes personnel dose and measurement time. Secondary radiation is analyzed to find specific mathematical combinations of signals, such as ratios of different signals, for which there is a significant difference between cases with and without explosive, e.g. RDX ($C_2H_6N_6O_6$). These specific mathematical combinations, or flags, would form the backbone of an algorithm-based approach in which an explosive's presence is indicated when flag values, or combinations of flag values, fall within a specific range.

In a previous study, neutron scatter behavior in a simulated cargo container geometry was characterized, with particular attention paid to the neutron and photon scatter peaks produced when 2.4- or 14.1-MeV neutrons interacted with targets of carbon, nitrogen, and oxygen [13]. The results from these simulations showed how neutron and photon energy tallies from particular elements were superimposed when other materials were used and identified signals and their origins. This formed the basis for current simulation work in the isolation of potential flags.

This work identifies the flags that form the preliminary basis of the proposed algorithm-based approach. Future work will include laboratory measurements to validate the idealized scenarios simulated here. The strongest flags found using this simplified geometry will then be tested and the final detection algorithm optimized. Future investigations would include factors such as unknown cargo types, multiple scatter off surrounding materials, and realistic detector response.

Monte Carlo Simulation

The simulation work used MCNP5 [14] and the relatively simple geometry in Fig. 5-1. Included was an isotropic neutron source positioned 3.04 m away from the center of a standard cargo container with external dimensions of 2.4 m × 6.2 m × 2.6 m and 0.346-cm thick steel walls. At a distance of 3.04 m from container center were seven 0.78 m radius detector hemispheres that sampled scattered neutrons at all possible scatter angles from transmission (0 degrees) to backscatter (180 degrees). Centered inside the container was a very large 93.5-cm radius target sphere composed of either RDX or one of four shielding materials. Shielding materials included water, vegetable oil, paper, or steel, as specified in Table 5-1. This large sphere, equivalent to 6,230 kg of RDX, was primarily used because the large size would maximize the magnitude of the individual flags. An additional advantage was the large volume minimized the effect of non-centered targets to some degree. The shielding geometry consisted of one shielding material distributed evenly throughout the container volume with a density of 0.46 g cm^{-3}, which approximated a typical total cargo mass. This artificially diffuse shielding drastically increased neutron mean free path in steel, but was used to simulate a realistic amount of material while maintaining the condition of content homogeneity.

Current, or MCNP5 F1, tallies for both photons and neutrons were taken at the hemispherical detector surfaces. Energy bins of 0.2-MeV were used for all tallies. A 0.05 MeV neutron energy cutoff, well below the neutron and photon peaks of interest, was used to speed calculations. The isotropic neutron source produced 2.4- or 14.1-MeV neutrons, approximating D-D and D-T neutron generators, respectively. To further conserve computational resources incident neutrons were biased towards the container in a conical beam. A sample MCNP input file may be found in Appendix A.

Methods of Flag Calculation

Tallies evaluated for use in flags included backscattered neutrons, inelastic photons, and ratios of neutron tallies at specific points. In all cases, flag determination was found by isolating the strongest flags, with flag strength and the general form of flag value as defined by eqns. (1.2) and (1.1), respectively. The final detection algorithm could combine several different flags from any of these methods. The 2.4-MeV D-D neutrons were expected to have limited use due to lower penetrability, but was still investigated as a possible neutron source.

Flags formed using the backscattered neutrons

The first type of flags relied solely on the backscattered neutron tallies. The neutron tallies for cases with and without RDX were subtracted and then examined manually to identify the neutron energies corresponding to the largest differences. The results for the subtracted backscattered neutron tallies for D-T neutron sources and each of the four shielding materials appear in Figures 5-2a and 5-2b. One of the most obvious features is the large positive peak near 3.0-MeV in the oil, water, and paper-shielded simulations. This positive peak indicates presence in the RDX case and not in the no-RDX case, as would be expected as nitrogen has several inelastic scatter peaks between 2.7 and 3.1 MeV, and these materials are nitrogen-poor in comparison to RDX. In the water and paper cases, but not the oil case, this large positive peak is followed by a significant negative peak around 3.2 MeV, probably due to the significant amount of oxygen in water and paper, with little in oil. The steel-shielded case showed a significantly smaller number of backscattered neutrons below 1.6 MeV when the RDX is present, probably due to the increased number of lighter elements. Perhaps the most interesting feature in all four shielding scenarios is the increased number of backscattered neutrons with energies between 10.2 and

11.2 MeV when RDX is present. As summarized in Table 5-2, this increase corresponds to flag values of 0.015, 0.028, and 0.016% in the number of backscattered neutrons for the oil, paper, and water cases. The flag value is two orders of magnitude larger, 2.1, in the steel-shielded case, which is unsurprising given how different RDX and steel are. This effect is similar to the backscatter "enhancement" found in other studies, and is due to the increased amount of elastic scatter off carbon, nitrogen, and oxygen when RDX is present [16]. It should be noted that some of this increase may be due to the addition of higher density material, RDX, in cases where there is already a significant amount of carbon and oxygen.

In a related calculation, the total number of backscattered neutrons was compared for cases with and without RDX. It has been shown that the presence of explosives can increase the reflected flux of thermal and high-energy neutrons [15-17]. For the cases with oil, water, and paper shielding flag values were 0.019% to 0.036% difference, while the steel-shielded case had a flag value of 0.11.

One of the most direct ways of measuring the amount of carbon, nitrogen, and oxygen is to compare the magnitudes of their respective elastic scatter peaks, which fall at 10.2-, 10.6-, and 11-MeV when using 14.1-MeV neutrons. Ratios of these peaks appear in Table 5-2. The largest percent differences were found in the nitrogen-carbon ratio in the organically shielded scenarios and in the oxygen-carbon ratios for the water- and steel-shielded simulations. As expected, the simulations using metallic shielding showed much larger differences in peak ratios. This method merits further study, especially if the shield mass is small relative to the explosive mass or if neutron spectroscopy is improved and can differentiate among the backscatter peaks of similarly-massed elements.

Advantages of using flags based on backscattered neutrons include the larger number of backscattered neutrons and, because the maximum amount of energy is transferred to the target nucleus, backscatter provides the maximum elastic scatter peak separation. Furthermore, in many one-sided applications it may not be feasible to measure neutrons at angles other than backscatter. The most significant disadvantage is the interference due to uncollided neutrons, necessitating extensive shielding of the source, detector, or both.

Flags formed using ratios at a given energy at different angles

In the next strategy, ratios were taken of the neutron tally at a given energy for two different scatter angles such that flag strength (f_s) is defined as:

$$f_s = \frac{n(E_1, A_1)}{n(E_2, A_2)}, \tag{5.1}$$

where $n(E,A)$ are the neutron tallies for one particular energy and two different angles. The most significant flags for all four shielding materials appear in Table 5-3. These flags showed flag strengths of 5-10 for the oil, paper and water scenarios and exceeded 25 in the steel-shielded case.

There was significant overlap between the flag identities in the different shield scenarios with D-T source neutrons, which would be ideal for use on unknown cargo. One major advantage of using this type of flag is related to the self-normalizing nature of comparing ratios, which compensates for some variations in target composition. Furthermore, other studies have shown that it is possible to sensitize fast neutron detectors to certain energies, which would allow an easier, less expensive detection alternative to full neutron spectroscopy [18].

Flags formed using neutron scattering peaks at different angles

For the next flag strategy, the energy bins corresponding to inelastic and elastic neutron scatter peaks of carbon, nitrogen, and oxygen were isolated for each of the seven scatter angle ranges, for a total of 100 peaks. Flags were formed by taking the ratio of each peak with all others for a total of 10,000 ratios. The most promising flags are shown in Table 5-4. Flag strength for the top five flags in oil, paper, and water scenarios ranged between 3.4 and 7.4. Flag strengths in the steel cases ranged from 48 to 62. Almost all the flags involved comparing one of the elastic backscatter peaks of carbon (10.2 MeV), nitrogen (10.6 MeV), or oxygen (11.0 MeV), with lower energy peak at transmission angles.

This strategy shares many of the advantages of the method discussed in section 4.2, but allows for greater flexibility in neutron energy, and a greater probability of exploiting a “sweet spot” related to specific neutron interactions. Obvious advantages of using peak magnitudes are the improved counting statistics, and the potential of sensitizing the neutron detectors using the same interactions. Furthermore, some of the top flags compare at two very different energies, which may lead to a system in which a high level of neutron energy resolution is unnecessary. A comparison of the flags in Tables 5-3 and 5-4 shows that somewhat larger differences may be found using the earlier-discussed method in the oil, water, and paper-shielded cases, but not the steel-shielded case.

Flags formed comparing inelastic photon peak ratios

The photon-comparison method took the form of comparing ratios between neutron inelastic scatter photon peaks in hydrogen, carbon, nitrogen, and oxygen for cases with and without RDX. As mentioned earlier, there has been considerable study in using these types of photons in explosives-screening scenarios, but in this case they are being considered as part of a larger detection algorithm. The best flags using this method are in Table 5-5. Flag strength in photon peak tally ratios were around 0.30 to 0.46 for the oil, water, and paper-shielded cases, and approached 1.0 for the steel-shielded case.

Flags as a function of explosive amount and position

A major concern with the proposed method is the sensitivity of the specific flags to the position and amount of hidden explosive. A series of simulations was completed that investigated the effect on flag strength when either the amount or position of the explosive sphere was changed inside a cargo container filled with paper. Seven simulations were run with a sphere of RDX of mass 1000, 750, 500, 250, 100, 50, or 10 kg centered in the container. Six simulations had a 100-kg sphere positioned 75 cm from center in positive and negative x, y, and z directions. In the other four simulations, 100-kg spheres were positioned 130 cm from center at vectors <1,1,-1>, <-1,1,1>, <-1, -1,-1>, and <1,-1,1> with respect to the center.

As expected, the flag magnitude was shown to be dependent on RDX mass, with each type of flag reacting differently to the changing amounts of explosive. This relationship is illustrated in Fig. 5-3, where the magnitude of the prominent peak at 3 MeV seen in Fig. 5-2a for paper is plotted as a function of RDX mass on a log-log scale. A least squares fit displayed an R^2 value of 0.958, indicating a clear exponential relationship. Similarly, there was a strong linear relationship in the log-log plot of total backscattered neutrons versus RDX mass with an R^2 value of 0.984, as shown in Fig. 5-4.

The flags corresponding to the relative magnitudes of the neutron elastic scatter peaks were nonlinearly dependent on RDX mass, as illustrated in Fig. 5-5, although the values for the oxygen-carbon ratio comparison were so small that statistical uncertainties made clear determination of this relationship difficult. All of the flags formed by methods described in 4.2 and 4.4 showed a linear behavior, with respect to changing RDX mass, and R^2 values greater than 0.98, as illustrated in Fig. 5-6. Therefore, these flags were the least sensitive to changes in RDX mass.

The five different types of flags also had very different reactions to change of RDX position. Table 5-6 shows the average percent difference for each position relative to the center position for each type of flag. This table shows that the largest are found when the RDX sphere is moved towards the negative x direction, or closer to the neutron source, drastically decreasing the amount of shielding.

Limitations of Idealized Simulations

The simulated geometry is a simplification of an actual cargo container interrogation scenario. Typical surroundings, such as cement pad, ground, or personnel shielding, are not present. Cargo container contents are homogenous and the amount of simulated explosive was extremely large. The neutron sources are artificially collimated so they only irradiate the cargo container, ignoring the necessary shadow shielding and associated secondary radiation. Finally, the idealistic detector surfaces count every neutron or photon crossing its surface with perfect efficiency, ignoring the inefficiency, energy resolution, and other limitations of actual detectors. This preliminary work, however, is useful in determining which flags merit further study, even though one would expect that the flags would decrease in strength for more realistic conditions. Only the strongest flags, such as those with >1.0 flag strength, would likely be included in the explosives-detection algorithm. Background radiation could also strongly affect neutron and photon signatures. In these idealized simulations, flags were identified using a comparison of containers with and without RDX, which is significantly different from actual screening scenarios and may even lead to pursuit of unfeasible flags. However, the strongest flags discussed here still show significant potential.

Flag strength quantifications are useful in comparing one flag to another, but do not easily translate into the probability of actual explosives detection without considering the many factors and limitations found in screening scenarios, such as detector limitations, neutron interactions with surrounding materials, and container content inhomogeneities. Future work will quantify the effect of these and other factors to determine an accurate estimation of the detection probability, including the probabilities of false negatives and false positives.

Conclusions

There are many possible flags that may be used for determining the presence of hidden explosives in a simplified cargo container simulation. Because D-D neutrons have low penetrability of large targets, their use was eliminated in the explosives-detection system. Several of these flags showed very large percent differences between cases with and without the explosive RDX. It was further demonstrated that flags formed using ratios of neutron tallies at specific energies and angles are relatively independent of changes in explosive amount and position. Furthermore, many of the strongest flags have similar energies and angles, such that it may be possible to combine these flags into other flags that require less rigorous neutron spectroscopy or combine different types of flags such as photon peak tallies with neutron total tallies. Future efforts will test the flags found here in more realistic scenarios, as well as quantify the robustness of the proposed algorithm-based approach when confronted with actual detection limitations as well as the expected variations found in field applications.

Figures

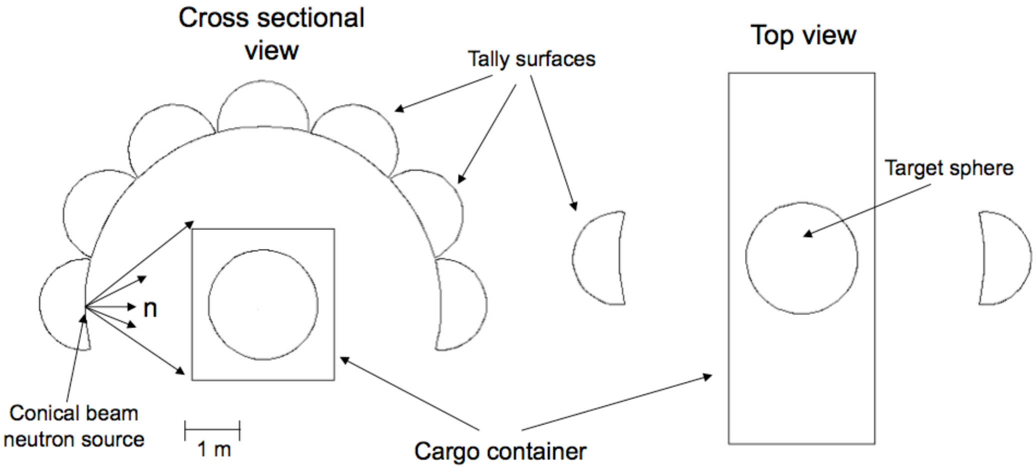

Figure 5-1. Simulation geometry showing cross section and top view of simulated cargo container with target and tally surface geometries and conical beam neutron source.

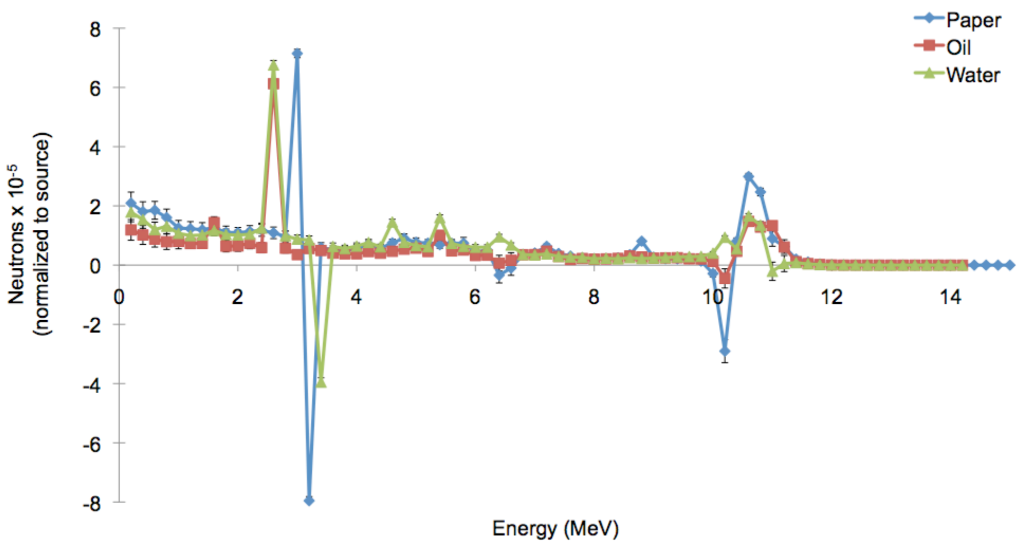

a.

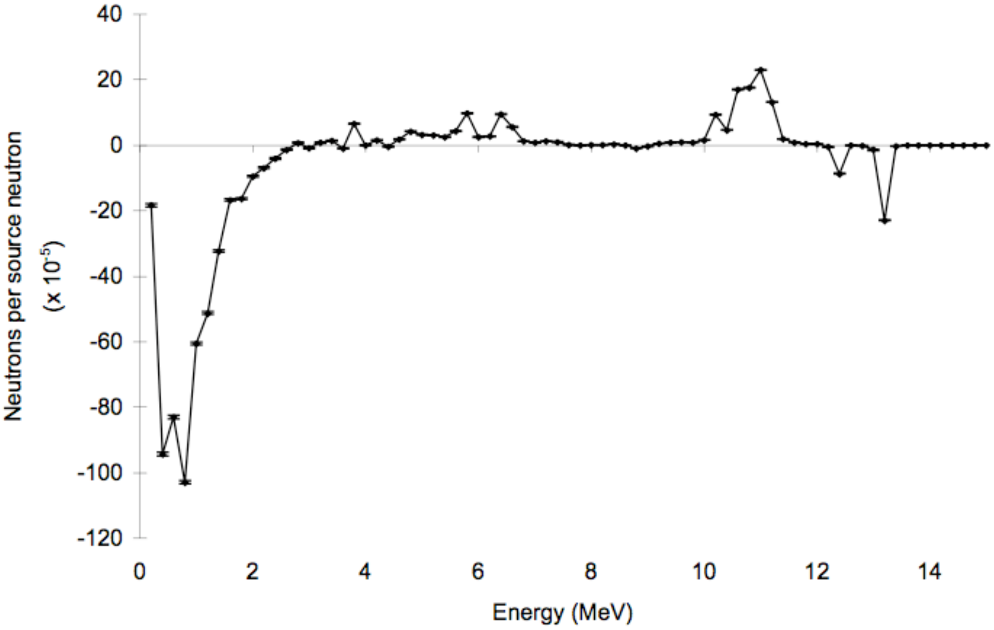

b.

Figure 5-2. Subtracted backscattered neutron tallies for the RDX case minus the no-RDX case with D-T source for a) oil-, water-, paper-, and b) steel-shielded targets.

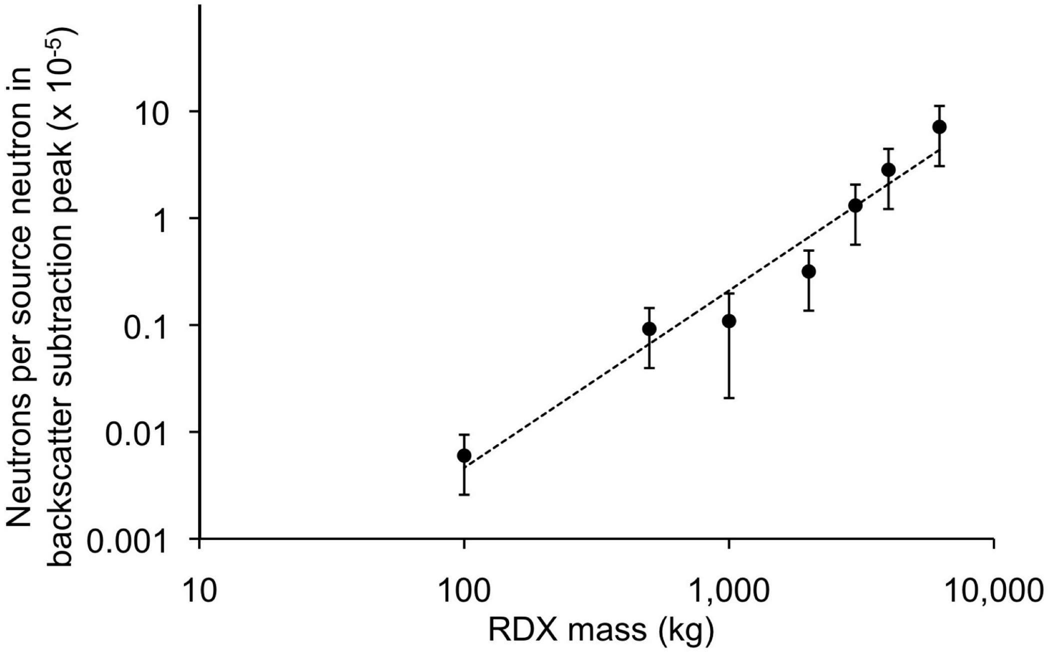

Figure 5-3. The magnitude of a representative peak from a subtracted backscatter neutron tally is plotted as a function of the amount of hidden RDX (kg) in a case with paper shielding and 14.1 MeV incident neutrons. A least squares fit shows a relationship between peak magnitude, p, and RDX mass, m, such that $p = (2.24 \cdot 10^{-6}) \times m^{1.658}$, with an R^2 value of 0.958.

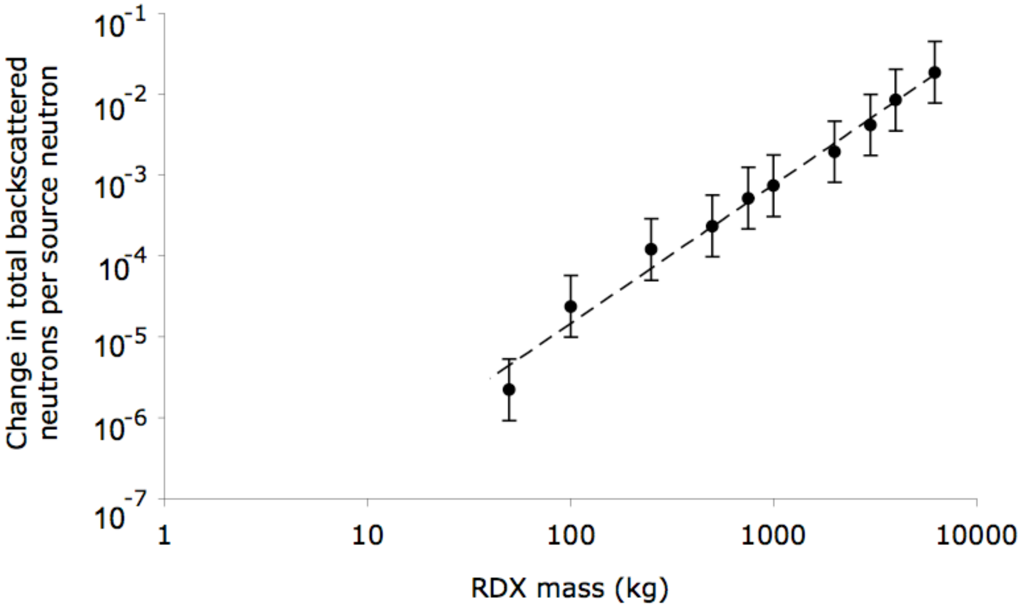

Figure 5-4. The change in the total number of backscattered neutrons per source neutron (n cm^2), n, is plotted against the mass of RDX (kg), in a paper shielded cargo container with 14.1 MeV incident neutrons. A least squares fit shows a relationship of n = $(5.44 \times 10^{-9}) \times m^{1.715}$, with an R^2 value of 0.984.

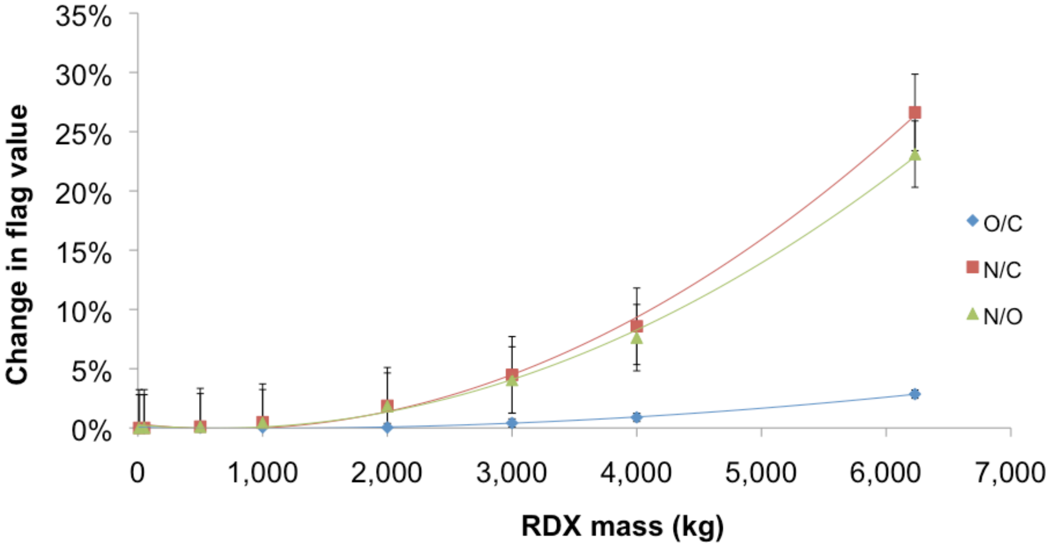

Figure 5-5. Differences in flag values formed from ratios of neutron elastic scatter peaks with and without RDX are plotted as a function of RDX mass (kg) for paper shielded RDX spheres and 14.1 MeV incident neutrons. A second order polynomial fit gives R^2 values greater than 0.99 for all three ratios. Some points with small RDX mass were discounted to limit biasing due to denser sampling at the lower explosive masses.

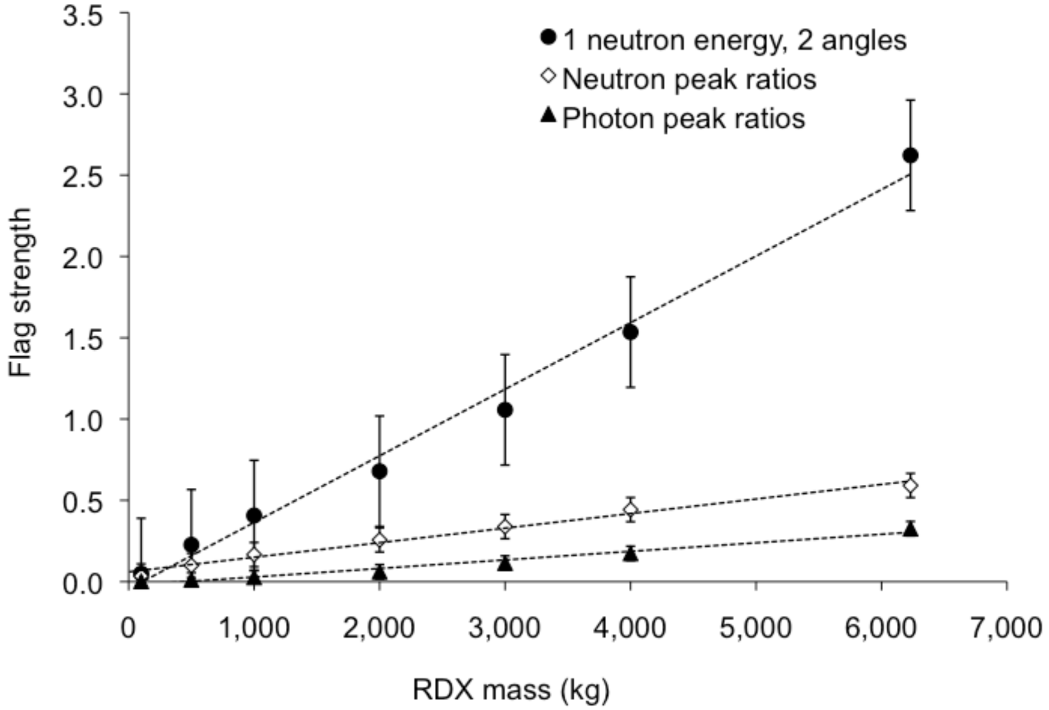

Figure 5-6. Flag strength for three types of flags as a function of RDX size for paper-shielded RDX and 14.1 MeV incident neutrons. The three types of flag, formed by taking ratios of neutron tallies at either a given energy at different angles, between different neutron peaks, or between different photon peaks, show a linear relationship between the percent difference and amount of RDX.

Tables

Table 5-1. Elemental compositions in atom percent of materials used in simulations [19].

Element	Air	Steel	RDX	Water	Paper	Oil
H	0.00%		28.6%	66.7%	47.6%	62.8%
C	0.01%	0.32%	14.3%		28.6%	33.5%
N	75.5%		28.5%			
O	23.2%		28.6%	33.3%	23.8%	3.70%
P	0.00%	0.04%				
S	0.00%	0.05%				
Ar	1.30%					
Fe	0.00%	99.6%				

Table 5-2. Flag strength for flags calculated using only backscattered neutrons.

Cargo contents:	Oil	Paper	Steel	Water
Total backscattered neutrons	0.0228 ± 0.0014	0.0185 ± 0.0011	0.109 ± 0.0053	0.036 ± 0.0026
10-12 MeV backscattered neutrons	0.0155 ± 0.0005	0.0196 ± 0.0006	2.08 ± 0.035	0.0158 ± 0.00040
Neutron backscatter peaks: O/C	0.0723 ± 0.0005	0.0283 ± 0.0001	0.408 ± 0.007	0.288 ± 0.0036
Neutron backscatter peaks: N/C	0.164 ± 0.0015	0.211 ± 0.0015	0.144 ± 0.0023	0.0603 ± 0.00090
Neutron backscatter peaks: N/O	0.110 ± 0.0012	0.232 ± 0.0017	0.309 ± 0.0047	0.214 ± 0.0019

Table 5-3. Top ten flags found by comparing neutron tallies at a given energy.

Flag identity (MeV, Degrees)	Flag strength	Flag identity (MeV, Degrees)	Flag strength
Oil (D-T source)		Water (D-T source)	
(11.6,120)/(11.6,0)	8.07 ± 2.78	(11.2,150)/(11.2,0)	9.99 ± 2.65
(10.6,150)/(10.6,0)	6.37 ± 1.96	(11.6,120)/(11.6,0)	7.52 ± 1.78
(11.2,150)/(11.2,0)	5.03 ± 1.37	(10.6,150)/(10.6,0)	7.47 ± 1.65
(11,180)/(11,0)	4.83 ± 1.36	(11,150)/(11,0)	5.94 ± 1.22
(11,150)/(11,0)	4.55 ± 1.28	(11.4,120)/(11.4,0)	5.70 ± 1.24
(10.8,150)/(10.8,0)	4.50 ± 1.23	(11,180)/(11,0)	5.61 ± 1.14
(11.4,150)/(11.4,0)	4.18 ± 1.09	(11.4,150)/(11.4,0)	5.37 ± 1.15
(11.4,120)/(11.4,0)	4.03 ± 1.05	(10.8,150)/(10.8,0)	5.30 ± 0.93
(11.2,150)/(11.2,30)	0.90 ± 0.15	(10.6,150)/(10.6,30)	1.91 ± 0.25
(11,180)/(11,30)	0.77 ± 0.11	(11,150)/(11,30)	1.19 ± 0.14
Paper (D-T source)		Steel (D-T source)	
(11.4,150)/(11.4,0)	10.0 ± 1.1	(11,150)/(11,0)	59.1 ± 2.4
(11.4,120)/(11.4,0)	9.69 ± 1.11	(11.2,150)/(11.2,0)	40.7 ± 2.1
(11.2,150)/(11.2,0)	5.99 ± 0.71	(11,150)/(11,30)	40.2 ± 1.6
(11.6,120)/(11.6,0)	5.84 ± 0.61	(11,180)/(11,0)	29.0 ± 0.9
(10.8,150)/(10.8,0)	5.10 ± 0.45	(11.6,120)/(11.6,0)	28.3 ± 1.8
(11,150)/(11,0)	4.96 ± 0.44	(11.2,150)/(11.2,30)	26.4 ± 1.2
(11,180)/(11,0)	4.87 ± 0.43	(10.6,150)/(10.6,0)	24.3 ± 0.9
(10.6,150)/(10.6,0)	4.72 ± 0.43	(11.4,120)/(11.4,0)	24.3 ± 1.1
(0.2,180)/(0.2,0)	2.62 ± 0.11	(10.8,150)/(10.8,0)	22.1 ± 0.8
(0.2,150)/(0.2,0)	2.61 ± 0.11	(11,180)/(11,30)	19.5 ± 0.6

Table 5-4. Neutron peak energies (MeV) and scatter angle (degrees) of both peaks making up the neutron peak comparison flag for 14.1 MeV incident neutrons.

Flag identity (MeV, degrees)	Flag strength	Flag Identity (MeV, degrees)	Flag strength
Water		Oil	
(11.0, 150)/(10.0, 0)	6.76 ± 2.26	(11.0, 150)/(7.8, 0)	7.44 ± 1.84
(11.0, 150)/(7.8, 0)	5.78 ± 1.87	(11.0, 150)/(10.0, 0)	5.3.0 ± 1.11
(11.0, 150)/(9.6, 0)	5.67 ± 1.79	(11.0, 150)/(8.2, 0)	4.33 ± 0.79
(11.0, 150)/(7.2, 0)	5.04 ± 1.35	(11.0, 150)/(9.6, 0)	3.41 ± 0.59
(11.0, 150)/(8.2, 0)	4.62 ± 1.31	(11.0, 150)/(6.8, 0)	3.37 ± 0.53
(11.0, 150)/(6.8, 0)	2.67 ± 0.54	(6.2, 0)/(11.0, 150)	3.28 ± 0.55
(6.2, 0)/(11.0, 150)	2.37 ± 0.54	(11.0, 150)/(7.2, 0)	2.62 ± 0.42
(11.0, 150)/(0.8, 0)	1.02 ± 0.13	(11.0, 150)/(0.8, 0)	1.64 ± 0.18
(11.2, 150)/(1.0, 0)	0.74 ± 0.09	(11.0, 150)/(1.0, 0)	1.15 ± 0.13
(11.0, 150)/(1.0, 0)	0.74 ± 0.09	(11.2, 150)/(1.0, 0)	1.06 ± 0.12
Paper		Steel	
(11.0, 150)/(10.0, 0)	5.42 ± 0.54	(11.0, 150)/(1.0, 0)	62.3 ± 1.6
(11.0, 150)/(9.6, 0)	5.01 ± 0.44	(11.0, 150)/(8.2, 0)	54.5 ± 2.1
(11.0, 150)/(7.8, 0)	4.98 ± 0.46	(11.0, 150)/(9.6, 0)	54.1 ± 2.0
(11.0, 150)/(7.2, 0)	4.93 ± 0.36	(11.0, 150)/(10.0, 0)	52.0 ± 2.4
(11.0, 150)/(8.2, 0)	4.69 ± 0.43	(11.0, 150)/(0.8, 0)	51.6 ± 1.3
(6.2, 0)/(11.0, 150)	4.56 ± 0.36	(11.0, 150)/(7.8, 0)	51.0 ± 1.9
(11.0, 150)/(6.8, 0)	4.07 ± 0.29	(11.0, 150)/(7.2, 0)	50.7 ± 1.8
(11.0, 150)/(0.8, 0)	3.2.0 ± 0.18	(11.2, 150)/(1.0, 0)	49.4 ± 1.1
(11.0, 150)/(1.0, 0)	2.64 ± 0.15	(6.2, 0)/(11.0, 150)	48.8 ± 1.6
(11.2, 150)/(1.0, 0)	2.61 ± 0.15	(11.0, 150)/(6.8, 0)	48.6 ± 1.7

Table 5-5. Photon peak energies and flag values corresponding to the most promising flags based on a comparing photon peaks.

Photons (MeV)	Flag strength	Photons (MeV)	Flag strength
Oil		Water	
5.2 /2.6	0.49 ± 0.0036	7.2 /4.6	0.35 ± 0.0012
5.2 /1.0	0.48 ± 0.0030	4.6 /2.6	0.34 ± 0.0016
5.2 /3.4	0.47 ± 0.0036	4.6 /3.8	0.33 ± 0.0011
5.2 /2.8	0.41 ± 0.0029	4.6 /2.8	0.33 ± 0.0012
5.2 /4.6	0.38 ± 0.0024	4.6 /3.4	0.31 ± 0.0015
5.2 /3.8	0.33 ± 0.0023	4.6 /1.0	0.30 ± 0.0010
6.8 /1.0	0.30 ± 0.0026	5.2 /6.2	0.29 ± 0.0014
7.2 /4.6	0.29 ± 0.0013	4.6 /1.8	0.27 ± 0.0011
6.8 /4.6	0.29 ± 0.0025	7.2 /5.2	0.27 ± 0.0013
6.2 /2.6	0.24 ± 0.0011	5.2 /2.6	0.26 ± 0.0015
Paper		Steel	
5.2 /2.6	0.46 ± 0.0027	4.6 /1.0	0.99 ± 0.0029
5.2 /6.2	0.44 ± 0.0022	4.6 /2.6	0.95 ± 0.0032
5.2 /3.4	0.44 ± 0.0027	4.6 /3.4	0.91 ± 0.0032
5.2 /2.8	0.43 ± 0.0023	4.6 /1.8	0.90 ± 0.0030
5.2 /3.8	0.41 ± 0.0021	4.6 /2.8	0.79 ± 0.0027
5.2 /1.0	0.40 ± 0.0020	2.4 /4.6	0.78 ± 0.0027
7.2 /5.2	0.38 ± 0.0020	6.8 /4.6	0.67 ± 0.0033
5.2 /4.6	0.33 ± 0.0017	6.2 /1.0	0.57 ± 0.0019
6.8 /1.0	0.26 ± 0.0018	6.2 /2.6	0.56 ± 0.0021
6.8 /4.6	0.25 ± 0.0018	6.2 /3.4	0.55 ± 0.0021

Table 5-6. Average deviation in percent of flag strength magnitude for a given type of flag when the explosive is displaced from the center of the cargo container.

Displaced position	Backscatter	1 Energy, 2 angles	Neutron peaks	Photon peaks
(0,0,75)	73% ± 50%	390% ± 640%	360% ± 640%	110% ± 150%
(0,0,-75)	76% ± 53%	150% ± 450%	130% ± 260%	38% ± 45%
(-75,0,0)	990% ± 1500%	240% ± 410%	280% ± 530%	1920% ± 3100%
(75,0,0)		67% ± 150%	82% ± 220%	74% ± 110%
(0,-75,0)		120% ± 290%	97% ± 220%	34% ± 45%
(0,75,0)		110% ± 310%	77% ± 170%	22% ± 34%
(75,-75,75)		120% ± 220%	110% ± 210%	2800% ± 4100%
(75,75,-75)		170% ± 500%	130% ± 280%	65% ± 67%
(-75,75,75)	120% ± 200%	420% ± 720%	390% ± 620%	500% ± 780%
(-75,-75,-75)	120% ± 200%	190% ± 520%	160% ± 310%	230% ± 340%
Average deviation	280%	200%	180%	580%
Average error	390%	420%	350%	870%

References

1. A. Buffler, "Contraband detection with fast neutrons ", Radiat. Phys. Chem. 71 (2004) 853-861.
2. A.L. Lehnert, K.J. Kearfott, "The detection of explosive materials: review of considerations and methods", Nucl. Technol. 172 (2010) 325-334.
3. A. Buffler, J.R. Tickner, "Detecting contraband using neutrons: challenges and future directions", Radiat. Meas. 45 (2010) 1186-1192.
4. C. Bruschini, "Commercial systems for the direct detection of explosives (for explosive ordnance disposal tasks)", École Polytechnique Fédérale de Lausanne (EPFL), 2001.
5. R.C. Runkle, T.A. White, E.A. Miller, J.A. Caggiano, B.A. Collins, "Photon and neutron interrogation techniques for chemical explosives detection in air cargo: A critical review", Nucl. Instrum. Methods Phys. Res. A 603 (2009) 510-528.
6. D. Brown, T. Gozani, "Thermal neutron analysis technology", P. SPIE 2936 (1997) 85-94.
7. H.-H. Hsu, K.J. Kearfott, "Effects of neutron source selection on land-mine detection efficiency", Nucl. Instrum. Methods Phys. Res. A 422 (1999) 914-917.
8. A. Buffler, K. Bharuth-Ram, F.D. Brooks, M.S. Allie, M. Herbert, M.R. Nchodu, B.R. Simpson, "Element analysis by fast neutron scattering", P. SPIE 2867 (1997) 192-197.
9. T. Gozani, M. Elsalim, M. Ingle, E. Phillips, "Gamma ray spectroscopy features for detection of small explosives", Nucl. Instrum. Methods Phys. Res. A 505 (2003) 482-485.
10. A. Buffler, F. Brooks, M. Allie, K. Bharuth-Ram, M. Nchodu, "Contraband detection by fast neutron scattering", Nucl. Instrum. Methods Phys. Res. B 173 (2001) 483-502.
11. F.D. Brooks, A. Buffler, M.S. Allie, K. Bharuth-Ram, M.R. Nchodu, B.R.S. Simpson, "Determination of HCNO concentrations by fast neutron scattering analysis", Nucl. Instrum. Methods Phys. Res. A 410 (1998) 319-328.
12. C. Fink, B. Micklich, T. Yule, P. Humm, L. Sagalovsky, M. Martin, "Evaluation of neutron techniques for illicit substance detection", Nucl. Instrum. Methods Phys. Res. B 99 (1995) 748 752.
13. A.L. Lehnert, K.J. Kearfott, "Fast neutron scattering behavior in simplified simulations of an explosives detection technique" Nucl. Sci. Eng. (in press) (2011).
14. R.A. Forster, L.J. Cox, R.F. Barrett, T.E. Booth, J.F. Briesmeister, F.B. Brown, J.S. Bull, G.C. Geisler, J.T. Goorley, R.D. Mosteller, S.E. Post, R.E. Prael, E.C. Selcow, A. Sood, "MCNP Version 5", Nucl. Instrum. Methods Phys. Res B. 213 (2004) 82-86.
15. C. Datema, L. van Der Schoor, V. Bom, C. van Eijk, "A portable landmine detector based on the combination of electromagnetic induction and

neutron backscattering", IEEE Nucl. Sci. Symp. Conf. Rec. 1 (2001) 406-409.

16. E. Hussein, M. Desrosiers, E. Waller, "On the use of radiation scattering for the detection of landmines", Radiat. Phys. Chem. 73 (2005) 7-19.
17. B. Kiraly, L. Olah, J. Csikai, "Neutron-based techniques for detection of explosives and drugs", Radiat. Phys. Chem. 61 (2001) 781-784.
18. H. Gomberg, G. Charatis, "Neutron elastic scatter for detection and identification of obscured objects", P. SPIE 1942 (1993) 276-288.
19. R.G. Williams III, C.J. Gesh, R.T. Pagh, "Compendium of material composition data for radiation transport modeling", report PNNL-15870, Pacific Northwest National Laboratory, Richland, Washington. 2006.

Chapter 6: Simulations for Developing a Flag-Based Active Neutron Interrogation Method for Explosives Detection in Sea-Land Cargo Containers

Abstract

Fast neutron interrogation for explosives detection has shown potential for the screening of sea-land cargo containers. Simulations were completed investigating the neutron scatter behavior of 14.1 MeV fast neutrons in such screening scenarios. Earlier efforts centered on Monte Carlo (MCNP5) simulations to identify flags, or specific calculations based on photons or neutrons produced as a result of fast neutron interaction that signal the presence of the explosive RDX ($C_3H_6N_6O_6$). Those simulations consisted of a simplified target geometry with artificially collimated neutron source and generalized organic, hydrogenous, or metallic types of cargo materials. In this study, the MCNP5 simulation was expanded to include a more accurate representation of the neutron source, target geometry, detector response, and realistic and varied container contents. The flags found using the earlier simulations were applied to the more realistic scenario models in order to determine the feasibility of the flags' use in a detection algorithm. Additional flags utilizing the simulated detector response were also investigated. The conditions under which specific flags were preferable were also examined. It was found that many flags performed well independent of the cargo type, while others, such as those using only neutron backscatter, were more highly dependent on cargo type. Furthermore, many of the best-performing flags were those that did not require stringent neutron spectroscopy, and would therefore be feasible with existing technology.

Introduction

Over the past few decades, many different strategies have been proposed for the detection of hidden explosives [1]. Several promising methods of non-invasive detection of bulk explosives employed neutron interrogation [1-3]. Its major advantages include high neutron penetrability and the ability to differentiate among light elements of similar atomic mass. Its difficulties include the desired requirements of tunable neutron production, neutron spectroscopy, and shielding.

Explosives screening is needed for relatively small explosive amounts, such as found in mail, landmines, improvised explosive devices, or hand-carried terrorist weapons. Other situations involve larger amounts, such as quantities sufficient to demolish large buildings that may be hidden inside vehicles or sea-land cargo containers. This study focused on the problem of bulk explosives detection in large cargo-filled sea-land containers.

Explosives detection using active neutron interrogation

There are three basic ways that neutrons are used in active interrogation of cargo [1-3]. In thermal neutron activation (TNA), the incident neutrons are absorbed by target nuclei, which then decay, emitting a high-energy characteristic photon, such as the 2.22 and 10.8 MeV photons produced by ^{1}H and ^{14}N, respectively [4-6]. Another method is based on inelastic neutron scattering, in which fast neutrons excite target nuclei, which emit characteristic photons as the fall back to ground state [7-10]. Important de-excitation photons include: 4.43 MeV from ^{12}C, 6.13 MeV from ^{16}O, and 1.64, 2.31, and 5.11 MeV from ^{14}N [6]. In the third strategy the scattered neutrons are measured directly. This may consist of measuring the number of scattered neutrons at specific angles [11,12] or spectroscopic measurements, often based on time-of-flight technology [8].

There is a wide variety of both neutron and photon detectors that could be used in explosives-detection systems. Photon spectroscopy is significantly easier than neutron spectroscopy and an energy resolution comparable to the 0.2 MeV energy bins presented here is easily achievable using semiconductor detector technology [13]. However, fast neutron spectroscopy with this level of energy resolution and reasonable detection efficiency is very difficult, if not impossible, with existing technology [13,14]. Furthermore, neutron energy calculations using time-of-flight are also quite difficult when scanning very large targets, such as a cargo container, due to uncertainties in interaction location and multiple scatters [8,15]. For this study, a simulated liquid scintillator (EJ-309, Eljen Technology, 1300 W. Broadway, Sweetwater, TX 79556) detector was chosen for its high detection efficiency, ability to separate photon and neutron events, and neutron spectroscopic capabilities via pulse height distribution unfolding [16].

Application of active neutron interrogation in the flag-based algorithm

The method discussed here involves use of both de-excitation photons and scattered neutrons. It therefore combines the advantages of two of the above strategies and makes efficient use of the interrogating neutrons, minimizing the personnel dose and screening time. Neutron activation was not considered at this point, as it requires significantly higher incident neutron flux due to lower interaction cross sections.

This method was presented previously as part of an algorithm-based approach using 14.1 MeV incident neutrons [17,18]. Preliminary exploratory simulations characterized the neutron scatter behavior of D-T neutrons in pure samples of carbon, nitrogen, oxygen, and iron, as well as water, oil, paper, and the explosive RDX ($C_3H_6N_6O_6$) [18]. Refined simulations later examined a simplified explosives-detection scenario consisting of a large sphere of RDX centered in a steel cargo container surrounded by hydrogenous, organic, or metallic cargo materials [17]. In that work, several strategies were used that identified significant differences between cases with and without RDX. Specific flags, generally manifested as ratios of specific neutron or photon tallies at certain energies and angles, were identified that best isolated these differences. Calculation of these specific flags gave the flag value (f), defined by:

$$f = \frac{n(E_1,A_1)}{n(E_2,A_2)} \quad \text{or} \quad f = \frac{p(E_1)}{p(E_2)}, \tag{6.1}$$

in which $n(E,A)$ is the neutron tally at a particular energy or energy range and angle and $p(E)$ is the photon tally at a particular energy or energy range. Flag strength (S) is a quantity that was used when determining which flags should be used to find explosives. This quantity is defined as:

$$S = \left| \frac{f_e - f_i}{f_i} \right|, \tag{6.2}$$

in which the flag strength (S) is a function of the flag value with only inert cargo, (f_i) and the flag value with an explosive present (f_e). Flags with the greatest flag strength are the most sensitive to the presence of explosive and are potentially the best flags to use in a detection algorithm. Uncertainties in flag value and flag strength are determined by propagating the statistical error provided in the simulation output through the flag value and flag strength calculations. The flags identified in these simplistic simulations would later form an integral part of the explosives detection algorithm in which changes in specific flag values would be used to determine the type of cargo and “trigger” in the presence of explosives, with additional steps to and minimize false positives due to cargo irregularities.

For this chapter, the flags found in the simplified explosives-detection scenario were tested in more realistic simulations. Added realism included the presence of environmental materials such as a concrete slab and soil or sand, and consideration of different container contents. Possible container contents, such as furniture, vegetables, or plastic, were approximated from a survey of cargo [19]. Other factors included a more realistic cargo distribution within the crate, a more accurate portrayal of the neutron source, and simulation of a neutron detector response. The simulated neutron detector response included both pulse height distributions (PHDs) and time-of-flight (TOF) distributions. It was expected that the inclusion of these realistic factors would result in signal degradation, with different flags displaying varying responses to each factor. These relationships are important to quantify to develop and further test the viability of an optimal explosives-detection algorithm prior to any experimental work.

It was observed in a previous work that many of the best-performing flags utilizing single-width 0.2 MeV energy bins were very similar [17]. For example, several consisted of a high-energy neutron tally at backscatter angles divided by a low-energy neutron tally at transmission angles. As an extension of this work, these “specific” flags were modified into new “combinatory” flags that utilized wider energy ranges instead of specific neutron energy bins. Similarly, these “combinatory” flags based on neutron energy ranges were translated into flags based on pulse height distribution (PHD) thresholds from the simulated neutron detector responses. Both the combinatory and PHD flags have the distinct advantage of less stringent neutron spectroscopy requirements.

Materials and Methods

Monte Carlo simulations

The simulation work was undertaken using a combination of MCNP5 [20] and MCNP-PoliMi [21]. All outputs were provided output in the form of text files. These results were analyzed with a custom parser designed using common data analysis package (MATLAB, 3 Apple Hill Drive, Natick, MA, USA 01760), as well as spreadsheet software (Excel, Microsoft, 1 Microsoft Way, Redmond WA, USA 98052). The basic geometry was a standard steel cargo container with 2.4 m × 6.2 m × 2.6 m exterior dimensions and 0.346 cm thick steel walls with an isotropic neutron source was located 4.44 m away from the container center. The cargo container was surrounded at 3.04 m by seven 0.78-m radius hemispherical surfaces that sampled scattered neutrons and photons at all possible scatter angles from transmission, 0°, to backscatter, 180°. An outer 10-cm radius sphere, centered around the cargo container, defined the outer limits of the simulation. Current, or MCNP5 F1 tallies, for both photons and neutrons were taken over each hemispherical surface using 0.2 MeV energy bins. A sample MCNP input file may be found in Appendix A.

Neutron sources

Because there were very few usable flags for 2.4 MeV incident neutrons due to their limited target penetrability and thresholds for inelastic scatter reactions of interest [17], only 14.1 MeV incident neutrons were utilized. An artificially collimated monoenergetic neutron source was employed to shorten computation time in prior work [17,18]. However, as D-T neutron generators emit neutrons almost isotropically, the explosives-detection system would require shielding around the source to minimize operator and bystander dose. A neutron shield 50 cm thick with layers of polyethylene and steel was designed that could adequately shield the surrounding area and maintain the monoenergetic incident neutron flux [22]. Modifications were made to this shield to produce a more conical beam. This involved an isotropic source positioned 4.44 m from the container center, as shown in Fig. 6-1.

Several simulations were completed using the shielded isotropic source. However, as these simulations took several days to run, later simulations used a biased conical neutron beam with a neutron energy distribution equivalent to the shielded source output as tallied at the container surface. This approximation was calculated using MCNP5 F1 tallies in concentric rings on a surface the same distance and orientation with respect to the shielded source as the side of the container facing the source. Further comparisons were made to ensure that the neutron flux, as measured in the detector surfaces, was not significantly different when the conical approximation beam replaced the shielded isotropic source.

Surrounding environment

Exclusion of materials in the surrounding environment, other than air, decreased calculation times, but resulted in falsely high signal-to-noise ratios due to eliminating the vast majority particle interactions outside the cargo container. To account for those interactions, the earlier simulation was changed such that cargo rested on a concrete slab 30 cm thick with the remainder of the outermost sphere below the slab filled with a standard soil [23] for a depth of at least 7 m below the source and cargo container. Additional simulations were completed with the container on a 10 cm thick steel plate over at least 7 m of sandy soil, as defined in Table 6-1. These simulations also included the source shield, as this is both a source of secondary scatter and perturbs the incident neutron flux from its monoenergetic state.

Container contents

Simulated container contents drawn from the literature included RDX, concrete, wood, brick, polyethylene, rubber, and various plastics [24]. Furniture, vegetables, meat, and clothing are all rather heterogeneous in nature and may vary significantly between individual cargos. The elemental compositions and densities of these and other simulated materials appear in Table 6-1. Furniture was approximated as 40% wood, 25% plastic, 25% metal, and 10% cloth. Clothing was assumed to be 100% cotton fibers. Vegetables, in the form of potatoes, were simulated as 75% water, 15% starch, 4% sugars, 2% fiber, and 2% protein, with a variety of trace elements [25]. Meat, in the form of lean beef, was considered to be 60% water, 22% protein, and 18% fat, also with a variety of trace elements [25].

Another part of the investigations presented here was observing the flag strength of the best-performing flags when interrogating containers with an explosive other than RDX. Therefore, flag strength was compared for cases with a paper-filled cargo container with 500 kg of explosive at its center. The identities and elemental compositions of the explosives considered are detailed in Table 6-2.

Cargo distribution

Simulations were completed that approximated the wooden crates of cargo present in many sea-land shipping containers. These crates were composed of hardwood, 3 cm thick and had exterior dimensions 100 cm × 100 cm × 20 cm. Each container enclosed stacks of crates containing steel (34 crates), vegetables (77 crates), or clothing (82 crates), for a total cargo mass of 21.6 metric tons. The crates were stacked on the container floor in 2 rows of 6, with 30 cm between the rows. A 500 kg rectangular (28 cm wide by 163.5 cm long by 60 cm tall) block of RDX was placed on the floor in the center of the container. This geometry is included as Fig. 6-2 and an example MCNP input file appears in Appendix A.

Neutron detector response

An important part of the development and analysis of the explosives-detection algorithm involved an accurate representation of neutron detector response. Earlier studies showed that it was possible to calculate the total, neutron, and photon PHDs and TOF responses of liquid scintillator-type (EJ-309, Eljen Technology, 2010 E. Broadway, Sweetwater, TX 79556, USA) neutron detectors [26]. The software MCNP-PoliMi [21], with the same input geometries as outlined above, was used to simulate the exact interactions inside the simulated detector active volume. A custom Fortran-based post-processor [27] was then used to calculate the relevant PHDs and TOFs.

The input files for the MCNP-PoliMi simulations included cards that specified analog mode (necessary for PoliMi), 0.01 MeV neutron and photon cut-off energies for data collection, and identification of the active detector volumes. These simulations used one of six different cargo materials: electronics, furniture, meat, paper, steel, and vegetables, each containing 500 kg of RDX. Inputs for the post-processor specified the type of detector ane the details of PHD and TOF calculation [27]. These included the integration time, amount of light output for neutrons and photons, and the time window for TOF calculations.

Other types of explosives

A series of simulations was completed that used one of several different explosives in place of RDX in scenarios in which a 500 kg sphere of explosive was placed inside a container homogenously filled with paper. These explosives included several nitrogenous materials: ammonium nitrate (NH_4NO_3), ethylene glycol dinitrate or EGDN ($C_2H_4N_2O_6$), octogen or HMX ($C_4H_8N_8O_8$), nitrocellulose ($C_6H_7(NO_2)_3O_5$), nitroglycerine ($C_3N_3H_5O_9$), pentaerythritol tetranitrate or PETN ($C_5H_8N_4O_{12}$), and trinitrotoluene or TNT ($C_7H_5N_3O_6$) [24]. Other explosives included acetone peroxide ($C_9H_{18}O_6$), black powder, and fertilizer [24]. An estimate of algorithm response for these scenarios was completed by comparing the flag strengths of the previously-identified flags for cases with RDX and the explosive in question. The explosives surrogate melamine was also considered, in order to investigate the response to inert nitrogenous material.

Application of explosives-detection techniques to simulation output

Five different types of flags were investigated for use in the explosives-detection algorithm. Several of these, including the backscatter neutron, monoenergetic neutron, and monoenergetic photon flags, were introduced in an earlier paper [17]. Conclusions reached in that earlier study resulted in both the combinatory and PHD flags discussed below.

The best flags of each type were determined by finding the top ten flags for every scenario in which 500 kg of RDX were concealed in cargo with the surrounding environment present. These top flags were identified by the largest flag strength in one of three categories: organic/hydrogenous cargo, inorganic/metallic cargos, and all/unknown cargo.

Flags based on backscattered neutrons

As discussed above, earlier simulations utilized an artificially biased conical source with no shielding. This allowed the 180° detection surface to be placed behind the source. However, when the shield was present the detection surface was forced in front of the source, overwhelming the tallies with incident neutrons. Therefore, the 150° detector surface was used in place of the 180° detector surface for those flags using only backscattered neutrons. These included comparing the total number and the 10-12 MeV neutrons for cases with and without RDX. Other types of flags that previously used backscattered neutrons were either eliminated or substituted the 150° scatter neutrons.

Monoenergetic neutron flags

There were two types of flags that used monoenergetic neutrons, defined as within one 0.2 MeV energy bin. The first type consisted of the ratio of the neutron tally at one particular angle and energy with another at the same energy but different angle. These flags took advantage of resonance scatter and absorption in the target, while use of ratios worked to normalize the tallies by the number of neutrons of the same energy produced at different scatter angles. A total of fifty-one flags of this type, specifically the best ones identified in prior work for simplified conditions [17], were calculated for the more realistic conditions described above.

The second type of monoenergetic neutron flag consisted of ratios of specific neutron elastic and inelastic scatter peak magnitudes and particular angles. The seventy most promising flags of this type, as identified in the earlier study [17,18], were calculated for the more realistic scenarios discussed above. This included comparing ratios of the elastic scatter peaks for carbon (10.2 MeV), nitrogen (10.6 MeV), and oxygen (11.0 MeV) at the 150° scatter surface, as a comparison of these three peaks provides one of the most direct measures of the relative elemental abundances.

Monoenergetic photon flags

As with the monoenergetic neutron flags, the photon tallies were divided into 0.2 MeV energy bins with a single bin defining the location of the photon peak. For the flags based on photon peak ratios, ratios of inelastic scatter-induced characteristic photons from carbon, nitrogen, oxygen, and iron were compared for cases with and without RDX. As photon emission is isotropic, the peak energies are not dependent on neutron scatter angle, so utilizing the photon tallies from only one detector surface (150°) was adequate. The top twenty-eight flags found in an earlier study utilizing simplified conditions were applied to the various scenarios studied here [17].

Combinatory flags

It was observed in an earlier paper [17] that the identities of many of the strongest flags were similar to that of other strong flags. This presents the possibility of using flags that combine different types of neutron and photon tallies to create flags that are both effective and require less rigorous neutron spectroscopy. A total of 47 of these combinatory flags were considered. These included ratios of all neutrons at two different angles and photon peak tallies normalized by these neutron tally ratios. Others were composed of ratios at different angles of neutron tallies below 1 MeV, above 10 MeV, or integrated from 4 to 8 MeV.

Neutron pulse height distribution (PHD) flags

The post-processor output included neutron, photon, and total PHDs and TOF distributions for every detector, as well as the combined PHD and TOF. As photon spectroscopy in the actual scanning system would be accomplished using dedicated detectors, it was not necessary to consider the photon PHDs in the described liquid-scintillation detectors at this time. Possible PHD flags mirrored several of the combinatory flags discussed earlier in that they used ratios of the number of neutrons in given energy ranges. For the PHD flags, these corresponded to the number of neutrons inside specific pulse height windows, with the domains as defined through application the relevant energy deposition equations [26]. For example, given that 10 MeV neutrons may deposit up to 4.88 MeVee in the liquid scintillator material, for the purpose of the flag the number of neutrons over 10 MeV was approximated by the integrated PHD greater than 4.88 MeVee. The resulting flag strengths, as defined by eqn. (6-2), were then compared with each other, as well as the analogous combinatory flag strengths, to find potential flags for the detection algorithm.

Results and Discussion

The use of realistic neutron sources

Isotropic vs. artificially collimated monoenergetic sources

As expected, there were significantly more uninteracted 14.1 MeV neutrons tallied the 150° and 120° detector tallies when the unshielded isotropic source was used instead of the monoenergetic cone source. Unattenuated neutrons in these two tallies were negligible for the conical source, but totaled 30% and 9%, respectively, of the 180° detector tally for the isotropic source. This is expected, as the conical beam was such that these two surfaces were completely outside the beam path but the partial shielding from the container and proximity to the isotropic source led to significant source interference at these detector surfaces. Other differences in isotropic source tallies included an increase by a factor of two for neutrons below 4 MeV as well as a 45% increase in the number with energy between the 11 MeV backscatter off oxygen and 14.1 MeV. This is mainly due to increased scatter off surrounding materials. Similarly, the increased interaction with the surroundings changed the photon flux, with 25% and 140% more photons tallied with energies at 3.8 and 5.2 MeV respectively for the isotropic neutron source. Due to the interference from the unshielded isotropic source, these simulations were not included in the identification of flags for the detection algorithm.

Effect of shielding an isotropic 14.1 MeV neutron source

A comparison of the neutron and photon tallies at the detector surfaces for cases with and without the neutron shield showed some distinctive differences. There was an ~99% reduction in the number of unscattered neutrons crossing the 150°, 120°, and 90° detector surfaces. Also expected was the large increase in low-energy neutrons tallied on all surfaces, due to the polyenergetic nature of the neutron beam caused by significant neutron scatter inside the shield. This increase varied from a factor of 2 for transmitted neutrons, 23 at the 90° detector surface, to a factor of 68 at the 180° detector surface. Furthermore, many photons were produced through interactions in the shielding, which accounted for a factor of 35 increase in the number of photons counted at the 180° detector surface when the shield was in place. Especially prominent among these were the 4.6 MeV photon from the de-excitation of ^{56}Fe, a 1.0 MeV photon formed from several ^{56}Fe de-excitation reactions, and a large number of lower-energy photons that were partially attenuated before exiting the shield.

Conical approximation of the shielded isotropic 14.1 MeV source

The artificially-biased conical source showed a factor of 7.4 decrease in the number of unattenuated 14.1 MeV neutrons in the 150° detector surface due to incomplete shielding at the extreme edges of the conical shield. However, neutron tallies were otherwise very similar and the use of the artificially-biased conical approximation was used in order to conserve computational resources. One disadvantage of the conical approximation was that the photons produced in the shield by the isotropic source were no longer present so the number of photons measured in the 150° detector, especially the iron photons, was somewhat reduced. This artificial inflation of the photon flag strength could be partially compensated for by using the total number of photons in all detection surfaces, though this made no difference in which flags were identified for use in the detection algorithm.

Neutron detector response

An example of the detector response, as calculated using MCNP-PoliMi, for the liquid scintillator detector at the 150° scatter position is shown in Fig. 6-3. In this example the photon spectrum (Fig. 6-3a) shows several inelastic scatter photons at 2.2, 4.6, 6.2, 7.8, and 9.0 MeV, while the elastically scattered neutrons between 10-12 MeV are clearly visible. The photons correspond to the de-excitation photons with energies of 2.31 MeV from nitrogen, 4.43 MeV from carbon, 6.13 from oxygen, and 7.89 MeV and 8.88 MeV from iron. The photon pulse height distribution (Fig. 6-3b) shows corresponding Compton edges at the expected 2.1, 4.2, 6.0, 7.7, and 8.6 MeV. Due to the way fast neutrons deposit energy in the liquid scintillator material, the maximum light output in MeVee is less than the energy deposited such that the pulse height does not exceed 8.9 MeVee for 14.1 MeV neutrons. As seen in Fig 6-3c, the majority of the photons started arriving at the detector after ~39 ns. This is similar to the 37 ns needed for 14.1 MeV neutrons to interact with the iron container and the resulting photons to reach the container, and significantly longer than the time needed for photons produced in the source shielding. This demonstrates that the majority of the photons reaching the detector originate inside the cargo container or surrounding environment and not in the source shielding. The minimum time needed for 14.1 MeV incident neutrons to elastically scatter on the container and reach the detector is ~59 ns and the vast majority of the neutrons arrive after this time.

Figs. 6-4a and 6-4b show an example of the PHD and neutron TOF distribution as a function of neutron scatter angle. As expected, the total proportion of high-energy neutrons decreased with decreasing scatter angle as fewer singly-scattered neutrons penetrated the necessary target thickness. The increasing source-detector distance is responsible for the shift in neutron arrival time. Figure 6-5 shows the neutron PHDs at the 150° for several different types of cargo material. Besides changes in the number of neutrons, the most significant differences are shown in the high-light output region between 9 MeVee, corresponding to the maximum light output from elastically scattered neutrons. As seen in the figure, the structure of the hydrogenous materials: water, meat, and vegetables, are very similar in this region. Due to its high atomic number, the steel cargo shows the largest number of high-energy neutrons followed by the other inorganic materials: electronics and furniture. It was decided not to pursue flags based on the TOF distributions because large target size led to high uncertainties in interaction position.

The average detection efficiency, as calculated by comparing the MCNP5 current tallies and the integrated PHDs, was 20±7%. As expected, the simulated detection efficiency was higher when neutron energy was lower, averaging 27±4% at the 0° detector and 11±2% at the 150° detector, where there were far more high-energy neutrons.

Flags based on backscattered neutrons

When the RDX mass was decreased from 6,000 kg, chosen in prior work as a position-independent means of determining optimal flags [17], to a more realistic 500 kg in a paper-cargo scenario, the flag strength based on the total number of backscattered neutrons decreased by a factor of ~2.5. Because of the increased scatter from surrounding soil, ground cover, and source shielding, flag strength further decreased by an additional 50% [17]. This meant that the flag strength fell below 0.01 for all cases except for 0.038 when homogenous steel cargo was used. Therefore, this type of flag was abandoned as part of the detection algorithm.

In the simplified cases of a previous study, it was observed that there was a significant difference in the number of backscattered neutrons with energies of 10-12 MeV for cases with and without RDX [17]. This energy range corresponds to a single elastic scatter of a 14.1 MeV neutron off carbon, nitrogen, or oxygen. However, once cargo material, RDX mass, heterogeneous packing, and the surrounding environment was changed as detailed above, these flag values fell below 0.01 for almost all cases. However, because singly-scattered neutrons interacting with steel fall outside this range, the flag strength was a measurable 0.10 when homogenous steel cargo was used.

One rather direct way of measuring the relative amounts of carbon, nitrogen, and oxygen is to compare the relative magnitudes of their elastic scatter peaks. These flags showed several promising possibilities in the simplistic cases [17], but the flag strengths dropped significantly when the surrounding soil and concrete slab or metal plate was included. Only the homogenous steel case exceeded flag strengths of 0.01, with 0.082 for oxygen-carbon, 0.063 for nitrogen-carbon, and a small 0.017 for nitrogen-oxygen peak ratio flags. Furthermore, distinguishing between peaks that vary by only 0.2 MeV is very difficult using current neutron spectroscopy technology.

Due to the small differences between RDX and no-RDX cases when using any of the described backscatter-based methods, the explosives-detection algorithm cannot rely solely on these types of calculations. However, neutron backscatter strategies have shown definite promise in cases in which the cargo is largely metallic in nature. This represents about 27% of cargo containers [19]. Therefore, backscatter-based methods, in combination with other flags, have the potential to form a powerful explosives-detection tool.

Monoenergetic neutron flags

The best overall flags that are calculated from ratios of single bin neutron tallies at different angles are shown in Table 6-3. Although there was variation in which flags were best for each type of cargo, every single one of the top five flags for each category of cargo type were in the top ten overall flags shown in Table 6-3. Furthermore, flag values were consistently either positive or negative for all cargo types. It was observed that many of these flags consisted of a ratio of the neutron flux at a relatively high energy, between 10.5 and 11.6 MeV, at two very different scatter angles (0°-30° and 120°-150°). This is essentially comparing the unscattered or slightly scattered neutron flux with the amount of single elastic scatter off elements heavier than carbon. Similarly, the flags based on neutron peaks generally consisted of the extremes of energy and angle.

Inclusion of the surrounding environment decreased flag strength for any given cargo type, although this effect was far less pronounced than for the backscatter-based flags. For example, adding the concrete slab and soil decreased the flag strength from over 0.90 in the idealistic case to between 0.50 and 0.75 for most of the flags shown in Table 6-3. Similarly, decreasing the RDX mass from 6,000 kg in the idealistic case to 500 kg decreased the flag strength by a roughly proportional amount. As expected, the lowest flag strengths were found in the crated geometries, as these simulations utilized both a smaller RDX mass, heterogeneous cargoes, and more realistic source. However, even these simulations had flag values in excess of 0.17 for at least one of the flags listed in Table 6-3.

Because of their relatively strong flag strength and relative insensitivity to shielding material, flags based on neutron tallies at a given energy and multiple angles are strong candidates for inclusion in an explosives-detection algorithm.

Monoenergetic photon flags

The best flags based on comparing relative photon peak magnitudes are shown in Table 6-4, these include the top five flags for each cargo category. Three of the most important photons in these flags are found in the 4.6, 5.2, and

6.2 MeV energy bins, corresponding to the 4.4, 5.1, and 6.1 MeV characteristic photons of carbon, nitrogen, and oxygen, respectively. The main disadvantage of this flag type is the comparatively low flag strengths. When using either neutron scatter-based flag, every simulation showed at least a 0.05 flag strength for at least one flag. However, most of the strongest photon-based flag calculations for any particular scenario were around or below 0.05. Although the relatively low flag magnitudes make it more difficult to discern the presence of RDX, photon energy spectroscopy is considerably more precise and accurate than neutron spectroscopy. Furthermore, there is a distinct advantage in using a different type of radiation for the source and the signal.

Combinatory flags

The strongest combinatory flags for organic, hydrogenous, inorganic, and unknown cargos are shown in Table 6-5. As may be seen in the table, there is significant overlap in flag identity between the different cargo types, and the flag strengths are considerably higher than for the more spectroscopy-intense flags discussed above. Furthermore, the relative uncertainty in flag strength, as calculated from the counting statistics of the signal collection, is only a small fraction of the average flag strength. Furthermore, there is much less variation, i.e. smaller σ, in flag strength over the different cargos. Many of the strongest flags would not require neutron spectroscopy at all, as they are based on a measurement of specific photon energies normalized by total neutron counts at two different angles. Most of the other strongest combinatory flags are based on a measurement of only the fastest neutrons at two different angles. This could be potentially measured using either time-of-flight or a threshold-based method.

Neutron pulse height distribution (PHD) flags

Table 6-6 shows the average flag strengths for the top neutron PHD flags over the six cargo materials. Statistical uncertainties were relatively low, generally below 0.05, due to the large number of particles in each pulse height range. In most cases, the PHD flag strengths were higher than the corresponding combinatory flag strengths. An exception to this was found for the steel cargo, due to its very different composition compared to RDX. As seen in the table, there were several flags in which using the PHD was a significant improvement over the combinatory flags. These flags, especially in combination with the partially photon-based combinatory flags, have strong potential for use in the explosives detection algorithm, especially because they do not require unfolding of the neutron PHDs to get the neutron energy spectrum.

Flags and other explosives

When comparing the flag strengths for the top flags shown in Tables 6-3 and 6-5 for paper-filled containers with different types of explosives it was found that, with the exception of fertilizer, the flag response was stronger for the other explosives than it was for RDX. This means that a flag triggering on RDX would also trigger on any of the given explosives except fertilizer. Furthermore, it was found that, with a few exceptions, the flags fell in the same order of increasing strength for RDX and the other explosives, i.e. the best or strongest flag for RDX was the best or strongest flag for all other explosives except fertilizer. The explosives surrogate melamine also showed flag strengths exceeding that of RDX, illustrating that other nitrogenous material could fool the proposed flag-based method.

Use of flags in the detection algorithm

As discussed earlier, methods relying on only backscattered neutrons are of limited use unless the cargo is metallic in nature. Furthermore, many of the highest performing flags were monoenergetic neutron flags, which are practically infeasible due to current limitations in neutron spectroscopy technology. However, many of these flags, such as neutron peak comparison flags with metallic cargo, were strong enough that they were still included in the event of improvements in neutron spectroscopy before deployment of the proposed system. As flag strength is strongly dependent on cargo material, the explosives algorithm will use different flags, depending on what type of cargo is present. Therefore, flag strengths were compared within the material groups of organic, hydrogenous, and inorganic/metallic in order to identify the best flags for each category of cargo. The top-performing flags for each category, as well as for an unknown cargo type are shown in Table 6-7. These flags will form the backbone of the explosives detection algorithm. It should be noted that PHD flags may be substituted for combinatory flags where appropriate.

Conclusions and Future Work

Several explosives-detection flags developed for active neutron interrogation using a D-T generator show promise under relatively realistic simulated conditions such as a realistic shielded source, varied bomb size and position, inclusion of the surrounding environment, several different cargo types, and complex cargo geometries. Simulation of realistic neutron detector response led the calculation of additional flags that were not dependent on stringent neutron spectroscopy.

Many flags demonstrated a high degree of independence with respect to cargo type and would therefore be very useful in scenarios in which the cargo is unknown. Other flags displayed higher flag strengths for certain classes of cargo material, such as the number of high-energy backscattered neutrons when RDX is hidden inside metallic cargo. These cargo-dependent flags may still be a valuable contribution to a flag-based algorithm, as they provide a definitive decision point when other methods have been used to determine the cargo type. Many of the strongest flags were formed from combinations of these more specific types of flags or from the neutron pulse height distributions (PHDs) themselves, which have the added advantage of requiring minimal neutron spectroscopy.

Now that the best flags for explosives detection in different types of cargo have been identified, future efforts are needed to further refine, define, and optimize the detection algorithm. Realistic photon and neutron detector responses, background contributions, and multiple scatters should be included in calculations considering the likelihood of false positives and false negatives. This optimization should also include consideration of factors such as system cost, ease of operation, and dose to personnel before proceeding with experimental verification.

Figures

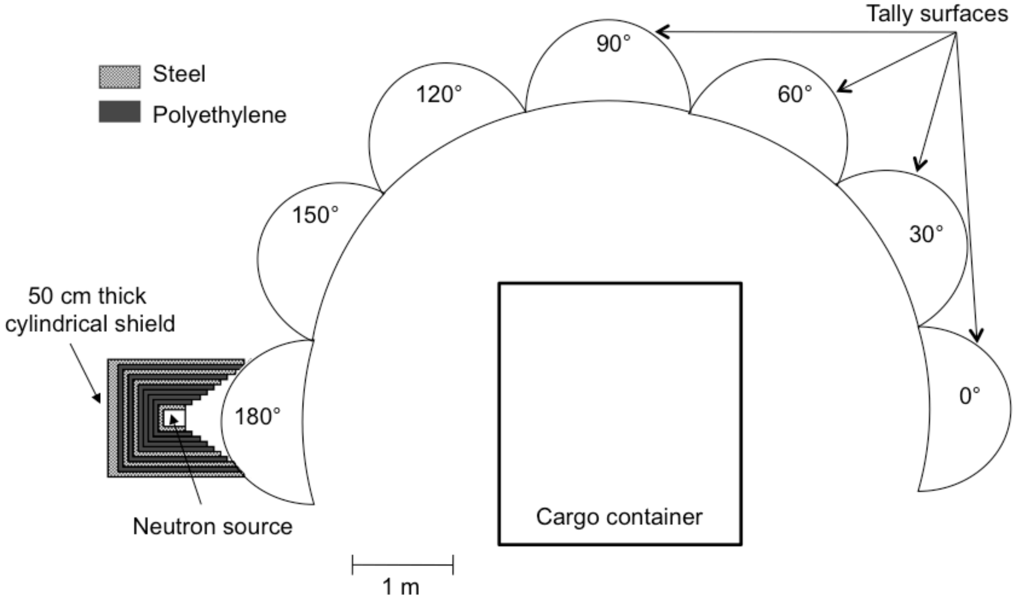

Figure 6-1. Geometry of shielded D-T source showing standard sea-land cargo container, hemispherical tally surfaces at seven ranges of neutron scatter, and isotropic neutron source in a cylindrical layered shield.

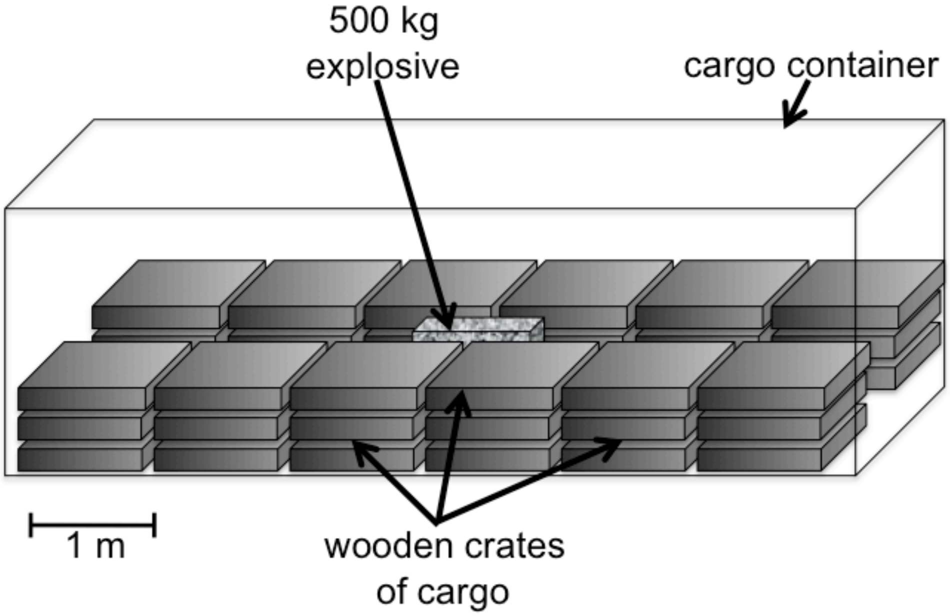

Figure 6-2. Example of crated geometry with block of explosive hidden in the center between crates of inert material.

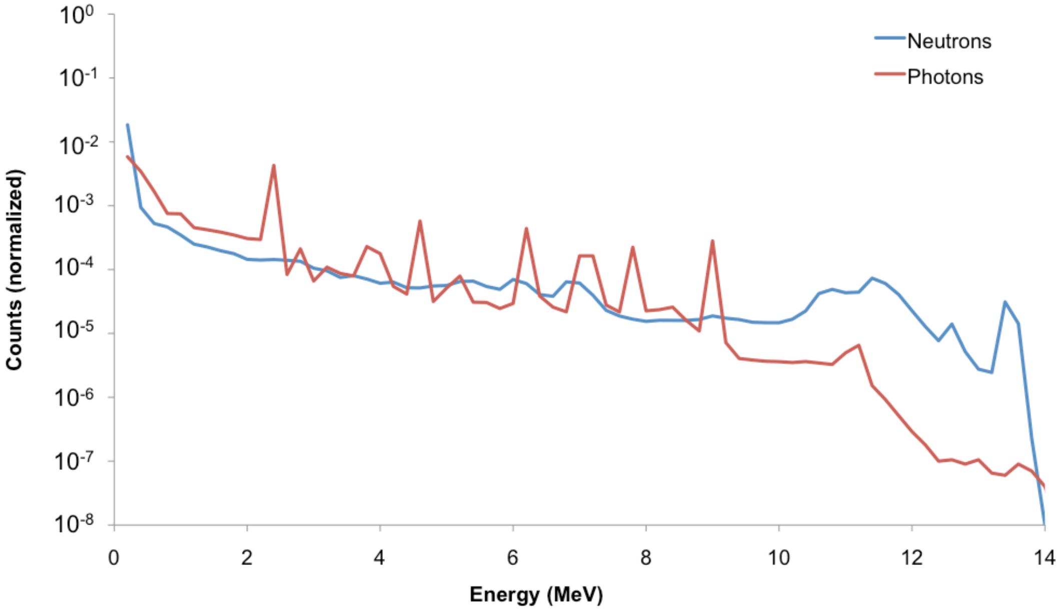

a.

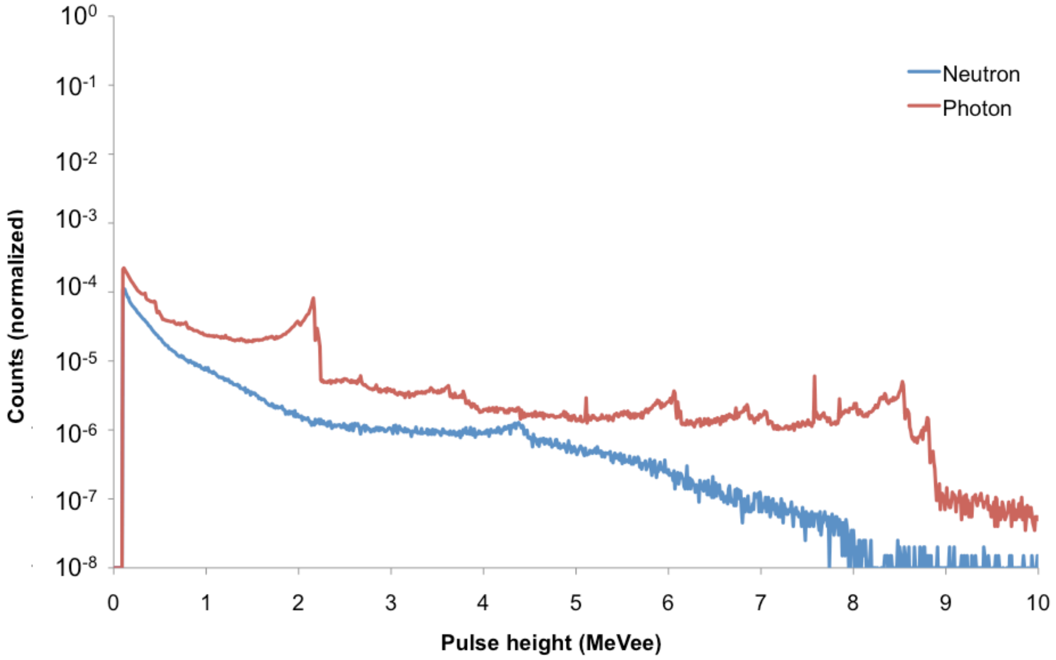

b.

Figure 6-3. An example of a) the neutron and photon energy distributions, b) the pulse height distributions, and c) the time-of-flight distributions produced in the 150 degree detector.

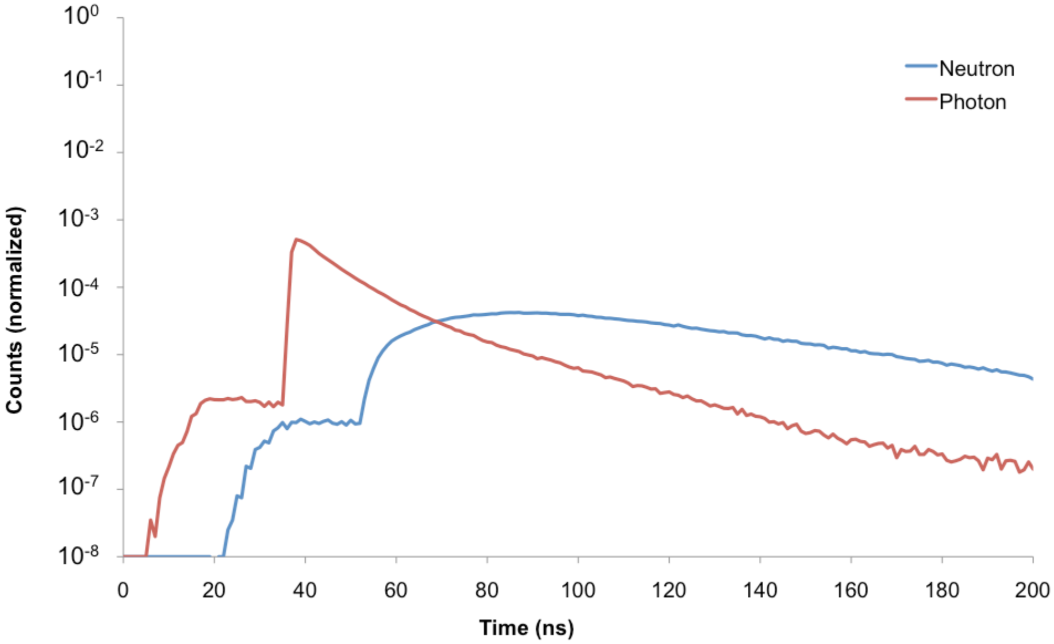

c.

Figure 6-3 (continued). An example of a) the neutron and photon energy distributions, b) the pulse height distributions, and c) the time-of-flight distributions produced in the 150 degree detector.

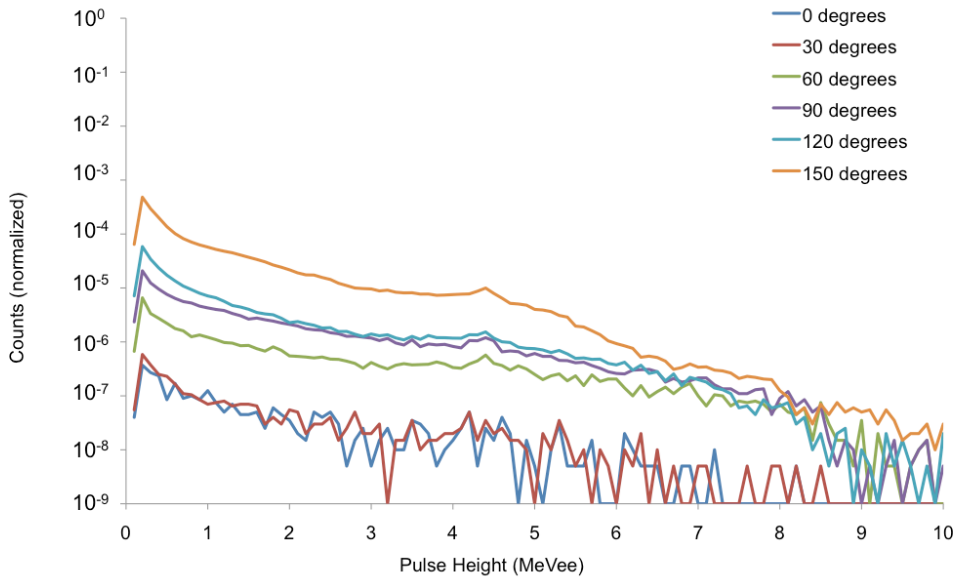

a.

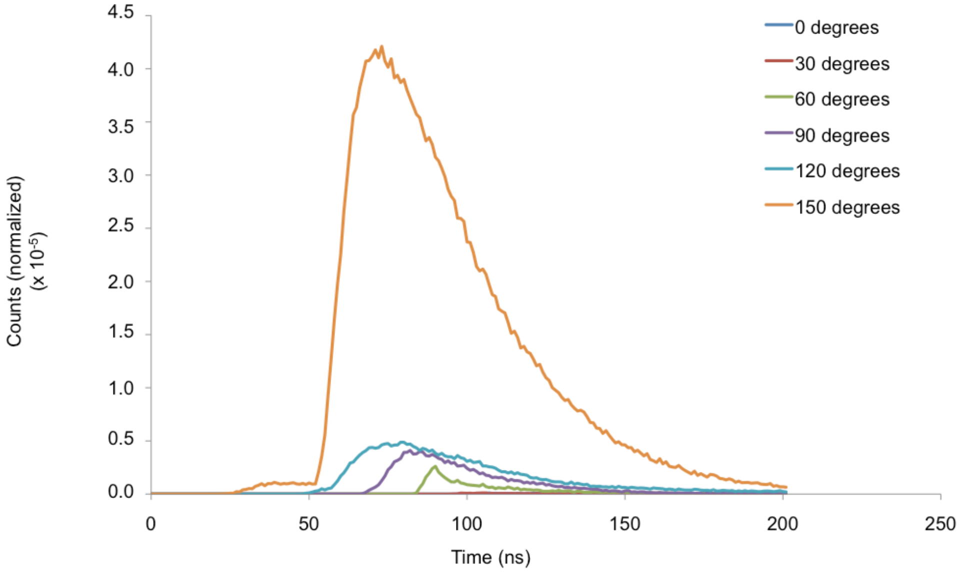

b.

Figure 6-4. Example of calculated detector response using MCNP-PoliMi and postprocessor with a) neutron pulse height as a function of scatter angle and b) neutron time-of-flight spectrum as a function of scatter angle for a paper-filled cargo container.

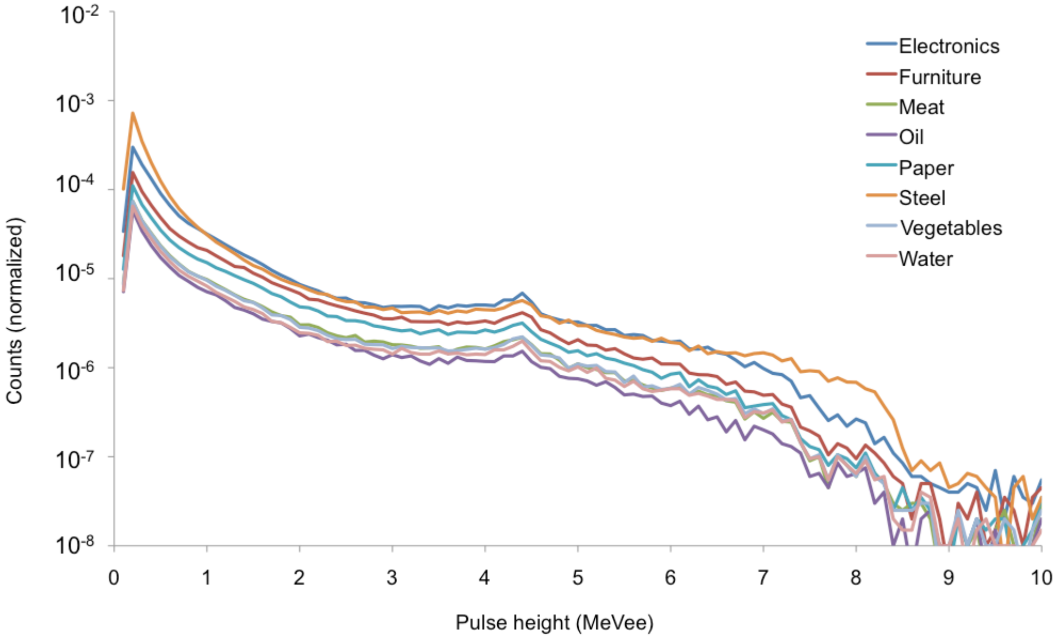

Figure 6-5. Neutron PHDs at the 150 degree detector for several different cargo materials.

Tables

Table 6-1. Densities and compositions, expressed as atom percents, of materials used in MCNP simulations.

Material	Density (g cm^{-3})	H	C	N	O	Other
Air	0.0012		0.01%	75.5%	23.2%	1.3% Ar
Steel	7.87		0.32%			99.6% Fe, 0.05% S, 0.04% P
RDX	1.82	28.6%	14.3%	28.5%	28.6%	
Soil[23]	1.75	29.4%	1.87%		50.455	2.59% Al, 13.54% Si, 1.43% K, 0.27% Fe
Sand	1.6			trace	65.5%	29.3% Si, 3.8% Al, 1.21% Ca
Concrete[24]	2.3	30.4%	0.29%		49.9%	0.92% Na, 1.03% Al, 15.1% Si, 0.71% K, 1.49% Ca, 0.16% Fe
Brick[24]	1.8				66.3%	0.39% Al, 32.3% Si, 0.72% Ca
Wood/paper[24]	0.70/0.60	47.6%	28.6%	23.8%		
Clothing	0.3	47.6%	28.6%		23.8%	
Melamine	1.57	40%	20%	40%		
Furniture	0.2	41.5%	31.7%		20.8%	3.03% Fe, 3.04% Al
Vegetables[25]	0.4	62.8%	5.7%	0.07%	31.4%	0.07% K, trace Ca, Fe, Mg, P, Na, S
Meat[25]	1.1	60.4%	14.5%	0.72%	24.2%	trace K, P, Fe, Mg, Ca, Na

Table 6-2. Densities and atom percent compositions of explosive materials used as cargo in MCNP simulations.

Material	Density	H	C	N	O	Other
Acetone Peroxide	1.22	55%	27%		18%	
Ammonium Nitrate	1.73	44%		22%	33%	
Black Powder	1.04	51%	7%	7%	23%	7.6% K, 3% Si
EGDN	1.49	29%	14%	14%	43%	
Gasoline	0.68	69%	31%			
HMX	1.9	29%	14%	29%	29%	
Nitrocellulose	1.66	29%	25%	13%	33%	
Nitroglycerin	1.13	25%	15%	15%	45%	
PETN	1.77	29%	17%	14%	41%	
RDX	1.82	29%	14%	29%	29%	
TNT	1.65	24%	33%	14%	29%	
Fertilizer	0.99	0%			0%	1% Na, 50% Cl, 48% K, trace Mg, Ca, Br

Table 6-3. Best-performing monoenergetic neutron flags over all cargo materials with 500 kg explosive and surrounding environment [17]. Shown are the average flag strengths and uncertainties as well as the variation in flag strength (σ) for the flag with different cargo materials. The level of variation is indicative of the flags' dependence on cargo type.

Neutron flag Identity (MeV, degrees)	Average flag strength	Flag strength variation
$\frac{(11.6\ \text{MeV},120^\circ)}{(11.6\ \text{MeV},0^\circ)}$	0.73 ± 0.16	1.5
$\frac{(11.4\ \text{MeV},120^\circ)}{(11.4\ \text{MeV},0^\circ)}$	0.61 ± 0.16	1.1
$\frac{(11.0\ \text{MeV},150^\circ)}{(10.0\ \text{MeV},0^\circ)}$	0.61 ± 0.45	0.92
$\frac{(11.2\ \text{MeV},150^\circ)}{(11.2\ \text{MeV},0^\circ)}$	0.58 ± 0.13	1.1
$\frac{(11.0\ \text{MeV},150^\circ)}{(9.6\ \text{MeV},0^\circ)}$	0.56 ± 0.45	0.79
$\frac{(11.0\ \text{MeV},150^\circ)}{(11.0\ \text{MeV},0^\circ)}$	0.54 ± 0.13	0.9
$\frac{(11.4\ \text{MeV},150^\circ)}{(11.4\ \text{MeV},0^\circ)}$	0.53 ± 0.17	0.89
$\frac{(10.8\ \text{MeV},150^\circ)}{(10.8\ \text{MeV},0^\circ)}$	0.53 ± 0.16	0.88
$\frac{(10.6\ \text{MeV},150^\circ)}{(10.6\ \text{MeV},0^\circ)}$	0.50 ± 0.23	0.76
$\frac{(11.0\ \text{MeV},150^\circ)}{(8.2\ \text{MeV},0^\circ)}$	0.48 ± 0.28	0.72
$\frac{(11.0\ \text{MeV},150^\circ)}{(6.8\ \text{MeV},0^\circ)}$	0.42 ± 0.18	0.56
$\frac{(11.0\ \text{MeV},150^\circ)}{(7.8\ \text{MeV},0^\circ)}$	0.42 ± 0.21	0.63

Table 6-4. Best-performing monoenergetic photon flags over all cargo materials with 500 kg explosive and surrounding environment. Shown are the average flag strengths and uncertainties as well as the variation in flag strength (σ) for the flag with different cargo materials.

Photon flag identity	Average flag strength	Flag strength variation
$\frac{5.2\ \text{MeV}}{6.2\ \text{MeV}}$	0.016 ± 0.0027	0.014
$\frac{5.2\ \text{MeV}}{2.6\ \text{MeV}}$	0.013 ± 0.0041	0.013
$\frac{5.2\ \text{MeV}}{4.6\ \text{MeV}}$	0.014 ± 0.016	0.017
$\frac{5.2\ \text{MeV}}{3.4\ \text{MeV}}$	0.012 ± 0.004	0.011
$\frac{4.6\ \text{MeV}}{2.6\ \text{MeV}}$	0.0080 ± 0.013	0.0070
$\frac{5.2\ \text{MeV}}{2.8\ \text{MeV}}$	0.012 ± 0.0036	0.013
$\frac{4.6\ \text{MeV}}{3.4\ \text{MeV}}$	0.0080 ± 0.014	0.007
$\frac{7.2\ \text{MeV}}{2.6\ \text{MeV}}$	0.0070 ± 0.005	0.0090
$\frac{5.2\ \text{MeV}}{3.8\ \text{MeV}}$	0.011 ± 0.0017	0.013
$\frac{6.2\ \text{MeV}}{1.8\ \text{MeV}}$	0.016 ± 0.0027	0.014

Table 6-5. Best-performing combinatory flags over all cargo materials with 500 kg explosive and surrounding environment. Shown are the average flag strengths and uncertainties as well as the variation in flag strength (σ) for the flag with different cargo materials.

Flag identity (MeV)	Average flag strength	Flag strength variation
$\frac{(>10\text{ MeV},150°)}{(>10\text{ MeV},0°)}$	0.39 ± 0.067	0.20
$\frac{(>10\text{ MeV},180°)}{(>10\text{ MeV},0°)}$	0.39 ± 0.059	0.19
$\frac{(>10\text{ MeV},120°)}{(>10\text{ MeV},0°)}$	0.39 ± 0.064	0.19
$\frac{\left[\frac{(\text{total neutron},150°)}{(\text{total neutron},0°)}\right]}{\text{C photon}}$	0.24 ± 0.017	0.12
$\frac{\left[\frac{(\text{total neutron},150°)}{(\text{total neutron},0°)}\right]}{\text{O photon}}$	0.24 ± 0.009	0.11
$\frac{\left[\frac{(\text{total neutron},90°)}{(\text{total neutron},0°)}\right]}{\text{C photon}}$	0.23 ± 0.007	0.12
$\frac{\left[\frac{(\text{total neutron},90°)}{(\text{total neutron},0°)}\right]}{\text{O photon}}$	0.23 ± 0.009	0.11
$\frac{\left[\frac{(\text{total neutron},150°)}{(\text{total neutron},0°)}\right]}{\text{N photon}}$	0.23 ± 0.006	0.11
$\frac{(\text{total neutron},180°)}{(\text{total neutron},0°)}$	0.23 ± 0.001	0.10

Table 6-6. Identities and strengths of flags based on neutron PHDs averaged over six cargo materials: electronics, furniture, meat, paper, steel, and vegetables. Also shown is average difference in flag strength between equivalent PHD and combinatory flags, with positive values indicating an improvement. PHD flag strengths were generally larger, except in the case of steel cargo.

Neutron flag ID	Average flag strength	Average flag strength difference	Average non-steel flag strength difference
$\frac{(6-10\ \mathrm{MeV},150^\circ)}{(6-10\ \mathrm{MeV},0^\circ)}$	0.74 ± 0.033	0.23	0.25
$\frac{(>10\ \mathrm{MeV},150^\circ)}{(>10\ \mathrm{MeV},0^\circ)}$	0.72 ± 0.023	-0.63	-0.09
$\frac{(>10\ \mathrm{MeV},120^\circ)}{(>10\ \mathrm{MeV},0^\circ)}$	0.71 ± 0.024	-0.62	-0.09
$\frac{(>10\ \mathrm{MeV},150^\circ)}{(4\text{ - }8\ \mathrm{MeV},0^\circ)}$	0.67 ± 0.046	0.26	0.25
$\frac{(>10\ \mathrm{MeV},150^\circ)}{(<1\ \mathrm{MeV},0^\circ)}$	0.38 ± 0.055	0.05	0.26
$\frac{(<1\ \mathrm{MeV},150^\circ)}{(<1\ \mathrm{MeV},0^\circ)}$	0.37 ± 0.056	0.14	0.27
$\frac{(<1\ \mathrm{MeV},120^\circ)}{(<1\ \mathrm{MeV},0^\circ)}$	0.37 ± 0.056	0.13	0.27
$\frac{(<1\ \mathrm{MeV},90^\circ)}{(<1\ \mathrm{MeV},0^\circ)}$	0.35 ± 0.057	0.12	0.26
$\frac{(<1\ \mathrm{MeV},60^\circ)}{(<1\ \mathrm{MeV},0^\circ)}$	0.34 ± 0.06	0.10	0.25
$\frac{(>10\ \mathrm{MeV},150^\circ)}{(<3\ \mathrm{MeV},30^\circ)}$	0.19 ± 0.022	-0.01	0.13
$\frac{(>10\ \mathrm{MeV},150^\circ)}{(<1\ \mathrm{MeV},30^\circ)}$	0.18 ± 0.054	-0.02	0.12
$\frac{(>10\ \mathrm{MeV},150^\circ)}{(>10\ \mathrm{MeV},30^\circ)}$	0.17 ± 0.025	0.07	0.16
$\frac{(4\text{ - }8\ \mathrm{MeV},90^\circ)}{(<1\ \mathrm{MeV},30^\circ)}$	0.17 ± 0.056	0.00	0.13

Table 6-7. Best-performing flags of any type for organic, hydrogenous, inorganic, and metallic cargo with 500 kg explosive and surrounding environment. Shown are the average flag strengths and uncertainties as well as the variation in flag strength (σ) for the flag with different cargo materials.

Flag identity (MeV, deg)	Average flag strength	σ	Flag identity (MeV)	Average flag strength	σ
Organic cargo			Hydrogenous cargo		
$\frac{(>10\ \text{MeV},120^\circ)}{(>10\ \text{MeV},0^\circ)}$	0.51 ± 0.064	0.47	$\frac{(>10\ \text{MeV},120^\circ)}{(>10\ \text{MeV},0^\circ)}$	0.26 ± 0.0144	0.06
$\frac{(>10\ \text{MeV},150^\circ)}{(>10\ \text{MeV},0^\circ)}$	0.51 ± 0.064	0.48	$\frac{(>10\ \text{MeV},150^\circ)}{(>10\ \text{MeV},0^\circ)}$	0.26 ± 0.0144	0.06
$\frac{(11\ \text{MeV},150^\circ)}{(10\ \text{MeV},0^\circ)}$	0.45 ± 0.45	0.66	$\frac{(11\ \text{MeV},150^\circ)}{(11\ \text{MeV},0^\circ)}$	0.15 ± 0.048	0.034
$\frac{(11\ \text{MeV},150^\circ)}{(9.6\ \text{MeV},0^\circ)}$	0.44 ± 0.45	0.71	$\frac{(11\ \text{MeV},150^\circ)}{(10\ \text{MeV},0^\circ)}$	0.16 ± 0.065	0.029
$\frac{(6-10\ \text{MeV},150^\circ)}{(6-10\ \text{MeV},0^\circ)}$	0.29 ± 0.0068	0.36	$\frac{\left[\frac{(\text{total neutron},150^\circ)}{(\text{total neutron},0^\circ)}\right]}{\text{C photon}}$	0.15 ± 0.0024	0.05
$\frac{\left[\frac{(\text{total neutron},150^\circ)}{(\text{total neutron},0^\circ)}\right]}{\text{C photon}}$	0.23 ± 0.0072	0.14	$\frac{\left[\frac{(\text{total neutron},150^\circ)}{(\text{total neutron},0^\circ)}\right]}{\text{O photon}}$	0.15 ± 0.0016	0.05
$\frac{\left[\frac{(\text{total neutron},150^\circ)}{(\text{total neutron},0^\circ)}\right]}{\text{O photon}}$	0.24 ± 0.004	0.14	$\frac{\left[\frac{(\text{total neutron},180^\circ)}{(\text{total neutron},0^\circ)}\right]}{\text{C photon}}$	0.15 ± 0.0024	0.05
$\frac{\left[\frac{(\text{total neutron},90^\circ)}{(\text{total neutron},0^\circ)}\right]}{\text{C photon}}$	0.23 ± 0.0072	0.14	$\frac{\left[\frac{(\text{total neutron},90^\circ)}{(\text{total neutron},0^\circ)}\right]}{\text{C photon}}$	0.15 ± 0.0024	0.05

Table 6-7 (continued). Top flags of any type for organic, hydrogenous, inorganic, and metallic cargo with 500 kg explosive and surrounding environment. Shown are the average flag strengths and uncertainties as well as the variation in flag strength (σ) for the flag with different cargo materials.

Flag identity	Average flag strength	σ	Flag identity (MeV, deg)	Average flag strength	σ
Inorganic cargo			All cargos		
$\frac{(>10\ \text{MeV},120^\circ)}{(>10\ \text{MeV},0^\circ)}$	1.89 ± 0.0055	2.56	$\frac{(>10\ \text{MeV},120^\circ)}{(>10\ \text{MeV},0^\circ)}$	0.99 ± 0.0639	1.49
$\frac{(>10\ \text{MeV},150^\circ)}{(<1\ \text{MeV},0^\circ)}$	0.61 ± 0.0169	0.76	$\frac{(>10\ \text{MeV},150^\circ)}{(>10\ \text{MeV},0^\circ)}$	1.0 ± 0.0665	1.5
$\frac{(>10\ \text{MeV},150^\circ)}{(>10\ \text{MeV},0^\circ)}$	1.9 ± 0.0165	2.58	$\frac{(>10\ \text{MeV},180^\circ)}{(>10\ \text{MeV},0^\circ)}$	0.99 ± 0.0587	1.48
$\frac{(10.8\ \text{MeV},150^\circ)}{(10.8\ \text{MeV},0^\circ)}$	1.1 ± 0.04	1.5	$\frac{(11\ \text{MeV},150^\circ)}{(10\ \text{MeV},0^\circ)}$	0.61 ± 0.45	0.92
$\frac{(11\ \text{MeV},150^\circ)}{(11\ \text{MeV},0^\circ)}$	1.1 ± 0.05	1.5	$\frac{(11.4\ \text{MeV},120^\circ)}{(11.4\ \text{MeV},0^\circ)}$	0.61 ± 0.16	1.13
$\frac{(11.2\ \text{MeV},150^\circ)}{(11.2\ \text{MeV},0^\circ)}$	1.3 ± 0.05	1.9	$\frac{(11.6\ \text{MeV},120^\circ)}{(11.6\ \text{MeV},0^\circ)}$	0.73 ± 0.15	1.5
$\frac{(11.6\ \text{MeV},120^\circ)}{(11.6\ \text{MeV},0^\circ)}$	1.7 ± 0.04	2.6	$\frac{\left[\frac{(\text{total neutron},150^\circ)}{(\text{total neutron},0^\circ)}\right]}{\text{C photon}}$	0.42 ± 0.0172	0.48
$\frac{\left[\frac{(\text{total neutron},150^\circ)}{(\text{total neutron},0^\circ)}\right]}{\text{N photon}}$	0.74 ± 0.0045	0.82	$\frac{\left[\frac{(\text{total neutron},150^\circ)}{(\text{total neutron},0^\circ)}\right]}{\text{N photon}}$	0.42 ± 0.0059	0.49
$\frac{\left[\frac{(\text{total neutron},150^\circ)}{(\text{total neutron},0^\circ)}\right]}{\text{O photon}}$	0.71 ± 0.0082	0.76	$\frac{\left[\frac{(\text{total neutron},150^\circ)}{(\text{total neutron},0^\circ)}\right]}{\text{O photon}}$	0.41 ± 0.0093	0.45

References

1. A. L. Lehnert and K. J. Kearfott, "The detection of explosive materials: review of considerations and methods," Nucl. Technol. 172, 325 (2010).
2. R. C. Runkle, T. A. White, E. A. Miller, J. A. Caggiano, and B. A. Collins, "Photon and neutron interrogation techniques for chemical explosives detection in air cargo: a critical review," Nucl. Instrum. Methods Phys. Res. A 603, 510 (2009).
3. A. Buffler and J. R. Tickner, "Detecting contraband using neutrons: challenges and future directions," Radiat. Meas. 45, 1186 (2010).
4. D. Brown and T. Gozani, "Thermal neutron analysis technology," P. SPIE 2936, 85 (1997).
5. T. Gozani, M. Elsalim, M. Ingle, and E. Phillips, "gamma ray spectroscopy features for detection of small explosives," Nucl. Instrum. Methods Phys. Res. A 505, 482 (2003).
6. A. Buffler, "Contraband detection with fast neutrons," Radiat. Phys. Chem. 71, 853 (2004).
7. B. Perot, C. Carasco, S. Bernard, A. Mariani, J.-L. Szabi, G. Sannie, V. Valkovic, D. Sudac, G. Viesti, M. Lunardon, C. Botosso, G. Nebbia, S. Pesente, S. Moretto, A. Zenoni, A. Donzella, M. Moszynski, M. Gierlik, W. Klamra, P. L. Tourneur, M. Lhuissier, A. Colonna, C. Tintori, P. Peerani, V. Sequeira, and M. Salvato, "Measurement of 14 MeV neutron-induced prompt gamma-ray spectra from 15 elements found in cargo containers" Appl. Radiat. Isot. 66, 421 (2008).
8. D. Sudac, D. Matika, and V. Valkovic, "Identification of materials hidden inside a sea-going cargo container filled with an organic cargo by using the tagged neutron inspection system," Nucl. Instrum. Methods Phys. Res. A 589, 47 (2008).
9. G. Boghen, A. Donzella, V. Filippini, A. Fontana, M. Lunardon, S. Moretto, S. Pesente, and A. Zenoni, "MCNP calculations for container inspection with tagged neutrons," Nucl. Instrum. Methods Phys. Res. B 241, 831 (2005).
10. G. Viesti, A. Donzella, G. Bonomi, C. Botosso, D. Fabris, M. Lunardon, S. Moretto, G. Nebbia, S. Pesente, F. Pino, L. Sajo-Bohus, and A. Zenoni, in “Detection of Liquid Explosives and Flammable Agents in Connection with Terrorism”, (Springer Netherlands, 2008), pp. 39.
11. E. Hussein, M. DEsrosiers, and E. Waller, "On the use of radiation scattering for the detection of landmines," Radiat. Phys. Chem. 73, 7 (2005).
12. C. P. Datema, V. R. Bom, and C. VAneijk, "Monte carlo simulations of landmine detection using neutron backscattering imaging," Nucl. Instrum. Methods Phys. Res. A 513, 398 (2003).
13. G. F. Knoll, Radiation Detection and Measurements, Fourth ed. (John Wiley and Sons, Inc., Ann Arbor, Michigan, 2010).
14. R. C. Runkle, A. Bernstein, and P. E. Vanier, "Securing special nuclear material: recent advances in neutron detection and their role in nonproliferation," Journal of Applied Physics 108, 111101 (2010).

15. V. Valkovic, D. Sudac, S. Blagus, K. Nad, J. Obhodas, B. Vekic, G. Nebbia, and S. Pesente, "Fast neutron inspection of sea containers for the presence of "dirty bomb"," Nucl. Instrum. Methods Phys. Res. B 263, 119 (2007).
16. S. D. Clarke, M. Flaska, S. Pozzi, and P. Peerani, "Neutron and gamma-ray cross-correlation measurements of plutonium oxide powder," Nucl. Instrum. Methods Phys. Res. A 604, 618 (2009).
17. A. L. Lehnert and K. J. Kearfott, "Preliminary identification of flags for a novel algorithm-based approach for explosives detection using neutron interrogation for a simulated idealized cargo container scenario," Nucl. Instrum. Methods Phys. Res. A 638, 201 (2011).
18. A. L. Lehnert and K. J. Kearfott, "Simplified simulation of fast neutron scattering for an explosives detection application," Nucl. Sci. Eng. 168, 278 (2011).
19. M.-A. Descalle, D. Manatt, and D. Slaughter, "Analysis of recent manifests for goods imported through us ports," Report No. UCRL-TR-225708, Lawrence Livermore National Laboratory (2006).
20. R. A. Forster, L. J. Cox, R. F. Barrett, T. E. Booth, J. F. Briesmeister, F. B. Brown, J. S. Bull, G. C. Geisler, J. T. Goorley, R. D. Mosteller, S. E. Post, R. E. Prael, E. C. Selcow, and A. Sood, "MCNP version 5," Nucl. Instrum. Methods Phys. Res. B 213, 82 (2004).
21. S. Pozzi, E. Padovani, and M. Marseguerra, "MCNP-PoliMi: a monte-carlo code for correlation measurements," Nucl. Instrum. Methods Phys. Res. A 513, 550 (2003).
22. Z. D. Whetstone and K. J. Kearfott, "Use of multiple layers of repeating material to effectively collimate an isotropic neutron source," Nucl. Technol. 176, 395 (2011).
23. K. F. Eckerman and J. C. Ryman, "External exposure to radionuclides in air, water, and soil," Report No. EPA-402-R-93-081, Oak Ridge National Laboratory. (September 1993).
24. R. G. Williams III, C. J. Gesh, and R. T. Pagh, "Compendium of material composition data for radiation transport modeling," Report No. PNNL-15870, Pacific Northwest National Laboratory (April 2006).
25. F. C. Hummel, M. L. Shepherd, H. Galbraith, H. H. Williams, and I. G. Macy, "Chemical composition of twenty-two common foods and comparison of analytical with calculate values of diets," The Journal of Nutrition, 41 (1942).
26. E. C. Miller, S. D. Clarke, M. Flaska, S. A. Pozzi, E. Padovani, “MCNPX-PoliMi post-processing algorithm for detector response simulations,” Journal of Nuclear Materials Management (in press) (2011).
27. S. A. Pozzi, E. Padovani, M. Flaska, and S. Clarke, “MCNPX-PoliMi matlab post-processing code version 1.9.” *ORNL/TM-2007/33.* (March 2007).

Chapter 7: A Flag-Based Algorithm and Associated Neutron Interrogation System for the Detection of Explosives in Sea-Land Cargo Containers

Abstract

Recent efforts in the simulation of sea-land cargo containers in active neutron interrogation scenarios resulted in the identification of several flags that indicated the presence of conventional explosives. These flags, defined by specific mathematical manipulations of the neutron and photon spectra, have been combined into a detection algorithm for screening cargo containers. The detection algorithm's steps include classifying the cargo type, identifying containers filled with explosives, triggering in the presence of concealed explosives, and minimizing the number of false positives due to cargo heterogeneity. The algorithm has been implemented in a simulated system that includes both neutron and photon detectors. This system will take less than ten minutes to scan a container and cost approximately $1M to construct. Dose calculations resulted in estimates of less than 0.5 mSv for a person hidden in the container, and an operator annual dose of less than 0.9 mSv.

Introduction

Explosives detection at sea ports

Due to the high throughput, limited personnel, and short time constraints, less than 2% of sea-land cargo containers are screened at United States ports of entry [1]. Smuggled conventional explosives are of particular concern and are detected by either searching for chemical traces left by the explosives, or scanning for the bulk material itself [2]. Many of these bulk detection methods are nuclear in nature and function through active interrogation with either photons or neutrons. The most common methods, X-ray or gamma ray interrogation, are relatively insensitive to the explosive material itself, as its electron density is generally quite similar to that of the surrounding cargo. Furthermore, X-ray interrogation of large targets is difficult due to low target penetration. Neutron interrogation has been widely studied as an explosives-detection technique due to high penetrating ability and direct interaction with target nuclei [1,3].

This chapter presents a neutron interrogation-based algorithmic approach that screens for explosives inside standard sea-land cargo containers using a shielded monoenergetic 14.1 MeV neutron source. Neutron and photon measurements at different angles around the container are used to calculate flags, defined by specific mathematical manipulations of the neutron and photon spectra. The detection algorithm‘s output is a simple “yes/no”, reached after combining specific flags in a series of steps that classifies the cargo material, identifies potential explosives-containing containers, and minimizes certain false positives. A major advantage of this method is that it combines several other detection methods, which maximizes signal carriers and thus reduces measurement time and personnel dose. Furthermore, combining the results from several other detection strategies into one algorithm exploits all the advantages of the other methods, while minimizing the detriment cause by their respective shortcomings.

Earlier papers on the algorithmic approach characterized the neutron scatter behavior of fast neutrons [4] and compared neutron scatter simulations with laboratory experiments [5], laying the groundwork for further simulations. Later work identified promising flags in idealistic as well as more realistic conditions [6,7] and tested combinations of flags to minimize the need for neutron spectroscopy [7]. This chapter discusses combining these flags into a coherent explosives-detection algorithm and presents a screening system that implements the detection algorithm in simulations.

Equipment for explosives detection with neutron interrogation

Neutron sources

Neutron sources for active neutron interrogation include isotropic sources, particle accelerators, and fusion-based neutron generators. Due to the inclusion of certain neutron and photon peaks in flag calculations, a monoenergetic source is desirable. A D-T neutron generator was chosen, as they are considerably less expensive than most accelerator-based sources and provide better target penetration than D-D neutron generators. In a 100% duty cycle, a D-T generator typically produces neutrons at a rate of 5×10^8 to 2×10^{10} n s^{-1}, with a slight forward bias to the outgoing neutrons [8]. Another advantage of neutron generators is the availability of associated particle imaging (API) technology which allows for both TOF measurements and “tagging” incident neutrons that are traveling in the desired direction [9,10,11].

Neutron detectors

Fast neutron detectors are based on either neutron moderation, fast neutron interactions, or elastic recoil reactions [2]. Detectors using neutron moderation contain a low energy neutron detector inside a moderating material, but are relatively slow and provide limited information on incident neutron energy. Other fast neutron detectors are based on the reactions ^{6}Li(n,α) and ^{3}He(n,p). However, these detectors have relatively low detection efficiency and problems arise due to competing reaction above a couple MeV. The most common fast neutron detectors are hydrogen-rich scintillators that are based on elastic recoil interactions inside the detector active volume. Plastic and liquid scintillators are relatively inexpensive, easily formed into a wide variety of shapes and sizes, and have fast response times. Liquid scintillators may also use pulse shape discrimination to isolate neutron and photon counts [12].

Photon detectors

The most common detectors used in gamma-ray spectroscopy are inorganic scintillators, such as thallium-doped sodium iodide (NaI(Tl)) and bismuth germanate (BGO). Scintillators are relatively inexpensive and can have relatively detection efficiencies. Semiconductor detectors, such as high-purity germanium (HPGe), have much better energy resolution, but must be cooled while in operation and are much more expensive. Recent advancements in room temperature semiconductor detectors, such as cadmium zinc telluride (CdZnTe) and mercuric iodide (HgI_2), have demonstrated excellent energy resolution, but may still be prohibitively expensive in terms of widespread deployment in cargo screening scenarios [12].

Implementation of flag-based detection algorithm

Previous simulations showed that flag values are strongly dependent on the identity of cargo material. Furthermore, a significant number of cargo manifests show human error and containers may have multiple cargo types [1]. One way to compensate for unknown or mistaken cargo is to maintain a database of certain flag values and use template-matching techniques to determine the material type before applying appropriate explosives-detection flags. An alternative strategy would be irradiating at several locations and looking for changes in certain explosives-sensitive flags as a function of container length. This second technique has the advantage of relative independence of cargo manifest accuracy or cargo type. Furthermore, multiple measurements are necessary for both strategies, as the 3.1 m container center-to-end distance is too far to be adequately penetrated by 14.1 MeV neutrons.

In the presented system, the flag values at five irradiation points, as well as the average flag values for the entire container, are used in a decision tree-type algorithm to determine if explosives are present. For the first step of the algorithm, average values of material-sensitive flags determine the type of cargo present. Explosives-sensitive flags for this type of cargo then determine if explosives are present by looking for deviations from average flag value at individual locations along the container length. An additional step would compare the average flag values with pure-explosives templates in case a container is filled with explosives. Finally, other steps would be included that minimize false positives, such as might result from inhomogeneities in the cargo distribution. This chapter is devoted to elucidating the structure and flag identities in the detection algorithm, as well as the associated equipment configuration.

Materials and Methods

Monte Carlo simulations

All simulations used either MCNP5 [13] or MCNP-PoliMi [14]. The simulated neutron detector responses were calculated using PoliMi and a post-processor [15]. All output text files were analyzed with a custom parser (MATLAB, 3 Apple Hill Drive, Natick, MA, USA 01760), as well as spreadsheet software (Excel, Microsoft, 1 Microsoft Way, Redmond, WA, USA 98052). Similarly, custom software was used to calculate the relevant flag values, flag strengths, and statistical uncertainty in flag calculations.

Scanning geometry

The simulations discussed here were based on the geometry shown in Fig. 7-1, with materials defined in Table 7-1. These simulations contained a sea-land cargo container with 2.4 m × 6.2 m × 2.6 m exterior dimensions and 0.346 m thick steel walls centered in a 20 m diameter sphere that defined the outer limits. The container was surrounded by air and rested on a 25 cm concrete slab over soil that filled the space between the slab and the 20 m sphere. A rectangular hole 130 cm wide × 243 cm long × 210 cm deep in the slab and soil contained the shielded neutron source, with additional space provided for the 120° and 150° detectors. For the five irradiations, the container was shifted such that the source faced the container at locations of 62 cm, 186 cm, 310 cm, 434 cm, and 558 cm from container end. An example MCNP-PoliMi input file for this geometry is shown in Appendix A.

Neutron and photon detection

Eleven cylindrical liquid scintillator detectors were distributed in 30° intervals at a distance of 2.25 m from the center of the container. Each had a radius of 40 cm and a thickness of 20 cm. The liquid scintillator EJ-309, as detailed in Table 7-1, was chosen because of its superior pulse shape discrimination capabilities [16]. Current, or MCNP5 F1, tallies sorted photons and neutrons into 0.2 MeV energy bins and symmetrical, i.e. same scatter angle, detectors were combined into the same tally. Due to isotropic emission, all photon tallies were combined into one tally. Neutron detector response functions were calculated in each detector using MCNP-PoliMi and the postprocessor.

Neutron source

Previous studies [4,6,7] relied on a shielded conical 14.1 MeV neutron source. However, simulations of the five-scan screening technique required a fan-shaped beam with limited overlap in irradiated volume. This beam had an isotropic D-T neutron source placed at the bottom of the rectangular well behind at least 50 cm of shielding, as illustrated in Figs. 7-1 and 7-2. The shield's composition was equivalent to an equal volume mixture of polyethylene and steel. The opening of the shield projected a 70 cm × 244 cm area on the facing container surface, which permitted full container width irradiation and 10% length-wise overlap between the five measurements.

Container cargo

The development of the detection algorithm required several types and distributions of cargo inside the cargo container. For the single-irradiation simulations that identified the material-sensitive flags, the inert materials were distributed evenly throughout the container volume, with density correspondingly adjusted to model typical cargo mass, with densities of 0.2 to 0.6 g cm^{-3} [1]. Similarly, cargo was homogeneously distributed in the five-scan simulation that found appropriate triggering thresholds in the detection algorithm. Cargos simulated included cloth, electronics, furniture, paper, steel, vegetables, and wheat, as defined in Table 7-1. An additional set of simulations was completed for use in the final step of the algorithm that used 500 kg spheres of artificially dense inert material inside homogenously distributed cargos of the same material.

Cargo container on a trailer bed

One potential difficulty in implementation of the algorithm is that the simulated conveyance of a moving surface or rail system may be impractical in a seaport environment. An alternative geometry was simulated in which the container was carried on a flatbed trailer with a 10 cm thick aluminum deck, six sets of two vulcanized rubber tires, and three steel axles, as shown in Fig. 7-3. An example of MCNP-PoliMi input for this geometry is shown in Appendix A.

Determination of the explosives-detection algorithm

As discussed above, the explosives-detection algorithm consists of several steps and results in a yes/no answer about the presence of explosives. These steps first determine the type of cargo material, as organic or hydrogenous cargos use different flags than inorganic or metallic cargos. The second step involves identifying the containers that might be filled with very large amounts of explosive. The next step involves applying flags appropriate to the given cargo type to find hidden explosives. Finally, containers with possible hidden explosives undergo a final step that minimizes false positives due to cargo heterogeneities. These steps require the calculation of three different types of flags, all of which are based on measurements of the exiting neutron and photon flux. These include material-sensitive, explosives-detection, and density-discriminatory flags. Due to the fact that many of the flags isolated earlier [6,7] require stringent neutron spectroscopy, two alternative detection algorithms were explored, one which uses the best-performing flags and one that uses the best flags that are currently technically feasible. The specific calculations in the algorithm were completed using a common mathematics and data analysis package (MATLAB).

Specification of cargo material

The identification of the material-sensitive flags was accomplished by examination of the results from simulations utilizing homogenous cargo distributions of the materials listed in Table 7-1. The chosen flags displayed the most consistent values, i.e. the smallest percent standard deviation, within a particular cargo type and the largest difference in average flag value compared to the other cargo type. Only two categories, organic/hydrogenous and inorganic/metallic, were examined, as finding explosives in low-Z, explosive-similar organic/hydrogenous materials uses different flags than the higher-Z inorganic/metallic materials. The material-sensitive flags were then organized into a material sub-algorithm by finding threshold flag values that successfully categorized cargo materials, with each step further narrowing down the identity of the unknown cargo. This was accomplished through an iterative trial and error process.

Identification of explosives-filled containers

It is also possible that the entire container could be packed with explosives. Therefore a step was included that identifies this type of threat through comparison with templates of certain flag values. Templates may consist of either absolute flag values, or the ratios of certain flags. A preliminary database of these templates was created using simulations of containers homogeneously filled with the eleven explosive materials listed in Table 7-2.

Triggering in the presence of hidden explosives

The next step in the algorithm involved the actual triggering in the presence of hidden explosives using the previously identified explosives-detection flags [7], and the results of the five-scan simulations. The flag values as a function of scanning position for cases without explosives were examined to determine appropriate triggering thresholds based on the highest flag values expected when explosives are not present.

Minimization of false positives due to cargo heterogeneity

The final step of the explosives-detection algorithm involved minimizing false positives due to heterogeneities in inert cargo distribution. To identify the density-discriminatory flags for this step, the results from simulations containing artificially dense objects was compared with those from equivalent simulations containing RDX. A comparison of the flag strengths for the two cases quantified the dependence of flag response on the density of hidden objects. Flags were identified that triggered only in the presence of explosives as well as those that triggered only in the presence of inert, dense objects.

Estimates of dose to personnel and cargo activation

An important concern is the expected radiation dose to both operators and people hidden inside a container during screening [17]. Dose was calculated using MCNP-PoliMi for the worst-case scenario in which an empty container went through all five scans of the explosives-detection system. Dose was estimated by multiplying the tallied neutron and photon fluence (MCNP F5) at a point by dose conversion factors found in ICRP Publication 574 [18] and ICRU report 47 [19]. A sufficient number of histories were calculated to keep statistical uncertainty below 2%.

Dose was calculated at seventeen separate points in and around the container. Outside the container, six calculations were made in one-meter increments from 2 m to 7 m from the container center normal to the long side. Other dose calculations were made centered inside the container above the scan 1, scan 2, and scan 3 positions at a height of 9 cm, 62 cm, and 128 cm from the container floor. Finally, two additional calculations were performed 128 cm from the floor above the scan 3 position, but were displaced laterally 60 cm and 120 cm from the center of the container.

Also considered was the residual activity when neutrons activate cargo materials. The interactions with the highest potential of significantly activating cargo appear in Table 7-3 [20,21]. Two worst-case scenarios were considered, one in which the entire cargo was aluminum, and another with a cargo of rock salt (NaCl). Another calculation utilized a cargo of potatoes, with the thought that any activation is more of a concern if the cargo is meant for human consumption. Calculations were carried out using activation software [22] based on standard decay [23] and cross section [24,25] data.

Results and Discussion

Detection algorithm

A diagram of the algorithm structure is shown in Fig. 7-4. Because many of the best flags required stringent neutron spectroscopy [6,7], two variations in the algorithm are presented. Although very similar in structure, the spectroscopic variation uses all of the best-performing flags [6,7], while the PHD algorithm is limited to the best-performing flags that do not require unfolding of the neutron pulse height distribution [7]. Sample MATLAB code for the detection algorithm is found in Appendix B.

Identification of explosives-filled containers

The first step in the algorithm was the identification of any cargo containers that are entirely filled with explosive through comparison with a stored template. Because flag values are highly dependent on the exact cargo composition and configuration, relative flag values, normalized to a single flag, were used instead of absolute flag values. A set of preliminary templates for several explosives: RDX, trinitrotoluene (TNT), fertilizer, and ethylene glycol dinitrate (EGDN), are shown in Table 7-4. However, as both the final templates and level of precision in template application will be highly dependent on the specific equipment, exact explosive, and cargo distribution they are beyond the scope of this study.

Materials determination

Five flags were identified for both algorithm variations that showed both the most consistent flag values within one cargo type, and the largest difference between the two types of cargo, and are shown in the first two columns of Table 7-5. It was found that better material categorization was accomplished using threshold values of certain ratios and sums of these five flags, with threshold values listed in column three of Table 7-5. Furthermore, step four of the material sub-algorithm, shown in Fig. 7-4, was not needed in the PHD algorithm. Testing of the materials algorithm showed correct sorting into organic/hydrogenous or inorganic/metallic categories for all of the homogenously distributed, single-material cargos studied here. As expected, there was more ambiguity in the case of heterogeneously distributed or mixed cargo, such as furniture.

Triggering in the presence of hidden explosives

For the cases in which smaller explosives are hidden in larger inert cargo masses, the algorithm depends on finding specific changes in certain flags, listed in Tables 7-6a and 7-6b, as a function of irradiation position [6,7]. The triggering technique identified here first required calculation of the height (h) of each flag at all positions (p). This is defined as:

$$h_{p=i} = \frac{f_{p=i} - \frac{\sum_{p\neq i} f_p}{4}}{\sum_p f_p} \qquad (7.1)$$

in which $f_{p=i}$ is the flag value at position i. The peak height for the flag (h_f) is then defined as the maximum h_p value for that particular flag. This calculation of the peak height can be thought of as the maximum percent difference between a flag value at one position and the average flag value at the other four positions. To compare the peak heights of different flags, the h_p values are shifted such that the minimum value is at zero. This is illustrated in Fig. 7-5 for the case of a large explosive hidden at position four, which creates a systematic increase in flag height of several of the flags from Table 7-6b at that position. Finally, the trigger value (h_t), defined as the maximum peak height over all the flags, is compared with a threshold value to determine if explosives are present. Examination of the cases without explosive showed that their trigger values exceeded 0.1 in only one case, so a trigger value of 0.1 was chosen as the threshold value. However, about 40% of inert materials exhibited an unusually high trigger value at an edge position, illustrated in Fig. 7-6. Therefore, a threshold value of 0.2 was used at edge positions. In some simulations without explosive there was a small asymmetry between the relative flag height at positions 1 and 5, probably due to a slight geometrical bias towards scanning position 1 generated from rounding errors when determining scanning positions.

Minimization of false positives due to cargo heterogeneity

The flags used in minimizing false positives due to cargo heterogeneity are listed in Table 7-7. To eliminate the false positives, trigger values were calculated for these two types of flags in the same manner as discussed above. If the trigger value of the density-only flags was greater, the possible explosive was dismissed as an inert object. It should be noted that the flags in this step have trigger values of less than 0.1, so it would not be useful to include these explosives-only-triggering flags in the previous stage of the detection algorithm.

Implementation of the explosives-detection algorithm

Neutron source

Implementation of the explosives-detection algorithm requires a fan-shaped beam produced by a D-T neutron generator, which have typical production rates of 5×10^8 to 2×10^{10} n s^{-1}. This fan beam will irradiate the standard 6.2 m-long cargo container a total of five times at distances of 0.62, 1.9, 3.1, 4.3, and 5.6 m from the end of the container. The generator shield has 50 cm thick walls of polyethylene and steel that produces a beam 2.6 m by 0.62 m at the surface of the container closest to the source, as shown in Figs. 7-1 and 7-2. Calculations based on statistical uncertainty in the simulation [4] and detection efficiency showed that 9×10^{10} incident neutrons per scan were sufficient to produce statistical uncertainties of less than 2% in all flag calculations.

Supporting infrastructure

Transport through the scanning apparatus is accomplished through use of a conveyor that carries the container over the neutron source under a roughly circular scaffold that holds the detectors equidistant from the container center. This scaffold should hold the detectors as close as reasonably possible to the container in order to maximize detection efficiency, so a distance of 2.5 m from container center, or at least 0.58 m from container edge, was chosen. The conveyor system may be either ground-based, such as series of rollers, or crane-based, suspending the containers from above.

One alternative to a conveyor-based system is to drive the container through the scanner on a flatbed truck. Simulations of the truck-based conveyance shown in Fig. 7-3 found that the presence of the wheels and axles significantly impacted the triggering flags such that trigger values for all cases were very high in the fifth scanning position, where two sets of axles and wheels were present, as illustrated in Fig. 7-7. This shows that the conveyance method should have the same distribution of support material along the length of the container. Therefore, future versions of the system could use a wheeled conveyance, as long as the wheels are evenly distributed or correction factors are used.

Photon detection

To maximize detection efficiency, several large photon detectors should be placed on the scaffold, either far enough from the source to minimize interference from the source, or collimated such that only photons originating in the container are detected. As the algorithm only requires 0.2 MeV energy resolution, an inorganic scintillator, such as NaI(Tl) or BGO, is sufficient. The photon detectors must be reasonably thick to maintain a high photon detection rate. NaI(Tl) crystals have good light output, sufficient energy resolution, and over 75% intrinsic efficiency when 10 cm thick [12]. Large NaI(Tl) crystals, such as those tested for use in portal monitors [26] have cross-sectional areas of 410 cm^2 (10 cm $\times$ 41 cm) and a 10 cm thickness. An array of 12 of these detectors would count approximately 8×10^8 photons in the two minute period, which would yield statistical uncertainties of around 3%.

Neutron detection

Currently available neutron spectroscopy technology makes implementation of the spectroscopic difficult at this time. However, the PHD algorithm was designed such that all neutron-based flags could be calculated using the response functions of EJ-309 liquid scintillators. The presented system includes eleven large EJ-309 neutron detectors distributed along the scaffold in 30° increments. These large neutron detectors have a 40 cm diameter and are 20 cm thick.

Measurement time, throughput and the total number of neutrons

Simulations of the presented system utilized 5×10^9 particle histories and yielded flag value statistical uncertainties of less than 3% for all but a few of the neutron flags in the spectroscopic algorithm, which were 5 to 8%. When the ~20% intrinsic efficiency of the neutron detectors, ~40% intrinsic efficiency [26] and decreased cross-sectional area of the photon detectors are considered, a total of 9×10^{10} incident neutrons are needed per scan to maintain the statistical uncertainty levels. This leads to a measurement time of a few seconds to a maximum of 2 minutes per scan, with a more typical measurement time of 1 minute, depending on the operating intensity of the neutron source. When the five irradiations, as well as physical positioning and transit are considered, total scanning time is approximately 10 minutes per container. This rate of only six containers per hour means that the system should either function as a secondary screening system, or several systems will be required at a given seaport. Measurement time could decrease to 5 to 6 minutes given the most powerful neutron generator.

Estimated cost

The production costs of the proposed system are reasonable, with the largest single expense the D-T neutron generator at around $300,000. The eleven neutron detectors, associated digitization, power hardware and computer should cost between $190,000 and $200,000. The NaI(Tl) photon detection system will cost another $70,000 to $100,000 [27]. Other costs will include shielding materials and the physical infrastructure of the detector structure and conveyance system for the containers. In all, the equipment needed for the system will be approximately $1M. Once the system is operational costs should be minimal, as the algorithm will be automated and operators will need little training.

Estimated dose

The estimated doses for ten locations in and around the container during a single five-scan application with 9×10^{10} neutrons per scan are shown in Table 7-8. As expected, the highest dose rates were near the container floor. However, the calculations show that an individual hidden in the container during a five-scan screening would receive between 0.15 mSv and 0.41 mSv. This is less than the 6.2 mSv average annual dose to a member of the public and similar to that received in a chest x-ray [28]. An operator, assuming six scans per hour and 2,000 hours worked per year, would be exposed to the radiation of approximately 12,000 scans. Without any added shielding an operator standing 5 m from the center of the container would receive a dose of approximately 39 mSv per year, which exceeds the occupational dose limit of 20 mSv per year. This dose is lowered significantly with the addition of 1 m of concrete shielding to 0.86 mSv, which is less than the average annual dose to a member of the public.

It was calculated [22] that the total activity in 21,600 kg cargo was 2.4 MBq for the rock salt and 160 MBq in the aluminum. This level of radioactivity is insufficient to cause significant dose in personnel. Furthermore, much of this activity is due to nuclides (^{38}Cl, ^{28}Al) with half-lives on the order of minutes. Fortunately, most of these nuclides are only present in small or trace amounts in edible cargos. A calculation for 21,600 kg of potatoes yielded a total induced activity of approximately 2.1 kBq, with the majority of the activity from radionuclides such as ^{19}O, ^{49}Ca, and ^{42}K, with half-lives of 27 s, 8.7 min, and 12 h, respectively. This shows that neutron activation of cargo in the proposed system is of trivial concern.

Future work

Future efforts will determine the capabilities of the explosives-detection system in cases with heterogeneous cargo distributions as well as determine the minimum detectable amount of explosive. Also of concern is the possible decreased detection probability when explosives are placed between scanning positions and the effect of measurement error, scatter in the environment, and photon detection concerns such as escape peaks. Furthermore, a more thorough statistical analysis of the relationship between flags and algorithm performance, as well as increased optimization of the trigger threshold values should improve the detection algorithm.

There are several possible improvements to the scanning system that should be explored in future work. It is possible that using photon detectors with higher energy resolution, such as CdZnTe, would improve algorithm performance enough that the added cost is worthwhile. Another possibility would be to scan multiple locations at the same time. While this may reduce scanning time by 2 to 5 minutes per container, it is very expensive and there may be significant interference. Another alternative is to use an associated particle imaging (API) system and capture-gated neutron detectors or a pulsed neutron generator and TOF calculations instead of neutron energy calculations [19]. However, the very large target and corresponding event position uncertainty greatly complicate these calculations and significantly increase measurement time.

Conclusions

An active neutron interrogation-based explosives-detection system has been presented that uses measurements at five different locations to determine the presence and approximate location of hidden explosives in cargo containers. The detection algorithm relies on both neutron and photon output from neutron elastic and inelastic scatter reactions by calculating flags formed from specific ratios of these measurements. These flags form the backbone of an algorithm that includes steps for cargo identification, identification of concealed explosives, and the minimization of false positives due to cargo heterogeneity. An additional step identifies containers filled with explosives. Implementation of the detection algorithm requires eleven liquid scintillator neutron detectors with pulse shape discrimination capabilities as well as several inorganic scintillators for photon spectroscopy. Dose estimates are well within acceptable levels for both system operators and concealed persons within a container. Materials for the proposed system should cost approximately $1M, and will be able to screen containers at a rate of at least six per hour.

Figures

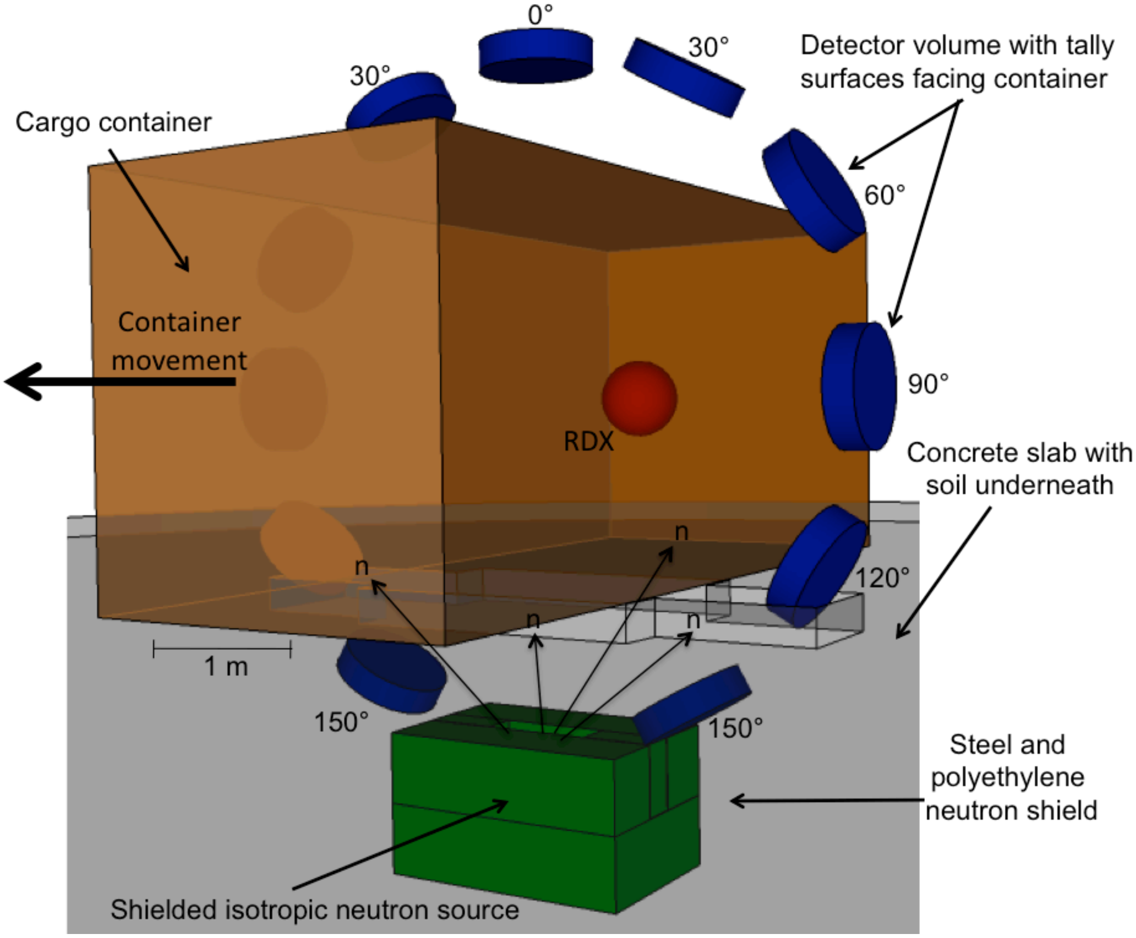

Figure 7-1. Illustration of container scanning geometry with empty container, except for explosive, located within ring of eleven detectors and over a shielded D-T neutron source. Irradiations take place at five locations along container as it moves through the detector array.

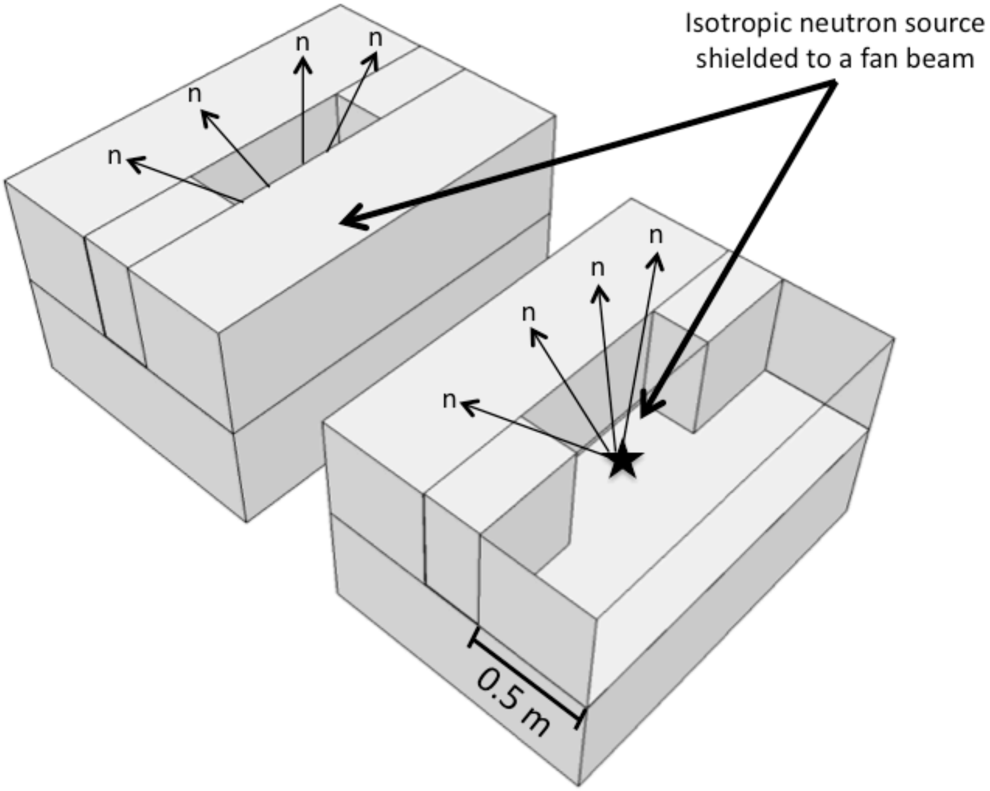

Figure 7-2. Detail of source shield of isotropic neutron source.

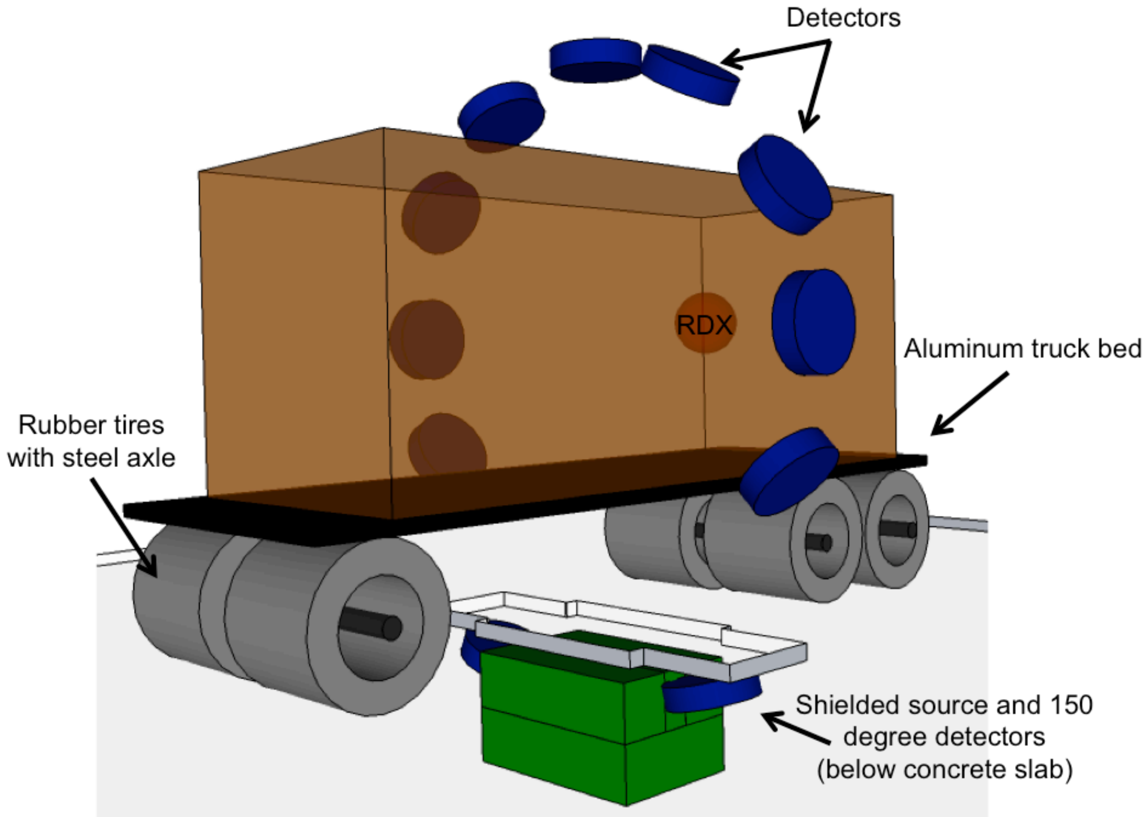

Figure 7-3. Alternative geometry with vehicular transport of container through the scanning apparatus.

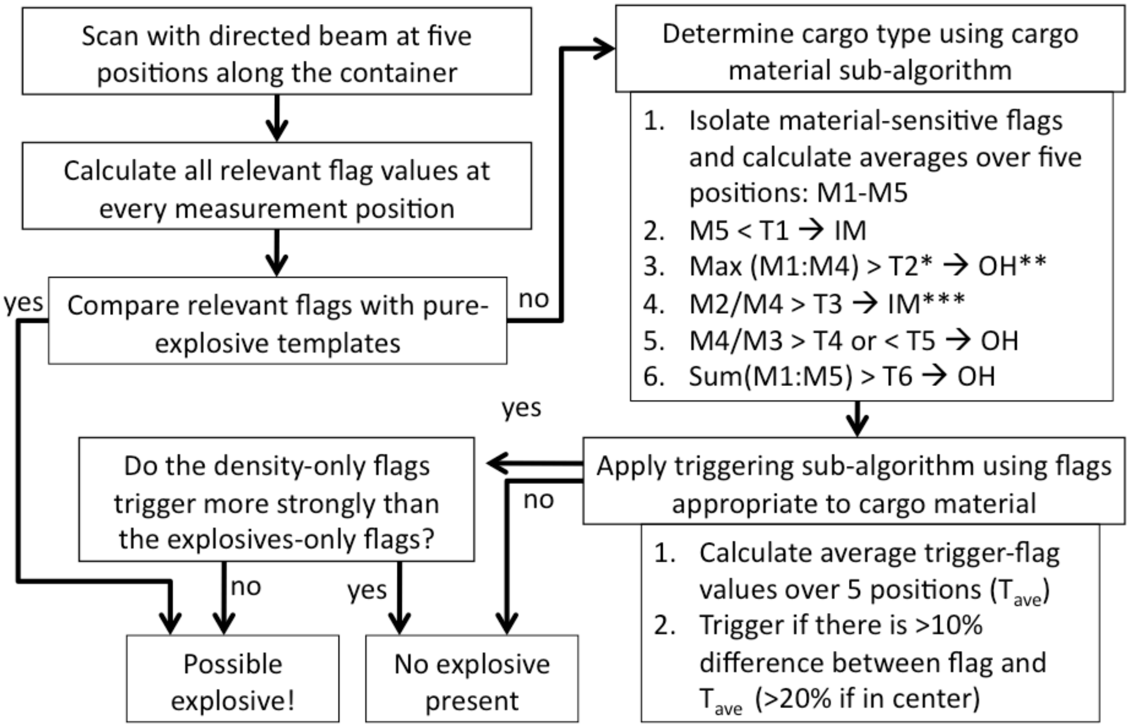

*T1-T5 thresholds: differ for spectroscopic/PHD

**Organic/Hydrogenous

***Inorganic/Metallic

Figure 7-4. Flow chart of explosives-detection algorithm.

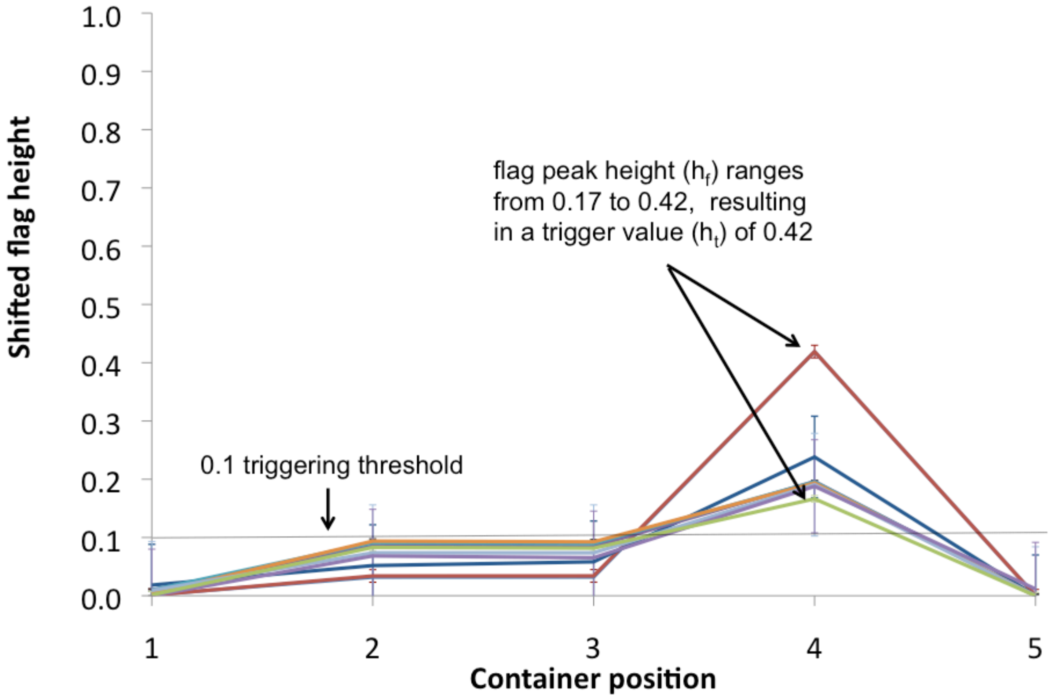

Figure 7-5. Example of change in explosives trigger flags as a function of container position for 300 kg of RDX at position 4 in a furniture-filled cargo container. Each line shows the response of one of the ten PHD explosives-detection flags in Table 7-6b.

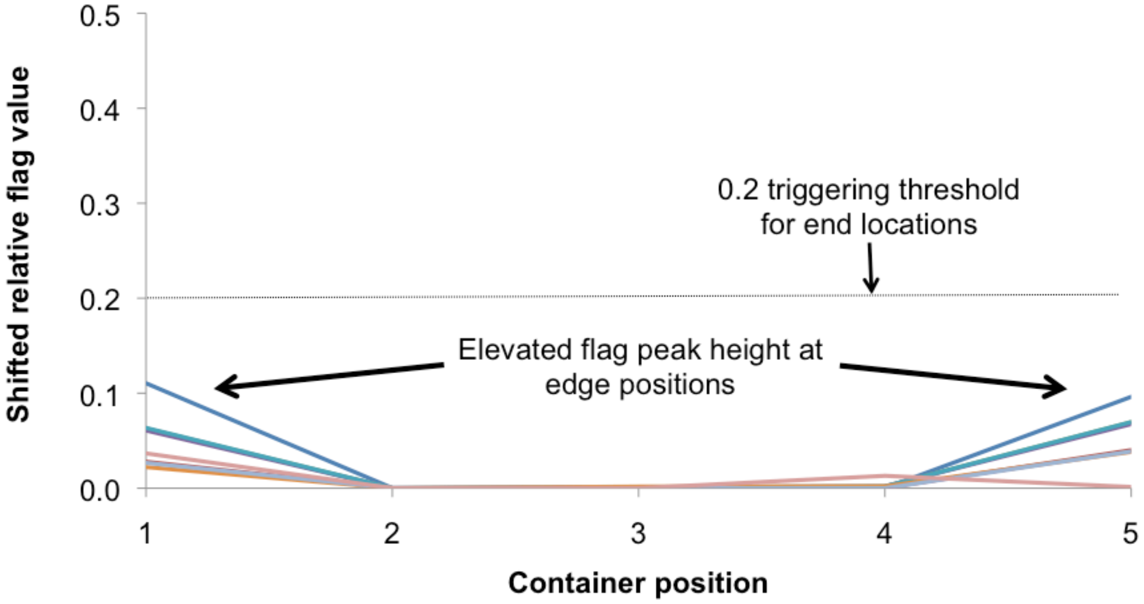

Figure 7-6. Example of the systematic bias in many cargo materials at the edge positions that mandates a 0.2 trigger threshold for these positions. In this example the container is homogenously filled with vegetable oil.

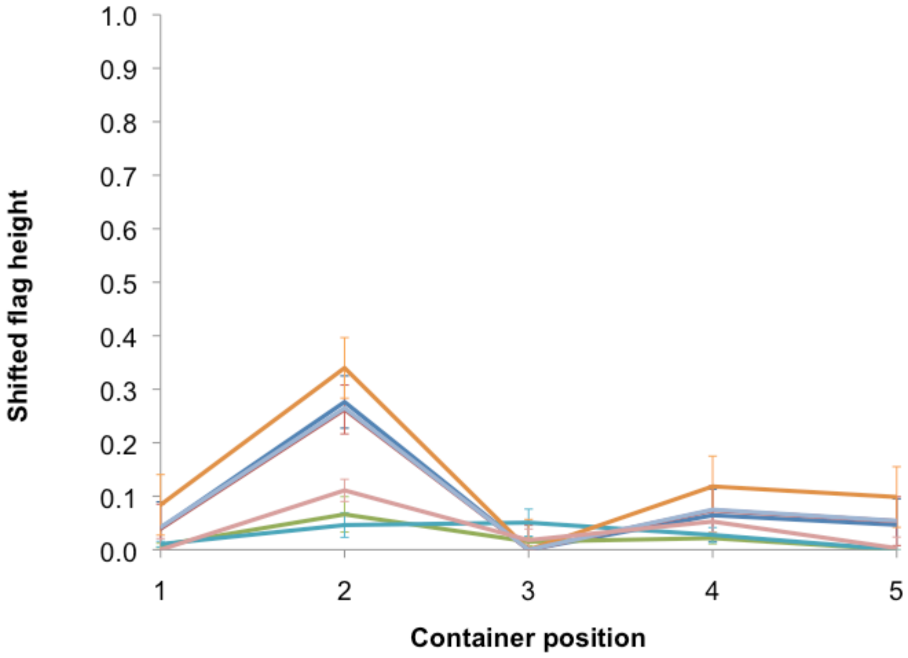

a.

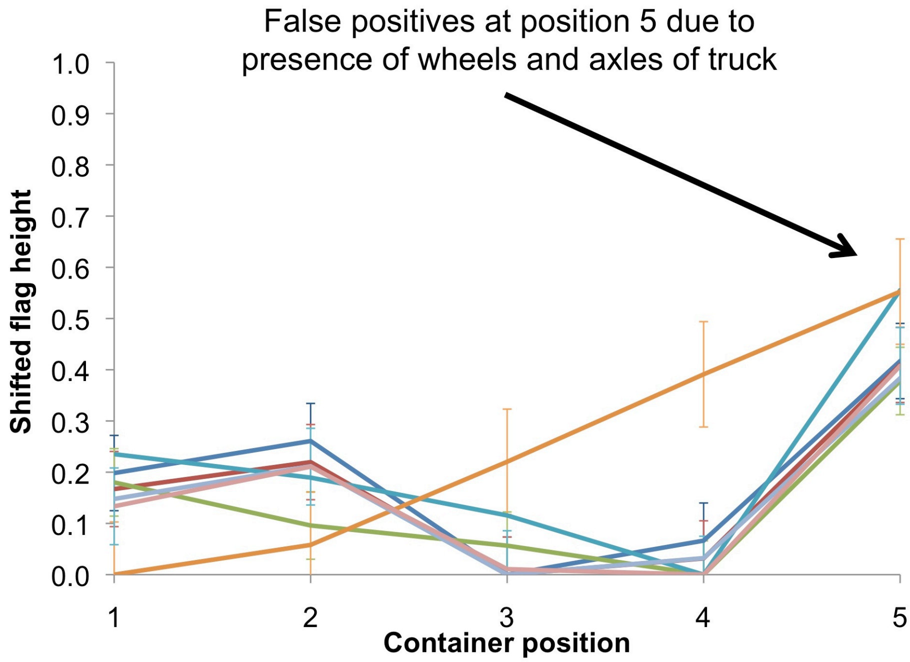

b.

Figure 7-7. Comparison of flag heights for a) conveyor-based and b) truck-based transport through scanning apparatus.

Tables

Table 7-1. Densities and compositions, expressed as atom percents, of inert materials used in MCNP simulation geometry, as adapted from [4,6,7].

Material	Density	H	C	N	O	Other
Air	0.0012		0.01%	75.5%	23.2%	1.3% Ar
Brick					66%	0.4.% Al, 32% Si, 1% Ca
EJ-309	0.916	55%	45%			
Concrete	2.3	30.4%	0.29%		49.9%	0.92% Na, 1.03% Al, 15.1% Si, 0.71% K, 1.49% Ca, 0.16% Fe
Cotton	1.1	48%	29%		24%	
Crude Oil	0.97	62%	37%			0.5% S
Electronics	0.329	26%	2%		47%	2.6% Al, 12% Si, 10% Ni, 0.3% Fe
Furniture	0.8	41%	32%		21%	3% Fe, 3% Al
Granite	2.73	0%	0%		62%	2.6% Na, 1.9%Mg, 6.5% AL, 21% Si, 1.4% K, 2% Ca, 2% Fe
Meat	1.1	60%	15%	1%	24%	trace K, P
Melamine	1.57	40%	20%			40% Si
Vegetable oil	0.918	63%	34%		4%	
Paraffin	0.93	68%	32%			
Plaster	0.85	7%			63%	15% Ca, 15% S
Plate Glass	2.4				60%	8.8% Na, 25% Si, 5.6% Ca
Polyester	1.4	36%	45%		18%	
Polyethylene	0.93	67%	33%			
Polystyrene	1.06	50%	50%			
Polyvinyl chloride	1.406	50%	33%			17% Cl
Rock Salt	2.18					50% Na, 50% Cl
Rubber	1.1	50%	31%			19% S
Sand	1.6			trace	65.5%	29.3% Si, 3.8% Al, 1.21% Ca
Steel	7.87		0.32%			99.6% Fe, 0.05% S, 0.04% P
Soil	1.75	29.4%	1.87%		50.5%	2.59% Al, 13.54% Si, 1.43% K, 0.27% Fe
Water	1	67%			33%	
Wheat	0.79	7%	37%	2%	53%	trace: S, Na, K, Ca, Mg, Fe, Cu, Zn, P, Cl
Wood/paper	0.6/0.3	48%	29%		24%	
Vegetables (potatoes)	1.6	63%	6%		31%	trace Ca, Fe, Mg, P, K, Na, S, Cl

Table 7-2. Explosive materials used to create explosive cargo templates, as adapted from [7].

Material	Density	H	C	N	O	Other
Acetone Peroxide	1.22	55%	27%		18%	
Ammonium Nitrate	1.73	44%		22%	33%	
Black Powder	1.04	51%	7%	7%	23%	7.6% K, 3% Si
EGDN	1.49	29%	14%	14%	43%	
Fertilizer	0.99	0%			0%	1% Na, 50% Cl, 48% K, trace Mg, Ca, Br
HMX	1.9	29%	14%	29%	29%	
Nitrocellulose	1.66	29%	25%	13%	33%	
Nitroglycerin	1.13	25%	15%	15%	45%	
PETN	1.77	29%	17%	14%	41%	
RDX	1.82	29%	14%	29%	29%	
TNT	1.65	24%	33%	14%	29%	

Table 7-3. Important reactions induced activity from neutron activation of cargo materials, as adapted from [19]. Activity based on incident thermal flux of 10^{13} n $cm^{-2}s^{-1}$ and epithermal flux of 10^{11} n $cm^{-2}s^{-1}$ [18].

Isotope	Reaction	Product	Half life	Photons [MeV]	Activity after 1 min irradiation [Bq μg^{-1}]
^{23}Na	(n,γ)	^{24}Na	15.0 h	1.37, 2.75	108
^{26}Mg	(n,γ)	^{27}Mg	9.46 m	0.84, 1.01	74.7
^{27}Al	(n,γ)	^{28}Al	2.24 m	1.78, 336	14,000
^{37}Cl	(n,γ)	^{28}Cl	37.2 m	2.17, 1.64	332
^{59}Co	(n,γ)	^{60}Co	1930 d	1.33, 1.17	0.472
^{63}Cu	(n,γ)	^{64}Cu	12.7 h	0.51, 262	274
^{116}Sn	(n,γ)	^{117m}Sn	13.6 d	0.16	0.0039

Table 7-4. Example of preliminary templates for several explosive-only cargos. Templates are based on the PHD detection algorithm.

Flag	RDX	TNT	Fertilizer	EGDN
$\frac{(>4.9\text{ MeVee},150^\circ)}{(<0.14\text{ MeVee},0^\circ)}$	1.00	1.00	1.00	1.00
$\frac{(2.1-4.9\text{ MeVee},150^\circ)}{(2.1-4.9\text{ MeVee},0^\circ)}$	1.16	1.10	1.47	1.10
$\frac{(>4.9\text{ MeVee},120^\circ)}{(>4.9\text{ MeVee},0^\circ)}$	0.66	0.61	0.45	0.64
$\frac{(>4.9\text{ MeVee},150^\circ)}{(>4.9\text{ MeVee},0^\circ)}$	1.27	1.19	0.94	1.25
$\frac{(>5.8\text{ MeVee},150^\circ)}{(>4.9\text{ MeVee},0^\circ)}$	0.73	0.69	0.57	0.72
$\frac{(>5.8\text{ MeVee},120^\circ)}{(>5.8\text{ MeVee},0^\circ)}$	0.67	0.65	0.42	0.65
$\frac{(>5.8\text{ MeVee},150^\circ)}{(>5.8\text{ MeVee},0^\circ)}$	1.26	1.25	0.85	1.23
$\frac{\left[\frac{(\text{total neutron},90^\circ)}{(\text{total neutron},0^\circ)}\right]}{(\text{C photon})}$	3.39×10^3	2.46×10^3	5.93×10^3	3.31×10^3
$\frac{\left[\frac{(\text{total neutron},150^\circ)}{(\text{total neutron},0^\circ)}\right]}{(\text{C photon})}$	1.13×10^4	8.36×10^3	1.09×10^4	1.10×10^4
$\frac{\left[\frac{(\text{total neutron},150^\circ)}{(\text{total neutron},0^\circ)}\right]}{(\text{N photon})}$	2.99×10^3	2.89×10^3	2.51×10^3	2.91×10^3
$\frac{\left[\frac{(\text{total neutron},150^\circ)}{(\text{total neutron},0^\circ)}\right]}{(\text{O photon})}$	2.16×10^4	2.70×10^4	6.05×10^4	2.12×10^4

Table 7-5. Identities of the top flags used in determining the type of cargo in an unknown container and the thresholds used in the material categorization.

Flag number	Flag identity (averaged over 5 scans)	Threshold
	Spectroscopic detection algorithm	
M1	$\frac{(>10\text{ MeV},150^\circ)}{(>10\text{ MeV},0^\circ)}$	T1 = 5
M2	$\frac{(6-10\text{ MeV},150^\circ)}{(6-10\text{ MeV},0^\circ)}$	T2 = 30
M3	$\frac{(>10\text{ MeV},120^\circ)}{(>10\text{ MeV},0^\circ)}$	T3 = 1.5
M4	$\frac{(11.4\text{ MeV},120^\circ)}{(11.4\text{ MeV},0^\circ)}$	T4 = 4.5 T5 = 1.4
M5	$\frac{(11\text{ MeV},150^\circ)}{(0.8\text{ MeV},0^\circ)}$	T6 = 50
	PHD detection algorithm	
M1	$\frac{(>4.9\text{ MeVee},150^\circ)}{(>4.9\text{ MeVee},0^\circ)}$	T1 = 7
M2	$\frac{(2.1-4.9\text{ MeVee},150^\circ)}{(2.1-4.9\text{ MeVee},0^\circ)}$	T2 = 45
M3	$\frac{(>4.9\text{ MeVee},120^\circ)}{(>4.9\text{ MeVee},0^\circ)}$	T3 = 3
M4	$\frac{(>5.8\text{ MeVee},120^\circ)}{(>5.8\text{ MeVee},0^\circ)}$	T4, T5 not needed
M5	$\frac{(>5.8\text{ MeVee},150^\circ)}{(<0.14\text{ MeVee},0^\circ)}$	T6 = 40

Table 7-6a. Identities of the top flags used in determining if explosives are present in an unknown container.

Spectroscopic algorithm	
Organic or hydrogenous cargo flags	
$\frac{(11\text{ MeV},150^\circ)}{(11\text{ MeV},0^\circ)}$	$\frac{\left[\frac{(\text{total neutron},150^\circ)}{(\text{total neutron},0^\circ)}\right]}{\text{C photon}}$
$\frac{(11\text{ MeV},150^\circ)}{(10\text{ MeV},0^\circ)}$	$\frac{\left[\frac{(\text{total neutron},90^\circ)}{(\text{total neutron},0^\circ)}\right]}{\text{C photon}}$
$\frac{(11\text{ MeV},150^\circ)}{(9.6\text{ MeV},0^\circ)}$	$\frac{\left[\frac{(\text{total neutron},150^\circ)}{(\text{total neutron},0^\circ)}\right]}{\text{O photon}}$
$\frac{(>10\text{ MeV},120^\circ)}{(>10\text{ MeV},0^\circ)}$	$\frac{(>10\text{ MeV},180^\circ)}{(>10\text{ MeV},0^\circ)}$
$\frac{(>10\text{ MeV},150^\circ)}{(>10\text{ MeV},0^\circ)}$	$\frac{(6-10\text{ MeV},150^\circ)}{(6\text{-}10\text{ MeV},0^\circ)}$
Metallic or inorganic cargo flags	
$\frac{(10.8\text{ MeV},150^\circ)}{(10.8\text{ MeV},0^\circ)}$	$\frac{\left[\frac{(\text{total neutron},150^\circ)}{(\text{total neutron},0^\circ)}\right]}{\text{C photon}}$
$\frac{(11.2\text{ MeV},150^\circ)}{(11.2\text{ MeV},0^\circ)}$	$\frac{\left[\frac{(\text{total neutron},150^\circ)}{(\text{total neutron},0^\circ)}\right]}{\text{N photon}}$
$\frac{(11.6\text{ MeV},120^\circ)}{(11.6\text{ MeV},0^\circ)}$	$\frac{\left[\frac{(\text{total neutron},150^\circ)}{(\text{total neutron},0^\circ)}\right]}{\text{O photon}}$
$\frac{(>10\text{ MeV},120^\circ)}{(>10\text{ MeV},0^\circ)}$	$\frac{(11\text{ MeV},150^\circ)}{(10\text{ MeV},0^\circ)}$
$\frac{(>10\text{ MeV},150^\circ)}{(>10\text{ MeV},0^\circ)}$	$\frac{(>10\text{ MeV},150^\circ)}{(<1\text{ MeV},0^\circ)}$

Table 7-6b. Identities of the top flags used in determining if explosives are present in an unknown container.

PHD algorithm	
Organic or hydrogenous cargo flags	
$\frac{(>5.8\ \text{MeVee},150^\circ)}{(>5.8\ \text{MeVee},0^\circ)}$	$\frac{\left[\frac{(\text{total neutron},150^\circ)}{(\text{total neutron},0^\circ)}\right]}{\text{C photon}}$
$\frac{(>5.8\ \text{MeVee},150^\circ)}{(>4.9\ \text{MeVee},0^\circ)}$	$\frac{\left[\frac{(\text{total neutron},90^\circ)}{(\text{total neutron},0^\circ)}\right]}{\text{C photon}}$
$\frac{(>4.9\ \text{MeVee},120^\circ)}{(>4.9\ \text{MeVee},0^\circ)}$	$\frac{\left[\frac{(\text{total neutron},150^\circ)}{(\text{total neutron},0^\circ)}\right]}{\text{O photon}}$
$\frac{(>4.9\ \text{MeVee},150^\circ)}{(>4.9\ \text{MeVee},0^\circ)}$	$\frac{(2.1-4.9\ \text{MeVee},120^\circ)}{(2.1\text{-}4.9\ \text{MeVee},0^\circ)}$
Metallic or inorganic cargo flags	
$\frac{(>5.8\ \text{MeVee},150^\circ)}{(>5.8\ \text{MeVee},0^\circ)}$	$\frac{\left[\frac{(\text{total neutron},150^\circ)}{(\text{total neutron},0^\circ)}\right]}{\text{C photon}}$
$\frac{(>5.8\ \text{MeVee},150^\circ)}{(>4.9\ \text{MeVee},0^\circ)}$	$\frac{\left[\frac{(\text{total neutron},150^\circ)}{(\text{total neutron},0^\circ)}\right]}{\text{N photon}}$
$\frac{(>4.9\ \text{MeVee},120^\circ)}{(>4.9\ \text{MeVee},0^\circ)}$	$\frac{\left[\frac{(\text{total neutron},150^\circ)}{(\text{total neutron},0^\circ)}\right]}{\text{O photon}}$
$\frac{(>4.9\ \text{MeVee},150^\circ)}{(>4.9\ \text{MeVee},0^\circ)}$	$\frac{(>5.8\ \text{MeVee},120^\circ)}{(>5.8\ \text{MeVee},0^\circ)}$
	$\frac{(>4.9\ \text{MeVee},150^\circ)}{(>0.14\ \text{MeVee},0^\circ)}$

Table 7-7. Identities of the best flags used in eliminating false positives due to the presence of inert objects of elevated density.

Organic or hydrogenous (OH) cargo flags	Metallic or inorganic cargo (IM) cargo flags
Explosives only triggering flags	
$\frac{\text{6.2 MeV photon}}{\text{1.8 MeV photon}}$	$\frac{\text{5.2 MeV photon}}{\text{3.8 MeV photon}}$
$\frac{\text{6.2 MeV photon}}{\text{2.4 MeV photon}}$	$\frac{\left[\frac{\text{(total neutron,150°)}}{\text{(total neutron,0°)}}\right]}{\text{N photon}}$
$\frac{\text{6.2 MeV photon}}{\text{2.6 MeV photon}}$	$\frac{\left[\frac{\text{(total neutron,90°)}}{\text{(total neutron,0°)}}\right]}{\text{N photon}}$
$\frac{\text{6.2 MeV photon}}{\text{2.8 MeV photon}}$	$\frac{\left[\frac{\text{(total neutron, 90°)}}{\text{(total neutron, 0°)}}\right]}{\text{O photon}}$
$\frac{\text{6.2 MeV photon}}{\text{3.4 MeV photon}}$	$\frac{\left[\frac{\text{(total neutron,150°)}}{\text{(total neutron,0°)}}\right]}{\text{O photon}}$
Dense object only triggering flags (same for OH and IM cargos)	
$\frac{\text{5.2 MeV photon}}{\text{1.0 MeV photon}}$	$\frac{\text{5.2 MeV photon}}{\text{2.6 MeV photon}}$
$\frac{\text{6.8 MeV photon}}{\text{1.0 MeV photon}}$	$\frac{\text{4.6 MeV photon}}{\text{3.4 MeV photon}}$
$\frac{\text{4.6 MeV photon}}{\text{2.6 MeV photon}}$	$\frac{\text{5.2 MeV photon}}{\text{3.4 MeV photon}}$

Table 7-8. Dose estimates at various locations for a single container scan consisting of one-minute irradiations with a 5×10^8 n s^{-1} D-T neutron generator.

Location	Dose (mSv)
2 m outside container center	0.378
3 m outside container center	0.00606
4 m outside container center	0.0321
5 m outside container center	0.00321
5 m outside container center, shielded	0.0000717
6 m outside container center	0.00200
7 m outside container center	0.00136
Centered above scan 1	0.151
Centered above scan 2	0.167
Centered above scan 3	0.169
62 cm from floor above scan 1	0.224
62 cm from floor above scan 2	0.230
62 cm from floor above scan 3	0.230
9 cm from floor above scan 1	0.396
9 cm from floor above scan 2	0.405
9 cm from floor above scan 3	0.405
1.3 m from bottom, 9 cm from side, above scan 3	0.150
1.3 m from bottom, 69 cm from side, above scan 3	0.162

References

1. M.-A. Descalle, D. Manatt, D. Slaughter, “Analysis of recent manifests for goods imported through US ports”, Report UCRL-TR-225708, Lawrence Livermore National Laboratory (2006).
2. A.L. Lehnert, K.J. Kearfott, "The detection of explosive materials: review of considerations and methods", Nucl. Technol. 172 (2010) 325-334.
3. A. Buffler, J.R. Tickner, "Detecting contraband using neutrons: challenges and future directions", Radiat. Meas. 45 (2010) 1186-1192.
4. A.L. Lehnert, K.J. Kearfott, “Simplified simulation of fast neutron scattering for an explosives detection application”, Nucl. Sci. Eng. 168 (2010) 278-286.
5. A.L. Lehnert, K.J. Kearfott, “D-D Neutron Scatter Measurements for an Explosives Detection Technique”, (unpublished) (2011).
6. A.L. Lehnert, K.J. Kearfott, “Preliminary identification of flags for a novel algorithm-based approach for explosives detection using neutron interrogation for a simulated idealized cargo container scenario”, Nucl. Instrum. Methods Phys. Res. A 638 (2011) 201-205.
7. A.L. Lehnert, K.J. Kearfott, “Simulations for developing a flag-based active neutron interrogation method for explosives detection in sea-land cargo containers”, Nucl. Technol. (submitted for publication) (2011).
8. D. Chichester, J. Simpson, "Compact accelerator neutron generators", The Industrial Physicist, (2003) 22-25.
9. V. Valkovic, D. Sudac, D. Matika, "Fast neutron sensor for detection of explosives and chemical warfare agents", Appl. Radiat. Isot. 68 (2009) 888-892.
10. V. Valkovic, D. Sudac, S. Blagus, K. Nad, J. Obhodas, B. Vekic, G. Nebbia, S. Pesente, "Fast neutron inspection of sea containers for the presence of ‘dirty bomb’", Nucl. Instrum. Methods Phys. Res. B 263 (2007) 119-122.
11. D.L. Chichester, M. Lemchak, J.D. Simpson, "The API 120: A portable neutron generator for the associated particle technique", Nucl. Instrum. Methods Phys. Res. B 241 (2005) 753-758.
12. G.F. Knoll, “Radiation detection and measurements”, Third ed., John Wiley and Sons, Inc., Ann Arbor, Michigan, 2010.
13. R.A. Forster, L.J. Cox, R.F. Barrett, T.E. Booth, J.F. Briesmeister, F.B. Brown, J.S. Bull, G.C. Geisler, J.T. Goorley, R.D. Mosteller, S.E. Post, R.E. Prael, E.C. Selcow, A. Sood, “MCNP Version 5”, Nucl. Instrum. Methods Phys. Res. B 213 (2004) 82-86.
14. S. Pozzi, E. Padovani, M. Marseguerra, “MCNP-PoliMi: a Monte-Carlo code for correlation measurements”, Nucl. Instrum. Methods Phys. Res. A 513 (2003) 550-558.
15. E. C. Miller, S.D. Clarke, M. Flaska, S. Pozzi, E. Padovani, “MCNPX-PoliMi Post-Processing Algorithm for Detector Response Simulations”, J. Nucl. Mater. Manag. (in press) (2011).
16. J.L. Dolan, M. Flaska, S. Pozzi, D.L. Chichester, “Measurement and characterization of nuclear material at Idaho National Laboratory”, Report INL/CON-09-16103, Idaho National Laboratory, (2009).

17. O. Hupe, U. Ankerhold, “Determination of ambient and personal dose equivalent for personnel and cargo security screening”, Radiation Protection Dosimetry, 121 (2006) 429-437.
18. International Commission on Radiation Protection (ICRP), “Conversion coefficients for use in radiological protection against external radiation,” Oxford: ICRP Publication 74 (1997).
19. International Commission on Radiation Units and Measurements (ICRU), “Measurement of Dose Equivalents from External Photon and Electron Radiations,” Report 47, Bethesda, MD (1992).
20. G. Erdtmann, Neutron activation tables, Verlag Chemie, New York, 1976.
21. D.L. Smith, B.J. Micklich, "Neutron activation data for neutron interrogation", AIP Conf. Proc. 769 (2005) 1698-1701.
22. Neutron activation calculator. World Information Service on Energy Uranium Project. available at: http://www.wise-uranium.org/rnac.html
23. Radioactive decay data for application to radiation dosimetry and radiological assessments. Radiation Safety Information Center. Oak Ridge National Laboratory.
24. S.F. Mughabghab, “Thermal neutron capture cross sections resonance integrals and G-factors”, International Nuclear Data Committee, Report INDC(NDS)-440 (2003).
25. National Nuclear Data Center, “NuDat”, Brookhaven National Laboratory, available at: http://www.nndc.bnl.gov/nudat2/
26. P.L. Reeder, D.C. Stromswold, “Performance of large NaI(Tl) gamma-ray detectors over temperature -50ºC to +60ºC”, Report PNNL-14735, Pacific Northwest National Laboratory, Richland, WA, 2004.
27. D.C. Stromswold, E.R. Siciliano, J.E. Schweppe, J.H. Ely, B.D. Milbrath, R.T. Kouzes, B.D. Geelhood, “Comparison of plastic and NaI(Tl) scintillators for vehicle portal monitor applications”, Nucl. Instrum. Methods Phys. Res. A, 550 (2005) 647-674.
28. National Council on Radiation Protection and Measurements, “Ionizing radiation exposure of the population of the United States”, Report 160 (2009).

Chapter 8. Evaluation of an Explosives-Detection Algorithm for Use in Sea-Land Cargo Containers

Abstract

One potential avenue for the illicit transportation of highly explosive material is through the use of sea-land cargo containers. An algorithm based on neutron and photon measurements during active neutron interrogation with 14.1 MeV neutrons was developed. In this method, specific flags based on ratios of photon and neutron measurements function to characterize unknown cargo material, test for the presence of explosives, and minimize the number of false positives due to cargo heterogeneity. The detection algorithm has now been evaluated for effectiveness over a wide range of explosive sizes, positions, and cargo configurations. This evaluation includes a study of various sources of uncertainty, including those inherent in the measurement technique and from outside sources such as background radiation. An estimate of the false positive and false negative rates was completed for various measurement conditions and trigger thresholds. Results showed that, although minimum detectable explosive mass depended on the surrounding cargo material, explosive position, and cargo configuration, a 200 kg sphere of RDX could be reliably detected.

Introduction

The smuggling of chemical explosives in shipping containers presents several difficulties. Conventional x-ray scanning techniques cannot easily penetrate the large target masses and are further disadvantaged due to the similarities in electron density between explosive material and low-Z inert media. Furthermore, high throughput rates require minimal delay in the screening process. Active neutron interrogation shows promise in the detection of explosives under these conditions [1].

Explosives detection algorithm and detection system

A flag-based detection algorithm was devised that uses the neutron and photon measurements from 14.1 MeV active neutron interrogation of cargo containers to discern the presence of explosives [2]. This algorithm was developed in several stages, the first of which involved the characterization of neutron scattering behavior using Monte Carlo simulations [3]. Next, laboratory measurements confirmed the validity of calculated neutron detector response functions that form the backbone of several flag calculations [4]. These flags were then isolated using idealized simulations [5] and tested under more realistic simulated conditions [6]. The flags may be formed from ratios of neutron measurements, such as neutron measurements within a 0.2 MeV energy bin at different scatter angles, ratios of wider ranges of neutron energy at different scatter angles, ratios of total neutron count rates in different detectors, or ratios of neutrons within certain pulse height thresholds at different angles. Flags based on photons are generally ratios of the characteristic photons produced by the de-excitation of carbon, nitrogen, or oxygen after inelastic neutron scatter. Other flags are formed using combinations of the above neutron and photon measurements.

This explosives-detection algorithm utilized flags in several different steps. The first step involved the sorting of unknown cargos into either inorganic/metallic cargos or organic/hydrogenous cargos. The next step involved explosives detection in the case in which the entire container is filled with explosives by matching the relative values of several key flags to templates of different explosive materials. Next, the algorithm calculated the trigger value, defined as the maximum relative change in an explosives-detection flag at one particular position relative to the other four. This trigger value is then compared with a predetermined threshold value. The threshold value may vary depending on which of the five positions the trigger value is calculated. If the algorithm triggers at this step, it proceeds to the final step in which the values of several different flags are compared in order to minimize false positives due to the presence of denser but inert heterogeneities in the cargo. Implementation of the detection algorithm involves a system in which the cargo container is transported through a ring of detectors and over a buried D-T neutron generator. An earlier paper provided a detailed description as well as cost and dose estimates for system operation. [2]

One important issue to consider is the feasibility of calculating the flags that require relatively stringent neutron spectroscopy. Several of the flags are based on fast neutron energy of ranges of 0.2 MeV, which is difficult to achieve with a high detection efficiency using available neutron detectors. Therefore, two separate detection algorithms were described, the spectroscopic algorithm utilized only the best-performing flags, even if it is not currently possible to efficiently implement them, while the pulse height distribution (PHD) algorithm used ranges in neutron pulse height distributions instead of stringent neutron spectroscopy, and is therefore fully implementable with currently available technology. All of the flags are described in earlier papers [2,6].

Evaluation of the detection algorithm

The purpose of this chapter is to evaluate the performance of the detection algorithm under various conditions through calculation the detection probability, system specificity and sensitivity. Some factors considered include random measurement fluctuations, explosive size and position, and heterogeneous cargo configurations. Quantitative assessment of many of these factors was accomplished through analysis of their effect on the trigger values, as defined above. Consideration of these factors also allowed for a further optimization of the detection algorithm through refinement of the trigger thresholds. Other sources of uncertainty include counting statistics, the effect of photon escape peaks on photon-based flag performance, the presence of background radiation and signal degradation due to multiple neutron scatters in the shielding and surrounding environment.

Materials and Methods

Monte Carlo simulations and data analysis

All of the simulations were completed using either MCNP5 [7] or MCNP-PoliMi [8]. The results from the PoliMi simulations were input into a postprocessor that calculated the detector response of the eleven neutron detectors [9]. This detector response included both PHDs and time-of-flight (TOF) distributions, though the TOF information was not used due to high levels of uncertainty in the interaction position because of the very large target mass.

General MCNP and MCNP-PoliMi geometry

A detailed description of the simulation geometry was discussed in an earlier paper [2], although the general form is provided in Fig. 8-1 as a reference, with all material atomic compositions listed in Table 8-1. In this geometry, a standard-sized cargo container is located on a 25-cm-thick concrete slab over a standard soil. Eleven 20 cm thick, 40 cm radius neutron scintillation fluid EJ-309 detectors surround the container [10,11,12]. The isotropic 14.1 MeV neutron source is located 160 cm below the bottom of the container and is shielded into a fan beam by a mixture of polyethylene and steel that is at least 50 cm thick. The fan beam is sufficiently broad such that the entire container width is irradiated and thick enough for a 10% overlap of adjacent measurements. In addition to the calculated neutron detector responses, MCNP F1 tallies are calculated on the detector surfaces facing the cargo container.

Heterogeneous cargo geometries

As the detection system is designed to find explosives through discovery of variations in particular flag values, it is very likely that more heterogeneous cargo configurations would prove problematic. Therefore, several geometries were tested that utilized crated cargo instead of homogenized cargo. Three different cargo types were considered: steel machine components, clothing, and furniture. All geometries included cargo inside wooden boxes that measured 100 cm × 100 cm × 20 cm and were stacked 12 at a time with six rows of two crates in each level. The total number of crates varied depending on cargo density, with the total mass equaling the maximum cargo load of the containers. The scenarios with simulated steel parts had 34 crates of steel with density 4 g cm^{-3}, crated paper scenarios had 135 crates at 0.8 g cm^{-3}, and furniture scenarios had 64 crates at 2 g cm^{-3}.

Along with explosive-free simulations of each cargo, the heterogeneous simulations used one of two explosive configurations. In the first configuration, a rectangular box of RDX was placed between the two rows of cargo-filled crates, as shown in Fig 8-2a. This box of RDX had a width of 28 cm and a height and length of 62.6 cm for the 200 kg box, 76.7 cm for the 300 kg box, and 88.6 cm for the 400 kg box. In the second configuration, one to four crates of cargo were substituted with an equally-sized box of RDX. Each of the RDX crates contained 274 kg of RDX and substituted for crates located in the middle of neighboring stacks, as shown in Fig. 8-2b.

Data analysis and implementation of the detection algorithm

Simulation output files included a text file of the F1 tally outputs, as well as text files for the PHD and TOF distribution calculated with the postprocessor. These were combined using a custom parser designed using a common mathematics and data analysis package (MATLAB, 3 Apple Hill Drive, Natick, MA, USA 01760), as well as spreadsheet software (Excel, Microsoft, 1 Microsoft Way, Redmond, WA, USA 98052). Similarly, custom MATLAB programs were used to calculate the relevant flag values, flag strengths, and statistical uncertainty in flag calculations. Other programs applied the detection algorithm, uncertainty analysis, and simulated measurement error.

Sources of uncertainty in MCNP simulations

Photon escape peaks

All of the proposed flags formed using de-excitation photons were based on a 0.2 MeV energy bin width in the photon tallies. This level of energy resolution is easily achievable using available photon spectroscopy technology.

However, one issue not considered in the earlier simulations was the effect of the single, 0.511 MeV, or double, 1.22 MeV, escape peaks in actual photon measurements. One easy way to check the effectiveness of the current photon-based flags and include the escape peaks was to use the energy range between the photopeak energy and the photopeak minus 1.22 MeV in place of the single photopeak energy bin. The magnitude of this effect was estimated by finding the change in photon-based flag strengths for homogenous cargos with 200 kg of concealed RDX when the flags were calculated with and without the increased range of photon energies.

Measurement error

Previous measurements showed that a 10% margin of error provided a conservative approximation of the uncertainty due to equipment measurement error, especially as much of the uncertainties due to light collection are included in the postprocessor [4,9]. In order to quantify the effect of measurement error on the flag calculations, an iterative computer program was created using a common software package (MATLAB). In this program, a random error was introduced to each tally and PHD in the simulation output files. This error fell within the Gaussian distribution defined by a 10% standard deviation from the “true” value provided by the simulation output. This process was iterated enough times such that average trigger values converged to within 2% of the average expected with infinite iterations. [13,14,15] The MATLAB code for creating the perturbed data is found in Appendix B.

Neutron source and multiple-scatters

The primary sources of non-equipment-based noise in the neutron signal are from multiple-scatters in the environment and the source shield. As well as neutron scatter in the environment, over 80% of the total photons originate outside the cargo container, the majority in the source shielding. This behavior was incorporated into the five-scan simulations through inclusion of an isotropic neutron source and accurate depiction of the source shield and surrounding environment. In this way, the effect of multiple scatters was part of the initial flag value and uncertainty calculations. Furthermore, because of a standardized scanning geometry, the amount of scatter outside the container should remain relatively constant between measurements and any remaining variations would have less impact than the random measurement error.

Performance under different conditions

Changing explosive size

An earlier study [5] investigated the effect of explosive size on flag strength. It was found that there was a linear relationship between flag strength and explosive size for “specific” neutron flags, i.e. the flags based on ratios of specific 0.2 MeV energy bin neutron tallies. These previous calculations depended on a single measurement in a lateral irradiation configuration instead of the vertical configuration described above. As an extension of the earlier investigation, and in order to estimate the minimum detectable explosive mass in a given configuration, a series of simulations was completed in which a 5, 10, 50, 100, 200, 300, or 400 kg sphere of RDX was concealed centered above one of the five scanning locations. Homogenous cargo materials included clothing, electronics, furniture, meat, paper, steel, vegetables, and wheat. The relationship between explosive mass and detection probability was estimated by plotting the trigger value as a function of explosive mass in both the spectroscopic and PHD explosives-detection algorithms.

Changing explosive position

Earlier studies [5] took a preliminary look at the effect of the position of the explosive position on flag strength, or the difference in flag value with and without a 500 kg sphere of RDX. This was expanded on by applying the explosives-detection algorithm to a series of simulations in which one of the more difficult cargo materials, paper, was homogenously distributed in a cargo container with 200 kg spheres of RDX at various locations. These locations included seventeen positions centered in the container along its length; vertical displacements of ±30 cm, ±60 cm, and ±90 cm above the center position; nine lateral displacements within ±90 cm from center, and two additional cases in which the explosive was displaced 60 cm laterally and ±60 cm vertically from the center.

Another set of simulations was completed in which 200 kg of explosives were placed in different locations in a cargo representing furniture. These simulations were necessary because an earlier study found that, while most inert cargos displayed increased trigger values at scanning positions one and five, a few, including paper, showed increases at the center position [2]. The furniture simulations had explosives along the container at fifteen positions between 35 cm and 585 cm from container end. Additionally, depth displacements of -90 cm, -60 cm, -30 cm, and 60 cm were simulated, along with width displacements of 15 cm, 45 cm, 60 cm, and 90 cm.

Detection probability calculations

In order to estimate the detection probability, including estimating the false negative (FN), false positive (FP), true negative (TN), and true positive (TP) rates, 4,000 randomly perturbed spectra were input into the detection algorithm. In the cases in which RDX was present, the percentage of positive algorithm results that correctly identified the location of the explosive gave an estimate of the TP rate. Similarly, the proportion of iterations without any trigger gave an estimate of the false negative rate. The FP rate in these cases was estimated by the number of times the algorithm triggered in the wrong location. For the cases without RDX, The true negative rate was estimated by the proportion of non-triggering iterations, while FPs were defined by the number of times the algorithm triggered at any of the five scanning locations.

Optimization of explosives-triggering thresholds

Initial triggering thresholds were chosen in an earlier paper [2] based on observation of simulations of homogenous cargo with 200 kg sphere of RDX. It was found that the vast majority of cargos showed elevated values at the edges, i.e. positions 1 and 5, due to asymmetries in cargo scanning at these positions.

Therefore trigger thresholds of 0.2 were chosen for possible explosives in these positions, while a threshold of 0.1 was used for positions 2, 3, and 4 [2]. However, further optimization of these trigger thresholds was explored in this study. Nine different trigger thresholds, shown in Table 8-2, were applied in the detection algorithm described above with 4,000 iterations of 118 randomly-perturbed simulation results [2]. Homogenous cargos used in the optimization process included clothing, electronics, furniture, meat, paper, steel, vegetables, and wheat, with the atomic compositions shown in Table 8-1. Explosives ranged from absent to 500 kg spheres. Receiver-operating characteristic (ROC) curves were used to choose optimum trigger thresholds using average FP and average TP rates calculated from all the homogenous cargos as described above [16,17,18].

Results and Discussion

Sources of uncertainty in MCNP simulations

Photon escape peaks

When the photon-based flags were recalculated using the increased photon energy range to compensate for losses in photon escape peaks most showed little change or an improvement in flag strength. As shown in Table 8-3, 33% of the flags had decreases in flag strength of more than 0.10, while 33% had changes of less than 0.10 and another 33% showed an improvement of more than 0.1. Furthermore, the extended photon energy range increased average triggering rate by 4% with a 0.1 trigger threshold, and by 6% with a 0.2 trigger threshold. Another important thing to note that all of the photon-based flags used in the explosives-triggering step of the detection algorithm showed either no significant change, or an improvement of around 0.3 when the increased photon energy range was used. Therefore, it is valid to conclude that compensating for photon escape peaks will have either minimal change or actually improve the effectiveness of the detection algorithm, with any negative impact occurring in the final step of the algorithm.

Measurement error

Examples of perturbed neutron spectra and pulse height distributions are shown in Figs. 8-3a and 8-3b. It was found that 4,000 iterations were more than sufficient to estimate the expected peak heights, as the average did not change by more than 2% with an increased number of iterations. Inclusion of measurement error had a significant effect on the detection rate, as the random perturbations could occasionally change the trigger value by as much as 30-50%, which increased both the number of false positives and false negatives. Scenarios for which the unperturbed trigger value was below the detection threshold saw a corresponding increase in successful detections.

Environmental radiation interference

As with any radiation measurement, the background radiation must be considered when estimating the performance of a measurement system. Earlier measurements in the laboratory demonstrated that liquid scintillator-based detectors of the same type as the proposed system measured background count rates of about 30 counts per second, with about 0.5% of counts due to neutrons [4]. Calculations showed an intrinsic detection efficiency of approximately 13% for neutrons, yielding a neutron background rate of 1.15 n s^{-1} [4]. The proposed detectors are considerably larger, with a neutron detector counting efficiency of approximately 20%, based on comparisons of the PHDs and F1 tallies. The larger active volume also increases the photon detection probability leading to a conservative estimate of 100 background photon counts per second, with only 0.23 neutron counts per second. Simulations showed that, given an incident neutron source rate of 10^8 n s^{-1}, all of the detectors experienced fluxes exceeding 1,500 neutrons and 10,000 photons per second. This corresponds to source-produced count rates of 290 neutron and 4,800 photon counts per second. Therefore, the background-produced count rates do not contribute significantly to either the neutron or photon measurements.

Neutron source and multiple-scatters

The primary source of noise in the neutron signal is from multiple-scatters in the environment and the source shield. Furthermore, over 80% of the total inelastic-scatter photons originate outside the cargo container, mostly in the source shielding. This behavior was incorporated into the five-scan simulations through inclusion of an isotropic neutron source and accurate depiction of the source shield and surrounding environment. In this way, the effect of multiple scatters was part of the initial flag value and uncertainty calculations. Furthermore, because of a standardized scanning geometry, the amount of scatter outside the container should remain relatively constant between measurements and any remaining variations would have less impact than the 10% variation produced through random measurement error.

Optimization of explosives-triggering thresholds

The ROC curves shown in Fig. 8-4 demonstrate the relationship between FP rate and the TP rate for the nine different triggering thresholds listed in Table 8-2. As seen in the figure, both algorithms occupy the far upper right corner, away from the FP=TP line, and therefore have a relatively high figure of merit [16]. Due to its higher TP rate for a given FP rate, the PHD algorithm is superior in performance to the spectroscopic algorithm for cases with more than 100 kg of RDX. All detection thresholds showed increased TP rates when applied to the PHD detection algorithm. The final choice of the trigger threshold will depend on what FP and TP rates are considered acceptable. These rates are shown in Table 8-4, along with the TP/FP ratio. The highest ratios signify the best trade-off between TP and FP rates. This is found, for both algorithms, in threshold T5, which corresponds to a value of 0.2 for any scanning position. This threshold also corresponds to the lowest TP rate, which may be unacceptable when detecting something as dangerous as explosives. However, using threshold T9, or 0.175 at the edges and 0.125 elsewhere, increases the average TP rate to 38% and 57% for the spectroscopic and PHD algorithms, respectively, while keeping the average FP rate below 3% for both cases. It should be noted that the relatively low TP rates in the table are due to averaging from cases with small amounts of explosive.

Performance under different conditions

Explosive size

It was found that the trigger value, for a given cargo, was linearly dependent on explosive mass, with correlation coefficients ranging from 0.83 to 0.99 in the spectroscopic algorithm and 0.78 to 0.98 in the PHD algorithm. This is shown in Figs. 8-5a and 8-5b for the spectroscopic and PHD algorithms, respectively. This was expected, as earlier studies found a roughly linear relationship between flag strength, which the trigger values are based on, and explosive mass [6]. Applying trigger threshold T9, i.e. 0.175 at positions 1 and 5 and 0.125 at 2, 3, and 4, provides estimates of the theoretically possible minimum detectable mass (MDM) of detectable explosive for both algorithms. As seen in the figures, trigger values were considerably higher in the PHD algorithm, which leads to smaller MDMs, as well as potentially better overall performance. As expected, some cargo materials better concealed the explosive, such that the MDMs in these materials were significantly larger. The largest MDMs were found in organic/hydrogenous materials such as meat, paper, and vegetables, with MDMs ranging from 100 to 150 kg in the PHD algorithm and 250 to 350 kg with the spectroscopic algorithm. Inorganic materials, such as steel and electronics, performed better with MDMs of 30 to 100 kg and 20 to 45 kg for the spectroscopic and PHD detection algorithms, respectively. Mixed and intermediate cargo materials had MDMs of 70 to 130 kg for the spectroscopic algorithm and 30to 60 kg in the PHD algorithm. It is expected that the MDM would increase when factors such as more realistic cargo distributions and measurement error are considered.

Explosive position

As expected, the performance of the detection algorithm was sensitive to explosive position within the container. It was expected that the trigger value would decrease significantly when the explosive was positioned between scanning positions. This is because the explosive would increase flag values at adjacent scanning locations and therefore decrease the difference between any single flag value and the average flag value, from which the trigger value is calculated. For the two scenarios with homogenous paper or furniture cargo, it was found that the trigger value varied by more than 0.25 along the length of the container. As shown in Fig. 8-6a, the trigger value was greatest in the center position and considerably lower at the ends. In most cases, trigger values were also higher when the explosive was centered above a scanning position. As expected, there was much less variation in trigger value, 0.1 to 0.12, when the explosive was shifted across the width of the container. This is shown in Fig. 8-6b, in which the increased values at the outer edges means that detection probability should actually increase when the explosive is further from the center position. Fig. 8-6c shows the variation in trigger value when the explosive is raised or lowered from its centered position. Variation in trigger value for these scenarios varied between 0.1 and 0.25.

Heterogeneous cargo geometry and explosive configuration

The trigger values for the simulations in which a box of RDX was placed in the center of a cargo container filled with crates of cargo are shown in Table 8-5. As seen in the table, all trigger values far exceeded the highest studied threshold value of 0.2 and therefore had a 100% detection probability. These high trigger values were not unexpected, as the explosive was exposed to both the source and several detectors with little cargo material interfering.

Trigger values, and therefore detection probabilities, decreased dramatically when the explosive took the place of one to four crates in the container. As seen in Table 8-5, trigger values for these scenarios were well below the minimum triggering threshold of 0.1 for all cases except steel cargo with three or more crates of RDX. As each crate contains 274 kg of explosive, the near-zero detection rates in low-Z cargo of large explosive masses in these geometries is a weakness that must be accounted for before final implementation of the system. However, it should be noted that the crates of RDX in the paper scenario were between scanning positions one and two, while the furniture scenario had RDX between positions four and five. As discussed in the previous section, positioning the explosives in these positions significantly decreases the trigger value. However, these simulations demonstrate that the proposed algorithm and associated system has weaknesses in that strategically placed explosives in cargo containers would probably not be detected.

Explosives detection probability

As discussed above multiple applications of random measurement error to simulation data allowed the calculation of expected TP rates in scenarios with varying amounts of explosive, as shown in Table 8-6. As expected, inorganic or metallic materials, such as electronics and steel have the highest detection probability for a given explosive mass, and therefore the smallest MDM. This is due to the fact that RDX is more similar, chemically, to organic/hydrogenous materials. The calculated MDMs compared favorably with the theoretical MDMs discussed above, with approximately 50 kg more explosives than the theoretical MDM reaching an almost 100% TP rate. The FP rates for both crated and homogenous cargo distributions with zero explosives are shown in Table 8-7. As seen in the table, both algorithms had FP rates of less than 5%, with rates in homogenous cargo generally lower than the crated geometries. As expected, the PHD algorithm performed considerably better than the spectroscopic detection algorithm in both TP and FP rates, mostly due to larger trigger values using this algorithm.

The one exception to the PHD algorithms' superior performance was in the cases in which one to four crates in the heterogeneous geometry were replaced with RDX. As expected from their low trigger values, these scenarios had low detection rates, less than 5% for all RDX masses with paper or furniture, and requiring three crates of RDX to have a 71% detection rate in the steel scenario. For these cases, the spectroscopic algorithm performed better, detecting three crates of steel, while the PHD algorithm could not even reliably detect four. It is surmised that this is because the use of the more specific flags in the spectroscopic algorithm provide better sensitivity for cases in which the density of the surrounding cargo closely matches that of the explosive.

Another potential source of false readings comes from if either the material determination or the dense object correction reach inaccurate conclusions. This does not happen with the materials simulated here, but may occur with cargo that is unlike the particular materials studied here, or with containers in which different types of cargo is distributed heterogeneously in the container. The best way to minimize these errors is to test a wider range of materials and cargo distributions and better optimize the thresholds used in both parts of the algorithm.

Advantages and disadvantages of the proposed system

The proposed system exhibits all the advantages of neutron-based explosives detection systems, such as the ability to differentiate between light elements and high target penetration. Furthermore, the proposed system, the first to combine both neutron and photon signals in a simple algorithm, has the advantage of fewer incident neutrons as compared to thermal neutron activation or inelastic photon based methods and less stringent neutron spectroscopy requirements than many neutron detection based methods. Other advantages are the relatively low cost of the detectors and the potential for using neutron pulse height distributions instead of complicated unfolding algorithms for the neutron flags. Provided that a powerful D-T neutron generator were used, the proposed system allows for throughput rates that are slower than x-ray screening, but considerably faster than other neutron screening techniques. However, the current algorithm is only able to reliably detect large explosives and has a relatively high false-positive rate that would further slow the screening process. Another disadvantage of the system is that the algorithm depends on a relatively homogenous distribution of inert cargo in the container. If more than one type of cargo is present in different locations, or multiple explosives are distributed along the container length, the triggering algorithm will be compromised.

Conclusions and Future Work

It was shown that specific flags, designed to trigger in the presence of explosives, could work together to produce a feasible explosives-detection algorithm that can be implemented using currently-existing technology. Performance of this algorithm was evaluated under various scenarios, including changing mass and position of the explosive, both homogeneous and heterogeneous cargo distributions, and accounting for random measurement error. Other factors included sources of error such as photon escape peaks and background radiation. It was found, after optimization of the triggering thresholds, that the system could reliably detect 200 kg explosives in homogenous cargos when the explosive was centered above a scanning position. However, deviation in placement and cargo distribution may decrease detection probability dramatically.

Future efforts should explore improvements to both the detection algorithm and the implementation system. This could include increasing the number of cargo type categories, and varying the triggering portion of the algorithm according to the material. Treating the symmetrical, i.e. same scatter angle, detectors individually and testing other flags based on the neutron pulse height distributions could also further improve algorithm performance. Probably the greatest improvement could be accomplished by either increasing the number of scans or comparing the average trigger values of adjacent scans to the average of the other three in order to detect explosives positioned between scanning positions. It is possible that artificial intelligence techniques, such as neural networks, could be used to further optimize the algorithm, such as in materials identification or the influence of inert but dense objects in the container [19].

Figures

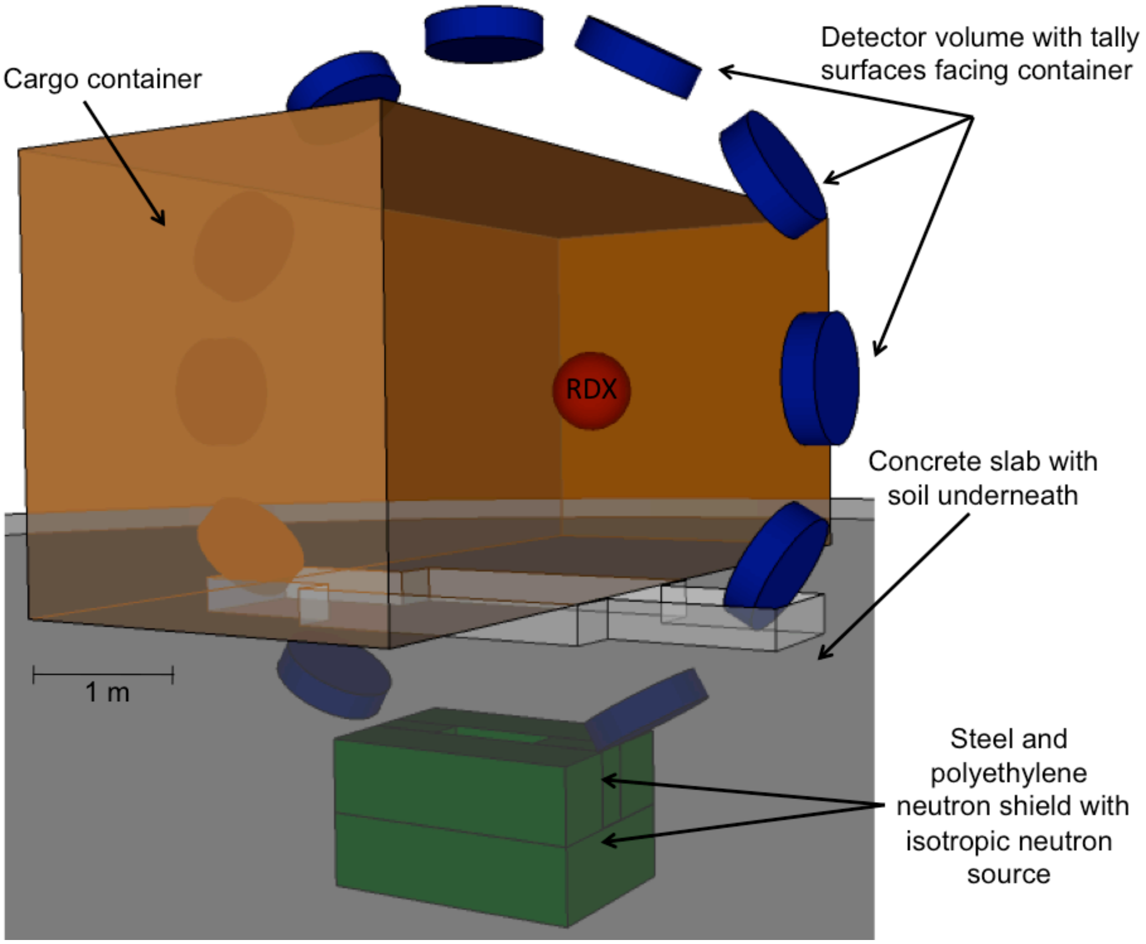

Figure 8-1. General geometry of the explosives-detection system

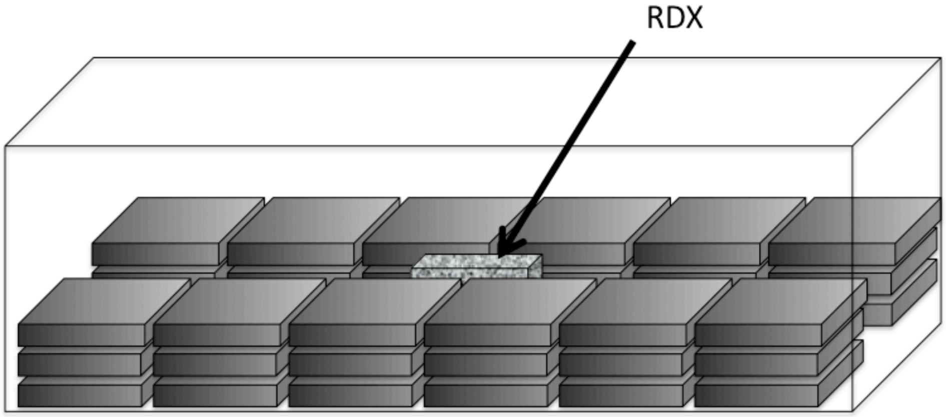

a.

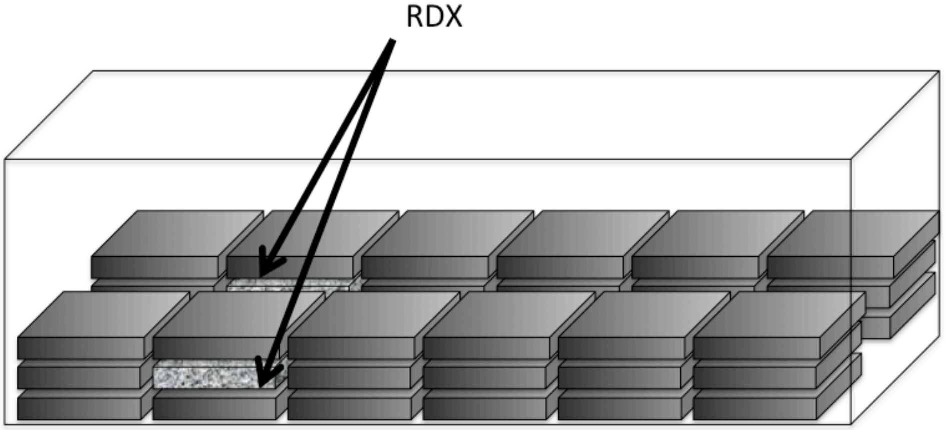

b.

Figure 8-2. Heterogeneous cargo geometry with a) centered 200, 300, or 400 kg box of RDX, and b) RDX replacing 1-4 crates of cargo, with two crates shown.

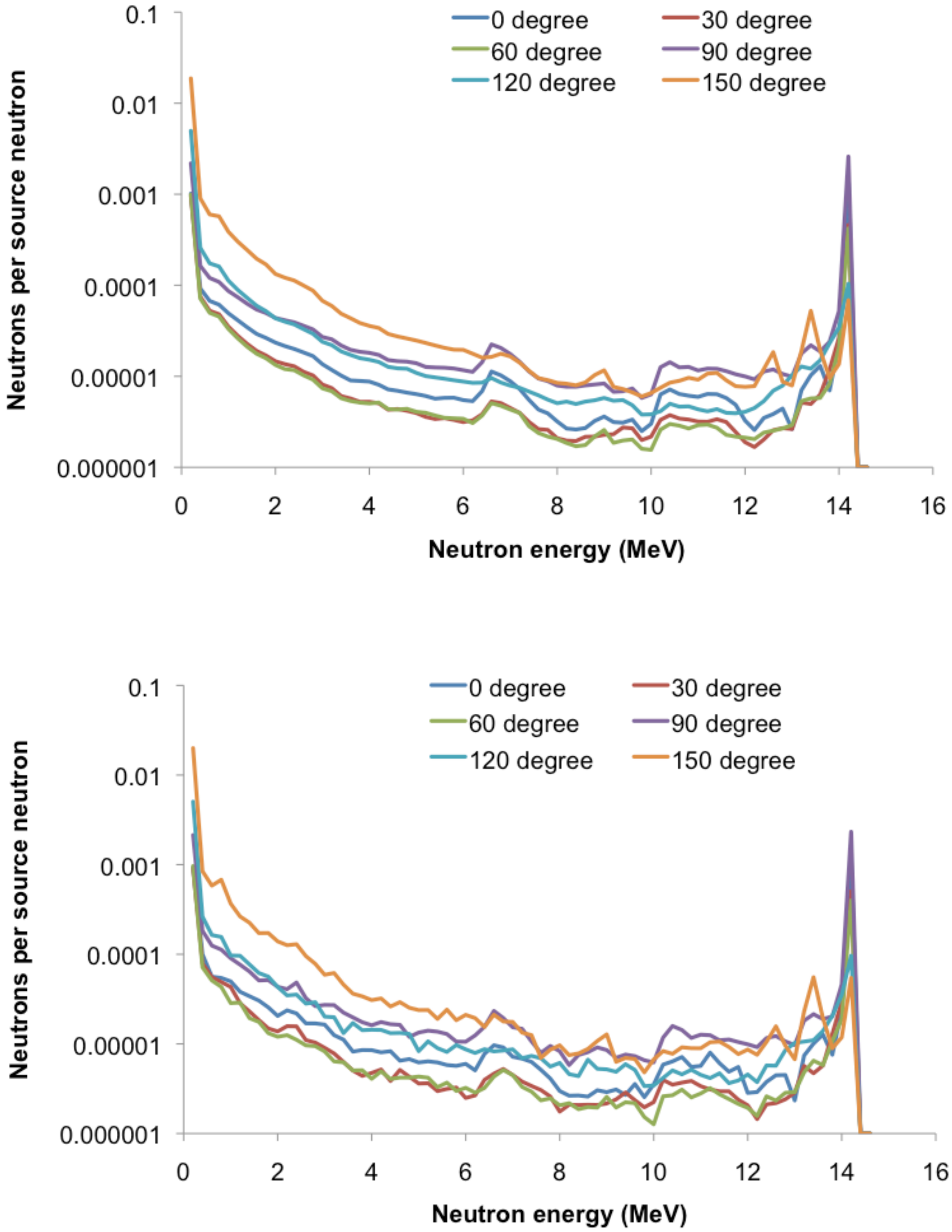

a.

Figure 8-3. Illustration of implementation of 10% measurement error for a) neutron energy tallies and b) neutron pulse height distributions at detectors tallying neutrons at different scatter angles.

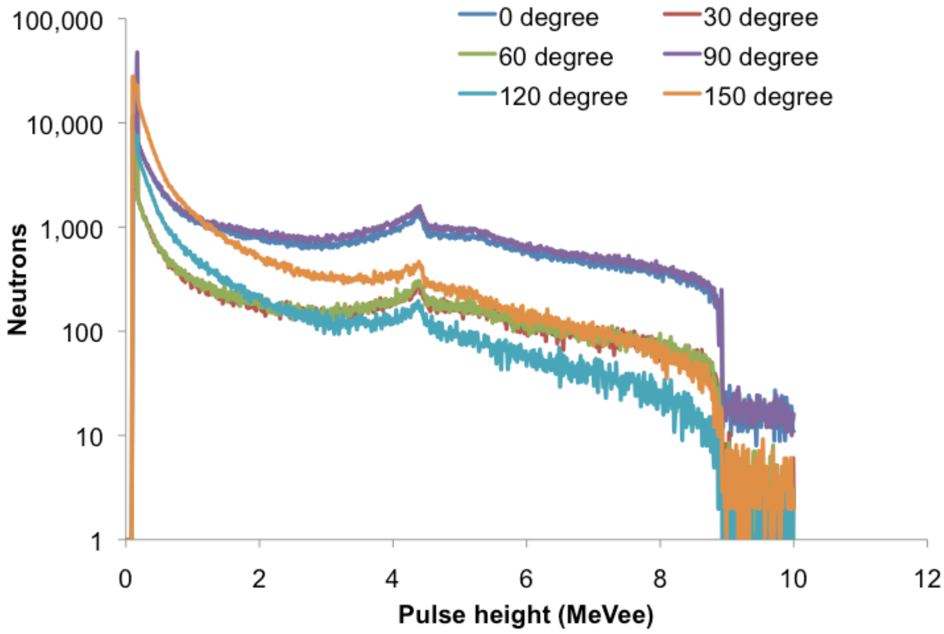

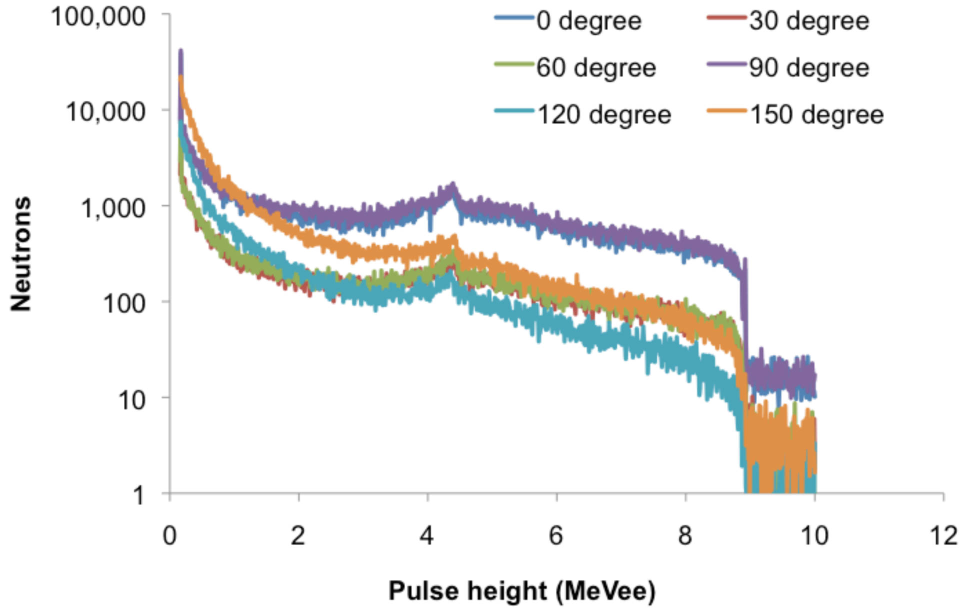

b.

Figure 8-3 (continued). Illustration of implementation of 10% measurement error for a) neutron energy tallies and b) neutron pulse height distributions at the different scatter angles.

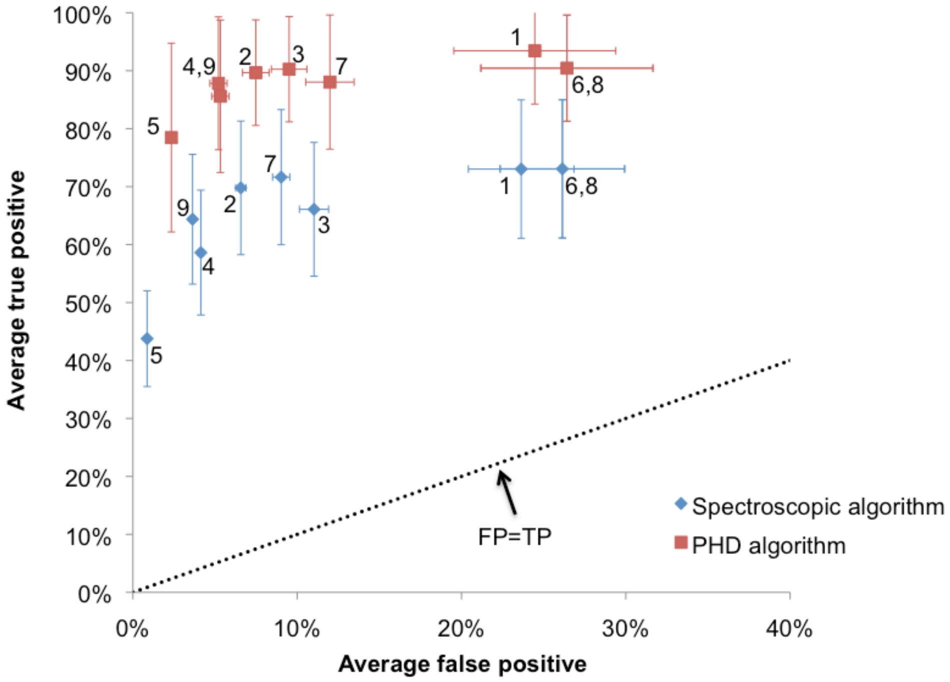

Figure 8-4. Receiver-operating characteristic curves for the Spectroscopic and PHD detection algorithms. False positive rates are averaged over all homogenous cargos and true positives for homogenous cases with greater than 100 kg RDX. Numbers refer to threshold numbers as listed in Table 8-2.

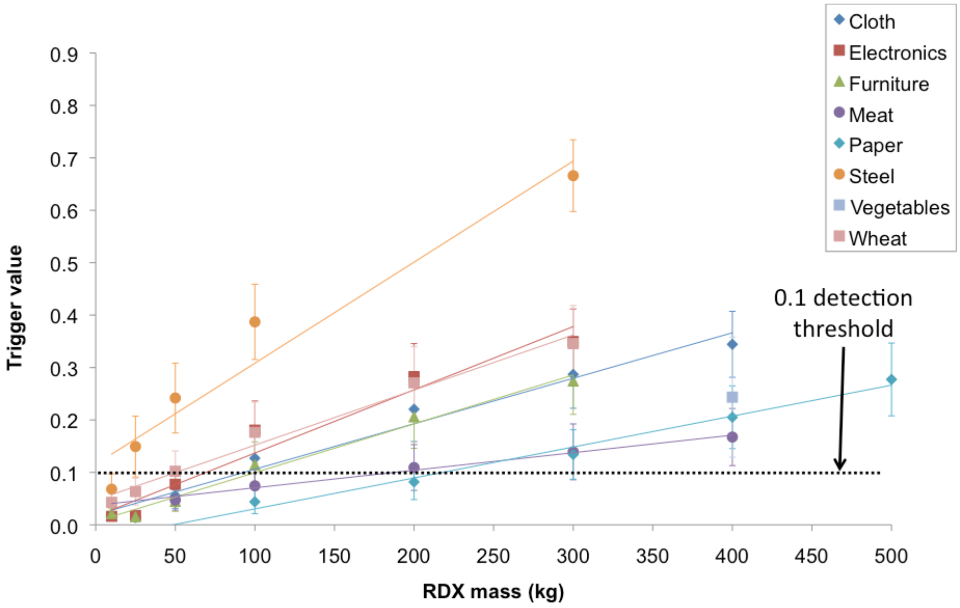

a.

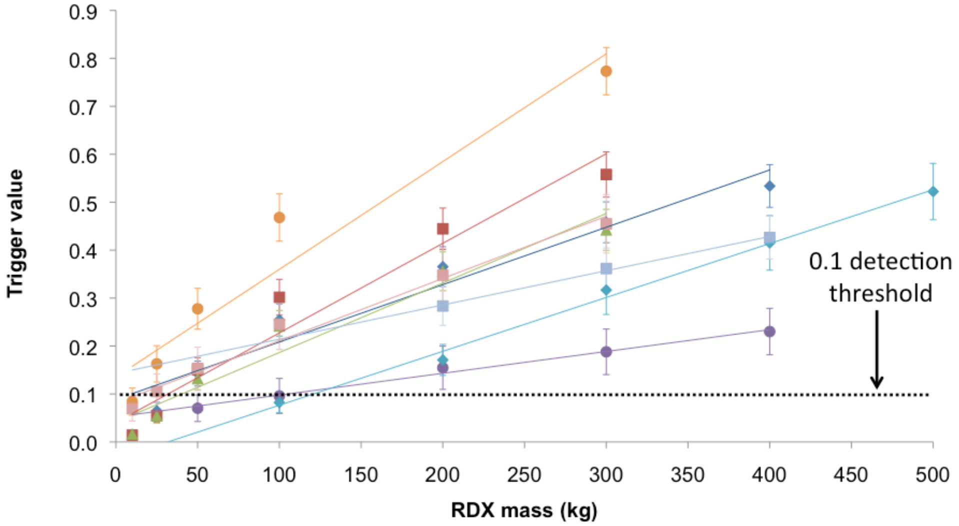

b.

Figure 8-5. Trigger values as a function of explosive mass in homogeneous cargo simulations for a) spectroscopic algorithm and b) PHD algorithm. Shown along with an example 0.1 detection threshold.

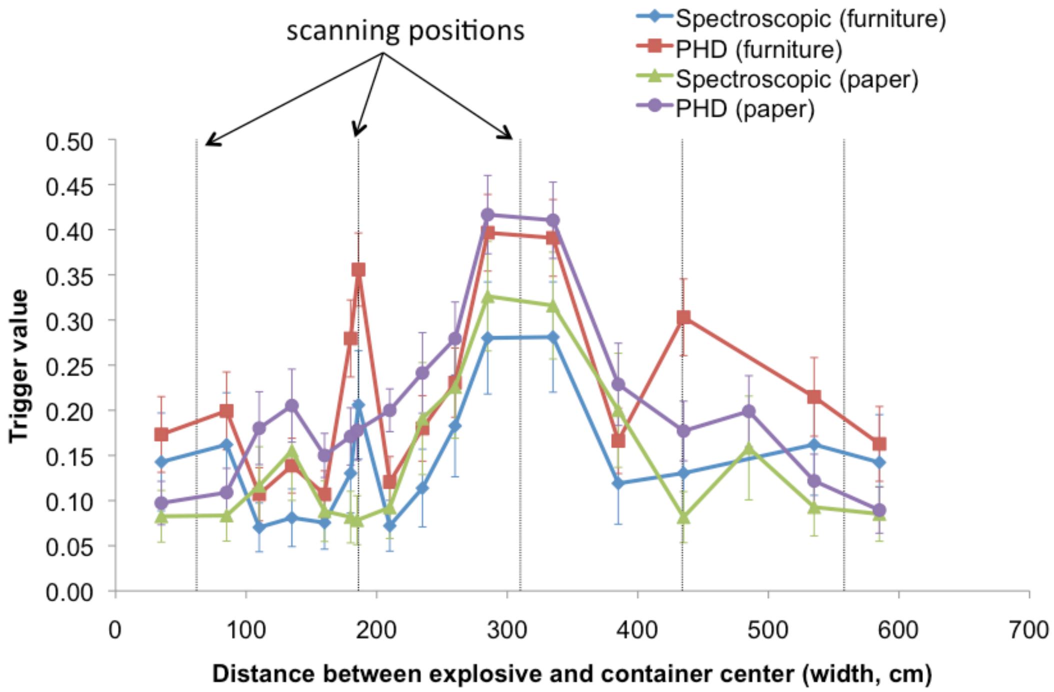

a.

Figure 8-6. Trigger value as a function of explosive position in furniture or paper cargo along a) container length with marked scanning positions, b) container width, and c) container height.

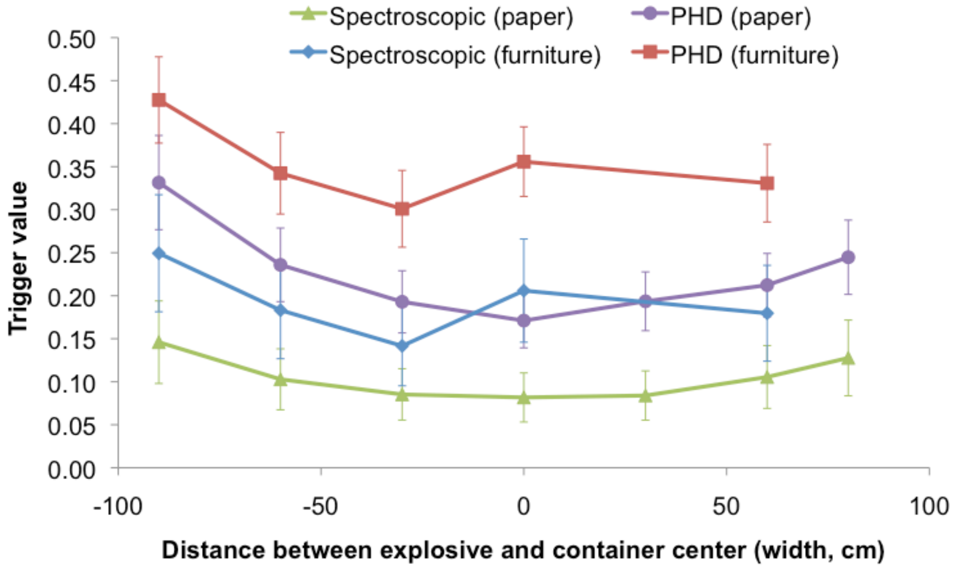

b.

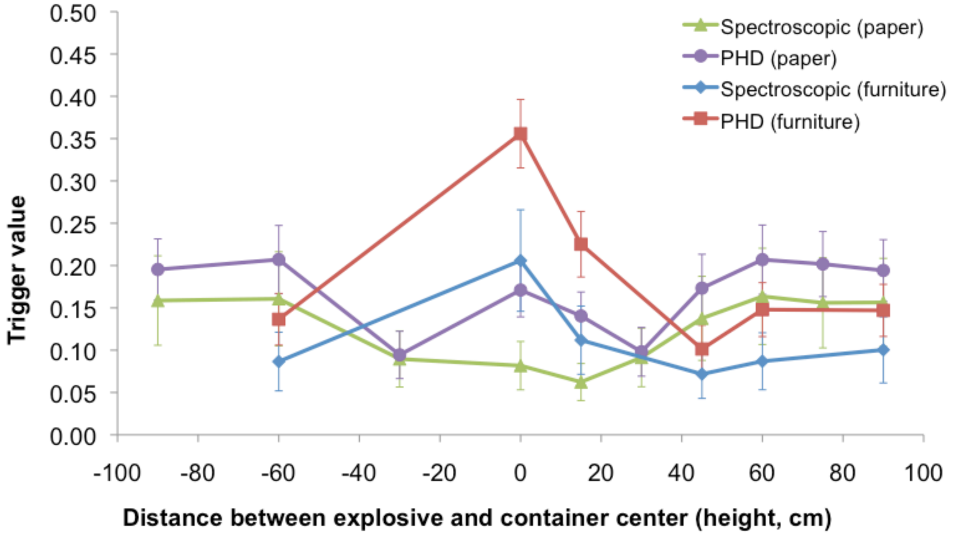

c.

Figure 8-6 (continued). Trigger value as a function of explosive position in furniture or paper cargo along a) container length with marked scanning positions, b) container width, and c) container height.

Tables

Table 8-1. Atomic compositions of materials in Monte Carlo simulations, as adapted from [2,5,6].

Material	Density	H	C	N	O	Other
Air	0.0012		0.01%	75.5%	23.2%	1.3% Ar
Clothing	1.1	48%	29%		24%	
Concrete	2.3	30%	0%		50%	1% Na, 1% Al, 15% Si, 1% K, 1.5% Ca, trace Fe
Liquid scintillator (EJ-309)	0.916	54.8%	45.2%			
Electronics	0.329	26%	2%		47%	2.6% Al, 12% Si, 10% Ni, 0.3% Fe
Furniture	0.8	41%	32%		21%	3% Fe, 3% Al
Meat	1.1	60%	15%	1%	24%	trace K, P
Paper, wood	0.6 or 0.7	48%	29%		24%	
Polyethylene	0.93	67%	33%			
RDX						
Soil	1.75	29.4%	1.87%		50.5%	2.59% Al, 13.54% Si, 1.43% K, 0.27% Fe
Steel	7.87		0.32%			99.6% Fe, 0.05% S, 0.04% P
Vegetables (potatoes)	1.6	63%	6%		31%	trace Ca, Fe, Mg, P, K, Na, S, Cl
Wheat	0.79	7%	37%	2%	53%	trace: S, Na, K, Ca, Mg, Fe, Cu, Zn, P, Cl

Table 8-2. Trigger threshold values tested in detection algorithm.

Threshold Number	Position 1	Position 2	Position 3	Position 4	Position 5
T1	0.10	0.10	0.20	0.10	0.10
T2	0.20	0.10	0.10	0.10	0.20
T3	0.15	0.10	0.10	0.10	0.15
T4	0.15	0.15	0.15	0.15	0.15
T5	0.20	0.20	0.20	0.20	0.20
T6	0.10	0.10	0.10	0.10	0.10
T7	0.125	0.125	0.125	0.125	0.125
T8	0.175	0.175	0.175	0.175	0.175
T9	0.175	0.125	0.125	0.125	0.175

Table 8-3. Effect of photon escape peaks on relevant flag values.

Photon flag identity	Average change in flag strength	Photon flag identity	Average change in flag strength
$\frac{6.2\text{ MeV photon}}{2.4\text{ MeV photon}}$	0.20 ± 0.08	$\frac{6.8\text{ MeV photon}}{1.0\text{ MeV photon}}$	-0.27 ± 0.16
$\frac{6.2\text{ MeV photon}}{1.8\text{ MeV photon}}$	0.26 ± 0.16	$\frac{6.2\text{ MeV photon}}{3.4\text{ MeV photon}}$	-0.25 ± 0.1
$\frac{5.2\text{ MeV photon}}{3.8\text{ MeV photon}}$	-0.15 ± 0.13	$\frac{6.2\text{ MeV photon}}{2.8\text{ MeV photon}}$	0.31 ± 0.21
$\frac{5.2\text{ MeV photon}}{3.4\text{ MeV photon}}$	-0.01 ± 0.09	$\frac{\left[\frac{(\text{total neutron},90^\circ)}{(\text{total neutron},0^\circ)}\right]}{\text{O photon}}$	0.29 ± 0.15
$\frac{5.2\text{ MeV photon}}{2.6\text{ MeV photon}}$	0.01 ± 0.06	$\frac{\left[\frac{(\text{total neutron},90^\circ)}{(\text{total neutron},0^\circ)}\right]}{\text{N photon}}$	0.06 ± 0.06
$\frac{5.2\text{ MeV photon}}{1.0\text{ MeV photon}}$	-0.15 ± 0.15	$\frac{\left[\frac{(\text{total neutron},90^\circ)}{(\text{total neutron},0^\circ)}\right]}{\text{C photon}}$	-0.01 ± 0.14
$\frac{4.6\text{ MeV photon}}{3.4\text{ MeV photon}}$	-0.10 ± 0.08	$\frac{\left[\frac{(\text{total neutron},150^\circ)}{(\text{total neutron},0^\circ)}\right]}{\text{O photon}}$	0.30 ± 0.15
$\frac{4.6\text{ MeV photon}}{2.6\text{ MeV photon}}$	-0.10 ± 0.13	$\frac{\left[\frac{(\text{total neutron},150^\circ)}{(\text{total neutron},0^\circ)}\right]}{\text{N photon}}$	0.06 ± 0.06
$\frac{6.2\text{ MeV photon}}{2.6\text{ MeV photon}}$	0.33 ± 0.22	$\frac{\left[\frac{(\text{total neutron},150^\circ)}{(\text{total neutron},0^\circ)}\right]}{\text{C photon}}$	-0.01 ± 0.14

Table 8-4. Average true positive (TP) and false positive (FP) rates with different trigger thresholds for homogenous cargos containing between 10 kg and 400 kg RDX. Also shown is the ratio of true positives to false positives.

Threshold number	Threshold: scan position	Average TP	Average FP	TP/FP
	Spectroscopic			
6	0.100: all positions	48.5%	9.83%	4.93
8	0.175: all positions	48.5%	9.83%	4.93
1	0.200: 3 0.100: 1, 2, 4, 5	47.6%	9.27%	5.13
3	0.150: 1, 5 0.100: 2, 3, 4	43.0%	4.47%	9.61
7	0.125: all positions	42.3%	3.99%	10.6
2	0.200: 1, 5 0.100: 2, 3, 4	39.5%	3.79%	10.4
9	0.175: 1, 5 0.125: 2, 3, 4	38.0%	1.89%	20.1
4	0.150: all positions	35.8%	1.64%	21.8
5	0.200: all positions	26.9%	0.62%	43.8
	PHD			
6	0.100: all positions	68.2%	8.72%	7.83
8	0.175: all positions	68.2%	8.72%	7.83
1	0.200: 3 0.100: 1, 2, 4, 5	68.2%	8.28%	8.23
3	0.150: 1, 5 0.100: 2, 3, 4	62.7%	4.38%	14.3
7	0.125: all positions	61.9%	4.48%	13.8
2	0.200: 1, 5 0.100: 2, 3, 4	58.7%	3.91%	15.0
9	0.175: 1, 5 0.125: 2, 3, 4	57.3%	2.81%	20.4
4	0.150: all positions	56.0%	2.72%	20.6
5	0.200: all positions	45.8%	2.00%	22.9

Table 8-5. Trigger values for crated geometries with box of RDX in the center of the container. Each crate of RDX contains 274 kg of explosive.

Cargo	RDX	Trigger value (Spectroscopic)	Trigger value (PHD)
Furniture	0	0.0455	0.0455
Paper	0	0.0554	0.0594
Steel	0	0.0664	0.0493
Centered box of RDX			
Furniture	200 kg	2.91	3.27
Furniture	300 kg	3.10	3.40
Furniture	400 kg	3.25	3.48
Paper	200 kg	2.70	3.15
Paper	300 kg	3.00	3.34
Paper	400 kg	3.23	3.46
Steel	200 kg	1.98	2.32
Steel	300 kg	2.09	2.42
Steel	400 kg	2.17	2.48
Cargo crates replaced with RDX			
Furniture	1 crate	0.0457	0.0455
Furniture	2 crates	0.0458	0.0455
Furniture	3 crates	0.0457	0.0452
Furniture	4 crates	0.0460	0.0452
Paper	1 crate	0.0558	0.0593
Paper	2 crates	0.0560	0.0595
Paper	3 crates	0.0557	0.0596
Paper	4 crates	0.0560	0.0597
Steel	1 crate	0.0613	0.0439
Steel	2 crates	0.0698	0.0450
Steel	3 crates	0.197	0.0968
Steel	4 crates	0.349	0.134

Table 8-6. True positive rates as a function of explosive size in homogeneous cargo simulations with explosive centered above one scanning position.

RDX (kg)	Cloth	Electronics	Furniture	Meat	Paper	Steel	Vegetables	Wheat
Spectroscopic detection algorithm								
10	0%	0%	0%	2%	0%	3%	0%	1%
25	1%	1%	1%	4%	0%	18%	0%	2%
50	4%	13%	4%	7%		71%	0%	10%
100	32%	75%	27%	17%	1%	100%	1%	41%
200	87%	99%	81%	36%	21%		12%	86%
300	99%	100%	98%	57%	60%	100%	38%	99%
400	100%			76%	89%		72%	
500					99%			
PHD detection algorithm								
10	0%	0%	0%	6%	0%	3%	0%	3%
25	5%	9%	4%	6%	0%	43%	0%	13%
50	79%	97%	72%	20%		100%	1%	38%
100	100%	100%	100%	35%	16%	100%	31%	93%
200	100%	100%	100%	80%	99%		100%	100%
300	100%	100%	100%	94%	100%	100%	100%	100%
400	100%			99%	100%		100%	
500					100%			

Table 8-7. False positive rates in homogenous and crated cargo geometries.

Cargo	Spectroscopic algorithm	PHD algorithm
Cloth (homogenous)	0.40%	0.00%
Electronics (homogenous)	1.53%	0.08%
Furniture (homogenous)	0.50%	0.03%
Meat (homogenous)	3.08%	4.18%
Paper (homogenous)	4.90%	0.55%
Steel (homogenous)	1.60%	0.10%
Vegetables (homogenous)	0.73%	0.33%
Wheat (homogenous)	1.88%	0.65%
Furniture (crated)	4.38%	1.13%
Paper (crated)	2.58%	0.28%
Steel (crated)	3.85%	0.40%

References

1. A.L. Lehnert, K.J. Kearfott, "The detection of explosive materials: review of considerations and methods", Nucl. Technol. 172 (2010) 325-334.
2. A.L. Lehnert, K.J. Kearfott, "A flag-based algorithm and associated neutron interrogation system for the detection of explosives in sea-land cargo containers", unpublished (2011)
3. A.L. Lehnert, K.J. Kearfott, “Simplified simulation of fast neutron scattering for an explosives detection application”, Nucl. Sci. Eng., 168 (2010) 278-286.
4. A.L. Lehnert, K.J. Kearfott, “D-D Neutron Scatter Measurements for an Explosives Detection Technique”, Nucl. Instrum. Methods Phys. Res. A (submitted for publication) (2011).
5. A.L. Lehnert, K.J. Kearfott, “Preliminary identification of flags for a novel algorithm-based approach for explosives detection using neutron interrogation for a simulated idealized cargo container scenario”, Nucl. Instrum. Methods Phys. Res. A 638 (2011) 201-205.
6. A.L. Lehnert, K.J. Kearfott, “Simulations for Developing a Flag-Based Active Neutron Interrogation Method for Explosives Detection in Sea-Land Cargo Containers”, Nucl. Technol. (submitted for publication) (2011).
7. R.A. Forster, L.J. Cox, R.F. Barrett, T.E. Booth, J.F. Briesmeister, F.B. Brown, J.S. Bull, G.C. Geisler, J.T. Goorley, R.D. Mosteller, S.E. Post, R.E. Prael, E.C. Selcow, A. Sood, “MCNP Version 5”, Nucl. Instrum. Methods Phys. Res. B 213 (2004) 82-86.
8. S. Pozzi, E. Padovani, M. Marseguerra, “MCNP-PoliMi: a Monte-Carlo code for correlation measurements”, Nucl. Instrum. Methods Phys. Res. A 513 (2003) 550-558.
9. E. C. Miller, S.D. Clarke, M. Flaska, S. Pozzi, E. Padovani, “MCNPX-PoliMi Post-Processing Algorithm for Detector Response Simulations”, J. Nucl. Mater. Manag. (in press) (2011).
10. J.L. Dolan, M. Flaska, S. Pozzi, D.L. Chichester, “Measurement and characterization of nuclear material at Idaho National Laboratory”, report: INL/CON-09-16103, Idaho National Laboratory, 2009.
11. S.D. Clarke, M. Flaska, S. Pozzi, P. Peerani, “Neutron and gamma-ray cross-correlation measurements of plutonium oxide powder”, Nucl. Instrum. Methods Phys. Res. A, 604 (2009) 618-623.
12. T. Zak, S.D. Clarke, M.M. Bourne, S. Pozzi, Y. Xu, T. Downar, P. Peerani, “Neutron spectroscopy of plutonium oxide using matrix unfolding approach”, Nucl. Instrum. Methods Phys. Res. A, 622 (2010) 191-195.
13. K.J. Kearfott, S. Han, K. McMahan, E. Samei, “Sensitivity of a mixed field dosimetry algorithm to uncertainties in thermoluminescent element readings”, Health Phys, 68 (1995) 340-349.
11. K.J. Kearfott, S. Han, E.C. Wagner, E. Samei, C.-K. C Wang, “Numerical simulation of a TLD pulsed laser-heating scheme for determination of shallow dose and deep dose in low-let radiation fields”, Appl. Radiat. Isot. 52 (2000) 1419-1429.

15. Z.D. Whetstone, S.C. Dewey, K.J. Kearfott, "Simulation of a method for determining one-dimensional ^{137}Cs distribution using multiple gamma spectroscopic measurements with an adjustable cylindrical collimator", Appl. Radiat. Isot. 69 (2011) 790-802.
16. T. Gozani, "The role of neutron based inspection techniques in the post 9/11/01 era", Nucl. Instrum. Methods Phys. Res. B 213 (2004) 460-463.
17. T. Gozani, M. Elsalim, M. Ingle, E. Phillips, "Gamma ray spectroscopy features for detection of small explosives", Nucl. Instrum. Methods Phys. Res. A 505 (2003) 482-485.
18. F.C. De Lucia Jr., J.L. Gottfried, C.A. Munson, A.W. Miziolek, "Double pulse laser-induced breakdown spectroscopy of explosives: initial study towards improved discrimination", Spectrochimica Acta Part B 62 (2007) 1399-1404.
19. H.R. Vega-Carrillo, V.M. Hernandez-Davila, E. Manzanares-Acuña, G.A. Mercado, E. Gallego, A. Lorente, W.A. Perales-Munoz, J.A. Robles-Rodríguez, "Artificial neutron networks in neutron dosimetry", Radiat. Prot. Dosim. 118 (2006) 251-259.

Chapter 9. Statistical Modeling to Improve a Flag-Based Explosives-Detection Algorithm based on Active Neutron Interrogation

Abstract

Earlier efforts have identified an algorithm that uses neutron and photon measurements from active neutron interrogation to find explosives hidden in cargo containers. This algorithm uses flags, in the form of specific mathematical manipulations of the exiting neutron and photon radiation at different angles, to first classify the cargo type, then search for hidden explosives, and finally minimize certain false positives due to cargo heterogeneities. Statistical modeling software has now been applied to the previously-identified flags in an effort to improve the detection algorithm. Statistically-modeled algorithms were developed for three subsets of the screening scenarios. The new detection models have shown accurate results exceeding 98% for simplified screening scenarios and 80%-90% when more realistic conditions are considered. Comparison of the statistically-modeled algorithm with previously-developed detection algorithms found an increase in the figure of merit, defined to have a value between 0.5 and 1.0, from 0.72 to 0.77. Estimates of the expected error due to statistical fluctuations in radiation measurement found that the statistically-modeled algorithm varied by about twice as much as the earlier algorithms.

Introduction

The possibility of hidden explosives in sea-land cargo containers presents a real threat to security. Due to the dire consequences of successful smuggling and extremely high throughput at sea ports, scanning for explosives in an efficient and effective manner is necessary [1]. Most strategies currently employed depend on x-ray or other photon-based imaging of container contents

[2]. However, the dearth of significant metallic components in explosive material, as well as similarities in electron density to inert cargos, makes detection difficult [2].

Cargo screening by active neutron interrogation

One of the more promising strategies for detecting chemical explosives in large volumes, such as cargo containers, is active neutron interrogation. In active neutron interrogation, the signal may come from either the characteristic photons produced during neutron absorption or inelastic scatter, or from the scattered neutrons themselves [2]. The method studied here combines both photons and neutrons into a detection algorithm and therefore maximizes the number of signal carriers, which minimizes both measurement time and dose to personnel.

Development of an explosives-detection algorithm

The studied detection algorithm was developed during earlier efforts that involved the simulation of several explosives-screening scenarios involving cargo containers. The simulations were completed using the Monte Carlo software MCNP5 [3] or MCNP-PoliMi [4], with a custom post-processor [5] used to calculate the neutron detector response in several cases. In these simulations, a standard 2.4 m × 6.2 m × 2.6 m steel cargo container was placed on a concrete slab and irradiated from a monoenergetic 14.1-MeV neutron source, as produced by a D-T neutron generator. The container was surrounded by detectors that tallied neutron and photon flux in 30° scatter increments. Steps in algorithm development included characterization of the neutron scatter [6], identification of flags under idealistic conditions [7], testing these flags and identifying others in more realistic simulations [8], and validation of the simulated neutron detector responses using laboratory measurements [7].

A flag-based algorithm for explosives detection

The results from the earlier simulations identified many different flags that could be used in the algorithm. These flags are generally defined as ratios of either neutrons or photons at one energy and angle, divided by either neutrons or photons at another energy and angle. The best-performing flags were identified by isolating the ones with the greatest percent difference for cases that were identical except for the presence of the explosive RDX ($C_3H_6N_6O_6$).

Types of flags

The first class of flags was defined by the ratio of neutrons of within a 0.2 MeV energy range as measured at a particular detector. This type of flag best took advantage of neutron scatter peaks produced during elastic and inelastic scatter, but were ultimately not included due to limitations in technologically feasible neutron spectroscopy [7]. However, knowledge of the best performing flags of this type led to another class of flags that are very similar, but use wider neutron energy ranges, 1-2 MeV, at the same scatter angles as before [8]. Other neutron-based flags used the ratios of total backscattered and transmitted neutrons [7,8]. A final type of neutron-based flag was calculated directly from the neutron detector pulse height distributions (PHDs) and therefore did not require any unfolding of the neutron spectrum, as would be required for neutron spectroscopy [8]. Photon-based flags included ratios of the characteristic photons from neutron inelastic scatter off hydrogen, carbon, nitrogen, and oxygen nuclei as well as certain flags that combined these photons with neutron measurements at specific angles [7,8].

Algorithm structure

Because of the enormous variety in container cargos, the detection algorithm is based on finding significant changes in flag value as a function of container position that may signal the presence of an explosive [9]. Therefore, the container is irradiated at multiple locations along its length, which also compensates for limited target penetration that prevents total container volume scanning with a single irradiation. It was found that five irradiations with a fan-shaped neutron beam were sufficient to interrogate the entire container without increasing measurement time unnecessarily [9].

It was also determined that the best-performing flags in organic or hydrogenous cargos were different than those for metallic or inorganic cargos

[7,8]. Therefore the first step of the algorithm was to categorize an unknown cargo using empirically-determined material-sensitive flags [8,9]. The next step involved identifying potential containers that were completely filled with explosive through comparison with pre-determined flag templates. Next, a triggering sub-algorithm searched for significant changes in the explosives-sensitive flags as a function of position and returned a positive result if the trigger value (T) exceed a predetermined threshold amount [9]. Finally, containers with possible explosives went through an additional step that minimized the number of false positives due to the presence of unusually dense, but inert, objects [9].

Algorithm performance

Further efforts quantified the performance of the detection algorithm under various conditions while taking into account sources of error such as measurement uncertainties and environmental interference [10]. Estimates made of the minimum detectable amounts of explosive in different types of cargo yielded results in the range of 50-100 kg for inorganic/metallic cargos and 100-200 kg for organic/hydrogenous cargos [10]. Detection probability for each case was estimated using a 10% standard deviation random perturbation of simulation results, similar to what would be expected in a real measurement [11-14]. It was found that algorithm performance was significantly decreased if the explosive was not centered above one of the five scanning locations [10]. Furthermore, detection was particularly difficult when the simulated cargo was distributed heterogeneously, in this case palletized on the container floor [10]. The purpose of this study is to investigate possible improvements to the detection algorithm through application of statistical modeling software.

Materials and Methods

Statistical modeling

For this study, the software package IBM SPSS v. 19 (IBM Corporation, 1 New Orchard Road, Armonk, New York) was used to run binary logistic regression tests [15] on combinations of variables in order to build a model that correctly predicted the presence or absence of the explosive RDX. As with all models created using binary logistic regression, the model was in the form:

$$\ln\left(\frac{P}{1-P}\right) = z = \beta_0 + \beta_1 x_1 + \beta_2 x_2 + \cdots + \beta_k x_k, \qquad (9.1)$$

in which P is the probability of a positive result, x_i are variables in the model, with fitted parameters β. The software output includes the maximum likelihood estimates of the parameters β_0 and multipliers β_1 through β_k, along with standard error for the β values, the Wald χ^2 values. Also provided is the odds ratio, e^{β}, which represents a measure of the effect on P of changing the value of variable x_i by one and provides a measure of the importance of the given variable. At this stage, the default cut-off value of 0.5 was used, such that only cases in which the probability P exceeded 0.5 were considered to contain an explosive. Potential models were evaluated according to the number of false negatives and false positives, as well as whether the included variables were statistically significant using a 95% confidence interval.

The model was determined through a process of elimination in which all flags were tested in groups of three to five. Any that had significance levels below 0.1 were then considered as potentially statistically significant. Next, these variables were tried in different combinations in order to maximize the percent that were correctly identified. Finally, the relative number of true positive, true negative, false positive, and false negative cases resulting from application of the potential models were used to pick the best one.

Variables in the statistical model

A total of 137 variables were considered when testing different detection models. These variables were derived from 38 unique flags, shown in Tables 9-1 and 9-2, that showed significant differences between cases with and without explosive in earlier studies [7,8,9]. As before, these flags were calculated at each of the five scanning locations in a given screening scenario, but three types of variables were calculated for each of the 38 flags. The first of these, the flag range (R_f) for flag f is defined as:

$$R_f = \frac{f_{\max} - f_{\min}}{\mu_f}, \tag{9.2}$$

in which f_{max}, f_{min} , and μ_f are the maximum, minimum, and average values for the particular flag. The next variable, peak height (P_f), may be thought of the percent difference between the maximum and average flag values, and is defined as:

$$P_f = \frac{f_{\max} - \mu_f}{\mu_f}. \tag{9.3}$$

The third type of flag-derived variable, the trigger value (T_f), is closely related to the peak height and was first used in the triggering sub-algorithm of original detection algorithm [9]. The trigger value maximizes the difference between the maximum flag value, where the explosive is most likely to be located, and the baseline flag value of the other four locations. It is defined by:

$$T_f = \max_s\left(\frac{f_{s=i} - \mu_{f,s\neq i}}{\mu_{f,s\neq i}}\right), \tag{9.4}$$

in which s is one of the five scanning positions, i.

Earlier efforts showed that, in many cases, the best indicator of the presence of explosives was not the trigger value of one particular flag, but was the maximum trigger value for all the flags [9,10]. Therefore, the maximum, median, and average of each of the range, peak height, and trigger value were also considered as possible variables in the detection model.

Because explosives located between adjoining scanning locations would raise the flag values at both locations and not create a clear “peak” in the trigger value, these scenarios are difficult to discern using only the variables discussed above. Therefore, it was useful to compare the off-center flag value, defined by the average flag value at two adjoining locations, with the other three off-center flag values. Therefore, the off-center range, off-center peak height, and off-center trigger value was calculated for each of the 38 flags and the maximum, median, and average off-center quantities were considered as possible variables in the model. Also considered were the maximum, median, and average of all trigger values and the total spectroscopic and PHD trigger values from the original detection algorithm [9].

Cargo container screening scenarios

A total of 178 cargo-screening scenarios were included when creating the statistical model of the improved explosives-detection algorithm. In many cases, the inert cargo material was distributed homogenously through the entire container with an explosive positioned directly above a scanning location such that the total cargo mass equaled the maximum container capacity of 21,600 kg. Cargos in this configuration included cotton, electronics, furniture, meat, paper, vegetables, and grain with explosives ranging from 0 to 500 kg [8]. Other simulated screening scenarios contained no explosive, but covered a wider range of homogenous cargos: bricks, concrete, crude oil, glass, stone, melamine, vegetable oil, paraffin, polyethylene, polystyrene, plaster, rubber, salt, and water. Another set of simulations included a 200 kg sphere of explosive inside paper or furniture cargo, but placed the explosive at different locations inside the container. Other scenarios attempted to “fool” the detection algorithm by having artificially dense, but inert, materials in place of an explosive. Still others made detection considerably more difficult by distributing the cargo heterogeneously inside the container by simulating a crated geometry in which the explosive was hidden among the crates [9].

Data subsets

In the process of constructing a more general detection model, the above-mentioned screening scenario data were separated into several levels of decreasing detection probability in the original algorithm [10]. In the most idealized cases, the cargo was distributed evenly throughout the container with zero to 400 kg explosive centered above one of the screening locations. These included 51 cases with explosive and 22 without. In the homogenous screening scenario data set the cargo was again distributed homogenously but additional scenarios had the explosive positioned away from the centered locations or displaced vertically relative to the neutron source. In this subset there were 116 cases with explosives and 22 cases without. The most difficult detection scenarios were the ones with either hidden inert objects or cargo heterogeneously distributed in crates on the container floor. The final detection model, which included all types of screening scenarios, contained a randomly-selected half of the scenarios with 70 cases with explosive and 19 without.

Results and Discussion

Explosives screening models for selected data sets

The best-performing model that correctly predicted the presence of explosive in 99% of idealistic scenarios is shown in Table 9-3. As shown in the table, all statistical significance values, or p-values, were no greater than 0.1. Out of 51 cases with explosive and 22 without, there was one false negative and zero false positives. This is which is remarkable give that most of the small explosives, with a mass of 10 kg, were detected. Table 9-3 also shows a very effective model for detecting explosives in any of the homogenous cargo scenarios, including the more difficult cases with displaced explosives. This model also performed very well, with a 99% accuracy rate, one false positive, and two false negatives. This model was based on four variables, two of which had p-values below 0.05. One variable had a higher p-value of 0.26, but elimination of this variable decreased the accuracy by more than 5%. The final model presented in Table 9-3 is for a randomly-selected half of all the simulated detection scenarios, including the ones that were undetectable in the old algorithms [10]. The accuracy in this four-variable model was lower, 87%, and included one false negative and nine false positives. All variables except the constant had p-values below 0.07.

It is useful to note that all models, with a single exception, relied solely on flags that may be calculated using available neutron and photon detector technology. The single exception of this was the first flag listed in the homogenous-scenarios algorithm, which required more stringent neutron spectroscopy. However, an alternative model used only easily calculated flags, but increased the number of false negatives by two. This model is shown in Table 9-4.

Application of detection model to control data

When the model based on a random half of the screening scenarios was applied to the full 178 scanning scenarios, the accuracy decreased to 80%, with 31 false positives and five false negatives out of a data set containing 41 scenarios without RDX and 137 with RDX. The false positive cases showed no obvious pattern, with both homogenous and heterogeneous cargos of both types appearing as false positives. However, changing the threshold to 0.8 decreased the false positive rate by a factor of 2 while keeping the true positive rate above 75%. All of the false negatives were found in electronics cargo, with explosive masses in idealistic electronics below 100 kg and below 200 kg in other cases. Most of these scenarios were also false negatives in the earlier algorithms [10]. However, these RDX-positive-probability in these cases was above 0.39 and therefore quite close to the original threshold of 0.5.

Detection probability thresholds

Adjusting the critical threshold value that divided positive and negative model results can have a dramatic effect on the false positive and false negative rates. While it is always necessary to find a balance between the two, the case of explosives detection has some special considerations. First of all, the potential consequences of a false negative, i.e. loss of life and property on a large scale, are severe. However, too many false positives will dramatically slow down the flow of cargo through very busy ports. The different detection models were applied to all screening scenarios and the relationship between threshold and correct identification of true positives or true negatives is shown in Fig. 9-1. As shown in the figure, the true positive and true negative rates intersect at different thresholds for the different detection models. The three-statistically-derived algorithms discussed above function best when detection thresholds are between 0.7 and 0.9. The threshold for the final algorithm will depend on the acceptable rate of false positives and false negatives.

The previously-studied spectroscopic and PHD detection algorithms determined the presence or absence of explosive by comparing the trigger value, with a value between zero and one, to a predetermined threshold, much like *P* in the statistically-modeled algorithms discussed here. The true positive and true negative rates for these algorithms as a function of threshold value are included in Fig. 9-1 as a point of comparison.

Measurement error and comparisons with earlier algorithms

One important facet of the earlier studies was how the inclusion of a random 10% measurement error affected the trigger values, and therefore the detection rate. This random perturbation of the simulation data and subsequent calculation of trigger values, repeated many times, showed that the 10% variation in simulation output led to an average 3.9% variation in spectroscopic trigger value and 3.4% variation in the PHD trigger value [10]. When this procedure was repeated for the statistically-modeled algorithms, the 10% data perturbation resulted in 4.8%, 5.0%, and 7.7% variations in the p-values for the idealistic, homogenous, and all-scenario models, respectively. This increase in *P* variation is mainly due to error propagation of several variables in the statistically-modeled algorithms, while error in the earlier algorithms is mainly dependent on the one flag showing the largest change in the presence of RDX.

Another useful tool in comparing the performance of the detection algorithms is the receiver operating characteristic (ROC) curve. ROC curves are plots of the true positive (TP) rate versus the false positive (FP) rate and are a common way to visualize and analyze the behavior of diagnostic systems [16]. The area under a ROC curve is often used as a figure of merit to quantitatively compare different diagnostic tests [16]. This figure of merit will vary from 0.5, which represents a random choice between positive and negative results, and 1.0, which represents a perfect diagnostic test [16].

Fig 9-2a shows the ROC curves for the three-statistically-modeled algorithms as well as the spectroscopic and PHD algorithms as applied to homogenous cargo screening scenarios. Fig. 9-2b shows the same ROC curves when the five algorithms are applied to all screening scenarios. As seen in Fig. 9-2a, the homogenous scenarios statistically-derived model is farthest from the FP=TP line, which represents an ineffective (i.e. random) test, and is therefore the most effective in finding explosives in homogenous cargo screening scenarios. As expected, performance of all detection algorithms decreased significantly when applied to all of the screening scenarios, as shown by comparing Figs. 9-2a and 9-2b.

Table 9-5 lists the figures of merit, as defined by the area under the ROC curve, for the five algorithms when applied to both homogenous and all screening scenarios. This table shows that, for homogenous scenarios, both the idealistic scenario and homogenous scenario statistically-modeled algorithms exceeded the earlier algorithms. However, when all screening scenarios were considered, only the all-scenario statistically-modeled algorithm performed better than the earlier algorithms, with a figure of merit of 0.77 compared to the other's 0.70-0.72. This improvement is partly due to the fact that the earlier algorithms were designed using mainly homogenous cargos while analysis for the statistically-modeled algorithm was based on all available types of simulation data.

Consequences of low-prevalence realities

As is the case with any test designed around realities in which the prevalence of true positives is extremely low, the vast majority of the positive test results will be false positives. For example, if the proposed method were used as a primary screening technique in an environment in which the prevalence of explosives was 0.01%, and detection thresholds were set such that there was a 20% FP rate and 80% TP rate, only 0.04% of the positive readings would actually have explosives. This rate improves significantly if the algorithm were used as a secondary scanning system behind a primary scanning system, such as one that increased the prevalence of containers with explosive to 1%. In this case, 3.8% of positive readings would actually contain explosives.

Advantages and disadvantages of the proposed system

Conclusions and Future Work

Efforts using statistical modeling software to improve a flag-based explosives detection algorithm have shown promise, increasing the figure of merit, defined to have a value between 0.5 and 1.0, from 0.72 to 0.77. Models have been found that correctly identify the presence or absence of the explosive RDX more than 80% of the time. Different models have been explored for cases with both heterogeneous and homogenous cargo configurations. Results have shown that the statistically-modeled algorithm performed better than both of the detection algorithms proposed in previous chapters when applied to all screening scenarios. Future efforts should explore statistically-modeled algorithms in greater depth, along with testing new variables and new combinations of the variables discussed above. Furthermore, the new model should be rigorously tested with additional simulations before experimental validation.

Figures

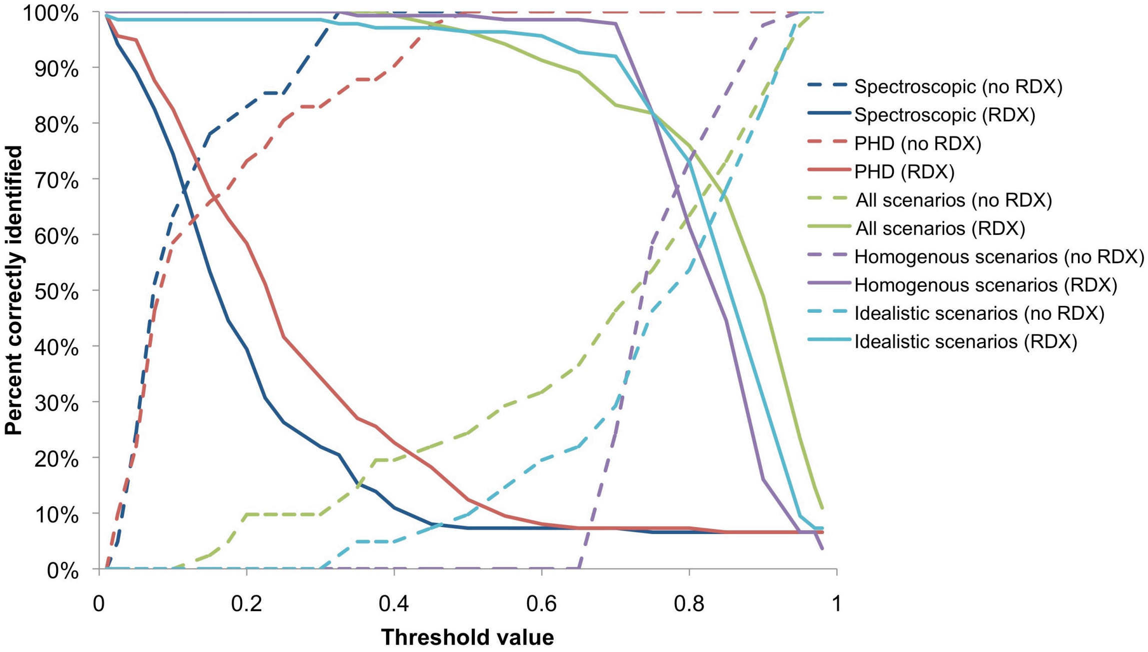

Figure 9-1. Relationship between the triggering cut-off threshold and the percent of correctly identified screening scenarios with and without the explosive RDX for the three statistically-derived detection models as well as the earlier spectroscopic and PHD algorithms.

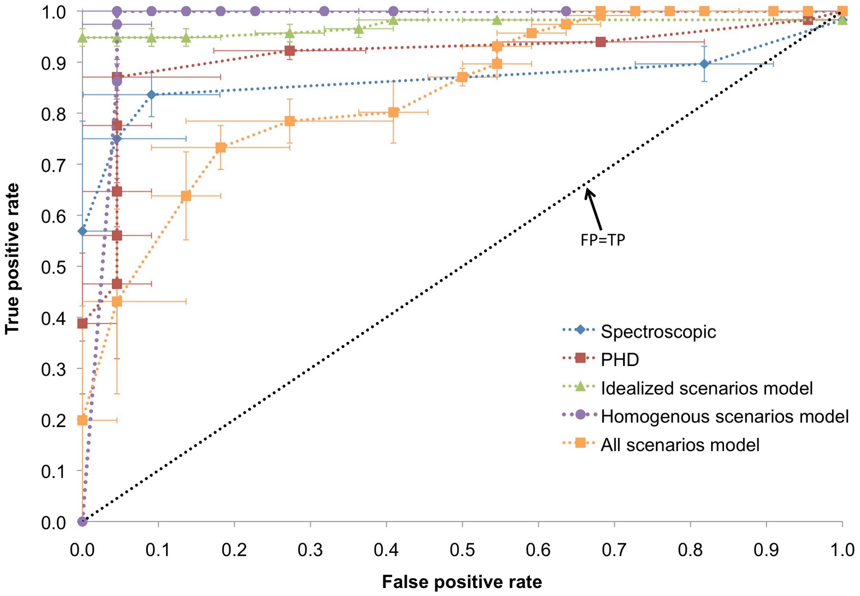

a.

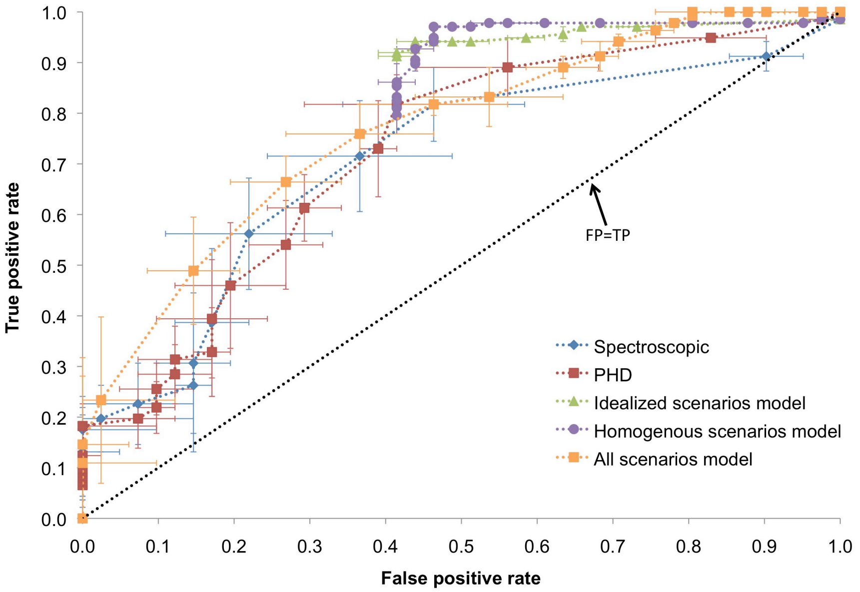

b.

Figure 9-2. ROC curves for the five different detection algorithms when applied to a) homogenous and b) all screening scenarios. Also shown is the false positive (FP) equals true positive (TP) line. Error bars reflect uncertainty due to 10% random measurement error and lines serve only to guide the eye.

Tables

Table 9-1. List of neutron-based flags used in statistical model development.

Neutron peak	Neutron energy range	Neutron PHD
$\frac{(10.8\ \text{MeV},150^\circ)}{(10.8\ \text{MeV},0^\circ)}$	$\frac{(>10\ \text{MeV},120^\circ)}{(>10\ \text{MeV},0^\circ)}$	$\frac{(>4.9\ \text{MeVee},150^\circ)}{(<0.14\ \text{MeVee},0^\circ)}$
$\frac{(11\ \text{MeV},150^\circ)}{(11\ \text{MeV},0^\circ)}$	$\frac{(>10\ \text{MeV},150^\circ)}{(>10\ \text{MeV},0^\circ)}$	$\frac{(>5.8\ \text{MeVee},150^\circ)}{(<0.14\ \text{MeVee},0^\circ)}$
$\frac{(11.2\ \text{MeV},150^\circ)}{(11.2\ \text{MeV},0^\circ)}$	$\frac{(6-10\ \text{MeV},150^\circ)}{(6-10\ \text{MeV},0^\circ)}$	$\frac{(>5.8\ \text{MeVee},150^\circ)}{(>4.9\ \text{MeVee},0^\circ)}$
$\frac{(11.4\ \text{MeV},120^\circ)}{(11.4\ \text{MeV},0^\circ)}$	$\frac{(>10\ \text{MeV},150^\circ)}{(<1\ \text{MeV},0^\circ)}$	$\frac{(2.1-4.9\ \text{MeVee},150^\circ)}{(2.1-4.9\ \text{MeVee},0^\circ)}$
$\frac{(11.6\ \text{MeV},120^\circ)}{(11.6\ \text{MeV},0^\circ)}$		$\frac{(>4.9\ \text{MeVee},120^\circ)}{(>4.9\ \text{MeVee},0^\circ)}$
$\frac{(11\ \text{MeV},150^\circ)}{(0.8\ \text{MeV},0^\circ)}$		$\frac{(>4.9\ \text{MeVee},150^\circ)}{(<4.9\ \text{MeVee},0^\circ)}$
$\frac{(11\ \text{MeV},150^\circ)}{(10\ \text{MeV},0^\circ)}$		$\frac{(>5.8\ \text{MeVee},120^\circ)}{(>5.8\ \text{MeVee},0^\circ)}$
$\frac{(11.\text{MeV},150^\circ)}{(9.6\ \text{MeV},0^\circ)}$		$\frac{(>5.8\ \text{MeVee},150^\circ)}{(>5.8\ \text{MeVee},0^\circ)}$

Table 9-2. List of photon- and neutron-photon-based flags used in statistical model development.

Photon peak	
$\frac{5.2\ \text{MeV}}{1.0\ \text{MeV}}$	$\frac{6.2\ \text{MeV}}{2.6\ \text{MeV}}$
$\frac{6.8\ \text{MeV}}{1.0\ \text{MeV}}$	$\frac{6.2\ \text{MeV}}{2.8\ \text{MeV}}$
$\frac{6.2\ \text{MeV}}{1.8\ \text{MeV}}$	$\frac{4.6\ \text{MeV}}{3.4\ \text{MeV}}$
$\frac{6.2\ \text{MeV}}{2.4\ \text{MeV}}$	$\frac{5.2\ \text{MeV}}{3.4\ \text{MeV}}$
$\frac{4.6\ \text{MeV}}{2.6\ \text{MeV}}$	$\frac{6.2\ \text{MeV}}{3.4\ \text{MeV}}$
$\frac{5.2\ \text{MeV}}{2.6\ \text{MeV}}$	$\frac{5.2\ \text{MeV}}{3.8\ \text{MeV}}$
Combined neutron-photon	
$\frac{\left[\frac{\text{total neutrons, } 150^\circ}{\text{total neutrons, } 0^\circ}\right]}{\text{C photons}}$	$\frac{\left[\frac{\text{total neutrons, } 90^\circ}{\text{total neutrons, } 0^\circ}\right]}{\text{N photons}}$
$\frac{\left[\frac{\text{total neutrons, } 90^\circ}{\text{total neutrons, } 0^\circ}\right]}{\text{C photons}}$	$\frac{\left[\frac{\text{total neutrons, } 150^\circ}{\text{total neutrons, } 0^\circ}\right]}{\text{O photons}}$
$\frac{\left[\frac{\text{total neutrons, } 150^\circ}{\text{total neutrons, } 0^\circ}\right]}{\text{N photons}}$	$\frac{\left[\frac{\text{total neutrons, } 90^\circ}{\text{total neutrons, } 0^\circ}\right]}{\text{O photons}}$

Table 9-3. Best-performing models for explosives detection in idealized scenarios, explosives detection in homogenous cargos, and explosives detection in all scenarios. Also shown are the statistical significance (p-value) and maximum likelihood estimate of the multiplying parameter (B).

Number cases	Percent accuracy	Variable	p-value	B
		Explosives detection in idealized scenarios		
73	99%	Maximum R	0.039	-105
		Maximum T	0.044	-611
		Median T	0.045	928
		Mean P	0.092	305
		$P\left[\frac{(>5.8\text{ MeVee},150^\circ)}{(>5.8\text{ MeVee},0^\circ)}\right]$	0.095	148
		Constant	0.052	-12.1
		Explosives detection in homogenous cargos		
138	99%	$P\left[\frac{(11\text{ MeV},150^\circ)}{(0.8\text{ MeV},0^\circ)}\right]$	0.043	-27.3
		$T\left[\frac{(>4.9\text{ MeVee},120^\circ)}{(>4.9\text{ MeVee},0^\circ)}\right]$	0.022	99.9
		$T\left[\frac{(>5.8\text{ MeVee},150^\circ)}{(>5.8\text{ MeVee},0^\circ)}\right]$	0.13	-40.4
		Maximum off-center T	0.26	17.3
		Constant	0.087	-2.95
		Explosives detection in random half of all scenarios		
89	87%	Median off-center T	0.066	22.1
		$T\left[\frac{5.2\text{ MeV photons}}{1.0\text{ MeV photons}}\right]$	0.12	-28.4
		$T\left[\frac{6.8\text{ MeV photons}}{1.0\text{ MeV photons}}\right]$	0.035	28.1
		$P\left[\frac{5.2\text{ MeV photons}}{2.6\text{ MeV photons}}\right]$	0.044	-40.1
		Constant	0.084	1.62

Table 9-4. Alternative model for explosives detection in homogenous scenarios utilizing only flags calculated using currently available technology. Also shown are the statistical significance values (p-value) and fitted multiplier parameter (B).

Number cases	Percent accuracy	Variable	p-value
138	98%	Maximum R	0.29
		$P\left[\frac{(>5.8\text{ MeVee},150^\circ)}{(>5.8\text{ MeVee},0^\circ)}\right]$	0.0010
		Median T	0.0070
		Maximum T	0.010
		Constant	0.11

Table 9-5. Figure of merit, defined by area under ROC curve, for the five explosives-detection models for homogenous screening scenarios and all screening scenarios.

Explosives-detection model	In homogenous Screening Scenarios	In all Screening Scenarios
Idealistic	0.97	0.56
Homogenous	0.97	0.57
All scenarios	0.84	0.77
PHD	0.91	0.72
Spectroscopic	0.87	0.70

References

1. M.-A. Descalle, D. Manatt, D. Slaughter, “Analysis of recent manifests for goods imported through US ports”, Report UCRL-TR-225708, Lawrence Livermore National Laboratory (2006).
2. A.L. Lehnert, K.J. Kearfott, "The detection of explosive materials: review of considerations and methods", Nucl. Technol. 172 (2010) 325-334.
3. R.A. Forster, L.J. Cox, R.F. Barrett, T.E. Booth, J.F. Briesmeister, F.B. Brown, J.S. Bull, G.C. Geisler, J.T. Goorley, R.D. Mosteller, S.E. Post, R.E. Prael, E.C. Selcow, A. Sood, “MCNP Version 5”, Nucl. Instrum. Methods Phys. Res. B 213 (2004) 82-86.
4. S. Pozzi, E. Padovani, M. Marseguerra, “MCNP-PoliMi: a Monte-Carlo code for correlation measurements”, Nucl. Instrum. Methods Phys. Res. A 513 (2003) 550-558.
5. E. C. Miller, S.D. Clarke, M. Flaska, S. Pozzi, E. Padovani, “MCNPX-PoliMi Post-Processing Algorithm for Detector Response Simulations”, Journal of Nuclear Materials Management (in press) (2011).
6. A.L. Lehnert, K.J. Kearfott, “Simplified simulation of fast neutron scattering for an explosives detection application”, Nucl. Sci. Eng. 168 (2010) 278-286.
7. A.L. Lehnert, K.J. Kearfott, “Preliminary identification of flags for a novel algorithm-based approach for explosives detection using neutron interrogation for a simulated idealized cargo container scenario”, Nucl. Instrum. Methods Phys. Res. A 638 (2011) 201-205.
8. A.L. Lehnert, K.J. Kearfott, “Simulations for developing a flag-based active neutron interrogation method for explosives detection in sea-land cargo containers”, (unpublished) (2011).
9. A.L. Lehnert, K.J. Kearfott, “A flag-based algorithm and associated neutron interrogation system for the detection of explosives in sea-land cargo containers”, (unpublished) (2011).
10. A.L. Lehnert, K.J. Kearfott, “Evaluation of an explosives-detection algorithm for use in sea-land cargo containers”, (unpublished) (2011)
11. A.L. Lehnert, K.J. Kearfott, “D-D Neutron Scatter Measurements for an Explosives Detection Technique”, Nucl. Instrum. Methods Phys. Res. A (submitted for publication) (2011).
12. K.J. Kearfott, S. Han, K. McMahan, E. Samei, “Sensitivity of a mixed field dosimetry algorithm to uncertainties in thermoluminescent element readings”, Health Phys, 68 (1995) 340-349.
13. K.J. Kearfott, S. Han, E.C. Wagner, E. Samei, C.-K. C Wang, “Numerical simulation of a TLD pulsed laser-heating scheme for determination of shallow dose and deep dose in low-let radiation fields”, Appl. Radiat. Isot. 52 (2000) 1419-1429.
14. Z.D. Whetstone, S.C. Dewey, K.J. Kearfott, "Simulation of a method for determining one-dimensional ^{137}Cs distribution using multiple gamma spectroscopic measurements with an adjustable cylindrical collimator”, Appl. Radiat. Isot. 69 (2011) 790-802.

15. J.E. King, “Binary logistic regression”, in: Best Practices in Quantitative Methods, Sage Publications, Inc. (2008)
16. T. Fawcett, “An introduction to ROC analysis”, Pattern Recognition Letters, 27 (2006) 861-874.

Chapter 10: Conclusions and Future Work

Summary of Findings

The problem of explosives detection has been under intensive study for several decades. Explosives detection in large targets, such as the standard land-sea cargo containers studied here, has proven especially difficult. Several strategies based on nuclear technology have been tested, with varying degrees of success. Although neutron interrogation has the potential to be an extremely effective method due to high target penetrability and ability to distinguish among light elements, it has yet to be deployed in cargo scanning on a large scale. The basic strategies for explosives detection using neutron interrogation include thermal neutron activation, measurement of characteristic de-excitation photons, and measurements of the reflected and transmitted neutron flux. In this study, the photon and neutron products of neutron interactions in target material have been combined in a novel way that maximizes the number of signal carriers and thus decreases the number of incident neutrons. This innovative strategy relies on the calculation of flags, generally in the form of ratios of specific neutron or photon measurements, and then combining these flags into a detection algorithm. This algorithm is designed to be fully automatic and functions with a wide variety of cargo materials. This dissertation details the steps leading to the development of the algorithm and its application in an explosives-screening system.

The first step of the algorithm development, as described in Chapter 3, involved the characterization of the neutron scatter interaction products in the cargo container. This included identification of the neutron and photon peaks produced when fast neutrons scattered off targets of hydrogen, carbon, nitrogen, oxygen, and iron at different angles. Once these characteristic neutron and photon peaks were identified, other targets of interest were included in the simulations. These targets included hydrogenous (water), organic (vegetable oil), and metallic (steel) materials and results showed the expected combination of the earlier-identified features. Several of the most distinct features, such as inelastic photon peaks, inelastic neutron peaks, as well as the elastically-scattered neutrons, formed the basis of potential flags. These highly simplified simulations demonstrated that it was possible to discern the expected neutron and photon peaks, and that these peaks were superimposed in the expected manner when more than one element was present in the target.

The next step involved benchmarking the simulations with laboratory measurements, as discussed in Chapter 4. These measurements utilized a D-D neutron generator, several different scatter materials including the explosives-surrogate melamine, as well as two different neutron detectors. One detection system, which utilized a coarse neutron spectroscopy system, measured the change in both total and high-energy neutron flux when target materials were in place. The other system also counted total neutron flux, but allowed a more detailed manipulation of the pulse height distribution (PHD), including separation of the neutron and photon pulses. These measured results were compared with simulations, including simulations of the detector PHDs. It was found that both the changes in neutron flux and the PHDs compared favorably between the simulation and measurement, with correlation coefficients of greater than 0.75 and 0.97, respectively. The results of this study demonstrated that basic approximations in the simulation geometry allowed an accurate portrayal of neutron scatter and a 10% error due to measurement was reasonable.

The next chapter utilized the characteristic features found in Chapter 3 to find the most significant differences in cases with and without explosive under idealistic conditions. These flags fell into one of four categories: based solely on the backscatter neutron spectrum, ratios of specific neutron tallies at one energy and different angles, ratios of select neutron peaks, and ratios of photon peaks. The best-performing flags were then identified for the three types of cargo: metallic, organic, and hydrogenous. This chapter also explored the effect of the position and amount of explosive on the flag calculations. It was found that flag strength was highly dependent on source-explosive distance, but flag strength for flags based on neutron tally ratios responded in a linear fashion. Similarly, these flags showed a predictable, roughly linear response to changes in explosive mass.

Chapter 6 expanded on the findings of Chapter 5 by testing the previously identified flags in a more realistic simulated environment. This included a more accurate representation of a shielded D-T neutron generator, inclusion of the surrounding environment, and expansion on the materials inside the cargo containers. Other simulations utilized a palletized distribution of cargo in the container instead of the homogenous distribution used earlier. The results from these simulations also served to build on the earlier flag selection by forming the basis of “combinatory” flags that combined the identities of several of the best-performing flags from the previous chapter into flags that required far less stringent neutron spectroscopy. Further testing showed that the combinatory flags performed as well as, or better than, the more specific flags that they were based on. Another aspect of the added realism was the simulation of the neutron detector response using MCNP-PoliMi. The simulated detector response included calculated time-of-flight and PHDs. Several flags were then tested that converted the energy thresholds of the combinatory flags into pulse height thresholds in the pulse height distributions, creating flags that did not require any unfolding of the neutron spectrum. Results showed that several explosives-detection showed promise under relatively realistic simulated conditions. Furthermore, in most cases the PHD-based flags performed better than, or as well as, the combinatory flags. Finally, the very best flags for explosives-detection were identified for two types of cargo materials: organic/hydrogenous and inorganic/metallic.

In Chapter 7 these flags were put together into an explosives detection algorithm. This algorithm had three main steps: materials determination, explosives detection, and correction for cargo inhomogeneities, along with an additional step that identified entirely explosives-filled containers. The explosives portion of the algorithm was triggered when the values of certain flags exceeded their average value over the container by a certain threshold amount. This algorithm is applied as part of a detection system in which cargo containers are irradiated with a 14.1 MeV fan beam from below at five evenly distributed points for less than two minutes each along the length of the container. Surrounding the container in a ring are eleven large liquid scintillation neutron detectors and several photon detectors. Transport through the detection system by either a conveyor belt or rail apparatus that held the containers from above or below. The dose estimate for operators behind a concrete shield is less than the average annual dose to a member of the public, as is that to an individual hidden in the container for one pass through the scanning system. It was estimated that each scanning system would cost approximately $1M and could scan one container every ten minutes.

The detection algorithm and associated scanning system was further optimized and evaluated in Chapter 8. This included optimization of the algorithm trigger thresholds and estimates of the algorithm sensitivity and specificity. Several sources of error were considered, including a conservative 10% random measurement error, the effect of photon escape peaks, and noise due to multiple neutron interactions in the surrounding environment. Receiver-operating characteristic curves for the proposed algorithm showed that it performed very well in relatively homogenous cargos. Algorithm performance was quantified for cases with heterogeneous cargo configurations as well as a function of explosive size and position. Given the influence of these factors, it was possible to estimate the minimum detectable amount of explosive in “more difficult” organic cargos, such as paper, to approximately 200 kg while amounts as small as 25 kg could be identified in metallic cargos.

Chapter 9 discussed improvements to the detection algorithm using statistical modeling software. The software incorporated several flags found earlier into several types of variables and performed binary logistic regression on them in order to create a model that correctly identified containers with explosives. These models showed superior performance to the earlier algorithms, especially in heterogeneous cargos or in cases in which the explosive was not centered over a scanning location and could correctly identify the presence or absence of the explosive RDX more than 80% of the time.

The proposed system has several advantages over other nuclear-based explosives detection systems. Like other active neutron interrogation systems, the method discussed here depends on detecting the actual explosive material, instead of metallic components, as is used in photon interrogation techniques. Because the proposed system uses both neutrons and photons in a simple, automatic algorithm, interrogation times are considerably shorter than other neutron-based methods and do not require highly skilled operating personnel. Furthermore, the algorithm may be implemented without using stringent neutron spectroscopy or other expensive and time-consuming detection technologies. However, the current algorithm is only able to detect large explosives and has a relatively high false positive rate.

Future Directions

There are several ways in which the proposed system could be improved, as well as further studies that could more clearly define the abilities and limitations of the current implementation of the detection algorithm. Future systems could utilize better detection technology, which could potentially significantly improve both the minimum detectable amount and the false positive/false negative rate.

Changes and optimization of explosives detection algorithm

As mentioned above, preliminary efforts have shown that it is possible to improve the detection algorithm using statistical modeling of several flags. These efforts should be expanded, both in testing new variables and combinations of variables, and exploring new screening scenarios. The current algorithm is relatively good at differentiating between organic/hydrogenous materials and inorganic/metallic cargos. However, intermediate cargo types, such as furniture or toys, are often mislabeled. The modeling software could potentially be used to find a model that better differentiated between cargo types. An increase in the number of cargo types considered, and optimization of the materials-determination portion of the algorithm would improve algorithm performance. Other potential improvements could be made by optimizing the triggering thresholds, depending on the type of cargo and flag identity. Treating the symmetrical, i.e. same scatter angle, detectors individually and testing other flags based on the neutron pulse height distributions could also further improve algorithm performance. Another change could be to add adjacent trigger values together, and compare the sum with the other three sums of adjacent trigger values in order to better detect explosives located between the scanning positions. Another improvement could be made by testing the use of wider energy bins in place of the 0.2 MeV energy bins currently being used in the two remaining detection flags based on single neutron bin ratios. It is also possible that other well-performing flags could be made using the PHD or time-of-flight distributions that would further decrease the need for neutron spectroscopy. Further efforts should examine how well the algorithm functions when different types of cargo are present within one container and when the cargo is distributed heterogeneously throughout the container. It is possible that artificial intelligence techniques, such as neural networks, could be used to further optimize the algorithm, such as in materials identification or the influence of inert but dense objects in the container.

Improvements to screening system

Other ways that MCNP-PoliMi could be used to improve the proposed system include optimization of the positions and numbers of neutron and photon detectors as well as the source shielding and position. Another improvement that may prove necessary is better photon spectroscopy, such as cadmium zinc telluride (CdZnTe) and future efforts should be made to better model the photon detector response in the explosives-detection system. Perhaps the greatest improvement could be made by considering combining the current active neutron interrogation system with a photon scanning system. Use of a powerful photon source could provide tomographic information on the structure and relative electron density of the container’s contents. This information would improve the materials-determination portion of the detection algorithm and could also eliminate false measurements by acting as a confirmation of the results obtained through neutron interrogation. As is the case with any changes to the system technology, there are intrinsic trade-offs between resolution, detection efficiency, and container throughput that must be considered in the optimization process. Eventually, measurements must be made using a D-T neutron generator to test simulation results.

Other applications of flags or the detection algorithm

Many of the flags discussed in this study have the potential for other explosives-screening applications. Scanning other large targets, such as air freight containers, could potentially use the algorithm and screening system discussed here with minimal modifications. Smaller explosives screening scenarios, such as for luggage or mail could potentially use the flags in modified algorithms, probably through comparison to explosive templates. There is also the potential that these smaller screening scenarios could use the multiple-irradiation method discussed here, but with a D-D neutron generator instead of D-T neutron generator.

Other contraband screening problems, such as those for narcotics or special nuclear material could use modified versions of the algorithm discussed here. These substances would require different flags in the algorithm, but the strategy of identifying changes in flags as a function of position could be applied to almost any scenario in which one is searching for bulk contraband in large targets. Furthermore, many of the strategies for improving the algorithm discussed here, such as binary logistic regression, would be applicable to these other screening scenarios.

Appendix A: Simulation Input Examples

Neutron scatter characterization examples

Example with single compound target

```
c NES pure RDX target sphere
1 2 -7.87 3 -1 -7 8 -11 12         imp:n=1 imp:p=1
2 2 -7.87 2 -4 -7 8 -11 12         imp:n=1 imp:p=1
3 2 -7.87 -5 7 -1 2 10 -9          imp:n=1 imp:p=1
4 2 -7.87 6 -8 -1 2 10 -9          imp:n=1 imp:p=1
5 2 -7.87 11 -9 -7 8 -1 2          imp:n=1 imp:p=1
6 2 -7.87 10 -12 -7 8 -1 2         imp:n=1 imp:p=1
7 1 -.0012 -3 4 -7 8 -11 12 #22 imp:n=1 imp:p=1
8 1 -.0012 -13 #1 #2 #3 #4 #5 #6 #7 #10 #11 #12 #13 #14 #15 #16 #17 #18 #19 #20
     #21 #22                        imp:n=1 imp:p=1
9 0 13                              imp:n=0 imp:p=0
10 0 -14 26                         imp:n=1 imp:p=1
11 0 -15 26                         imp:n=1 imp:p=1
12 0 -16 26                         imp:n=1 imp:p=1
13 0 -17 26                         imp:n=1 imp:p=1
14 0 -18 26                         imp:n=1 imp:p=1
15 0 -19 26                         imp:n=1 imp:p=1
16 0 -20 26                         imp:n=1 imp:p=1
17 0 -21 26                         imp:n=1 imp:p=1
18 0 -22 26                         imp:n=1 imp:p=1
19 0 -23 26                         imp:n=1 imp:p=1
20 0 -24 26                         imp:n=1 imp:p=1
21 0 -25 26                         imp:n=1 imp:p=1
22 3 -1.82 -27                      imp:n=1 imp:p=1            $RDX target

1 px 121.92
2 px -121.92
3 px 121.603
4 px -121.603
5 py 609.6
6 py -609.6
7 py 609.283
8 py -609.283
9 pz 152.4
10 pz -152.4
11 pz 152.083
12 pz -152.083
13 so 1000
14 sz 304.8 78
15 sz -304.8 78
16 sx 304.8 78
17 sx -304.8 78
```

```
18 s 152.4 0 263.965 78
19 s -152.4 0 263.965 78
20 s 152.4 0 -263.965 78
21 s -152.4 0 -263.965 78
22 s 263.965 0 152.4 78
23 s 263.965 0 -152.4 78
24 s -263.965 0 152.4 78
25 s -263.965 0 -152.4 78
26 so 304.8
27 so 93.5                                           $target sphere

mode p n
m1 6012 .0001 7014 .755 8016 .232 18000 .013        $air
m2 26000 .9959 6012 .0032 16032 .0005 15031 .0004 $carbon steel
m3 6012 .143 7014 .285 8016 .286 1001 .286          $RDX
sdef POS=-304.8 0 0 PAR=1 ERG=14.1 VEC=1 0 0 DIR=D1
si1 H 0.956 1                                       $cosine of angle needed
sp1 0 1
nps 100000000                                       $number of histories
e0 .2 .4 .6 .8 1 69I 15 20
f11:n 16
f21:p 16
f31:n 22
f41:p 22
f51:n 18
f61:p 18
f71:n 14
f81:p 14
f91:n 19
f101:p 19
f111:n 24
f121:p 24
f131:n 17
f141:p 17
f151:n 25
f161:p 25
f171:n 21
f181:p 21
f191:n 15
f201:p 15
f211:n 20
f221:p 20
f231:n 23
f241:p 23
```

Simulations for 2.4 MeV Neutron Scatter Experiments

90° neutron scatter with shielding block

```
c d-d generator with melamine target and MS2 on two wooden tables
c ------Cell Cards---------------------------------------
c 3456789 123456789 223456789 323456789 423456789 523456789 623456789 723456789
1 3 -0.65     -1                        imp:n=1 imp:p=1 $ short wooden table
2 3 -0.65     -2                        imp:n=1 imp:p=1 $ long wooden table
3 7 -0.874    -3                        imp:n=1 imp:p=1 $ active volume of detector
4 8 -0.329    -4                        imp:n=1 imp:p=1 $ electronics box of detector
5 2 -7.87     -5 6                      imp:n=1 imp:p=1 $ metal cylinder of mp320
7 8 -0.329    -7                        imp:n=1 imp:p=1 $ electronics of mp320
8 1 -0.000012 -6                        imp:n=1 imp:p=1 $ almost vacuum inside mp320
11 5 -1.57    -11                       imp:n=1 imp:p=1 $ melamine target
100 1 -0.0012 1 2 3 4 5 6 7 11 -91      imp:n=1 imp:p=1 $ air surrounding everything: change
depending on target and shield
101 1 -0.0012  92  93 -100              imp:n=1 imp:p=1 $ air outside wall
102 9 -2.3 91 -92                       imp:n=1 imp:p=1 $ concrete wall
109 10 -1.75 -93  -100                  imp:n=1 imp:p=1 $ soil under floor
110 0    100                            imp:n=0 imp:p=0 $ past the end of the world (imp=0)
c ------End Cell Cards----------------------------------

c ------Surface Cards------------------------------------
1 box   0.01 0    0       91.4 0 0  0 60.9   0  0 0 -5.08            $ short table
2 box   0    0.01 0.01    -60.9 0 0  0 183.01 0  0 0 -5.07           $ long table
3 rcc   26.39  30.45  1.875    -3.5 0 0       1.8749                 $ active volume
4 box   26.3901 17.65 0.011  22 0 0   0 25.6 0    0 0 25.6           $ detector electronics
5 rcc  -30.45 152.37 5.1    0 55.8 0    5.08                         $ outer cylinder of mp320
6 rcc  -30.45 152.87 5.1    0 54.8 0    4.6                          $ inner cylinder of mp320
7 box  -38.38 161.704 10.2  15.875 0 0  0 37.211 0 0 0 13.97         $ electronics box of mp320
91 box -300 -300 -91.44    600 0 0    0 600 0   0 0 300              $ inside of wall
92 box -400 -400 -191.44   800 0 0    0 800 0   0 0 500              $ outside of wall
93 pz  -192.92                                                       $ edge of floor
11 box -22.94 22.95 0.02    -15 0 0    0 15 0    0 0 14.15           $ melamine target
100 so 1000                                                          $ end of the world!!
c ---------end surface cards-------------------------------

c --------Material Cards----------------------------------
m1 6012 .0001 7014 .755 8016 .232 18000 .013             $ air p=0.0012
m2 26000 .9959 6012 .0032 16032 .0005 15031 .0004        $ carbon steel p=7.87
m3 1001 0.47619 6000 0.285714 8016 0.238095              $ wood p=0.65 (pine)
m4 1001 .667 8016 .333                                   $ water p=1
m5 1001 0.4 12000 0.2 14000 0.4                          $ melamine p=1.57
m6 6012 0.335 8016 0.037 1001 0.628                      $ vegetable oil p=0.918
m7 6012 0.335 6000 0.452                                 $ NE213 detector material p=0.874
m8 1001 0.257 6012 0.0187 8016 0.468 13027 0.0259 &
    14028 0.123 28000 0.1043                             $ det electronics material p=0.329467
m9 1001 0.304245  6012 0.002870  8016 0.498628  11023 0.009179 13027 0.010261 &
     14000 0.150505  19000 0.007114  20000 0.014882  &
       26000 0.001599                                    $ ordinary concrete p=2.3
m10 1001 0.2938 6012 0.0187 8016 0.5045 13027 0.0259 14028 &
  0.1354 19000 0.0143 26056 0.0027                       $ soil EPA GR 12 standard p=1.75
```

```
c ------- End Material Cards ------------------------------
c ------- Data Cards -------------------------------------
mode p n
sdef POS=-30.45 152.37 7.64 PAR=1 ERG=2.4          $ monoenergetic 2.4 MeV neutron source
nps 200000000                                       $ number of histories
c ---------- End Data Cards -------------------------------
c ---------- Tally Cards ---------------------------------
c f6 energy deposition tallies, MeV/g on MS2 detector and idealized MS2
f16:n 3                                             $ MS2 0.2 MeV energy bins
e16 .2 .4 .6 .8 1 69I 15 20                         $ 0.2 MeV Energy Bins
f26:p 3                                             $ MS2 0.2 MeV energy bins
e26 .2 .4 .6 .8 1 69I 15 20                         $ 0.2 MeV Energy Bins
f36:n 3                                             $ MS2 with MS2 energy bins
e36 .01 .5 1 1.5 2 3 4 5 6 7 8 9 10 12 14 16 18 20  $ MS2 energy bins
c ------End Tally Cards ---------
```

120° neutron scatter with shielding block

```
c d-d generator, oil-shielded melamine target, shielded MS2,120 deg scatter
c ------Cell Cards---------------------------------------
c 3456789 123456789 223456789 323456789 423456789 523456789 623456789 723456789 $
convenient column counter :)
1 3 -0.65     -1                    imp:n=1 imp:p=1 $ short wooden table
2 3 -0.65     -2                    imp:n=1 imp:p=1 $ long wooden table
3 7 -0.874    -3                    imp:n=1 imp:p=1 $ active volume of detector
4 8 -0.329    -4                    imp:n=1 imp:p=1 $ electronics box of detector
5 2 -7.87     -5 6                  imp:n=1 imp:p=1 $ metal cylinder of mp320
7 8 -0.329    -7                    imp:n=1 imp:p=1 $ electronics of mp320
8 1 -0.000012 -6                    imp:n=1 imp:p=1 $ almost vacuum inside mp320
12 5 -1.57    -11                   imp:n=1 imp:p=1 $ melamine target
21 4 -1       -21                   imp:n=1 imp:p=1 $ shielding box between det and source
22 6 -0.918   -22                   imp:n=1 imp:p=1 $ oil shield
100 1 -0.0012  1 2 3 4 5 6 7 11 21 22 -91     imp:n=1 imp:p=1 $ air surrounding everything
101 1 -0.0012  92  93 -100          imp:n=1 imp:p=1 $ air outside walls
102 9 -2.3 91 -92                   imp:n=1 imp:p=1 $ concrete
109 10 -1.75 -93  -100              imp:n=1 imp:p=1 $ soil under floor
110 0    100                        imp:n=0 imp:p=0 $ past the end of the world (imp=0)
c ------End Cell Cards-----------------------------------

c ------Surface Cards------------------------------------
1 box   0.01 30 0       91.4 0 0  0 76.2   0  0 0 -5.08              $ short table
2 box   0 0 0   -45.72 0 0  0 304.8 0  0 0 -5.07                     $ long table
3 rcc   27.94 102.79 5      -6.63 3.98 0      2.54                   $ active volume
4 box   42 84 0 -18.42 11.26 0 8.614 14.085 0 0 0 15.875             $ detector electronics
21 box  9.63 61.4 0   -20.68 12.42 0   9.15 15.24 0   0 0 27.94      $ shielding box
5 rcc   -22.86 0 5.09   0 55.8 0    5.08                             $ outer cylinder of mp320
6 rcc   -22.86 0.5 5.09   0 54.8 0    4.60                           $ inner cylinder of mp320
7 box   -30.79 9.334 10.17   15.875 0 0  0 37.211 0  0 0 13.97       $ electronics box of mp320
11 box  -34.29 133.27 0     22.86 0 0    0 11.43 0   0 0 20.32       $ melamine target
22 box  -35.56 119.3 0       25.4 0 0    0 13.97 0   0 0 25.4        $ oil shield
91 box -300 -300 -91.44    600 0 0    0 700 0   0 0 300              $ inside of concrete walls
92 box -400 -400 -191.44   800 0 0    0 900 0   0 0 500              $ outside of concrete walls
93 pz  -192.92                                                       $ edge of floor (bottom)
100 so 1000                                                          $ end of the world!!
c ---------end surface cards------------------------------

c --------Material Cards---------------------------------
m1 6012 .0001 7014 .755 8016 .232 18000 .013              $ air p=0.0012
m2 26000 .9959 6012 .0032 16032 .0005 15031 .0004         $ carbon steel p=7.87
m3 1001 0.47619 6000 0.285714 8016 0.238095               $ wood p=0.65 (pine)
m4 1001 .667 8016 .333                                    $ water p=1
m5 1001 0.4 12000 0.2 14000 0.4                           $ melamine p=1.57
m6 6012 0.335 8016 0.037 1001 0.628                       $ vegetable oil p=0.918
m7 6012 0.335 6000 0.452                                  $ NE213 detector material p=0.874
m8 1001 0.257 6012 0.0187 8016 0.468 13027 0.0259 14028 0.123 28000 0.1043  $ electronics
m9 1001 0.304245  6012 0.002870  8016 0.498628  11023 0.009179 13027 0.010261 &
     14000 0.150505  19000 0.007114  20000 0.014882  26000 0.001599       $ concrete p= 2.3
m10 1001 0.2938 6012 0.0187 8016 0.5045 13027 0.0259 14028 &
     0.1354 19000 0.0143 26056 0.0027                     $ soil EPA GR 12 standard p=1.75
c ------- End Material Cards -----------------------------
```

```
c ------- Data Cards --------------------------------------
mode p n
sdef POS=-22.86 41.83  5.09 PAR=1 ERG=2.4              $ monoenergetic 2.4 MeV neutron source
nps 200000000                                          $ number of histories
c ---------- End Data Cards -------------------------------
c ---------- Tally Cards ---------------------------------
c f6 energy deposition tallies, MeV/g on MS2 detector and idealized MS2
f16:n 3                                        $ MS2 0.2 MeV energy bins
e16 .2 .4 .6 .8 1 69I 15 20                    $ 0.2 MeV Energy Bins
f26:p 3                                        $ MS2 0.2 MeV energy bins
e26 .2 .4 .6 .8 1 69I 15 20                    $ 0.2 MeV Energy Bins
f36:n 3                                        $ MS2 with MS2 energy bins
e36 .01 .5 1 1.5 2 3 4 5 6 7 8 9 10 12 14 16 18 20   $ MS2 energy bins
c ------End Tally Cards ---------
```

90° neutron scatter with dual neutron detection systems (MCNP-PoliMi)

```
c d-d generator with paper target, MS2, and EJ-309 on tables and chair with water shielding from
8/19/10 measurement
c ------Cell Cards---------------------------------------
c 3456789 123456789 223456789 323456789 423456789 523456789 623456789 723456789 $
convenient column counter :)
1 3 -0.65     -1                        imp:n=1 imp:p=1 $ seat of chair
101 2 -7.87 -101 102                    imp:n=1 imp:p=1 $ table leg
102 1 -0.0012 -102                      imp:n=1 imp:p=1 $ inside of table leg
2 3 -0.65     -2                        imp:n=1 imp:p=1 $ long wooden table
201 2 -7.87 -201 202                    imp:n=1 imp:p=1 $ table legs/frame
202 1 -0.0012 -202                      imp:n=1 imp:p=1 $ inside of table legs/frame
3 11 -0.874    -3                       imp:n=1 imp:p=1 $ active volume of MS2
4 8 -0.329    -4                        imp:n=1 imp:p=1 $ electronics box of MS2
5 2 -7.87     -5 6                      imp:n=1 imp:p=1 $ metal cylinder of mp320
7 8 -0.329    -7                        imp:n=1 imp:p=1 $ electronics of mp320
8 1 -0.000012 -6                        imp:n=1 imp:p=1 $ almost vacuum inside mp320
9 7 -0.916    -8                        imp:n=1 imp:p=1 $ active volume of EJ-309
10 8 -0.329   -9                        imp:n=1 imp:p=1 $ electronics of EJ-309
12 3 -0.65  1    -11                    imp:n=1 imp:p=1 $ paper target
21 4 -1       -21                       imp:n=1 imp:p=1 $ shielding box between source and MS2
22 4 -1       -22                      imp:n=1 imp:p=1 $ shielding box between source and EJ-309
900 1 -0.0012  1 2 3 4 5 7 8 9 11 21 22 -91 &
    101 201                             imp:n=1 imp:p=1 $ air surrounding everything
901 1 -0.0012  92  93 -900              imp:n=1 imp:p=1 $ air outside walls
902 9 -2.3 91 -92                       imp:n=1 imp:p=1 $ concrete
909 10 -1.75 -93  -900                  imp:n=1 imp:p=1 $ soil under floor
910 0    900                            imp:n=0 imp:p=0 $ past the end of the world (imp=0)
c ------End Cell Cards-----------------------------------

c ------Surface Cards------------------------------------
1 box   50  23.5 0    -37 -27.3 0   27.3 -37 0   0 0 -5                 $ chair top
2 box   88.24 52 0     -147.3 -108.6 0   -37.98 51.5 0   0 0 -5         $ table top
101 rcc 45 -9.05 -5   0 0 -80    3                                      $ outside of chair leg
102 rcc 45 -9.05 -5   0 0 -80    2.5                                    $ inside of chair leg
201 box 88.24 52 -5     -147.3 -108.6 0   -37.98 51.5 0   0 0 -80       $ outside of table legs/frame
(approx by box)
202 box 87.74 52.5 -5.5   -146.3 -107.6 0   -36.98 50.5 0   0 0 -79  $ inside of table legs/frame
3 rcc   30.48 0 3.55    7.62 0 0      2.54                    `         $ active volume of MS2
4 box   38.1 -8.255 0.01    21.59 0 0   0 16.51 0   0 0 15.875          $ MS2 electronics
5 rcc  -18.346  41.9 5.1    55.8 0 0    5.08                            $ outer cylinder of mp320
6 rcc  -17.84  41.9 5.1    54.8 0 0    4.60                             $ inner cylinder of mp320
7 box  -9.451 33.96 10.2  37.211 0 0   0 15.875 0  0 0 13.97            $ electronics box of mp320
8 rcc  -30.48 0 10   -12.5 0 0   6.3                                    $ EJ-309 active volume
9 rcc  -42.98 0 10   -15 0 0    6                                       $ EJ-309 electronics and PMT
11 box -7.5 -7.5 0.011     15 0 0    0 15 0   0 0 16                    $ paper target (one ream)
21 box -37.6 16.9 0.01  22.67 -8.25 0 6.08 16.71 0  0 0 27.94           $ shielding box between
source and EJ-309
22 box  14.7 8.4 0.01   22.67 8.25 0  -6.08 16.71 0  0 0 27.94          $ MS2/source shielding box
91 box -300 -300 -91.44    600 0 0    0 600 0   0 0 300                 $ inside of concrete walls
92 box -400 -400 -191.44   800 0 0    0 800 0   0 0 500                 $ outside of concrete walls
93 pz  -192.92                                                          $ edge of floor (bottom)
```

```
900 so 1000                                                    $ end of the world!!
c ---------end surface cards-------------------------------

c --------Material Cards-----------------------------------
m1 6000.60c .0001 7014.60c .755 8016.60c .232 18000 .013       $ air p=0.0012
m2 26000 0.9959 6000.60c 0.0032 16032.60c 0.0005 15031.60c 0.0004   $ carbon steel p=7.87
m3 1001.60c 0.47619 6000.60c 0.285714 8016.60c 0.238095        $ wood p=0.65 (pine)
m4 1001.60c .667 8016.60c .333                                 $ water p=1
c m5 1001.60c 0.4 6000.60c 0.2 7014.60c 0.4                    $ melamine powder p=0.51
c m6 6000.60c 0.335 8016.60c 0.037 1001.60c 0.628              $ vegetable oil p=0.918
m7 1001 0.548 nlib=60c 6000 0.452 nlib=60c                     $ EJ 309 p=0.916
m8 1001.60c 0.257 6000.60c 0.0187 8016.60c 0.468 13027.60c 0.0259 &
  14028 0.123 28000 0.1043                                      $ electronics
m9 1001.60c 0.304 6000.60c 0.00287 8016.60c 0.4987 13027.60c 0.0103 &
  14000.60c 0.151 19000.60c 0.00711 20000 0.014882 26000 0.001599  $ concrete p= 2.3
m10 1001.60c 0.2938 6000.60c 0.0187 8016.60c 0.5045 13027.60c 0.0259 &
   14028 0.1354 19000.60c 0.0143 26056.60c 0.0027              $ soil p=1.75
m11 6000.60c .4519 1001.60c .5481                              $ NE-213 p=0.874
c ------- End Material Cards ------------------------------
c ------- Physics and data Cards ---------------------------
mode n p
PHYS:N  J    20
PHYS:P  J    1
CUT:N   2J   0
CUT:P   2J   0
RPOL 0.010 0.010                       $ RPOL (1)(2)= n,p cutoff E
IPOL 0 1 1 1 2J 1 9                    $ collect data from 1 cell (#9)
FILES 21 DUMN1                         $ for output files
DBCN                                   $ debug parallelizing
PRDMP 2J 1                             $ dump data file
sdef POS=0 41.9 7.64 PAR=1 ERG=2.4     $ monoenergetic 2.4 MeV neutron source
nps 40000000                           $ number of histories
c ---------- End Physics and Data Cards -------------------
c ---------- Tally Cards ---------------------------------
c f1 current tallies, on front faces of both detectors
f11:n 3.3                            $ MS2 0.2 MeV energy bins, neutron tally
e11 .2 .4 .6 .8 1 69I 15 20          $ 0.2 MeV Energy Bins
f21:p 3.3                            $ MS2 0.2 MeV energy bins, photon tally
e21 .2 .4 .6 .8 1 69I 15 20         $ 0.2 MeV Energy Bins
f31:n 3.3                           $ MS2 with MS2 energy bins, neutron tally
e31 .01 .5 1 1.5 2 3 4 5 6 7 8 9 10 12 14 16 18 20   $ MS2 energy bins
f41:n 8.3                           $ neutron tally on EJ-309
e41 .2 .4 .6 .8 1 69I 15 20         $ 0.2 MeV Energy Bins
f51:p 8.3                           $ photon tally on EJ-309
e51 .2 .4 .6 .8 1 69I 15 20         $ 0.2 MeV Energy Bins
c ----------- End Tally Cards ----------------------------
```

Explosives detection in container screening scenarios

Idealized detection scenario example

```
c RDX with water in cargo container d-t source
c ------Cell Cards--------------------------------------
c 3456789 123456789 223456789 323456789 423456789 523456789 623456789 723456789
1 2 -7.87 3 -1 -7 8 -11 12       imp:n=1 imp:p=1          $ far side of container (away from source)
2 2 -7.87 2 -4 -7 8 -11 12       imp:n=1 imp:p=1          $ near side of container (facing source)
3 2 -7.87 -5 7 -1 2 10 -9        imp:n=1 imp:p=1          $ front end of container
4 2 -7.87 6 -8 -1 2 10 -9        imp:n=1 imp:p=1          $ rear end of container
5 2 -7.87 11 -9 -7 8 -1 2        imp:n=1 imp:p=1          $ top of container
6 2 -7.87 10 -12 -7 8 -1 2       imp:n=1 imp:p=1          $ bottom of container
7 4 -0.460 -3 4 -7 8 -11 12 #22   imp:n=1 imp:p=1         $ interior the container
8 1 -.0012 -13 #1 #2 #3 #4 #5 #6 #7 #100 #30 #60 #90 #120 &
            #150 #180 #22      imp:n=1 imp:p=1            $ air around outside of detectors
c ------- Ideal hemispherical detectors
100 1 -0.0012 -100 26          imp:n=1 imp:p=1           $ 0 deg detector
30  1 -0.0012 -30 26           imp:n=1 imp:p=1           $ 30 deg detector
60  1 -0.0012 -60 26           imp:n=1 imp:p=1           $ 60 deg detector
90  1 -0.0012 -90 26           imp:n=1 imp:p=1           $ 90 deg detector
120 1 -0.0012 -120 26          imp:n=1 imp:p=1           $ 120 deg detector
150 1 -0.0012 -150 26          imp:n=1 imp:p=1           $ 1500 deg detector
180 1 -0.0012 -180 26          imp:n=1 imp:p=1           $ 180 deg detector
22  3 -1.82   -27              imp:n=1 imp:p=1           $ Target sphere
9 0 13                         imp:n=0 imp:p=0           $ Past the edge....
c ------End Cell Cards-----------------------------------

c ------Surface Cards-----------------------------------
1 px 121.92               $ outside far side (away from source)
2 px -121.92              $ outside near side (facing source)
3 px 121.574              $ inside far side (away from source)
4 px -121.574             $ inside near side (facing source)
5 py 310.217              $ outside front end
6 py -310.217             $ outside rear end
7 py 309.871              $ inside front end
8 py -309.871             $ inside rear end
9 pz 129.867              $ outside top of container
10 pz -129.867            $ outside bottom of container
11 pz 129.521             $ inside top of container
12 pz -129.521            $ inside bottom of container
13 so 1000                $ Outermost sphere
27 so 18.72               $ Target sphere
100 sx 304.8 78                $ 0 deg detector outside
30 s 263.965 0 152.4 78        $ 30 deg detector outside
60 s 152.4 0 263.965 78        $ 60 deg detector outside
90 sz 304.8 78                 $ 90 deg detector outside
120 s -152.4 0 263.965 78      $ 120 deg detector outside
150 s -263.965 0 152.4 78      $ 150 deg detector outside
180 sx -304.8 78               $ 180 deg detector outside
26 so 304.8                    $ inner surface of detectors
c ---------end surface cards------------------------------

c --------Material Cards----------------------------------
```

```
m1 6012 .0001 7014 .755 8016 .232 18000 .013          $ air p=0.0012
m2 26000 .9959 6012 .0032 16032 .0005 15031 .0004   $ carbon steel p=7.87
m3 6012 .143 7014 .285 8016 .286 1001 .286              $ RDX p=1.82
m4 1001 .667 8016 .333                                              $ water p=1.0
c ------- End Material Cards ------------------------------
c ------- Data Cards -------------------------------------
mode p n
sdef POS=-304 0 0 PAR=1 ERG=14.1  VEC=1 0 0 DIR=D1  $ monoenergetic 14.1 MeV neutron
source
si1 H 0.9194 1                                        $ cosine of angle needed for conical beam
sp1 0 1
nps 200000000                                         $ number of histories
e0 .2 .4 .6 .8 1 69I 15 20                            $ 0.2 MeV Energy Bins
cut:n j 0.05                                          $ neutron cut card
c ---------- End Data Cards -------------------------------
c ---------- Tally Cards ----------------------------------
c f1 current tallies
f11:n 100      $ 0 deg detector, neutron
f21:p 100      $ 0 deg detector, photon
f31:n 30       $ 30 deg detector, neutron
f41:p 30       $ 30 deg detector, photon
f51:n 60       $ 60 deg detector, neutron
f61:p 60       $ 60 deg detector, photon
f71:n 90       $ 90 deg detector, neutron
f81:p 90       $ 90 deg detector, photon
f91:n 120      $ 120 deg detector, neutron
f101:p 120     $ 120 deg detector, photon
f111:n 150     $ 150 deg detector, neutron
f121:p 150     $ 150 deg detector, photon
f131:n 180     $ 180 deg detector, neutron
f141:p 180     $ 180 deg detector, photon
c ------End Tally Cards ---------
```

Shielded 14.1 MeV isotropic neutron source with surrounding environment

```
c diffuse paper shielding, RDX, shielded isotropic d-t source
c ------Cell Cards--------------------------------------
c 3456789 123456789 223456789 323456789 423456789 523456789 623456789 723456789
c ---- Container --------------------------
1 2 -7.87 3 -1 -7 8 -11 12       imp:n=1 imp:p=1         $ far side of container (away from source)
2 2 -7.87 2 -4 -7 8 -11 12       imp:n=1 imp:p=1         $ near side of container (facing source)
3 2 -7.87 -5 7 -1 2 10 -9        imp:n=1 imp:p=1         $ front end of container
4 2 -7.87 6 -8 -1 2 10 -9        imp:n=1 imp:p=1         $ rear end of container
5 2 -7.87 11 -9 -7 8 -1 2        imp:n=1 imp:p=1         $ top of container
6 2 -7.87 10 -12 -7 8 -1 2       imp:n=1 imp:p=1         $ bottom of container
7 5 -.4602 -3 4 -7 8 -11 12 #22   imp:n=1 imp:p=1           $ interior the container
c ---- Detectors ---------------------------
100 1 -0.0012 -100 26           imp:n=1 imp:p=1         $ 0 deg detector
30  1 -0.0012 -30 26            imp:n=1 imp:p=1         $ 30 deg detector
60  1 -0.0012 -60 26            imp:n=1 imp:p=1         $ 60 deg detector
90  1 -0.0012 -90 26            imp:n=1 imp:p=1         $ 90 deg detector
120 1 -0.0012 -120 26           imp:n=1 imp:p=1         $ 120 deg detector
150 1 -0.0012 -150 26           imp:n=1 imp:p=1         $ 150 deg detector
180 1 -0.0012 -180 26           imp:n=1 imp:p=1         $ 180 deg detector
c --- Source shield ---------------------------
201  4 -0.94 201 -202   -301        imp:n=1 imp:p=1       $ polyethylene cylinder (1)
202  2 -7.86 202 -203   -302        imp:n=1 imp:p=1       $ steel cylinder (2)
203  2 -7.86 203 -204   -303        imp:n=1 imp:p=1       $ steel cylinder (3)
204  2 -7.86 204 -205   -304        imp:n=1 imp:p=1       $ steel cylinder (4)
205  2 -7.86 205 -206   -305        imp:n=1 imp:p=1       $ steel cylinder (5)
206  2 -7.86 206 -207   -306        imp:n=1 imp:p=1       $ steel cylinder (6)
207  4 -0.94 207 -208   -307        imp:n=1 imp:p=1       $ polyethylene cylinder (7)
208  2 -7.86 208 -209   -308        imp:n=1 imp:p=1       $ steel cylinder (8)
209  4 -0.94 209 -210   -309        imp:n=1 imp:p=1       $ polyethylene cylinder (9)
210  2 -7.86 210 -211   -310        imp:n=1 imp:p=1       $ steel cylinder (10)
c --- Other cells ---------------------------
8 1 -.0012 -13 #1 #2 #3 #4 #5 #6 #7 #100 #30 #60 #90 #120 #150 #180 #22 28 &
  #201 #202 #203 #204 #205 #206 #207 #208 #209 #210 imp:n=1 imp:p=1     $ air
10 6 -2.3 -28 29 -13            imp:n=1 imp:p=1             $ concrete slab
11 7 -1.75 -29 -13              imp:n=1 imp:p=1             $ ground
22  3 -1.8200   -27             imp:n=1 imp:p=1             $ Target sphere
9 0 13                          imp:n=0 imp:p=0             $ Past the edge....
c ------End Cell Cards-----------------------------------

c ------Surface Cards------------------------------------
c ---- Container -------------------------------
1 px 121.92                 $ outside far side (away from source)
2 px -121.92                $ outside near side (facing source)
3 px 121.603                $ inside far side (away from source)
4 px -121.603               $ inside near side (facing source)
5 py 310.217                $ outside front end
6 py -310.217               $ outside rear end
7 py 309.9                  $ inside front end
8 py -309.9                 $ inside rear end
9 pz 129.867                $ outside top of container
10 pz -129.867               $ outside bottom of container
11 pz 129.55                 $ inside top of container
12 pz -129.55                $ inside bottom of container
```

```
c ---- Detectors ---------------------------
100 sx 304.8 78                  $ 0 deg detector outside
30 s 263.965 0 152.4 78          $ 30 deg detector outside
60 s 152.4 0 263.965 78          $ 60 deg detector outside
90 sz 304.8 78                   $ 90 deg detector outside
120 s -152.4 0 263.965 78        $ 120 deg detector outside
150 s -263.965 0 152.4 78        $ 150 deg detector outside
180 sx -304.8 78                 $ 180 deg detector outside
26 so 304.8                      $ inner surface of detectors
c ---- Source Shield ------------------------
201  RCC  -444.001  0 0   22.4  0   0   9        $ inside surface of shield
202  RCC  -449      0 0   34.4  0   0   14       $ end of 1st poly layer
203  RCC  -454      0 0   46.5  0   0   19       $ inside thick steel
204  RCC  -459      0 0   58.5  0   0   24       $ inside thick steel
205  RCC  -464      0 0   70.5  0   0   29       $ inside thick steel
206  RCC  -469      0 0   82.5  0   0   34       $ inside thick steel
207  RCC  -474      0 0   94.5  0   0   39       $ end of large steel layer
208  RCC  -479      0 0   106.5 0   0   44       $ end of 2nd poly layer
209  RCC  -484      0 0   118.5 0   0   49       $ end of 2nd steel layer
210  RCC  -489      0 0   130.5 0   0   54       $ end of 3rd poly layer
211  RCC  -499      0 0   135.5 0   0   59       $ outside surface of shield
301 px -421.6                                    $ edge of layer 1
302 px -414.6                                    $ edge of layer 2
303 px -407.5                                    $ edge of layer 3
304 px -400.5                                    $ edge of layer 4
305 px -393.5                                    $ edge of layer 5
306 px -386.5                                    $ edge of layer 6
307 px -379.5                                    $ edge of layer 7
308 px -372.5                                    $ edge of layer 8
309 px -365.5                                    $ edge of layer 9
310 px -358.5                                    $ edge of layer 10
c ---- Other surfaces --------------------------
13 so 1000                        $ Outermost sphere
27 so 40.3                        $ Target sphere (500 kg RDX)
28 pz -130                        $ top surface of concrete slab
29 pz -160.48                     $ border between slab and ground
c ---------end surface cards------------------------------

c --------Material Cards----------------------------------
m1 6012 .0001 7014 .755 8016 .232 18000 .013           $ air p=0.0012
m2 26000 .9959 6012 .0032 16032 .0005 15031 .0004  $ carbon steel p=7.87
m3 6012 .143 7014 .285 8016 .286 1001 .286             $ RDX p=1.82
m4 1001 4 6000 2                                       $ polyethylene
m5 1001 0.47619 6000 0.285714 8016 0.238095            $ newspaper: p~=0.65
m6 1001 0.2938 6012 0.0187 8016 0.5045 13027 0.0259 14028 &
0.1354 19000 0.0143 26056 0.0027                       $ soil EPA GR 12 standard p=1.75
m7 1001 0.304245  6012 0.002870  8016 0.498628  11023 &
     0.009179 13027 0.010261 14000 0.150505  19000 &
     0.007114  20000 0.014882  26000 0.001599          $ ordinary concrete p=2.3
c ------- End Material Cards -----------------------------
c ------- Data Cards -------------------------------------
mode p n
sdef POS=-444 0 0 PAR=1 ERG=14.1                 $ monoenergetic isotropic 14.1 MeV neutron
source
nps 1000000000                                   $ number of histories
e0 0.1 0.2 147I 15 20                            $ 0.1 MeV Energy Bins
```

```
cut:n j 0.05                                             $ neutron cut card
c ---------- End Data Cards -------------------------------
c ---------- Tally Cards ----------------------------------
c f1 current tallies
f11:n 100               $ 0 deg detector, neutron
f21:p 100               $ 0 deg detector, photon
f31:n 30                $ 30 deg detector, neutron
f41:p 30                $ 30 deg detector, photon
f51:n 60                $ 60 deg detector, neutron
f61:p 60                $ 60 deg detector, photon
f71:n 90                $ 90 deg detector, neutron
f81:p 90                $ 90 deg detector, photon
f91:n 120               $ 120 deg detector, neutron
f101:p 120              $ 120 deg detector, photon
f111:n 150              $ 150 deg detector, neutron
f121:p 150              $ 150 deg detector, photon
f131:n 180              $ 180 deg detector, neutron
f141:p 180              $ 180 deg detector, photon
c ------End Tally Cards ---------
```

Heterogenous cargo packing: steel in crates with shielded source output

```
c original: crated metal shielding, RDX, conical shielded D-T source (shield still in place), cement
pad over soil
c ------Cell Cards--------------------------------------
c 3456789 123456789 223456789 323456789 423456789 523456789 623456789 723456789 $
convenient counter
c --- Main Parts --------------------------
1 2 -7.87 -1 2                    imp:n=1 imp:p=1        $ steel container
2 1 -.0012 -2 27 400 402 404 406 408 410 412 414 416 &
  418 420 422 424 426 428 430 432 434 436 438 440 &
  442 444 446 448 450 452 454 456 458 460 462 464 &
  466                             imp:n=1 imp:p=1        $ inside of container
10 7 -2.3 -28 29 -13              imp:n=1 imp:p=1        $ cement pad
11 6 -1.75 -29 -13                imp:n=1 imp:p=1        $ ground
22 3 -1.82     -27                imp:n=1 imp:p=1        $ Target box
28 1 -.0012 -13 28 1 #100 #30 #60 #90 #120 #150 &
   #180 #201 #202 #203 #204 #205 #206 #207 #208 &
   #209 #210                      imp:n=1 imp:p=1        $ air around everything
9 0 13                            imp:n=0 imp:p=0        $ Past the edge....
c ---- Detectors --------------------------
100 1 -0.0012 -100 26           imp:n=1 imp:p=1          $ 0 deg detector
30  1 -0.0012 -30 26            imp:n=1 imp:p=1          $ 30 deg detector
60  1 -0.0012 -60 26            imp:n=1 imp:p=1          $ 60 deg detector
90  1 -0.0012 -90 26            imp:n=1 imp:p=1          $ 90 deg detector
120 1 -0.0012 -120 26           imp:n=1 imp:p=1          $ 120 deg detector
150 1 -0.0012 -150 26           imp:n=1 imp:p=1          $ 150 deg detector
180 1 -0.0012 -180 26           imp:n=1 imp:p=1          $ 180 deg detector
c --- Source shield --------------------------
201  4 -0.94 201 -202   -301        imp:n=1 imp:p=1       $ polyethylene cylinder (1)
202  2 -7.86 202 -203   -302        imp:n=1 imp:p=1       $ steel cylinder (2)
203  2 -7.86 203 -204   -303        imp:n=1 imp:p=1       $ steel cylinder (3)
204  2 -7.86 204 -205   -304        imp:n=1 imp:p=1       $ steel cylinder (4)
205  2 -7.86 205 -206   -305        imp:n=1 imp:p=1       $ steel cylinder (5)
206  4 -0.94 206 -207   -306        imp:n=1 imp:p=1       $ polyethylene cylinder (6)
207  2 -7.86 207 -208   -307        imp:n=1 imp:p=1       $ steel cylinder (7)
208  4 -0.94 208 -209   -308        imp:n=1 imp:p=1       $ polyethylene cylinder (8)
209  2 -7.86 209 -210   -309        imp:n=1 imp:p=1       $ steel cylinder (9)
210  4 -0.94 210 -211   -310        imp:n=1 imp:p=1       $ polyethylene cylinder (10)
c --- Crates inside cargo container ------------
400  8  -0.8  -400  401  imp:n=1 imp:p=1    $ Crate itself (#400)
402  8  -0.8  -402  403  imp:n=1 imp:p=1    $ Crate itself (#402)
…
466  8  -0.8  -466  467  imp:n=1 imp:p=1    $ Crate itself (#466)
401  2  -4  -401    imp:n=1 imp:p=1        $ Interior of crate #400
403  2  -4  -403    imp:n=1 imp:p=1        $ Interior of crate #402
…
467  2  -4  -467    imp:n=1 imp:p=1        $ Interior of crate #466
c ------End Cell Cards-----------------------------------

c ------Surface Cards------------------------------------
c ---- Main parts ---------------------------
1 box -121.92 -309.6 -129.867  243.84 0 0  0 619.2 0  0 0 259.734       $ outside of container
2 box -121.603 -309.283 -129.55  243.206 0 0  0 618.566 0  0 0 259.1  $ inside of container
13 so 1000                                                             $ Outermost sphere
```

```
27 box -14 -81.5 -129  28 0 0  0 163.5 0  0 0 60                    $ Target (500 kg RDX)
28 pz -130                                          $ top surface of concrete slab
29 pz -155                                          $ border between slab and ground
c ---- Detectors ---------------------------
100 sx 304.8 78                $ 0 deg detector outside
30 s 263.965 0 152.4 78        $ 30 deg detector outside
60 s 152.4 0 263.965 78        $ 60 deg detector outside
90 sz 304.8 78                 $ 90 deg detector outside
120 s -152.4 0 263.965 78      $ 120 deg detector outside
150 s -263.965 0 152.4 78      $ 150 deg detector outside
180 sx -304.8 78               $ 180 deg detector outside
26 so 304.8                    $ inner surface of detectors
c ---- Source Shield -------------------------
201  RCC  -444.001  0 0   22.4  0   0   9        $ inside surface of shield
202  RCC  -449      0 0   34.4  0   0   14       $ end of 1st poly layer
203  RCC  -454      0 0   46.5  0   0   19       $ inside thick steel
204  RCC  -459      0 0   58.5  0   0   24       $ inside thick steel
205  RCC  -464      0 0   70.5  0   0   29       $ inside thick steel
206  RCC  -469      0 0   82.5  0   0   34       $ inside thick steel
207  RCC  -474      0 0   94.5  0   0   39       $ end of large steel layer
208  RCC  -479      0 0   106.5 0   0   44       $ end of 2nd poly layer
209  RCC  -484      0 0   118.5 0   0   49       $ end of 2nd steel layer
210  RCC  -489      0 0   130.5 0   0   54       $ end of 3rd poly layer
211  RCC  -499      0 0   135.5 0   0   59       $ outside surface of shield
301 px -421.6                        $ edge of layer 1
302 px -414.6                        $ edge of layer 2
303 px -407.5                        $ edge of layer 3
304 px -400.5                        $ edge of layer 4
305 px -393.5                        $ edge of layer 5
306 px -386.5                        $ edge of layer 6
307 px -379.5                        $ edge of layer 7
308 px -372.5                        $ edge of layer 8
309 px -365.5                        $ edge of layer 9
310 px -358.5                        $ edge of layer 10
c ---- Crates inside container -------------------------
400 box -115 -308 -129   100 0 0   0 100 0   0 0 20
402 box 15 -308 -129     100 0 0   0 100 0   0 0 20
…
467 box -113 206 -85       94 0 0   0 94 0   0 0 16
c ---------end surface cards-------------------------------

c --------Material Cards-----------------------------------
m1 6012 .0001 7014 .755 8016 .232 18000 .013       $ air p=0.0012
m2 26000 .9959 6012 .0032 16032 .0005 15031 .0004   $ carbon steel p=7.87
m3 6012 .143 7014 .285 8016 .286 1001 .286                      $ RDX p=1.82
m4 1001 4 6000 2                                                $ polyethylene
m5 1001 0.41495 6012 0.31703 8016 0.20747 26000 0.03027659 &
   13027 0.0302765                                               $ Furniture
m6 1001 0.2938 6012 0.0187 8016 0.5045 13027 0.0259 14028 &
   0.1354 19000 0.0143 26056 0.0027                              $ soil
m7 1001 0.304245  6012 0.002870  8016 0.498628  11023 0.009179 13027 0.010261 &
  14000 0.150505  19000 0.007114  20000 0.014882  26000 0.001599  $ concrete p=2.3
m8 1001 0.47619 6000 0.285714 8016 0.238095                      $ wood
c ------- End Material Cards ------------------------------
c ------- Data Cards -------------------------------------
mode p n
```

```
sdef POS=-444 0 0 PAR=1 ERG=D1 VEC=1 0 0 DIR=D2   $ conical 14.1 MeV neutron source
si1 0 0.1 0.2 147I 15 20
sp1 0 &                    $ Energies of neutrons produced with isotropic source inside the shield
1.86E-03 &
3.52E-03 &
…
0.00E+00
si2 H 0.9274 1                            $ cosine of angle needed
sp2 0 1
nps 1000000000                          $ number of histories
e0 0.1 0.2 147I 15 20                   $ 0.1 MeV Energy Bins
cut:n j 0.05                            $ neutron cut card
PRDMP 2J 1                              $ dump data file
c ---------- End Data Cards -------------------------------
c ---------- Tally Cards ---------------------------------
c f1 current tallies
f11:n 100        $ 0 deg detector, neutron
f21:p 100        $ 0 deg detector, photon
f31:n 30         $ 30 deg detector, neutron
f41:p 30         $ 30 deg detector, photon
f51:n 60         $ 60 deg detector, neutron
f61:p 60         $ 60 deg detector, photon
f71:n 90         $ 90 deg detector, neutron
f81:p 90         $ 90 deg detector, photon
f91:n 120        $ 120 deg detector, neutron
f101:p 120       $ 120 deg detector, photon
f111:n 150       $ 150 deg detector, neutron
f121:p 150       $ 150 deg detector, photon
f131:n 180       $ 180 deg detector, neutron
f141:p 180       $ 180 deg detector, photon
c ------End Tally Cards ---------
```

Explosives detection with 5-scan technique

Irradiation with fan beam, scanning position 4, 11 neutron detectors, homogeneous cargo (MCNP-PoliMi)

```
c diffuse meat, isotropic shielded D-T source in ground, cement pad over soil
c position 4 scan (4.34 m from edge), 400 kg RDX position 2
c ------Cell Cards---------------------------------------
c 3456789 123456789 223456789 323456789 423456789 523456789 623456789 723456789
c ---- Container --------------------------
1 2 -7.87 -1 2               imp:n=1 imp:p=1         $ container itself
2 5 -0.4 -2 27               imp:n=1 imp:p=1         $ inside container
c ------- EJ-309 neutron detectors ----------------------
100 8 -0.916 -100            imp:n=1 imp:p=1         $ 0 deg detector
30  8 -0.916 -30             imp:n=1 imp:p=1         $ 30 deg detector
60  8 -0.916 -60             imp:n=1 imp:p=1         $ 60 deg detector
90  8 -0.916 -90             imp:n=1 imp:p=1         $ 90 deg detector
120 8 -0.916 -120            imp:n=1 imp:p=1         $ 120 deg detector
150 8 -0.916 -150            imp:n=1 imp:p=1         $ 150 deg detector
212 8 -0.916 -212            imp:n=1 imp:p=1         $ 210 deg detector
240 8 -0.916 -240            imp:n=1 imp:p=1         $ 240 deg detector
270 8 -0.916 -270            imp:n=1 imp:p=1         $ 270 deg detector
300 8 -0.916 -300            imp:n=1 imp:p=1         $ 300 deg detector
330 8 -0.916 -330            imp:n=1 imp:p=1         $ 330 deg detector
c --- Source shield --------------------------
201  4 -4.4 -201            imp:n=1 imp:p=1         $ back of shield
202  4 -4.4 -202            imp:n=1 imp:p=1         $ -y side of shield
203  4 -4.4 -203            imp:n=1 imp:p=1         $ +y side of shield
204  4 -4.4 -204            imp:n=1 imp:p=1         $ +z side of shield
205  4 -4.4 -205            imp:n=1 imp:p=1         $ -z side of shield
c --- Other stuff --------------------------
8 1 -.0012 -13 #1 #2 100 30 60 90 120 240 270 &
  300 330 #22 28                        imp:n=1 imp:p=1  $ air around everything
10 7 -2.3 -28 29 25 -13 #26 120 240     imp:n=1 imp:p=1  $ cement pad
11 6 -1.75 -29 -13 25 26 120 150 212    imp:n=1 imp:p=1  $ ground
22 3 -1.82     -27                      imp:n=1 imp:p=1  $ Target sphere
25 1 -0.0012 -28 -25 120 150 212 240 26      imp:n=1 imp:p=1  $ cut-out in ground for detectors
26 1 -0.0012 -26 150 212 #11  #201 #202 #203 #204 &
  #205                                  imp:n=1 imp:p=1  $ Well in ground
9 0 13                                  imp:n=0 imp:p=0  $ Past the edge....
c ------End Cell Cards-----------------------------------

c ------Surface Cards------------------------------------
1 box -129.87 -434.22 -121.92 259.73 0 0  0 620.43 0 0 0 243.84      $ outside of box
2 box -129.52 -433.87 -121.57 259.04 0 0  0 619.74 0 0 0 243.15      $ inside of box
13 so 1000                                   $ Outermost sphere
25 RCC 0 -40 0  0 80 0       250             $ cut-out for detectors
26 BOX -340 -65 -122  210 0 0  0 130 0  0 0 243.8              $ Well for source and detectors
27 sy -248.22 37.44                         $ Target sphere (400 kg RDX)
28 px -130                                  $ top surface of concrete slab
29 px -155                                  $ border between slab and ground
c ---- Source Shield Surfaces ------------------------
201 BOX -340 -63 -88.7  50 0 0  0 126 0  0 0 177.4         $ back of shield
```

```
202 BOX -290 -63 -88.7  50 0 0  0  50 0  0 0 177.4          $ -y side of shield
203 BOX -290  13 -88.7  50 0 0  0  50 0  0 0 177.4          $ +y side of shield
204 BOX -290 -13  38.7  50 0 0  0  26 0  0 0  50           $ +z side of shield
205 BOX -290 -13 -38.7  50 0 0  0  26 0  0 0 -50           $ -z side of shield
c --------- Detector Surfaces --------------------
100 RCC  225    0    0       20    0    0     40         $ 0 deg detector
30  RCC  194.86 0  112.5     17.32 0   10     40    $ 30 deg detector
60  RCC  112.5  0  194.86    10    0   17.32  40    $ 60 deg detector
90  RCC    0    0  225        0    0   20     40         $ 90 deg detector
120 RCC -112.5  0  194.86   -10    0   17.32  40   $ 120 deg detector
150 RCC -194.86 0  112.5    -17.32 0   10     40   $ 150 deg detector
212 RCC -194.86 0 -112.5    -17.32 0  -10     40   $ 210 deg detector
240 RCC -112.5  0 -194.86   -10    0  -17.32  40   $ 240 deg detector
270 RCC    0    0 -225        0    0  -20     40         $ 270 deg detector
300 RCC  112.5  0 -194.86    10    0  -17.32  40    $ 300 deg detector
330 RCC  194.86 0 -112.5     17.32 0  -10     40    $ 330 deg detector
c ---------end surface cards------------------------------

c --------Material Cards----------------------------------
m1 6000.60c .0001 7014.60c .755 8016.60c .232 18000 .013       $ air p=0.0012
m2 26000 0.9959 6000.60c 0.0032 16032.60c 0.0005 15031.60c 0.0004     $ carbon steel p=7.87
m3 6000.60c 0.143 7014.60c 0.285 8016.60c 0.286 1001.60c 0.286        $ RDX p=1.82
m4 1001.60c -0.0275 6000.60c -0.0825 26000 -0.89                    $ 1/2 poly, 1/2 steel by volume,
p=4.405
m5 1001.60c 0.604199 6000.60c 0.14512 7014.60c 0.0072276 8016.60c &
  0.2424 19000.60c 0.0005547 15031.60c 0.000469326               $ Meat p=1.1
m6 1001.60c 0.2938 6000.60c 0.0187 8016.60c 0.5045 13027.60c 0.0259 &
   14028 0.1354 19000.60c 0.0143 26056.60c 0.0027                  $ soil EPA GR 12 standard
p=1.75
m7 1001.60c 0.304 6000.60c 0.00287 8016.60c 0.4987 11023 0.009179 &
  13027.60c 0.0103 14000.60c 0.151 19000.60c 0.00711 20000 0.014882 &
  26000 0.001599                                                   $ ordinary concrete p= 2.3
m8 1001.60c 0.548 6000.60c 0.452                                   $ EJ 309 p=0.916
c ------- End Material Cards -----------------------------
c ------- Data Cards -------------------------------------
mode n p
nps 100000000                        $ number of histories
PHYS:N  J    20                      $ needed for analog mcnp
PHYS:P  J    1                       $ needed for analog mcnp
CUT:N   2J   0                       $ needed for analog mcnp
CUT:P   2J   0                       $ needed for analog mcnp
RPOL 0.010 0.010                     $ RPOL (1)(2) = n,p cutoff E
IPOL 0 1 1 1 2J 6 100 30 60 90 120 150 $ collect data from 6 det cells
FILES 21 DUMN1                       $ for output files
DBCN                                 $ debug parallelizing
PRDMP 2J 1                           $ dump data file
sdef POS=-289.9 0 0 PAR=1 ERG=14.1 $ monoenergetic conical 14.1 MeV neutron source
e0 .2 .4 .6 .8 1 69I 15 20           $ 0.2 MeV Energy Bins
c ---------- End Data Cards ------------------------------
c ---------- Tally Cards ---------------------------------
c f1 current tallies
f11:n 100.3       $ 0 deg detector, neutron
f21:p 100.3       $ 0 deg detector, photon
f31:n 30.3        $ 30 deg detector, neutron
f41:p 30.3        $ 30 deg detector, photon
f51:n 60.3        $ 60 deg detector, neutron
```

```
f61:p 60.3       $ 60 deg detector, photon
f71:n 90.3       $ 90 deg detector, neutron
f81:p 90.3       $ 90 deg detector, photon
f91:n 120.3      $ 120 deg detector, neutron
f101:p 120.3     $ 120 deg detector, photon
f111:n 150.3     $ 150 deg detector, neutron
f121:p 150.3     $ 150 deg detector, photon
f131:n 212.3     $ 210 deg detector, neutron
f141:p 212.3     $ 210 deg detector, photon
f151:n 240.3     $ 240 deg detector, neutron
f161:p 240.3     $ 240 deg detector, photon
f171:n 270.3     $ 270 deg detector, neutron
f181:p 270.3     $ 270 deg detector, photon
f191:n 300.3     $ 300 deg detector, neutron
f201:p 300.3     $ 300 deg detector, photon
f211:n 330.3     $ 330 deg detector, neutron
f221:p 330.3     $ 330 deg detector, photon
c ------End Tally Cards ---------
```

Irradiation with fan beam, 11 neutron detectors, container on truck bed (MCNP-PoliMi)

```
c diffuse paper, isotropic shielded D-T source in ground, cement pad over soil
c position 2 (3.1 m from edge), 200 kg RDX position 2
c ------Cell Cards---------------------------------------
c 3456789 123456789 223456789 323456789 423456789 523456789 623456789 723456789
c ---- Container --------------------------
1 2 -7.87 -1 2              imp:n=1 imp:p=1         $ container itself
2 5 -0.3 -2 27              imp:n=1 imp:p=1         $ inside container
3 9 -2.7 -3                 imp:n=1 imp:p=1         $ truck bed
4 10 -1.5 -5 4              imp:n=1 imp:p=1         $ wheel 1
5 10 -1.5 -7 6              imp:n=1 imp:p=1         $ wheel 2
6 10 -1.5 -9 8              imp:n=1 imp:p=1         $ wheel 3
7 10 -1.5 -11 10            imp:n=1 imp:p=1         $ wheel 4
8 10 -1.5 -16 15            imp:n=1 imp:p=1         $ wheel 5
9 10 -1.5 -18 17            imp:n=1 imp:p=1         $ wheel 6
19 2 -7.87 -19              imp:n=1 imp:p=1         $ rear axle
20 2 -7.87 -20              imp:n=1 imp:p=1         $ middle axle
21 2 -7.87 -21              imp:n=1 imp:p=1         $ front axle
c ------- EJ-309 neutron detectors ---------------------
100 8 -0.916 -100           imp:n=1 imp:p=1         $ 0 deg detector
30  8 -0.916 -30            imp:n=1 imp:p=1         $ 30 deg detector
60  8 -0.916 -60            imp:n=1 imp:p=1         $ 60 deg detector
90  8 -0.916 -90            imp:n=1 imp:p=1         $ 90 deg detector
120 8 -0.916 -120           imp:n=1 imp:p=1         $ 120 deg detector
150 8 -0.916 -150           imp:n=1 imp:p=1         $ 150 deg detector
212 8 -0.916 -212           imp:n=1 imp:p=1         $ 210 deg detector
240 8 -0.916 -240           imp:n=1 imp:p=1         $ 240 deg detector
270 8 -0.916 -270           imp:n=1 imp:p=1         $ 270 deg detector
300 8 -0.916 -300           imp:n=1 imp:p=1         $ 300 deg detector
330 8 -0.916 -330           imp:n=1 imp:p=1         $ 330 deg detector
c --- Source shield --------------------------
201  4 -4.4 -201            imp:n=1 imp:p=1         $ back of shield
202  4 -4.4 -202            imp:n=1 imp:p=1         $ -y side of shield
203  4 -4.4 -203            imp:n=1 imp:p=1         $ +y side of shield
204  4 -4.4 -204            imp:n=1 imp:p=1         $ +z side of shield
205  4 -4.4 -205            imp:n=1 imp:p=1         $ -z side of shield
c --- Other stuff ---------------------------
13 1 -.0012 -13 #1 #2 3 #4 #5 #6 #7 #8 #9 100 30 60 90 &
  19 20 21 120 150 212 240 270 300 330 #22 28 imp:n=1 imp:p=1  $ air around everything
10 7 -2.3 -28 29 25 -13 #26 150 212           imp:n=1 imp:p=1  $ cement pad
11 6 -1.75 -29 -13 25 26  150 212             imp:n=1 imp:p=1  $ ground
22 3 -1.82     -27                            imp:n=1 imp:p=1  $ Target sphere
25 1 -0.0012 -28 -25 150 212 26          imp:n=1 imp:p=1  $ cut-out in ground for detectors
26 1 -0.0012 -26 150 212 #11  #201 #202 #203 #204 &
  #205                                        imp:n=1 imp:p=1  $ Well in ground
99 0 13                                       imp:n=0 imp:p=0  $ Past the edge....
c ------End Cell Cards-----------------------------------

c ------Surface Cards------------------------------------
1 box -23.133 -186.217 -121.92 243.84 0 0  0 620.434 0 0 0 259.734   $ outside of box
```

```
2 box -23.479 -185.871 -121.574 243.148 0 0 0 619.742 0 0 0 259.042  $ inside of box
3 box -34.133 -246.75 -121.92   9.9 0 0 0 731.5 0 0 0 259.734        $ Bed of truck
4 RCC -80 -206 -120 0 0 100  35                    $ wheel 1 inside
5 RCC -80 -206 -120 0 0 100  40                    $ wheel 1 outside
6 RCC -80 -206 35 0 0 100 35                       $ wheel 2 inside
7 RCC -80 -206 35 0 0 100 40                       $ wheel 2 outside
8 RCC -80 -106 -120 0 0 100  35                    $ wheel 3 inside
9 RCC -80 -106 -120 0 0 100  40                    $ wheel 3 outside
10 RCC -80 -106 35 0 0 100 35                      $ wheel 4 inside
11 RCC -80 -106 35 0 0 100 40                      $ wheel 4 outside
15 RCC -80 440 -120 0 0 100 35                     $ wheel 5 inside
16 RCC -80 440 -120 0 0 100 40                     $ wheel 5 outside
17 RCC -80 440 35 0 0 100 35                       $ wheel 6 inside
18 RCC -80 440 35 0 0 100 40                       $ wheel 6 outside
19 RCC -80 -206 -120 0 0 255 8                     $ rear axle
20 RCC -80 -106 -120 0 0 255 8                     $ middle axle
21 RCC -80 440 -120 0 0 255 8                      $ front axle
13 so 1200                                         $ Outermost sphere
27 s 83 -0.217 0    29.71                          $ Target sphere (200 kg RDX)
25 RCC 0 -40 0  0 80 0       250                   $ cut-out for detectors
26 BOX -256 -65 -122  126 0 0  0 130 0  0 0 243.8      $ Well for source and detectors
28 px -130                                         $ top surface of concrete slab
29 px -155                                         $ border between slab and ground
c ---- Source Shield Surfaces ------------------------
201 BOX -255 -63   -88.7  50 0 0  0 126 0  0 0 177.4       $ back of shield
202 BOX -205 -61.3 -88.7  50 0 0  0  50 0  0 0 177.4       $ -y side of shield
203 BOX -205  11.3 -88.7  50 0 0  0  50 0  0 0 177.4       $ +y side of shield
204 BOX -205 -11.3  33.7  50 0 0  0  22.6 0  0 0  50       $ +z side of shield
205 BOX -205 -11.3 -33.7  50 0 0  0  22.6 0  0 0 -50       $ -z side of shield
c --------- Detector Surfaces ---------------------
100 RCC  378    0    0       20    0    0     40         $ 0 deg detector
30  RCC  347.86 0  112.5     17.32 0   10     40    $ 30 deg detector
60  RCC  265.5  0  194.86    10    0   17.32  40    $ 60 deg detector
90  RCC  153    0  225        0    0   20     40         $ 90 deg detector
120 RCC  40.5   0  194.86   -10    0   17.32  40    $ 120 deg detector
150 RCC -149.16 0  126.5    -18.51 0    7.56  40 $ 150 deg detector
212 RCC -149.16 0 -126.5    -18.51 0   -7.56  40 $ 210 deg detector
240 RCC  40.5   0 -194.86   -10    0  -17.32  40    $ 240 deg detector
270 RCC  153    0 -225        0    0  -20     40         $ 270 deg detector
300 RCC  265.5  0 -194.86    10    0  -17.32  40    $ 300 deg detector
330 RCC  347.86 0 -112.5     17.32 0  -10     40    $ 330 deg detector
c ---------end surface cards-------------------------------

c --------Material Cards----------------------------------
m1 6000.60c .0001 7014.60c .755 8016.60c .232 18000 .013                $ air p=0.0012
m2 26000 0.9959 6000.60c 0.0032 16032.60c 0.0005 15031.60c 0.0004 $ carbon steel p=7.87
m3 6000.60c 0.143 7014.60c 0.285 8016.60c 0.286 1001.60c 0.286         $ RDX p=1.82
m4 1001.60c -0.0275 6000.60c -0.0825 26000 -0.89        $ 1/2 poly, 1/2 steel by volume, p=4.405
m5 1001.60c 0.47619 6000.60c 0.285714 8016.60c 0.238095              $ newspaper: p~=0.65
m6 1001.60c 0.2938 6000.60c 0.0187 8016.60c 0.5045 13027.60c 0.0259 &
   14028 0.1354 19000.60c 0.0143 26056.60c 0.0027     $ soil EPA GR 12 standard p=1.75
m7 1001.60c 0.304 6000.60c 0.00287 8016.60c 0.4987 11023 0.009179 &
  13027.60c 0.0103 14000.60c 0.151 19000.60c 0.00711 20000 0.014882 &
  26000 0.001599                                                 $ ordinary concrete p= 2.3
m8 1001.60c 0.548 6000.60c 0.452                                 $ EJ 309 p=0.916
m9 13027.60c 1.0                                                 $ Aluminum for truck deck p=2.7
```

```
m10 1001.60c 0.5 6000.60c 0.3125 16032.60c 0.1875          $ Vulcanized Rubber p=1.5
c ------- End Material Cards -----------------------------
c ------- Data Cards -------------------------------------
mode n p
nps 100000000                              $ number of histories
PHYS:N  J     20                           $ needed for analog mcnp
PHYS:P  J     1                            $ needed for analog mcnp
CUT:N   2J    0                            $ needed for analog mcnp
CUT:P   2J    0                            $ needed for analog mcnp
RPOL 0.010 0.010                           $ RPOL (1)(2) = n,p cutoff E
IPOL 0 1 1 1 2J 6 100 30 60 90 120 150 $ collect data from 6 det cells
FILES 21 DUMN1                             $ for output files
DBCN                                       $ debug parallelizing
PRDMP 2J 1                                 $ dump data file
sdef POS=-204.9 0 0 PAR=1 ERG=14.1 $ monoenergetic conical 14.1 MeV neutron source
e0 .2 .4 .6 .8 1 69I 15 20                 $ 0.2 MeV Energy Bins
c ---------- End Data Cards ------------------------------
c ---------- Tally Cards ---------------------------------
c f1 current tallies
f11:n 100.3       $ 0 deg detector, neutron
f21:p 100.3       $ 0 deg detector, photon
f31:n 30.3        $ 30 deg detector, neutron
f41:p 30.3        $ 30 deg detector, photon
f51:n 60.3        $ 60 deg detector, neutron
f61:p 60.3        $ 60 deg detector, photon
f71:n 90.3        $ 90 deg detector, neutron
f81:p 90.3        $ 90 deg detector, photon
f91:n 120.3       $ 120 deg detector, neutron
f101:p 120.3      $ 120 deg detector, photon
f111:n 150.3      $ 150 deg detector, neutron
f121:p 150.3      $ 150 deg detector, photon
f131:n 212.3      $ 210 deg detector, neutron
f141:p 212.3      $ 210 deg detector, photon
f151:n 240.3      $ 240 deg detector, neutron
f161:p 240.3      $ 240 deg detector, photon
f171:n 270.3      $ 270 deg detector, neutron
f181:p 270.3      $ 270 deg detector, photon
f191:n 300.3      $ 300 deg detector, neutron
f201:p 300.3      $ 300 deg detector, photon
f211:n 330.3      $ 330 deg detector, neutron
f221:p 330.3      $ 330 deg detector, photon
c ------End Tally Cards ---------
```

Appendix B: Code Used in Data Analysis

EJ-309 data parsing and PHD analysis

Explosives Detection Algorithm (MATLAB)

Sample main algorithm

```
%%%%%%%%%%%%%%%%%%%%%%%%%
%% Explosives Detection Algorithm (main)   %%
%%    Algorithm                            %%
%% Adrienne Lehnert                        %%
%%    April 15, 2011                       %%
%%%%%%%%%%%%%%%%%%%%%%%%%
clear
clc
DATA=zeros(77,28,5); % initialize array for data (detector tallies at 5 positions)

Input = csvread('P5V.csv',0,0);
DATA(:,:,1)=Input(1:77,:);
DATA(:,:,2)=Input(78:154,:);
DATA(:,:,3)=Input(155:231,:);
DATA(:,:,4)=Input(232:308,:);
DATA(:,:,5)=Input(309:385,:);

[FlagLabels,AllFlags,FlagError]=AlgFlagMaker(DATA); %% Calculate the values of all flags and return with labels
[M]=MaterialFinal(AllFlags); %% Find the material type
[TriggersPD,r,TriggerLabels,TrigErrorPD,Triggers,P,TV,TriggerError]=TriggerFinal(AllFlags,FlagLabels,FlagError,M); % Do the trigger calculations

if (P==3 && TV>0.2) || (P~=3 && TV>0.1)
   [status]=DensityFinal(AllFlags,M);
end

Error=zeros(204,2);
for i=1:204
   Error(i,1)=mean(AllFlags(i,:));
   Error(i,2)=mean(FlagError(i,:));
end
```

Flag calculator (spectroscopic algorithm)

```
%%%%%%%%%%%%%%%%%%%%%%%%%%%
%% Calculates flags for detection algorithm        %%
%% Adrienne Lehnert                                %%
%% 1/23/11                                         %%
%%%%%%%%%%%%%%%%%%%%%%%%%%%

function [AlgFlagLabels,AlgFlags,AlgFlagError]=AlgFlagMaker(DATA)

AlgFlags=zeros(33,5);
AlgFlagError=zeros(33,5);
RELERROR=zeros(77,14,5); % relative error matrix
ABSERROR=zeros(77,14,5); % absolute error matrix
TALLY=zeros(77,8,5); % neutron and photon tally matrix

TALLY(:,1:7,:)=DATA(:,1:7,:); % populate neutron tallies
RELERROR(:,:,:)=DATA(:,15:28,:); % populate neutron and photon relative error
ABSERROR(:,:,:)=DATA(:,15:28,:).*DATA(:,1:14,:); % % populate neutron and photon absolute
error

for j=1:5
   for i=1:77
      TALLY(i,8,j)=sum(DATA(i,8:14,j)); % populate photon tally with sum of all photon tallies
      ABSERROR(i,8,j)=(sum((ABSERROR(i,8:14,j).^2)))^0.5; % calculate absolute error for
combined photons
      RELERROR(i,8,j)=ABSERROR(i,8,j)/TALLY(i,8,j); % calculate relative error for combined
photons
   end
end

ABSERROR(:,9:14,:)=[]; % truncate error matrices
RELERROR(:,9:14,:)=[];


%% Create Flag Labels
AlgFlagLabels{1,1}='(10.8 MeV,150 deg)/(10.8 MeV,0 deg)';
AlgFlagLabels{2,1}='(11 MeV,150 deg)/(11 MeV,0 deg)';
…
AlgFlagLabels{33,1}='(>10,150)/(<1,0)';
% End FlagLabel creation%%%

%% Integrate spectrum
for k=1:5
   % Calculate combinatory relative errors for combinatory flags, these are
   % temporary and are recalculated each time through the loop
   Cgam=RELERROR(23,8,k);
   Ngam=((ABSERROR(12,8,k)^2+ABSERROR(26,8,k)^2)^0.5)/(TALLY(12,8,k)+TALLY(26,8,k));
   Ogam=RELERROR(31,8,k);
   LT1=zeros(1,7);
   LT3=zeros(1,7);
   GT10=zeros(1,7);
   E4t8=zeros(1,7);
   E6t10=zeros(1,7);
```

```
    z=isnan(RELERROR);   % clean up NANs
    RELERROR(z)=0;
    z=isnan(ABSERROR);
    ABSERROR(z)=0;

    for j=1:7  % also temporary, so recalculate
        LT1(1,j)=(sum(ABSERROR(1:5,j).^2)^0.5)/(sum(TALLY(1:5,j)));
        LT3(1,j)=(sum(ABSERROR(1:15,j).^2)^0.5)/(sum(TALLY(1:15,j)));
        GT10(1,j)=(sum(ABSERROR(50:76,j).^2)^0.5)/(sum(TALLY(50:76,j)));
        E4t8(1,j)=(sum(ABSERROR(21:40,j).^2)^0.5)/(sum(TALLY(21:40,j)));
        E6t10(1,j)=(sum(ABSERROR(31:50,j).^2)^0.5)/(sum(TALLY(31:50,j)));
    end

    %% Calculate Flags %%
    AlgFlags(1,k)=TALLY(54,6,k)/TALLY(54,1,k);
    AlgFlags(2,k)=TALLY(55,6,k)/TALLY(55,1,k);
    …
    AlgFlags(32,k)=(sum(TALLY(31:50,6,k)))/(sum(TALLY(31:50,1,k)));
    AlgFlags(33,k)=(sum(TALLY(50:76,6,k)))/(sum(TALLY(1:5,1,k)));
    % Finished calculating flags

    %% Calculate Flag Error
    AlgFlagError(1,k)=((RELERROR(54,6,k)^2)+(RELERROR(54,1,k)^2))^0.5;
    AlgFlagError(2,k)=((RELERROR(55,6,k)^2)+(RELERROR(55,1,k)^2))^0.5;
…
    AlgFlagError(33,k)=((GT10(1,6)^2)+(LT1(1,1)^2))^0.5;
    % Finished Calculating Flag Error

    %% Clean up
    y=isinf(AlgFlags);% clean up NANs from 180 deg flags
    z=isnan(AlgFlags);
    AlgFlags(y)=0;
    AlgFlags(z)=0;
    y=isnan(AlgFlagError);
    z=isinf(AlgFlagError);
    AlgFlagError(y)=0;
    AlgFlagError(z)=0;
    clear y z
end

return
```

Materials identification

```
%%%%%%%%%%%%%%%%%%%%%%%%%%%%
%% Flag Algorithm for Explosives Detection       %%
%%      Material type definitions                      %%
%%          Adrienne Lehnert                          %%
%%            April 20, 2010                             %%
%%%%%%%%%%%%%%%%%%%%%%%%%%%%

function [M,MFlag_avg]=MaterialFinal2(AlgFlags)
MFlag=zeros(5,5);
MFlag_avg=zeros(5,1);
for i=1:5   %% Isolate material flag values and calculate averages
   MFlag(1,i)=AlgFlags(30,i);  % >10 MeV:150/0
   MFlag(2,i)=AlgFlags(32,i);  % 6-10 MeV:150/0
   MFlag(3,i)=AlgFlags(29,i);  % >10 MeV:120/0
   MFlag(4,i)=AlgFlags(4,i);   % (11.4 MeV,120 deg)/(11.4 MeV,0 deg)
   MFlag(5,i)=AlgFlags(6,i);   % (11.0 MeV, 150 deg)/(0.8 MeV, 0 deg)
end

for j=1:5
   MFlag_avg(j,1)=mean(MFlag(j,:)); % find the averages for all the material flags
end

if max(MFlag_avg)>11
%     disp('Cargo is Organic/Hydrogenous');
   M=1;
elseif (MFlag_avg(2,1)/MFlag_avg(4,1))>1.5
%     disp('Cargo is Inorganic/Metallic');
   M=2;
elseif (MFlag_avg(4,1)/MFlag_avg(3,1))>4.5 || (MFlag_avg(4,1)/MFlag_avg(3,1))<1.4
%     disp('Cargo is Organic/Hydrogenous');
   M=1;
elseif sum(MFlag_avg(:,1))>50
%     disp('Cargo is Organic/Hydrogenous');
   M=1;
else
%     disp('Cargo is Inorganic/Metallic');
   M=2;
end

return
```

Correcting for inert, dense objects in containers

```
%%%%%%%%%%%%%%%%%%%%%%%%%%%%
%% Flag Algorithm for Explosives Detection       %%
%%       Density Flag calculations               %%
%%          Adrienne Lehnert                     %%
%%            April 20, 2011                     %%
%%%%%%%%%%%%%%%%%%%%%%%%%%%%

function [status]=DensityFinal(AllFlags,M)
Indep=zeros(6,5);
Dep=zeros(6,5);

% Get density-Indepdent flags
if M==1 % get organic/hydrogenous density-independent flags
   Indep(1,:)=AllFlags(137,:);
   Indep(2,:)=AllFlags(139,:);
   Indep(3,:)=AllFlags(142,:);
   Indep(4,:)=AllFlags(146,:);
   Indep(5,:)=AllFlags(149,:);
   Indep(6,:)=AllFlags(151,:);
end

if M==2 % get metallic/inorganic flags
   Indep(1,:)=AllFlags(167,:);
   Indep(2,:)=AllFlags(168,:);
   Indep(3,:)=AllFlags(169,:);
   Indep(4,:)=AllFlags(172,:);
   Indep(5,:)=AllFlags(173,:);
   Indep(6,:)=AllFlags(174,:);
end

% Get density-dependent flags
if M==1 % get organic/hydrogenous density-independent flags
   Dep(1,:)=AllFlags(132,:);
   Dep(2,:)=AllFlags(134,:);
   Dep(3,:)=AllFlags(140,:);
   Dep(4,:)=AllFlags(141,:);
   Dep(5,:)=AllFlags(147,:);
   Dep(6,:)=AllFlags(148,:);
end

if M==2 % get metallic/inorganic flags
   Dep(1,:)=AllFlags(132,:);
   Dep(2,:)=AllFlags(134,:);
   Dep(3,:)=AllFlags(140,:);
   Dep(4,:)=AllFlags(141,:);
   Dep(5,:)=AllFlags(147,:);
   Dep(6,:)=AllFlags(148,:);
end

[ri,ci]=size(Indep);
[rd,cd]=size(Dep);
Indep_avg=zeros(ri,1); % Initialize Trigger avg flag values
```

```
Dep_avg=zeros(rd,1);
IndepPD=zeros(ri,ci);  % initiate percent difference matrix
DepPD=zeros(rd,cd);

for i=1:ri  % Calculate average values of trigger flags
   Indep_avg(i,1)=mean(Indep(i,:));
   IndepPD(i,:)=abs(Indep(i,:)-Indep_avg(i,1))./Indep_avg(i,1);
end
for i=1:rd
   Dep_avg(i,1)=mean(Dep(i,:));
   DepPD(i,:)=abs(Dep(i,:)-Dep_avg(i,1))./Dep_avg(i,1);
end
x=isnan(IndepPD);
y=isnan(DepPD);
Indep(x)=0;
DepPD(y)=0;

for j=1:6
   IndepPD(j,:)=IndepPD(j,:)-min(IndepPD(j,:));
   DepPD(j,:)=DepPD(j,:)-min(DepPD(j,:));
end

if mean(IndepPD)>mean(DepPD)  %% Determine if the object is explosive or benign
   status=1;
else
   status=0;
end

return
```

10% Perturbation of Simulation Data (MATLAB)

```
%%%%%%%%%%%%%%%%%%%%%%%%%%%%%%%%%%%%
% Make new PHD data with up to 10% standard deviation      %%
%              Adrienne Lehnert                             %%
%                 08/30/11                                  %%
%%%%%%%%%%%%%%%%%%%%%%%%%%%%%%%%%%%%

clear
clc

% fid1=fopen('tallyfiles.txt');
% fid2=fopen('PHDfiles.txt');
%
% inputs1=textscan(fid1,'%s');
% inputs1=inputs1{1};
% inputs2=textscan(fid2,'%s');
% inputs2=inputs2{1};
% fclose(fid1);
% fclose(fid2);
% length(inputs1)
% out=cell(1,20);

% for k=1:length(inputs1)

TrueTally=zeros(77,28,5);   % initialize array for tally data (detector tallies at 5 positions)
TruePHD=zeros(1000,6,5);    % initialize array for PHD data (6 detectors at 5 positions)

Input = csvread('P32V_tally.csv',0,0);
Input2= csvread('P32V_nPHD.csv',0,0);
TrueTally(:,:,1)=Input(1:77,1:28);
TrueTally(:,:,2)=Input(78:154,1:28);
TrueTally(:,:,3)=Input(155:231,1:28);
TrueTally(:,:,4)=Input(232:308,1:28);
TrueTally(:,:,5)=Input(309:385,1:28);
TruePHD(:,:,1)=Input2(1:1000,1:6);
TruePHD(:,:,2)=Input2(1001:2000,1:6);
TruePHD(:,:,3)=Input2(2001:3000,1:6);
TruePHD(:,:,4)=Input2(3001:4000,1:6);
TruePHD(:,:,5)=Input2(4001:5000,1:6);

n=4000; %%% Input the number of iterations with 10% standard deviation

MeasTally=zeros(77,28,5,n);
MeasPHD=zeros(1000,6,5,n);

for i=1:n              %%% Create data with 10% standard deviation gaussian
   R1=randn(77,14,5);  % random fluctuation in tally data
   MeasTally(:,1:14,:,i)=TrueTally(:,1:14,:)+(TrueTally(:,1:14,:).*(R1.*0.1));
   MeasTally(:,15:28,:,i)=TrueTally(:,15:28,:);
   R2=randn(1000,6,5); % random flucturation in PHD data
   MeasPHD(:,:,:,i)=TruePHD+(TruePHD.*(R2.*0.1));
end

MeasTally(77,:,:,:)=sum(MeasTally(1:76,:,:,:)); %%% Correct sum
```

```
%% Calculate the flag values and triggers for the original data
TDATA=zeros(77,28,5);
PHDData=zeros(1000,6,5);

[FlagLabels,TrueFlags_s,TrueError]=AlgFlagMaker(TrueTally);
[M_s]=MaterialFinal(TrueFlags_s);
[TrueTriggersPD,r,TriggerLabels,TrueTrigErrorPD,Triggers,P_s,TV_s]=TriggerFinal(TrueFlags_s,
FlagLabels,TrueError,M_s);
%
[TrueTriggersPD,r,TriggerLabels,TrueTrigErrorPD,Triggers,P_s,TV_s]=TriggerFinal(TrueFlags_s,
FlagLabels,TrueError,2);

[PHDFlags,PHDLabels]=PHDFlagMakerFINAL(TrueTally,TruePHD);  %% Calculate the values of
all flags and return with labels
[M_PHD,MFlag_PHDavg]=MaterialPHD(PHDFlags);             %% Find material type using non-
spectroscopic n flags
[TrigPD_PHD,TriggerLabels_PHD,Triggers_PHD,P_PHD,TV_PHD]=TriggerPHD(PHDFlags,PHD
Labels,M_PHD);
%
[TrigPD_PHD,TriggerLabels_PHD,Triggers_PHD,P_PHD,TV_PHD]=TriggerPHD(PHDFlags,PHD
Labels,2);
TVs_True=TV_s;
P_True=P_PHD;
TVphd_True=TV_PHD;
r=size(TrigPD_PHD,1);

%% initialize the variables for iterations of the noisy data
MeasFlags_s=zeros(33,5,n);
MeasError_s=zeros(33,5,n);
MeasTrigPD_s=zeros(10,5,n);
MeasTrigError_s=zeros(10,5,n);
TriggerResults_s=zeros(n,2);
pos_s=0;
triggered_s=zeros(n,1);

MeasFlags_PHD=zeros(26,5,n);
MeasError_PHD=zeros(26,5,n);
MeasTrigPD_PHD=zeros(r,5,n);
MeasTrigError_PHD=zeros(r,5,n);
TriggerResults_PHD=zeros(n,2);
pos_PHD=0;
triggered_PHD=zeros(n,1);

%% Calculate the Flag values and triggers for each iteration
M_spec=2;
M_PHD=2;
for i=1:n
   TDATA=MeasTally(:,:,:,i);
   PHDData=MeasPHD(:,:,:,i);

   % Spectroscopic detection algorithm
   [FlagLabels,AlgFlags,FlagError]=AlgFlagMaker(TDATA);    %% Calculate the values of all flags
and return with labels
   [M_spec,MFlag_avg]=MaterialFinal2(AlgFlags);           %% Find the material type using n
spectroscopic flags
```

```
[TrigPD_s,r_s,TriggerLabels_s,TrigErrorPD_s,Triggers_s,P_s,TV_s,TriggerError_s]=TriggerFinal(
AlgFlags,FlagLabels,FlagError,M_spec); % Do the trigger calculations
    MeasFlags_s(:,:,i)=AlgFlags;
    MeasTrigPD_s(:,:,i)=TrigPD_s;
    TriggerResults_s(i,1)=P_s;
    TriggerResults_s(i,2)=TV_s;
    if ((P_s==1 || P_s==5) && TV_s>0.2) || ((P_s==2 || P_s==3 || P_s==4) && TV_s>0.1)
        [status_s]=DensityFinal(AlgFlags,M_spec);
        triggered_s(pos_s+1)=P_s;
        pos_s=pos_s+1;
    end

    % PHD detection algorithm
    [PHDFlags,PHDLabels]=PHDFlagMakerFINAL(TDATA,PHDData);  %% Calculate the values
of all flags and return with labels
    [M_PHD,MFlag_PHDavg]=MaterialPHD(PHDFlags);             %% Find material type using non-
spectroscopic n flags

[TrigPD_PHD,TriggerLabels_PHD,Triggers_PHD,P_PHD,TV_PHD]=TriggerPHD(PHDFlags,PHD
Labels,M_PHD);
    MeasFlags_PHD(:,:,i)=PHDFlags;
    MeasTrigPD_PHD(:,:,i)=TrigPD_PHD;       %% Problem here
    TriggerResults_PHD(i,1)=P_PHD;
    TriggerResults_PHD(i,2)=TV_PHD;
    if ((P_PHD==1 || P_PHD==5) && TV_PHD>0.2) || ((P_PHD==2 || P_PHD==3 || P_PHD==4)
&& TV_PHD>0.1)
        [status_PHD]=DensityPHD(PHDFlags,M_PHD);
        triggered_PHD(pos_PHD+1)=P_PHD;
        pos_PHD=pos_PHD+1;
    end


end
```